

Moussa Labbadi · Kamal Elyaalaoui ·
Loubna Bousselamti ·
Mohammed Ouassaid ·
Mohamed Cherkaoui

Modeling, Optimization and Intelligent Control Techniques in Renewable Energy Systems

An Optimal Integration Of Renewable
Energy Resources Into Grid

Studies in Systems, Decision and Control

Volume 434

Series Editor

Janusz Kacprzyk, Systems Research Institute, Polish Academy of Sciences,
Warsaw, Poland

The series “Studies in Systems, Decision and Control” (SSDC) covers both new developments and advances, as well as the state of the art, in the various areas of broadly perceived systems, decision making and control—quickly, up to date and with a high quality. The intent is to cover the theory, applications, and perspectives on the state of the art and future developments relevant to systems, decision making, control, complex processes and related areas, as embedded in the fields of engineering, computer science, physics, economics, social and life sciences, as well as the paradigms and methodologies behind them. The series contains monographs, textbooks, lecture notes and edited volumes in systems, decision making and control spanning the areas of Cyber-Physical Systems, Autonomous Systems, Sensor Networks, Control Systems, Energy Systems, Automotive Systems, Biological Systems, Vehicular Networking and Connected Vehicles, Aerospace Systems, Automation, Manufacturing, Smart Grids, Nonlinear Systems, Power Systems, Robotics, Social Systems, Economic Systems and other. Of particular value to both the contributors and the readership are the short publication timeframe and the world-wide distribution and exposure which enable both a wide and rapid dissemination of research output.

Indexed by SCOPUS, DBLP, WTI Frankfurt eG, zbMATH, SCImago.

All books published in the series are submitted for consideration in Web of Science.

More information about this series at <https://link.springer.com/bookseries/13304>

Moussa Labbadi · Kamal Elyaalaoui ·
Loubna Bousselamti · Mohammed Ouassaid ·
Mohamed Cherkaoui

Modeling, Optimization and Intelligent Control Techniques in Renewable Energy Systems


An Optimal Integration Of Renewable Energy
Resources Into Grid

Moussa Labbadi
INSA Hauts-de-France
Université Polytechnique Hauts-de-France
Valenciennes, France

Loubna Bousselamti
Mohammed V University in Rabat
Rabat, Morocco

Mohamed Cherkaoui
Mohammed V University in Rabat
Rabat, Morocco

Kamal Elyalaoui
Mohammed V University in Rabat
Rabat, Morocco

Mohammed Ouassaid 
Mohammed V University in Rabat
Rabat, Morocco

ISSN 2198-4182

Studies in Systems, Decision and Control

ISBN 978-3-030-98736-7

<https://doi.org/10.1007/978-3-030-98737-4>

ISSN 2198-4190 (electronic)

ISBN 978-3-030-98737-4 (eBook)

© The Editor(s) (if applicable) and The Author(s), under exclusive license to Springer Nature Switzerland AG 2022

This work is subject to copyright. All rights are solely and exclusively licensed by the Publisher, whether the whole or part of the material is concerned, specifically the rights of translation, reprinting, reuse of illustrations, recitation, broadcasting, reproduction on microfilms or in any other physical way, and transmission or information storage and retrieval, electronic adaptation, computer software, or by similar or dissimilar methodology now known or hereafter developed.

The use of general descriptive names, registered names, trademarks, service marks, etc. in this publication does not imply, even in the absence of a specific statement, that such names are exempt from the relevant protective laws and regulations and therefore free for general use.

The publisher, the authors and the editors are safe to assume that the advice and information in this book are believed to be true and accurate at the date of publication. Neither the publisher nor the authors or the editors give a warranty, expressed or implied, with respect to the material contained herein or for any errors or omissions that may have been made. The publisher remains neutral with regard to jurisdictional claims in published maps and institutional affiliations.

This Springer imprint is published by the registered company Springer Nature Switzerland AG
The registered company address is: Gewerbestrasse 11, 6330 Cham, Switzerland

Preface

The present book *Modeling, Optimization and Intelligent Control Techniques in Renewable Energy Systems—An Optimal Integration Of Renewable Energy Resources Into Grid* publishes a good work in the field of renewable energy and control, presented in an informal and high-quality manner. The book's content is fascinating and appealing because it covers a wide range of technologies and control techniques, such as advanced robust control, intelligent control methods, wind farm, fractional-order controllers, algorithm optimizations, PV-CSP hybridization, thermal energy storage, dispatching strategy, modeling, mono-objective optimization and multi-objective optimization.

The goal is to include the theory, applications and perspectives on current and future advancements in renewable energy control and optimization, variable converters and related domains, as well as the paradigms and methodologies that underpin them.

The chapters in this book are written for graduate students, researchers, educators, engineers and scientists who need to know about mathematical analysis theories, methods and applications.

This book provides two parts. It has a total of 11 chapters, which are organized as follows: the first part focuses on applications of control theory on wind turbine and comprises six chapters.

The chapter *Introduction to Power System Stability and Wind Energy Conversion System* discusses the power system stability and the identification of the many forms and causes of instabilities in the power system such as voltage and frequency instability, as well as the frequency control types and the active power management capability constraints. The description of the grid code requirements for integration of wind energy conversion system into grid will be presented.

The chapter *Description and Modeling of Wind Energy Conversion System* presents the modeling of the different elements of the variable speed wind power system based on a squirrel cage induction generator, as well as modeling of grid, filters, transformer and transmission line. The infinite grid model, dynamic grid model, RL filter model and LCL filter model are considered. These models are developed in the (d, q) reference frame, using the Park transformation.

The chapter *Power Quality Improvement of Wind Energy Conversion System Using a Fuzzy Nonlinear Controller* proposes a fuzzy sliding mode control (Fuzzy-SMC) using a smooth function based on fuzzy logic. The proposed control algorithm is used to control the wind energy conversion system connected into the grid through a LCL filter with passive damping and to reduce the harmonics due to the chattering phenomenon. The proposed control system is validated by the numerical simulation and also validated experimentally using a test bench based on DSPace Board and three-phase inverter.

The chapter *Supervisory and Power Control Systems of a WF for Participating in Auxiliary Services* investigates a fuzzy PIFPI controller for reactive power and LVRT control in an uncompensated power system. The supervision system based on proportional distribution algorithm, according to three operating modes (MPPT control mode, PQ control mode and fault control mode) is developed to ensure the optimal operation of grid-connected wind farm based on the squirrel cage induction generator.

The chapter *LVRT Control Using an Optimized Fractional Order Fuzzy Controller of a Wind Farm* proposes the fractional order fuzzy controller (FOPI-Fuzzy-FOPI) to improve the voltage and reactive power responses and studies the problem of voltage drop in an uncompensated power system. The supervisory system ensures the cooperation between the different parts of the wind farm system and the optimal interaction between the wind turbines.

The chapter *Primary Frequency Control for Wind Farm Using a Novel PI Fuzzy PI Controller* addresses the participation of the wind farm in primary frequency control using inertial power reserve supported by pitch control strategy. The proposed PI-Fuzzy-PI (PIFPI) controller for primary frequency control ensures the balance between power demand and power production, provides high performance and satisfies the grid code requirements. The WF of 90 MW capacity is aggregated into a multi-machine model. It consists of 3 equivalent wind turbines based on squirrel cage induction generator and is connected to two grid areas.

The second part of this book includes five chapters and emphasis on the modeling and optimization of hybrid photovoltaic (PV)-concentrated solar power (CSP) systems coupled to a thermal energy storage system.

The chapter *Hybridization PV-CSP: An Overview* investigates an overview of hybrid photovoltaic (PV)-concentrated solar power (CSP) system. The challenges that can be addressed based on the world energy context are presented. In this context, renewable energy sources are presented as an ecological and economical alternative to fossil energies for the production of electricity. Then, the issues and proposed solution related to the grid integration of renewable energy sources are discussed. Finally, a survey of the literature on hybridization PV-CSP is presented.

The chapter *Detailed Modeling of Hybrid PV-CSP Plant* focuses on modeling of hybrid PV-CSP systems. Firstly, the mathematical model is presented to calculate the hourly electrical power produced by the PV plant and the hourly electrical power generated by the solar field of the CSP plant based on parabolic trough technology. Finally, a dispatch strategy is proposed in order to manage the power flows in the hybrid PV-CSP system to supply the requested load.

The chapter *Techno-economic Parametric Study of Hybrid PV-CSP Power* proposes a parametric study of three main solar plants (PV, CSP and hybrid PV-CSP). This study focuses on evaluating the influence of decision parameters (PV orientation angles, solar multiple (SM), thermal energy storage capacity (TES) and fraction of hybridization) on solar power plants, by calculating the electrical annual energy and electricity cost. Several simulations have been established and discussed in detail to evaluate the optimal configuration of the PV-CSP in comparison with PV plant and CSP plant.

The chapter *Optimal PV-CSP System Sizing Using Mono Objective Optimisation* addresses a mono objective optimization model to find the optimum size of hybrid PV-CSP plant so as to meet the requested load with possible minimum electricity cost and highest efficiency. Hybrid particle swarm optimization (PSO)–Cuckoo search (CS) algorithm have been used through this model for determining the optimum size of the PV-CSP system, and the minimum electricity cost at a pre-determined level of capacity factor value, in order to satisfy two types of requested load.

The chapter *The Multi-objective Optimization of PV-CSP Hybrid System with Electric Heater* presents a multi-objective optimization approach of the hybrid PV-CSP system coupled to an electric heater (EH), which is used to convert the excess electrical energy from the PV plant into thermal energy that will be stored for later use. Therefore, a model of the PV-CSP-EH plant was established and a multi-objective optimization using the genetic algorithm was adopted. The purpose of the optimization is to minimize the electricity cost and dumped energy and to maximize the capacity factor simultaneously. The Final optimal configurations are obtained from the Pareto front by applying a decision-making method.

Valenciennes, France
Rabat, Morocco
Rabat, Morocco
Rabat, Morocco
Rabat, Morocco
December 2021

Moussa Labbadi
Kamal Elyaalaoui
Loubna Bousselamti
Mohammed Ouassaid
Mohamed Cherkaoui

Acknowledgements

My special thanks go to my parents, my brother and my friends for their moral and encouragement.

Valenciennes, France

Moussa Labbadi

My special thanks go to all members of my family, my father Mohamed Elyaalaoui, who passed away too early, my mother, my friends for their support and baby Joudi, who was born at the same time as this book.

Rabat, Morocco

Kamal Elyaalaoui

Thanks first and last to Allah for the utmost help and support during this work. Thanks to my parents, my sisters, my brother and my friends, without their support and most of all love, the completion of this work would not have been possible.

Rabat, Morocco

Loubna Bousselamti

Contents

Part I Intelligent Control on Wind Farm

1	Introduction to Power System Stability and Wind Energy Conversion System	3
1.1	Introduction	3
1.2	Stability of the Electrical Power System	4
1.3	Power System Stability and Wind Energy Conversion System	4
1.4	Voltage Dips and Grid Code Requirements	5
1.4.1	Voltage Stability	6
1.4.2	Types of Voltage Stability	6
1.4.3	Main Causes of Voltage Instability	7
1.4.4	Grid Code Requirements for Voltage Dip	8
1.5	Frequency Stability and Grid Code Requirements	8
1.5.1	Main Causes of Frequency Instability	9
1.5.2	Example of Frequency Instability	10
1.5.3	Grid Code Requirements	12
1.5.4	Frequency Control	13
1.6	Conclusion	15
	References	16
2	Description and Modeling of Wind Energy Conversion System	19
2.1	Introduction	19
2.2	Wind Turbine	20
2.2.1	Modeling of Turbine in Per Unit Notation	20
2.2.2	Modeling of the Shaft in Per-unit System	22
2.3	Modeling of the Squirrel-Cage Asynchronous Generator in the Park Reference Frame	22
2.3.1	Modeling of SCIG in the Park Reference Frame	23
2.3.2	Electrical Equations of Generator in Park Reference Frame	23

2.3.3	Per-unit System for Modeling	23
2.3.4	Electromagnetic Torque and Power	25
2.4	Modeling of the RL Filter in pu System	26
2.5	Modeling of Transformer and Transmission Line	27
2.5.1	Transformer Model	27
2.5.2	Transmission Line Model	28
2.6	Modeling of the LCL Filter	28
2.6.1	Model of LCL Filter in (abc) Reference Frame	29
2.6.2	Model of LCL Filter in Park Reference Frame	30
2.7	Electrical Power Network	31
2.7.1	Infinite Grid Model	31
2.7.2	Dynamic Model of Grid	31
2.8	Conclusion	32
	References	32
3	Power Quality Improvement of Wind Energy Conversion System Using a Fuzzy Nonlinear Controller	35
3.1	Introduction	35
3.2	Modeling of Grid-Side System	35
3.2.1	Modeling of DC Bus	35
3.2.2	Model of Filter	38
3.3	SMC of Grid-Side Converter	39
3.3.1	SMC of Grid-Side Current	39
3.3.2	Analysis of System Stability	41
3.3.3	Sliding Mode Control of Grid Current Without RC Sensor	43
3.3.4	Fuzzy Smooth Function of FSMC	43
3.3.5	FSMC Stability Analysis	44
3.4	Simulation Validation	46
3.4.1	Comparative Study of Filters and Their Control Systems	46
3.4.2	Robustness Test Against Variation of Parameters	49
3.5	Experimental Validation Approach	52
3.5.1	Comparative Study Between RL Filter and LCL Filter	52
3.5.2	Comparative Study for Control Methods Using LCL Filter	53
3.5.3	Robustness Test	54
3.6	Conclusion	55
	References	61

4	Supervisory and Power Control Systems of a WF for Participating in Auxiliary Services	63
4.1	Introduction	63
4.2	Wind Farm Supervision System	64
4.2.1	Power Dispatching Using Proportional Distribution Algorithm	64
4.2.2	Supervisory System Configuration	65
4.3	Transient Control Modes of Wind Turbines	69
4.3.1	MPPT Control Mode	69
4.3.2	PQ Control Mode	69
4.3.3	Fault Control Mode	70
4.3.4	Validation and Discussion	71
4.4	Fault Control Strategy Using Hierarchical Fuzzy Controller	77
4.4.1	Dynamic Model of Grid for Voltage-Reactive Power Control	77
4.4.2	Voltage Control at PCC	79
4.4.3	Proposed Fuzzy Hierarchical Controller	80
4.4.4	Validation and Discussion	82
4.5	Conclusion	85
	References	86
5	LVRT Control Using an Optimized Fractional Order Fuzzy Controller of a Wind Farm	87
5.1	Introduction	87
5.2	Wind Farm Management According to Grid Code Recommendations	88
5.2.1	Central Supervision Unit	88
5.2.2	Local Supervision Unit	88
5.2.3	System Protection	89
5.3	Power System Modeling	89
5.3.1	Objectives of the Study and Choice of Model Type	89
5.4	Wind Farm Management According to Grid Code Requirements	91
5.4.1	Grid Code Requirements	91
5.5	Proposed Fault Control Strategy	92
5.5.1	Voltage Control	92
5.5.2	Design of Fractional Order PIFO-Fuzzy-PIFO Controller	92
5.5.3	Fractional Order Preliminaries	94
5.5.4	Proposed FOPI-Fuzzy-FOPI Fractional Order Controller	95

5.6	Validation and Discussion	96
5.6.1	Comparative Study of Voltage and Reactive Power Responses	98
5.6.2	Performance of the Supervision System	101
5.7	Conclusion	104
	References	105
6	Primary Frequency Control for Wind Farm Using a Novel PI Fuzzy PI Controller	107
6.1	Introduction	107
6.2	Aggregate Model for Frequency-Power Response Study	108
6.2.1	Aggregate Model of the Wind Farm	108
6.2.2	Equivalent Parameters of Aggregated Model	111
6.2.3	Power System Model for Frequency Control	111
6.2.4	Adaptation of Power System Model to Grid Code Recommendations	115
6.3	Proposed Hierarchical Fuzzy Logic Controller for Primary Frequency Control	116
6.3.1	Power Reserve Control	116
6.3.2	Frequency Control	118
6.4	Simulation Results and Discussion	121
6.4.1	Comparative Study of the Frequency and Power Responses	121
6.4.2	Dynamic Behavior of WTs	122
6.5	Conclusion	125
	References	125
 Part II Modeling, Optimization and Sizing of Hybrid PV-CSP Plants PV-CSP Hybrid Plants		
7	Hybridization PV-CSP: An Overview	129
7.1	Introduction	129
7.2	Global Energy Context	129
7.3	Renewable Energies Sources (RES)	131
7.3.1	The Context of Integration of Renewable Energies Sources in the Electrical Grid	131
7.3.2	Issues Related to the Integration of Renewable Energies Sources	131
7.3.3	Proposed Solutions	132
7.4	Solar Energy	133
7.5	Hybrid Energy Systems (HES)	133
7.5.1	PV Hybrid Systems	134
7.5.2	CSP Hybrid Systems	135

7.6	PV-CSP Hybridization	136
7.7	Literature Review on PV-CSP Hybridization	137
7.8	Conclusion	140
	References	140
8	Detailed Modeling of Hybrid PV-CSP Plant	145
8.1	Introduction	145
8.2	Solar Position	145
8.3	PV Model	148
8.4	CSP Model	153
8.5	Dispatch Strategy	161
8.6	Conclusion	161
	References	162
9	Techno-economic Parametric Study of Hybrid PV-CSP Power Plants	165
9.1	Introduction	165
9.2	Technical and Economic Assessment	165
	9.2.1 Technical Assessment	166
	9.2.2 Economic Assessment	166
9.3	Site Selection	168
9.4	Parametric Study of Solar Power Plants	168
	9.4.1 The PV Plant	168
	9.4.2 The CSP Plant	172
	9.4.3 The Hybrid PV-CSP Plant	175
9.5	Findings	179
9.6	Conclusion	180
	References	180
10	Optimal PV-CSP System Sizing Using Mono Objective Optimisation	183
10.1	Introduction	183
10.2	Optimization Problem Statement	183
	10.2.1 Objective Function	183
	10.2.2 Constraint	184
	10.2.3 Decision Variables	184
10.3	Optimization Algorithm	184
10.4	Result and Discussion	188
	10.4.1 Case 1	188
	10.4.2 Case 2	190
	10.4.3 Comparative Study (A PV-CSP Plant and a CSP Plant)	190
10.5	Conclusions	192
	References	192

11	The Multi-objective Optimization of PV-CSP Hybrid System with Electric Heater	195
11.1	Introduction	195
11.2	Literature Review	195
11.3	System Modeling	197
11.4	Optimization Problem Statement	198
11.5	Multi-objective Optimization Algorithm	198
11.6	Multi-criteria Decision-Making Method	199
11.7	Results and Discussion	201
11.8	Conclusions	206
	References	206
12	Summary and Scope	209
12.1	Summary of Full Text	209
12.2	Future Research Prospect	211
Appendix A: Part I: Parameters and Preliminaries of Wind Energy Conversion System and Controllers		213
Appendix B: Part II: Technical and Economic Parameters of PV and CSP Plants		223

Abbreviations

ADC	Analog-to-digital converter
AESO	Alberta Electric System Operator
CF	Capacity factor
CRPC	Constant Reactive Power Control
CSP	Concentrated solar power
DAC	Digital-to-analog converter
DFIG	Double-Fed Asynchronous Generator
EES	Electrical energy storage
EH	Electric heater
ENTSO-E	The European Network of Transmission System Operators for Electricity
FAM	Full Aggregated Model
FLC	Fuzzy Logic Controller
FO	Fractional Order
FOC	Fractional Order Controller
FOPI-fuzzy-FOPI	Fractional-order PI Fuzzy PI controller
Fuzzy-SMC	Fuzzy Sliding Mode Control
GCR	Grid Code Requirements
HES	Hybrid energy systems
HFC	Hierarchical Fuzzy Controller
HRES	Hybrid renewable energy system
IEA	International energy agency
IEC	International Electrotechnical Commission
LCOE	Levelized cost of electricity
LFSM	Limited Frequency Sensitive Mode
LFSM-U	Limited Frequency Sensitive Mode under-frequency
LVRT	Low Voltage Ride through
MMM	Multi-Machine Model
MPPT	Maximum Power Point Tracking
ONEE	Office National of Electricity

PB	Power block
PCC	Point of Common Coupling
PDA	Proportional Distribution Algorithm
PDF	PD-Fuzzy controller
PFC	Primary frequency control
PID	Proportional–Integral–Derivative
PIF	PI-Fuzzy controller
PIFPI	PI-Fuzzy-PI
PMSG	Permanent Magnet Synchronous Generator
PQ control	Active and reactive powers control
PSOA	Particle Swarm Optimization Algorithm
PV	Photovoltaic
PWM	Pulse-Width Modulation
SAM	Semi-Aggregated Model
SCIG	Squirrel Cage Induction Generator
SF	Solar field
SG	Synchronous Generator
SMC	Sliding Mode Control
TES	Thermal energy storage
THD	Total Harmonic Distortion
TSO	Transmission System Operator
UCTE	Union for Coordination of Transmission of Electricity
WPP	Wind Power Plant

Acronyms

System Variables

λ	The speed ratio
β	The blade orientation angle
V_{base}	Base voltage
$V_{nominal}$	Nominal voltage
P_{base}	Base power
$P_{nominal}$	Nominal power
C_{em}	Electromagnetic torque developed by the generator
s	Is the Laplace operator
V_{sd}	d-axis component of stator voltage
V_{sq}	q-axis component of stator voltage
V_{rd}	d-axis component of rotor voltage
V_{rq}	q-axis component of rotor voltage
i_{sd}	d-axis component of stator current
i_{sq}	q-axis component of stator current
i_{rd}	d-axis component of rotor current
i_{rq}	q-axis component of rotor current
ω_s	Stator frequency
ω_g	Grid frequency
P	Active power
Q	Reactive power
ϕ_{sq}	d-axis component of stator flux
ϕ_{sd}	q-axis component of stator flux
ϕ_{rq}	d-axis component of rotor flux
ϕ_{rd}	q-axis component of rotor flux
v_1	Voltages at the output of the filter
v_2	Voltages at the output of the transformer

v_g	Voltages at PCC
i_f	Current flowing through the filter
v_{1d}	d-axis components of grid voltage
v_{1q}	q-axis components of grid voltage
v_{md}	d-axis components of voltage at the converter output
v_{mq}	q-axis components of voltage at the converter output
u_I	Voltages at the filter input
u_G	Voltages at the filter output

Parameters

H_p	Blade inertia constant
H_h	Inertia constant of the hub
H_g	Inertia constant of the generator
f	Coefficient of friction in “pu”
R_s	Stator resistance
R_r	Rotor resistance
l_s	Stator leakage inductance
l_r	Rotor leakage inductance
L_m	Mutual inductance
R_f	RL filter resistance
L_f	RL filter inductance
R_F	LCL filter resistance
C_F	LCL filter capacitance
R_{RL}	RL filter resistance
L_{RL}	RL filter inductance
R_{on}	Internal resistance
R_{snub}	Snubber resistance
T_f	The fall time
T_t	Tail time
V_f	Forward voltage
R_{ca}	Resistance of line and cable
L_{ca}	Inductance of line and cable
C_{ca}	Capacitor of line and cable
R_{tr}	Resistance of transformer
L_{tr}	Inductance of transformer
R_f	Resistance of filter
L_f	Inductance of filter
Tr	Low-pass filter time constant
$[Ka, Ta]$	Regulator gain & time constant

$[K_e, T_e]$	Exciter
$[T_b, T_c]$	Transient gain reduction
$[K_f, T_f]$	Damping filter gain & time constant
$[E_{fmin}, E_{fmax}, K_p]$	Regulator output limits and gain
$[V_{t0}(pu), V_{f0}(pu)]$	Initial values of terminal voltage and forward voltage
P_{tr}	Transformer nominal power
R_f	R_L Filter resistance
L_f	R_L Filter inductance
R_{1-eq}	Resistance of primary of the transformer
R_{2-eq}	Resistance of secondary of the transformer
L_{1-eq}	Inductance of primary of transformer
L_{2-eq}	Inductance of secondary of transformer
R_{L-eq}	Resistance of PI section line
L_{L-eq}	Inductance of PI section line
C_{L-eq}	Capacitor value of PI section line
D	Load damping coefficient
R	Droop referred to percent speed regulator
ω_0	Rated rotor speed
V_n	Rated voltage (RMS Ph-Ph)
H_G	Inertia constant of the grid generator
T_G	Governor time constant
T_{CH}	Turbine time constant
L_i	Inductance of converter side
L_g	Grid side inductance
C_f	The filter capacitor
R_f	The damping resistor
δ_s	Solar declination
ω_s	Hour angle
α_s	Solar altitude
θ_z	Zenith angle
γ_s	Solar azimuth
ϕ_s	Latitude
λ_s	Longitude
d	Number of the day
E_{time}	Equation of time
Tz	Time zone
γ	Azimuth angle
i	Tilt angle
θ_{PV}	Incidence angle for PV module
G_{tilted}	Global tilted irradiance
B_{tilted}	Beam tilted irradiance
D_{tilted}	Diffuse tilted irradiance
R_{tilted}	Reflected irradiance
B_n	Direct normal irradiance

G_h	Global horizontal irradiance
D_h	Diffuse horizontal irradiance
ρ	Albedo
P_{DC}	Power output generated by solar PV field
A_{ref}	Area of PV module
N_{module}	Number of modules
η_{module}	PV module efficiency
$T_{module,ref}$	PV module temperature under standard test conditions
$\eta_{module,ref}$	PV module efficiency under standard test conditions
γ_f	Power temperature coefficient
T_c	PV cell temperature
T_{amb}	Ambient temperature
V_{wind}	Wind velocity
$\eta_{inverter}$	Inverter efficiency
f_{losses}	Factor losses
$P_{el,pv}$	Output power of a PV system
P_{pv}	PV installed capacity
$p_{th,incident}$	Thermal power incident on the solar field
A_{field}	Solar field's area
$p_{th,absorbed}$	Thermal power absorbed by the solar field
η_{sf}	Field efficiency
θ_{csp}	Incidence angle for solar collector
η_{shadow}	Shading losses
η_{end}	End losses
$L_{spacing}$	Spacing between the collector's rows
A_{col}	Width of the collector
L_{col}	Length of the collector
L_{focal}	Focal length of the solar collector
η_{col}	Collector efficiency
η_{rec}	Receiver efficiency
P_{CSP}	CSP installed capacity
η_{pb}	Power block efficiency
SM	Solar multiple
$p_{th,losses}$	Heat losses
$p_{th,rec}$	Receiver losses
$p_{th,pipe}$	Pipe system losses
$T^{sf,in}$	Inlet temperature
$T^{sf,out}$	Outlet temperature
C_{tes}	System storage capacity
h_{tes}	Storage duration

List of Figures

Fig. 1.1	Stability classification of the electrical power system	5
Fig. 1.2	Simplified equivalent scheme of transmission line	7
Fig. 1.3	German grid code requirements: a Fault voltage profile, b Curve of reactive current versus voltage drop for Voltage control by the reactive current injection [31]	9
Fig. 1.4	Map of the UCTE area divided into three zones [36]	11
Fig. 1.5	Frequency records until the splitting of a zone (area splitting) [36]	11
Fig. 1.6	Frequency records after the division of the zones [36]	12
Fig. 1.7	Electrical interconnections between Morocco and its neighbor countries [37]	12
Fig. 1.8	ENTSO-E grid code requirements, a Active power response characteristics versus frequency deviation, b Activation time of active power frequency response	13
Fig. 1.9	Schematic of the frequency control type with activation periods, after power imbalance	14
Fig. 1.10	Active power management capability constraints	15
Fig. 2.1	Structure of the wind turbine generator.	20
Fig. 2.2	Turbine model implemented in MATLAB/Simulink.	21
Fig. 2.3	Curves of the power coefficient $C_p(\lambda, \beta)$: a for different values of β and b $C_p(\lambda, \beta)$ versus λ and β	21
Fig. 2.4	Shaft and wind turbine model.	22
Fig. 2.5	Block diagram of the generator model	25
Fig. 2.6	Scheme of the electrical system linking source to the grid	26
Fig. 2.7	Equivalent simplified electrical scheme of a single phase of the transformer brought back to the primary.	27
Fig. 2.8	Electrical scheme of the three-phase transmission line	28
Fig. 2.9	Electrical scheme of filter, transformer and transmission line	28

Fig. 2.10	a Single-phase equivalent scheme of the LCL filter and b Model block of the LCL filter	30
Fig. 2.11	Single-phase electrical scheme of the infinite power network with short-circuit impedance	31
Fig. 2.12	Synoptic scheme of the power network with the possibility of parameterization for participation in the auxiliary service.	32
Fig. 3.1	Block diagram of the studied system with LCL filter and converter control	36
Fig. 3.2	The Gaussian membership functions: a Input membership functions b Output membership functions and c Surface of output versus input.	45
Fig. 3.3	Modeling scheme in MATLAB/Simulink used to obtain the simulation results	47
Fig. 3.4	Simulation results of SMC using LCL filter and without RC sensor	47
Fig. 3.5	The simulation results of SMC with the LCL filter and the use of sensors at the RC branch. a THD of the current, b Power and DC bus voltage and c Current passing through RC branch of the filter	48
Fig. 3.6	Simulation results of SMC with the RL filter without taking into account the power loss: a current THDi and b Power and voltage of DC bus	48
Fig. 3.7	Simulation results of SMC used for current control with the RL filter and the PI controller used for V_{dc} control: a current THDi and b Power and voltage of DC bus	49
Fig. 3.8	Simulation results of SMC for RL filter taking into account power loss: a THD of the current and b Power and voltage of DC bus.	50
Fig. 3.9	Simulation results of fuzzy SMC for the LCL filter taking into account the power loss and without using sensor in the RC branch: a THD of current and b Power and voltage of the DC bus	50
Fig. 3.10	Simulation results of robustness test against parameter variation of -60% of DC bus capacitance value (using RL filter and SMC for current control). a DC bus voltage control using SMC and b V_{dc} voltage regulation using PI controller	51
Fig. 3.11	Simulation results of robustness test of the proposed Fuzzy-SMC control against parameter variations of -60% : a variation of the LCL filter parameters and b variation of the DC bus capacitance value.	51
Fig. 3.12	Synoptic diagram of the experimental platform.	52
Fig. 3.13	Flow chart for coupling inverter to grid	53

Fig. 3.14	Experimental results of three phases at output of RL filter, a three-phase voltages, b three-phase currents, c THDv of voltage and d THDi of current.	54
Fig. 3.15	Experimental results of three phases at output of LCL filter, a three-phase voltages, b three-phase currents, c THDv of voltage and d THDi of current.	55
Fig. 3.16	Experimental results of SMC with LCL filter and RC sensor, a three-phase voltages, b three-phase currents c THDv with maximum values, d THDi with maximum values, e three-phase currents of RC branch and f currents of 'd' and 'q' axes of RC branch of LCL filter	56
Fig. 3.17	Experimental results of the sliding mode control with LCL filter and without RC sensor, a Three-phase voltages, b Three-phase voltages c THDv with maximum values, d THDi with maximum values	57
Fig. 3.18	Experimental results of the fuzzy sliding mode control with LCL filter and without RC sensor, a Three-phase voltages, b Three-phase currents, c THDv with maximum values, d THDi with maximum values	58
Fig. 3.19	Experimental results of active power at the LCL filter output using: a Vector control, b Conventional SMC, c Fuzzy-SMC, and d SMC with RC sensor addition	59
Fig. 3.20	The two circuits of the switching relays for connection to the grid and variation of the filter inductance	60
Fig. 3.21	THD of current and voltage for robustness test of proposed Fuzzy-SMC during LCL filter inductance variation of -50%	60
Fig. 4.1	Block diagram of the wind farm connected to the power network.	64
Fig. 4.2	Diagram of the adopted proportional distribution algorithm	66
Fig. 4.3	Schematic of the supervision system configuration	67
Fig. 4.4	Overall diagram of wind farm and converter control	70
Fig. 4.5	Global schematic of WF connected to the grid developed in MATLAB/Simulink	72
Fig. 4.6	Simulation results for scenario 1: a Grid voltage, b Three wind profiles.	73
Fig. 4.7	Simulation results for scenario 1: a Reactive current at PCC (pu), b Voltage V_{dc} of 1st wind turbine	74
Fig. 4.8	Simulation results for scenario 1: Active and reactive powers of Wind farm	74
Fig. 4.9	Simulation results for scenario 1: a 1st wind turbine power, b 2nd wind turbine power and c 3rd wind turbine power	75

Fig. 4.10	Simulation results for scenario 2: PQ control from 0 to 6 s, MPPT control from 6 to 12 s and voltage drop from 80% to 9 s: a grid voltage, b the three wind profiles	76
Fig. 4.11	Simulation results for scenario 2: PQ control from 0 to 6 s, MPPT control from 6 to 12 s and voltage drop from 80% to 9 s: a Reactive current at PCC (pu), b current at PCC (pu)	77
Fig. 4.12	Active and reactive power at PCC for scenario 2: a wind farm and b 1 st wind turbine	78
Fig. 4.13	Active and reactive power at PCC for scenario 2: a 2 nd wind turbine wind turbine and b the 3 rd wind turbine	79
Fig. 4.14	Overall structure of the test system of the electrical power network with the possibility of parameterization of voltage-reactive power control $Q(V)$ of the power network.	80
Fig. 4.15	The proposed control strategy: a Schematic of the voltage control at the PCC and references for the active and reactive power generation, b Block diagram of the hierarchical PIFPI controller.	81
Fig. 4.16	Shapes of fuzzy membership functions: a Input variables, b Output variable	82
Fig. 4.17	Reactive power and voltage response for different controllers: a voltage at PCC, b reactive power response	83
Fig. 4.18	Reactive power and voltage response for different controllers: a active power response, b zoom of active power response	84
Fig. 5.1	Structures of the configured supervisory system and its main units	89
Fig. 5.2	The block diagram of the dynamic power system test $Q(V)$ for voltage control through reactive power injection.	91
Fig. 5.3	Proposed control system: a Diagram block for power references generation according to the three operating modes, b Design layout of fractional order PIFO-Fuzzy-PIFO controller with PSO parameter optimization	93
Fig. 5.4	Flowchart of PSO algorithm for optimization the fractional order operators using Matlab/Simulink model.	94
Fig. 5.5	The impact of fractional order parameter λ on the voltage response	97
Fig. 5.6	Simulation results of different reactive power and voltage controllers: a voltage at the PCC, b reactive power response	98
Fig. 5.7	Simulation results of the different reactive power and voltage controllers: a active power response, b zoom of the active power response	99

Fig. 5.8	Simulation results of a scenario that includes PQ control [2, 6s], MPPT control [6, 10s] and voltage fault control activated at time 9 s. a PCC voltage, b the three wind profiles.	101
Fig. 5.9	Simulation results of a scenario that includes PQ control [2, 6s], MPPT control [6, 10s] and voltage fault control activated at time 9 s. a Active power b Reactive power.	102
Fig. 5.10	Simulation results of a scenario including PQ control [2, 6s], MPPT control [6, 10s] and voltage fault control activated at time 9 s. a PCC current, b the DC bus voltages of the 3 WTs	103
Fig. 6.1	Model of the wind farm as a cluster of 30 wind turbines.	108
Fig. 6.2	Aggregate models of the wind farm	109
Fig. 6.3	Overall diagram of the farm connected to the electrical grid.	110
Fig. 6.4	Turbine connected to a synchronous generator supplying an isolated load.	112
Fig. 6.5	Transfer function relating speed and torques.	112
Fig. 6.6	Transfer function linking mechanical speed and power in “per unit” notation	113
Fig. 6.7	Global electrical grid diagram including generators and loads with the possibility to control the frequency and active power.	114
Fig. 6.8	Ideal steady-state characteristics of a governor with speed droop	115
Fig. 6.9	Power reserve control, a Optimal and deloaded power curves, b Block diagram for generating the pitch angle. Where T_β is the time constant of the pitch system servo motor. The speed and range of the pitch angle variation are set to $\pm 10^\circ/s$ and 0° to 90° , respectively	117
Fig. 6.10	Generation of power and torque references for frequency control	119
Fig. 6.11	Gaussian membership functions for the inputs and the output.	119
Fig. 6.12	Block diagram of the proposed hierarchical fuzzy controllers: a PIFPI controller, b PDFPI controller	120
Fig. 6.13	Block diagram of inertial controller for frequency control	121
Fig. 6.14	Frequency responses (Hz) at the PCC: a using the five controllers, b their zoom.	122
Fig. 6.15	The power response: a Active power (MW) and b Reactive power (MVAR) at PCC	123
Fig. 6.16	Behaviours of the 3 WT-equs: a pitch angle response (degrees) and b active power response at the PCC (MW)	124
Fig. 6.17	DC bus voltage responses of the three equivalent wind turbines	124

Fig. 7.1	The breakdown of energy demand by source for the year 2020 [1]	130
Fig. 7.2	Energy breakdown of world electricity production, 1971–2021 [1]	131
Fig. 7.3	Applications of solar energy	134
Fig. 7.4	PV-CSP hybridization scenarios	137
Fig. 8.1	The annual variation of the solar declination (δ_s)	147
Fig. 8.2	The annual variation of the equation of time (E_{time})	147
Fig. 8.3	Model of the PV plant	149
Fig. 8.4	Model of the CSP plant	154
Fig. 8.5	Solar field control Mode 1: HTF freeze protection, Mode 2: Warm-up and Mode 3: Normal operation.	159
Fig. 8.6	Model of PV-CSP plant	161
Fig. 9.1	a Annual DNI profile b Annual GHI profile.	169
Fig. 9.2	Daily solarradiation (DNI and GHI)	169
Fig. 9.3	The influence of varying the tilt and orientation angle on the annual energy produced bythe PV plant	171
Fig. 9.4	The influence of varying tilt angle on the annual energy and the LCOE of the PV plant (for southern orientation)	171
Fig. 9.5	The influence of TES size value on the CSP system energy produced: a TES = 6 h, b TES = 12 h (CSP plant with 100MW and SM = 3).	173
Fig. 9.6	Variation of annual energy as function of TES size for different values of solar multiple.	173
Fig. 9.7	Variation of LCOE as function of TES size for different values of solar multiple	174
Fig. 9.8	The annual energy generated of all simulated scenarios	176
Fig. 9.9	The LCOE of all simulated scenarios	176
Fig. 9.10	The variation of electrical annual energy, capacity factor, and LCOE according to solar multiple for $h_{tes} = 12h$	178
Fig. 10.1	Load profiles.	188
Fig. 10.2	The convergence of PSO-CS algorithm (Case 1, Load 1).	189
Fig. 10.3	The convergence of PSO-CS algorithm (Load 2)	191
Fig. 11.1	Simplified diagram of the PV-CSP-EH plant $P^{th,SF}$: Thermal power produced by solar field (CSP), $P^{SF,PB}$: Thermal power directly used by the power block from the solar field, $P^{to,TES}$: Thermal power sent to the TES, $P^{from,TES}$: Thermal power used by the power block from the TES system, P^{PV} : Electrical power produced by the PV plant, $P^{to,load}$: Electrical power directly used to satisfy the load from the PV, $P^{to,EH}$: the electrical power rejected by the PV plant and which will be sent to the EH, $P^{EH,TES}$: Dumped electrical powerand $P^{PV,CSP}$: Electrical power used to satisfy the load.	197
Fig. 11.2	Pareto front obtained by optimization of the PV-CSP-EH	201

Fig. 11.3	Pareto front in terms of PV installed capacity.	202
Fig. 11.4	Pareto front in terms of CSP installed capacity.	202
Fig. 11.5	Pareto front in terms of electric heater capacity	203
Fig. 11.6	Pareto front in terms of solar multiple	203
Fig. 11.7	Pareto front in terms of TES size	204
Fig. A.1	The realised measurement circuits.	219
Fig. A.2	Photo of the designed LCL filter	220
Fig. A.3	SEMIKRON three-phase inverter and its connectors.	221

List of Tables

Table 1.1	Parameters for the complete activation of the active power range and the maximum allowable periods	13
Table 3.1	Comparison between the performance of the filters and their proposed controls	49
Table 4.1	Types of protection	68
Table 4.2	Fuzzy logic rules for the voltage controller	82
Table 4.3	Combination of voltage and reactive power controllers Reactive power controller	84
Table 5.1	Fuzzy logic rules for the proposed controller the voltage controller	96
Table 5.2	Combination of controllers for voltage and reactive power control	100
Table 6.1	Fuzzy logic rules for primary frequency control	120
Table 6.2	Frequency responses for an acceptable deviation from deadband of 0.01 Hz	123
Table 7.1	PV-CSP projects around the world [43, 45–47].	137
Table 9.1	Simulated configurations	175
Table 10.1	Mathematical test functions	187
Table 10.2	Statistics for algorithms (PSO, CS et PSO-CS)	187
Table 10.3	PSO-CS parameters	188
Table 10.4	Optimization results (Load 1)	190
Table 10.5	Optimization results (Load 2)	191
Table 10.6	Optimization results for CSP plant alone (Load 1 and 2)	191
Table 11.1	Optimization results (PV-CSP-EH power system)	204
Table 11.2	Optimization results (PV-CSP power system)	205
Table A.1	Parameters of the inverter, RL filter and LCL filter	214
Table A.2	Control system parameters in per unit notation	214
Table A.3	IEEE recommended practices and requirements for harmonic control in electrical power systems.	215

Table A.4	Limit values for harmonic voltage (MV, HV and EHV)	215
Table A.5	Parameters of line, transformer and filter.	215
Table A.6	Parameters of the excitation system.	216
Table A.7	Parameters of the filter, transformer Tr1-1 and transmission line L1-1	216
Table A.8	Parameters of the grid synchronous generator	217
Table A.9	Single phase parameters of the LCL filter	218
Table A.10	The RL filter parameters of Single phase	218
Table B.1	Technical parameters of the PV plant	223
Table B.2	Economic parameters of the PV plant	224
Table B.3	Technical parameters of the CSP plant	224
Table B.4	Economic parameters of the PV plant	225

Part I

Intelligent Control on Wind Farm

Chapter 1

Introduction to Power System Stability and Wind Energy Conversion System



1.1 Introduction

Global warming is currently considered as one of the most critical issues that the environment may face in the next fifty years. Greenhouse gas (GHG) emissions from power plants around the world are considered to be one of the major contributors to climate change [1]. Many countries are turned towards new renewable energy such as hydro, solar, and wind power to solve the problem of global warming providing an efficient solutions to climate change [1]. Therefore, the use of the renewable energy leads to the liberation of the power production market and the decentralization of the electricity power system. On the other hand, they give rise to several new technical problems in the field of electrical engineering, which influence on the power system stability connected to the renewable energy resources. Among these energy sources, the wind energy is considered a promising technology in strong growth [1]. It is a non-polluting, inexhaustible energy (extraction of wind energy), profitable in far regions (isolated areas) and can be complementary to traditional energy sources. These advantages have led to an increase integration of wind energy resources in Moroccan power network and it is currently classified as the second renewable energy source. Most grid-connected wind turbines are controlled to deliver the maximum power with a unity power factor, or to guarantee the required power predetermined by the transmission system operator (TSO) and meet the grid code requirements. The wind turbines are quickly disconnected during the grid fault, such as the short circuits or voltage drop. This disconnection leads to an imbalance between the demand and supply of electrical power, which causes several problems such as the frequency deviation and voltage fault [2, 3]. If the energy reserve distributed over the entire power system is insufficient to compensate the imbalance power and solve the energy shortage, a “blackout” may occur. Indeed, during the grid fault the wind turbines must be controlled to remain connected to the power system and the participate in the system stability. The wind farms must meet the requirements given by TSO to participate in ancillary services (Regulation of the voltage and frequency of grid).

According to some technical conditions for connection to the European grid, wind power plants must provide power reserves in the identical way as conventional power plants [4, 5]. The frequency deviations from its reference value will be compensated by increasing the energy output of the machines connected to the grid. All three types of frequency control will be activated (primary, secondary and tertiary) until the system stability is ensured [5, 6]. Consequently, the development of control strategies and the configuration of the supervision system must respect all operating conditions. Most works in the literature propose control strategies based on nonlinear controls and the use of filters such as LCL filter [7, 8, 41]. Nonlinear controls such as sliding mode control, backstepping and fuzzy logic are proposed in the literature to keep the robustness of the controlled systems [9–12, 42] and participate in the power system stability.

This chapter deals with the problems of voltage stability of the power system and the identification of the different categories of instabilities in the power system. In addition, the description of the grid code requirements for integration of wind energy conversion system into grid will be presented.

1.2 Stability of the Electrical Power System

An electric power system can be characterized by its frequency and its different voltage levels. In the last century, the stability of these quantities is considered as an important issue for the safety of the electrical system. The electrical power system stability is defined by its capability to return to its normal operation after being subjected to a physical disturbance. System stability can be affected by several factors such as the increase in interconnections; use of new technologies; transporting of large quantities of energy over long distances; environmental pressures on transmission expansion; increase in electricity demand in a heavily loaded areas where it is not feasible or economical to install new power plants; and utilization of new load models due to the liberating of the electricity market. Under the conditions of voltage and frequency instability, the power system stability can be affected. Figure 1.1 provides a global overview of the power system stability categories and desired controls. Consequently, the instability of voltage and frequency become the major research topic in the field of electrical engineering and power control systems because of the different events of instability that occurred in the world [13–15].

1.3 Power System Stability and Wind Energy Conversion System

In most countries, the quantity of renewable energy injected into power networks represents a significant part of total power production. The penetration of wind power in power networks has increased rapidly and is substituting the power generated by

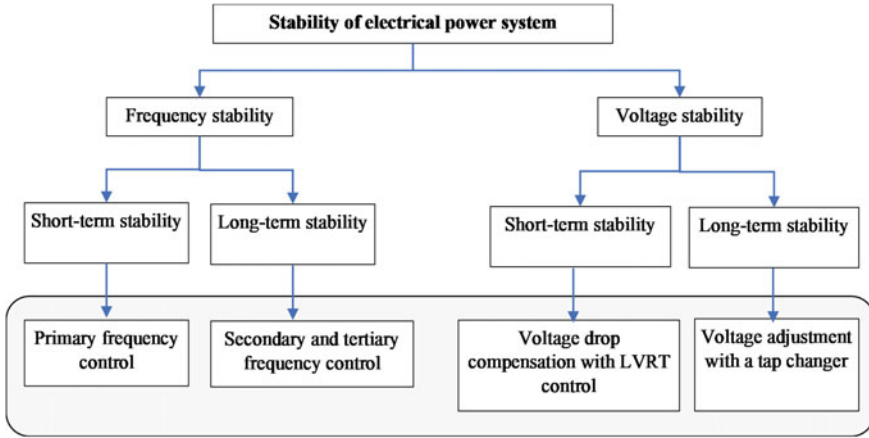


Fig. 1.1 Stability classification of the electrical power system

conventional power plant based on synchronous generators. As a result, the overall behavior of the power system is being affected. For fixed speed wind turbines, the deterioration of voltage stability is mainly because of the the large quantity of reactive power consumed by the wind turbines during their operation and also due to unexpected disturbances of the power system. The current developed wind turbines behave differently according to their generator type, when subjected to grid faults and disturbances. The Induction generators consume reactive energy and behave like a induction motors leading to the local grid voltage instability [16, 17]. Variable speed wind turbines are more and more used because of their advanced capability to participate in control of the grid voltage [18]. Indeed, this type of wind turbine can consume or generate the reactive power and their power factor can be adequately regulated. The influence of power produced by the wind power plants on short-term and long-term stability is discussed in [19, 20]. The results show that the voltage stability can be improved with reactive power control. The impact of the increasing of the installed wind power on the frequency stability is studied in Refs. [21, 40]. This reference proposes an additional control loop to provide an inertial response like the conventional power plant based on synchronous generator do.

1.4 Voltage Dips and Grid Code Requirements

The study of voltage and frequency stability has become an important field of research in the electrical power system, after several incidents of power system instability around the world. This has led to the establishment of the grid code requirements for grid-connected wind energy conversion system.

1.4.1 Voltage Stability

Voltage stability is defined as the ability of a power system to maintain a constant voltage on all buses across the whole system and to ensure that the balance between generation and demand is maintained or restored withing acceptable limits. Instability can result in voltage dropping or gradual increasing on some buses. A major cause of voltage instability is the sudden loss of load in an area and the disconnection of transmission lines and devices by means of protection systems, which might lead to a cascade of faults and failures. This catastrophic cascading failures can lead to loss of stability and voltage collapse in large interconnected power system causing blackout and failure of production. Voltage collapse is more dangerous complex than voltage drop and instability. These series of events that accompany voltage instability leading to a blackout or an unacceptable low voltages in a significant portion of the power network [22]. Voltage drop is often caused by simple or multiple low probability disturbances. If the power system subjected to a sudden variation of reactive power demand due to an unexpected situation, the additional demand is required and should be satisfied by the reactive power reserves of compensatory system (synchronous generators or static compensators). Generally, if there is a sufficient reserve, the system will stabilise at an acceptable voltage level. But sometimes, because of a combination of events and system states, as well as the lack of additional reactive power, a voltage drop can lead to a total or partial system failure [22].

1.4.2 Types of Voltage Stability

Voltage is an important parameter in an electric power system that indicates an imbalance of reactive power in a specific area. Therefore, there are local voltage stability problems (of each zone) and global voltage stability problems, caused by small or large disturbances [23]. Voltage stability can be further divided into two categories:

- Long-term voltage stability: we are interested here in a “series of reactions” caused by overloaded branches, transformer tap actions, etc. The instability in this case is generally global developing over a period of a few minutes to a few hours and leading to voltage collapse [24, 25].
- Short-term voltage stability: this refers to the loss of short-term voltage stability which occurs as a result of a line outage or generator failure. The instability develops in a period of several hundred milliseconds to a few seconds [26–28]. In recent years, several power outages have occurred worldwide due to the short-term voltage stability problem [27], such as the events in North America [13], Athens [14] and Brazil [15].

1.4.3 Main Causes of Voltage Instability

Voltage is a physical quantity that is measured and fluctuates according to the state of the power network, i.e. the network topology, generation, load, transmission line and transformer. These factors may depend on TSO decisions and system contingencies such as tripping of generators or transmission devices. The simplest way to model the conductors used for power transmission is as a resistor in series with an inductance (see Fig. 1.2): The flow of a current through this conductor will create a voltage drop ΔV . This voltage drop versus the active and reactive power flowing in the conductor, can be expressed such as:

$$\Delta V = V_s - V_g = \frac{R_L * P + X_L * Q}{V_g} \quad (1.1)$$

For a power transport system $X_L \gg R_L$, then:

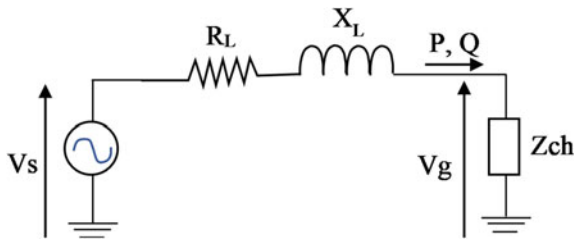
$$\Delta V = \frac{X_L * Q}{V_g} \quad (1.2)$$

Thus, it can be seen that the voltage is dependent on the reactive power fluctuations and impedance values of the transmission line. The voltage levels are maintained by reactive power generation provided by different power plant devices. The main factor causing voltage instability in most cases is the load. In order to respond to a disturbance, the power consumed by the loads should be restored by the power control systems. The restored loads increase the reactive power consumption on a high voltage level, which leading to further voltage reduction. A depletion situation generating a voltage collapse when the dynamics of the load attempts to restore power consumption beyond the capabilities of the electrical transmission system and power generation units [29, 30].

A voltage collapse can be aggravated by:

- Excessive use of the shunt capacitor, because the voltage dip leads to the decrease in reactive power produced by a capacitor ($Q = -V^2/X_C$), where X_C is the reactance.
- Incapacity of the system to satisfy the required reactive power.

Fig. 1.2 Simplified equivalent scheme of transmission line



- Sudden strong disturbances, like the loss of a generator or a heavily loaded line.
- Inadequate cooperation between the different control and protection systems.

1.4.4 Grid Code Requirements for Voltage Dip

Transmission system operators impose a specific standards for managing wind turbines subjected to grid faults. As reported by the German grid code, the wind farms must remain connected to the grid and ensure a stable operation despite the voltage dip, which the voltage profile is presented in Fig. 1.3a [31, 32]. Figure 1.3b shows the reactive current provided by the farm the voltage control, when the voltage exceeds a range defined by the dead band of $\pm 10\%$ of nominal voltage. The reference [33, 41] shows that the German grid code gives an updated dead band range of $\pm 5\%$ around nominal voltage for a grid-connected offshore wind farm. Beyond this dead band, the reactive current should be increased according to (1.3).

$$I_q - I_{q0} = 2 \frac{V - V_0}{V_n} I_n \quad (1.3)$$

Where I_q : Reactive current. I_{q0} : Value of reactive current before the grid fault. $I_n = 1$ pu: Value of rated current. V : Measured value of voltage. V_0 : Value of Voltage before grid fault. $V_n = 1$ pu: Value of rated voltage. Depending on the magnitude of the voltage drop and the dead band defined by the range of $[0.95 V_n \text{ and } 1.05 V_n]$ and also if the grid fault does not meet the defined grid code requirements, a quarter of the generators must be switched off from the grid after 1.5, 1.8, 2.1 and 2.4 ms, respectively [31, 33].

1.5 Frequency Stability and Grid Code Requirements

High penetration of renewable energy in power systems would reduce the inertia and power reserve for frequency control. Therefore, it is difficult to maintain frequency stability in power system with high renewable energy integration. Frequency instability is considered currently as one of the most important challenges for secure and stable operation, which can lead to system collapse in the presence of the most serious disturbances, leading sometimes to blackout. Therefore, frequency stability in a power system is defined as the capability to maintain a constant frequency or to ensure the frequency variation within a unacceptable dead band imposed by TSOs.

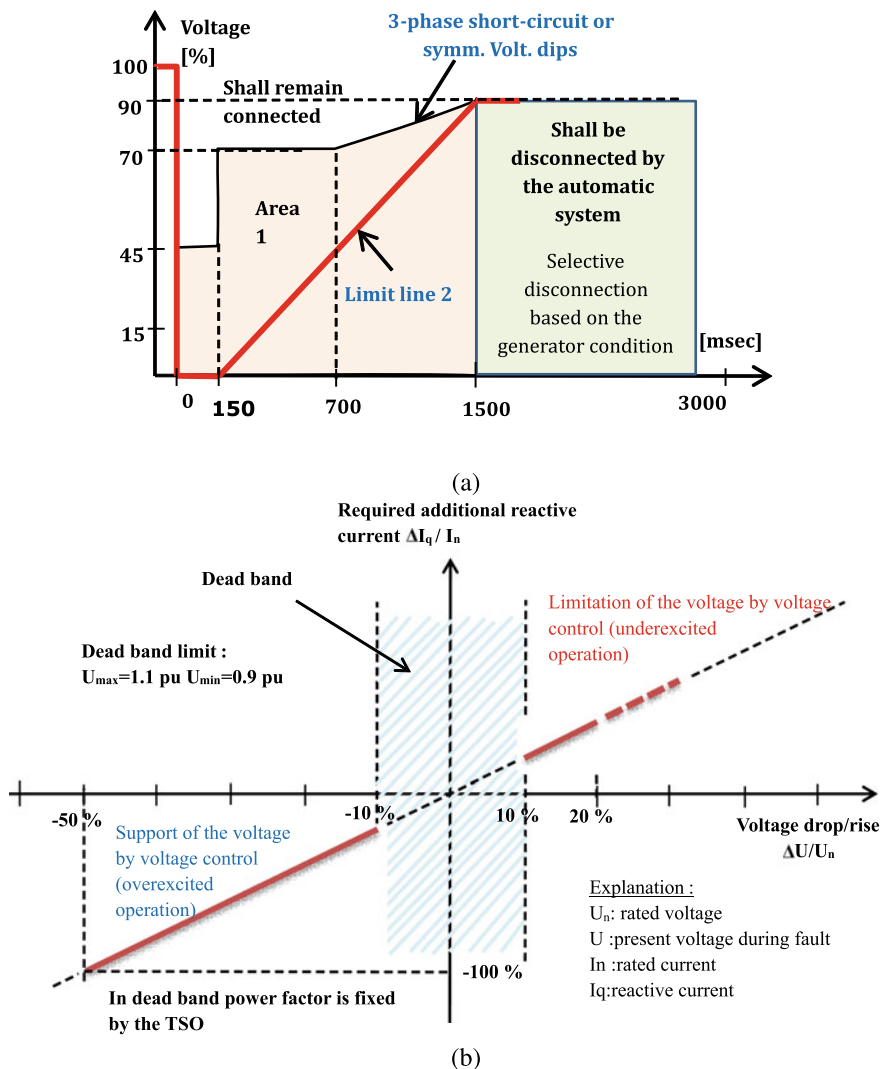


Fig. 1.3 German grid code requirements: **a** Fault voltage profile, **b** Curve of reactive current versus voltage drop for Voltage control by the reactive current injection [31]

1.5.1 Main Causes of Frequency Instability

Maintaining the frequency at its nominal value means adjusting the balance power between generation and demand in real time. This balance is threatened by the loss of a generating resource or by untimely load shedding or other faults. The generation resources participating in the frequency control act to stabilize the system and bring

the frequency back to its nominal value. After and during the frequency deviation, the active power should be immediately injected with a fast response. These response depends on the operating time required by different operators/system controllers and the size of the system. After a disturbance due to a loss of generator, the rate of change of frequency is inversely proportional to the energy of rotation (E_r) stored mainly in synchronous generators that supply loads directly. The stored rotational energy of each synchronous generator ($E_r = 0.5J\omega_m^2$), is related to its inertia constant in “pu” H_g by $H_g = \frac{E_r}{S_b}$, where “J” inertia constant in “SI”, S_b is the rated power, and ω_m is the generator speed [34]. The rate of change of frequency after a power imbalance ΔP can be expressed by [34]:

$$\frac{df}{dt} = \frac{\Delta P}{2H_g} \quad (1.4)$$

It can be observed from Eq. (1.4) that the higher the inertia of the system, the lower the rate of change of the frequency for a given disturbance. Thus, the frequency deviation depends directly on the power variation.

1.5.2 Example of Frequency Instability

The analysis study of the behavior of power generation during the event of November 4, 2006 constitutes an extremely serious incident, which affected the European inter-connected electricity transmission network [35, 36] (see Fig. 1.4), (the blackout was avoided thanks to the solidarity between the electricity networks). After cascading overloads and tripping of lines, the UCTE (Union for Coordination of Transmission of Electricity) network split into three large separate systems (Fig. 1.4). The western zone has been faced with a significant power imbalance between supply and demand. The total generation of the western zone is 182,700 MW and the power imbalance caused by missing import from the east is 8,940 MW. This large imbalance power caused a rapid frequency deviation (within 8 s) to 49 Hz (from 50 to 49 Hz) in the UCTE (see Figs. 1.5 and 1.6). Figure 1.5 shows the frequency records recovered by the measurement systems in the three zones from 10h10:06 to 10h10:30 PM, and Fig. 1.6 shows the Landesbergen–Wehrendorf line trip and the time stamp after the zone split [36]. The frequency dip also led to the disconnection between the European and Moroccan grids to protect the Maghreb power system [37]. Figure 1.7 shows the electrical interconnections between Morocco and neighborhood countries. This event provided a better assessment of the impact of power imbalance on the electrical system in critical situations. Since then, in many countries the technical standards for grid-connected wind farms have evolved so that such problems are no longer encountered. They define the minimum time that wind turbines must be in operation and connected to grid within a imposed frequency range. Some of these specifications also indicate that wind farms with sufficient large-scale power

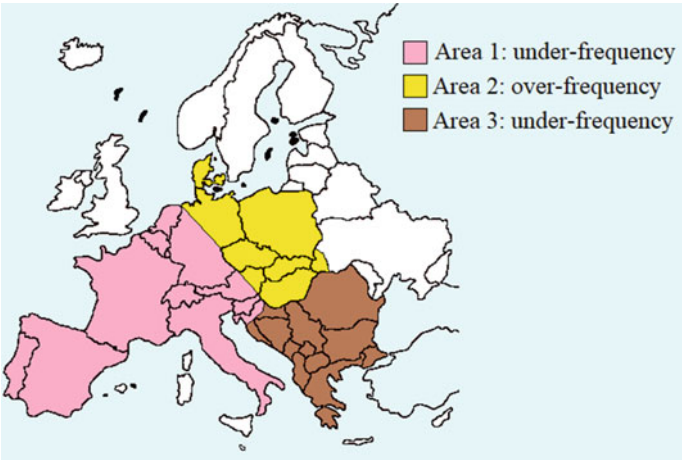


Fig. 1.4 Map of the UCTE area divided into three zones [36]

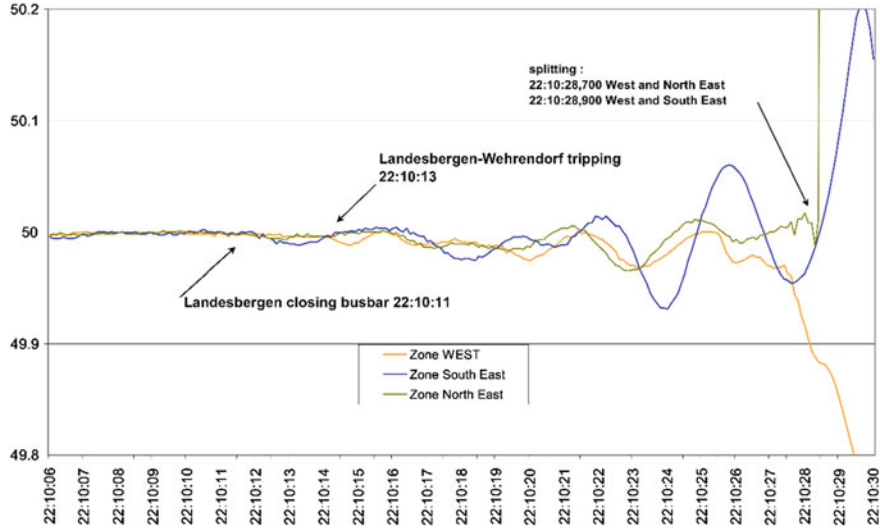


Fig. 1.5 Frequency records until the splitting of a zone (area splitting) [36]

(usually >5 MW) must be capable of reducing their power under the grid operator demand. This means that they must be equipped with means of communication with a control center or supervision system. The operators would thus have the ability to control and supervise all the wind turbines and also change the references for active and reactive power production [41, 43].

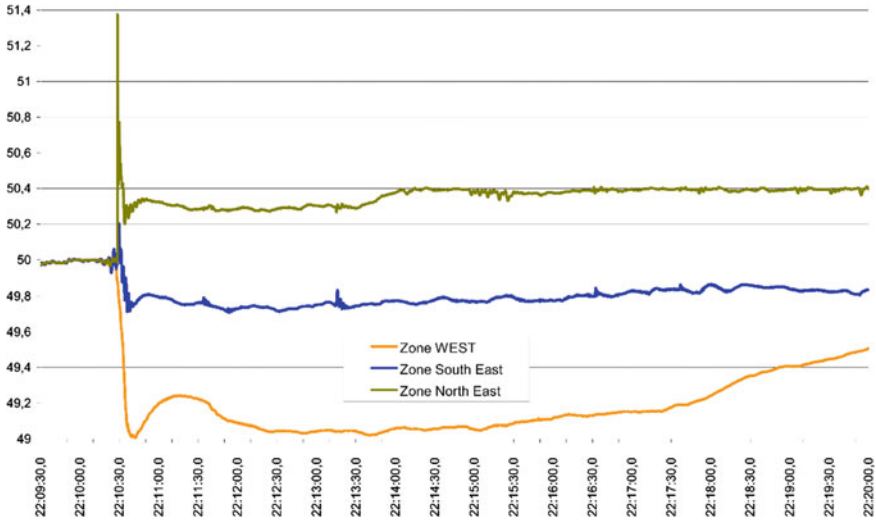


Fig. 1.6 Frequency records after the division of the zones [36]



Fig. 1.7 Electrical interconnections between Morocco and its neighbor countries [37]

1.5.3 Grid Code Requirements

In recent years, the electrical power systems are facing a significant increase of wind turbine energy penetration, which can lead to frequency control difficulties due to unpredictable wind speeds. This increasing integration [1] leads to the establishment of grid code requirements.

As discussed in [4], the grid code requirements given by the European Network of Transmission System Operators for Electricity (ENTSO-E), imposes for wind farms to produce more energy during the grid frequency deviation below the nominal value and to reduce the power generation during the frequency increase above the nominal value of 50 Hz. The type C of wind power plant (WPP) is defined in Section 10 of the European grid code [4] for a voltage at the PCC less than 110 kV and the maximum power capacity equal to or greater than a limit of 75 MW.

The primary response for these kinds of WPPs should be activated at a frequency limit of 49.8 Hz with a droop (d) between the range of 2 and 12% and power range between 1.5 and 10% computed using the maximum capacity of the generated power, as illustrated in Fig. 1.8a. The WFs must meet the requirements given by ENTSO-E for the Limited Frequency Sensitive Mode (LFSM) and the Limited Frequency

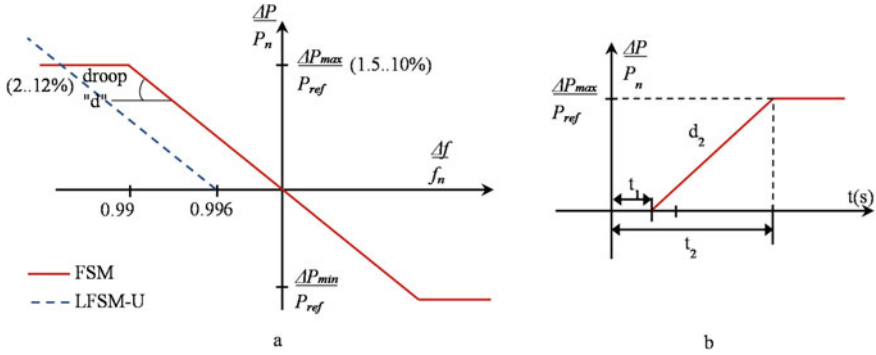


Fig. 1.8 ENTSO-E grid code requirements, **a** Active power response characteristics versus frequency deviation, **b** Activation time of active power frequency response

Table 1.1 Parameters for the complete activation of the active power range and the maximum allowable periods

Parameters	Range or values
The active power range related to the maximum capacity and the frequency response range	1.5–10%
t1: The maximum allowable initial delay, unless otherwise justified for power generation technologies with inertia	2 s
t2: The maximum allowable time for full activation of the frequency response, unless a long activation time is allowed by the TSO	30 s

Sensitive Mode under-frequency (LFSM-U). The response of active power for frequency control in LFSM (zero dead-band and insensitivity), is given in Fig. 1.8a. Where: P_{ref} is the reference of active power to determine ΔP is related. ΔP is the generator active power variation. f_n is the rated value of frequency (50 Hz) and Δf is the frequency variation. Under-frequencies less than 49.8 Hz, the WF must provide an amount of active power versus frequency respect to the droop “ d ”. The characteristics presented in Fig. 1.8a, and according to the time periods ($t_1 = 2$ s and $t_2 = 30$ s) specified by the TSO in Fig. 1.8b and Table 1.1 [4, 5].

1.5.4 Frequency Control

Frequency control is considered to be one of the important control systems for ensuring the stability and security of the power system. The main objective of this control is to ensure the balance between generation and power demand. There are three types of frequency control to compensate the frequency variations around its nominal value: primary, secondary and tertiary frequency control [5, 6, 38] (see Fig. 1.9). Each control is related to a reserve of energy. The primary reserve is the additional power

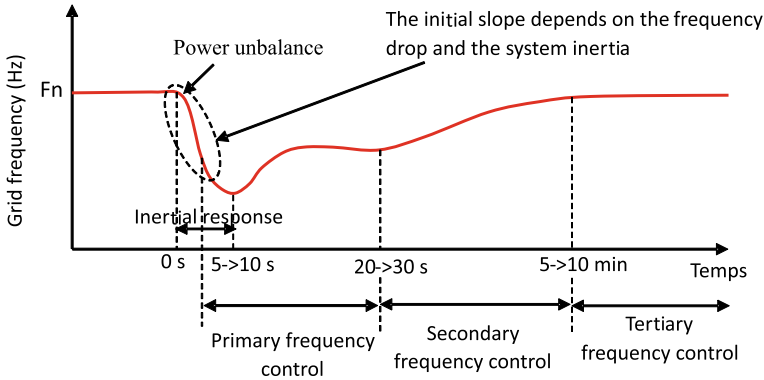


Fig. 1.9 Schematic of the frequency control type with activation periods, after power imbalance

capacity created using the kinetic energy of the machines connected to the grid. The primary reserve is used during the activation of the primary frequency control after a few seconds of the power imbalance. The purpose is to quickly ensure a power balance and to stabilize the frequency in an acceptable dead band [40]. Activation of the primary control is followed by the activation of the secondary control (within a few minutes). While the tertiary control is activated to support the secondary control reserve. Secondary and tertiary reserve control are activated manually by transmission system operators only [4]. All these reserves should be provided until the power is perfectly balanced.

Under grid code conditions for wind farms operating with a voltage greater than or equal to 100 kV [39], there are five different types of active power controls depending on the state and operating conditions requested by the TSO (see Fig. 1.10):

- **Absolute power constraint:** In case of low energy demand and high wind production, the grid operator imposes to the wind farm to limit its power to a maximum, in order not to pay the energy costs if there is no demand and to evacuate the surplus power production to the neighboring countries, without any financial compensation. Below this power limit, the wind turbines can operate normally.
- **Delta production constraint:** For this type of control, an amount of power must be reserved by limiting the available power to a percentage, so that the wind turbines can participate in the primary frequency control.
- **Balance control:** In this control, the farm's power is controlled to follow a fixed set point. This value must be increased or decreased rapidly to ensure that the production/consumption balance is maintained.
- **Power gradient constraint:** In this case, the power increase is limited to a slope (MW/s), in order to limit the contribution of the farm to the frequency control during strong wind variations. To achieve this functionality, the farm should be equipped with a good wind prediction tool with a very short delay (order of ten seconds).

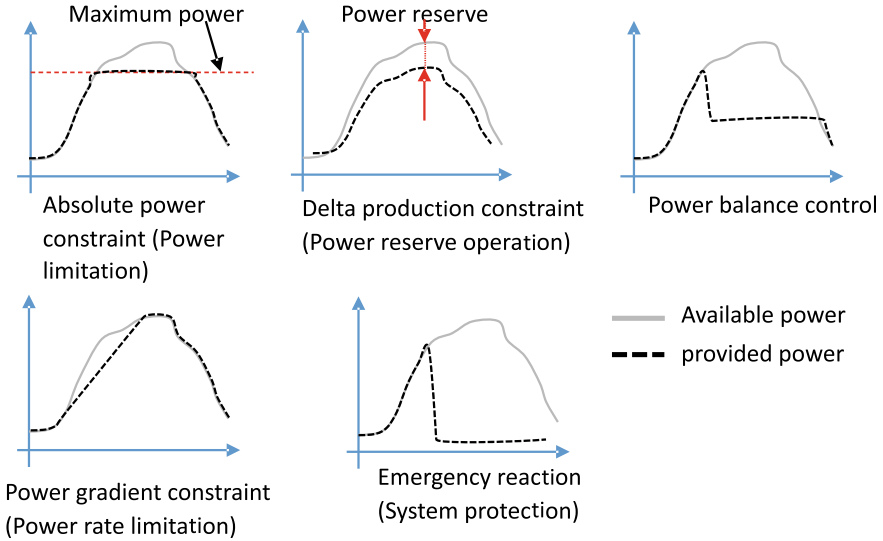


Fig. 1.10 Active power management capability constraints

- **Emergency reaction (“System protection”):** in case of overproduction on the grid where there is no need for power from the wind farm, the wind turbines must quickly reduce their power and should be completely cleared in a duration of less than 30 s if necessary, until the disappearance of the emergency signal transmitted by the control center. The value of this power is predefined and updated by the TSO.

1.6 Conclusion

In this chapter the underlying causes of voltage and frequency instability are presented. The different categories of behavior during instability that are important for the analysis of power system stability are identified. The description of the grid connection regulations is also presented.

References

1. Global Wind Energy Council (GWEC), GWEC Global Wind Report, April 2018. <https://gwec.net/wp-content/uploads/2019/04/GWEC-Global-Wind-Report-2018>
2. Almeida, D., Rogério, G., Lopes, J.: Participation of doubly fed induction wind generators in system frequency regulation. *IEEE Trans. Power Syst.* **22**(3), 944–950 (2007)
3. Obaid, Z.A., Cipcigan, L.M., Muhssin, M.T.: Fuzzy hierarchal approach-based optimal frequency control in the Great Britain power system. *Electric Power Syst. Res.* **141**, 529–537 (2016)
4. ENTSO-E: Entso-e network code for requirements for grid connection applicable to all generators. <https://www.entsoe.eu>. Accessed 12 Feb 2016
5. Díaz-gonzález, F., Hau, M., Sumper, A., Oriol, G.-B.: Participation of wind power plants in system frequency control: review of grid code requirements and control methods. *Renew. Sustain. Energy Rev.* **34**, 551–564 (2014)
6. Courtecuisse, V., Robyns, B., Francois, B., Marc, P., Jacques, D.: Variable speed wind generators participation in primary frequency control. *Wind Eng.* **32**(3), 299–318 (2008)
7. Liserre, M., Blaabjerg, F., Dell'Aquila, A.: Step-by-step design procedure for a grid-connected three-phase PWM voltage source converter. *Int. J. Electron.* **91**(8), 445–460 (2004)
8. Huang, M., Blaabjerg, F., Loh, P.C., et al.: Stability analysis and active damping for LLCL-filter based grid-connected inverters. In : *Power Electronics Conference (IPEC-Hiroshima 2014-ECCE-ASIA)*, 2014 International, IEEE, pp. 2610–2617 (2014)
9. Yin, X.-X., Lin, Y.-G., Li, W., Liu, H.-W., Gu, Y.-J.: Fuzzy-logic sliding-mode control strategy for extracting maximum wind power. *IEEE Trans. Energy Conv.* **30**(4), 1267–1278 (2015)
10. Yin, X.-X., Lin, Y.-G., Li, W., Gu, Y.-J., Lei, P.-F., Liu, H.-W.: Sliding mode voltage control strategy for capturing maximum wind energy based on fuzzy logic control. *Electr. Power Energy Syst.* **70**, 45–51 (2015)
11. Lekhchine, S., Bahi, T., Abadlia, I., Bouzeria, H.: PV-battery energy storage system operating of asynchronous motor driven by using fuzzy sliding mode control. *Int. J. Hydrog. Energy* (9) (2016)
12. Sun, D., Wang, X., Fang, Y.: Backstepping direct power control without phase-locked loop of AC/DC converter under both balanced and unbalanced grid conditions. *IET Power Electr.* **9**(8), 1614–1624 (2016)
13. Andersson, G., Donalek, P., Farmer, R., Hatziaargyriou, N., Kamwa, I., Kundur, P., Martins, N., Paserba, J., Pourbeik, P., Sanchez-Gasca, J., Schulz, R., Stankovic, A., Taylor, C., Vittal, V.: Causes of the 2003 major grid blackouts in North America and Europe, and recommended means to improve system dynamic performance. *IEEE Trans. Power Syst.* **20**(4), 1922–1928 (2005)
14. Vournas, C.D., Nikolaidis, V.C., Tassoulis, A.A.: Postmortem analysis and data validation in the wake of the 2004 Athens blackout. *IEEE Trans. Power Syst.* **21**(3), 1331–1339 (2006)
15. Conti, J.P.: The day the samba stopped. *Eng. Technol.* **5**(4), 46–47 (2010)
16. Fayek, H.M., Elamvazuthi, I., Perumal, N., Venkatesh, B.: The impact of DFIG and FSIG wind farms on the small signal stability of a power system. In: *2014 5th International Conference on Intelligent and Advanced Systems (ICIAS)* (2014). <https://doi.org/10.1109/icias.2014.6869505>
17. Haque, M.H.: Impacts of fixed speed wind generators on static voltage stability of distribution systems
18. An, Haejoon, Ko, Heesang, Kim, Hongwoo, Kim, Hyungoo, Kim, Seokwoo, Jang, Gilsoo, Lee, Byongjun: Modeling and voltage-control of variable-speed SCAG-based wind farm. *Renew. Energy* **42**, 28–35 (2012)
19. Londero, R.R., Affonso, C.de.M., Vieira, J.P.A.: Long-term voltage stability analysis of variable speed wind generators. *IEEE Trans. Power Syst.* **30**(1), 439–447 (2015). <https://doi.org/10.1109/tpwrs.2014.2322258>
20. Akhmatov, V.: Analysis of dynamic behavior of electric power system with large amount of wind power. Ph.D. Dissertation, Technical University of Denmark (2003)

21. Lalor, G., Mullane, A., O'Malley, M.: Frequency control and wind turbine technologies. *IEEE Trans. Power Syst.* **20**(4), 1905–1913 (2005)
22. Johansson, S.: Long-term voltage stability in power systems-alleviating the impact of generator current limiters. Technical Report No. 335, University of Technology (1998)
23. Cutsem, T.V., Vournas, C.: *Voltage Stability of Electrical Power System*. Kluwer Academic, Norwell (1998)
24. Faiz, J., Siahkolah, B.: *Electronic tap-changer for distribution transformers*. Springer Science & Business Media, Berlin (2011)
25. Sarimuthu, C.R., Ramachandaramurthy, V.K., Agileswari, K.R., Mokhlis, H.: A review on voltage control methods using on-load tap changer transformers for networks with renewable energy sources. *Renew. Sustain. Energy Rev.* **62**, 1154–1161 (2016). <https://doi.org/10.1016/j.rser.2016.05.016>
26. Kawabe, K., Ota, Y., Yokoyama, A., Tanaka, K.: Novel dynamic voltage support capability of photovoltaic systems for improvement of short-term voltage stability in power systems. *IEEE Trans. Power Syst.* **32**(3), 1796–1804 (2017). <https://doi.org/10.1109/tpwrs.2016.2592970>
27. Dong, Y., Xie, X., Zhou, B., et al.: An integrated high side var-voltage control strategy to improve short-term voltage stability of receiving-end power systems. *IEEE Trans. Power Syst.* **31**(3), 2105–2115 (2015)
28. Xu, Y., Zhang, R., Zhao, J., et al.: Assessing short-term voltage stability of electric power systems by a hierarchical intelligent system. *IEEE Trans. Neural Netw. Learning Syst.* **27**(8), 1686–1696 (2015)
29. Taylor, C.W.: *Power System Voltage Stability*. McGraw-Hill, New York (1994)
30. Kundur, P.: *Power System Stability and Control*. McGraw-Hill Professional, New York (1994)
31. Florin, I., Daniela, H.A., Poul, S., Antonio, C.N.: Mapping of grid faults and grid codes. Technical University of Denmark, Roskilde, Denmark, Risø. National Laboratory (2007)
32. Allagui, M., Hasnaoui, O.B., Belhadj, J.: Exploitation of pitch control to improve the integration of a direct drive wind turbine to the grid. *J. Electr. Syst.* **9**(12), 179–190 (2013)
33. Shin, H., Jung, H.-S., Sul, S.-K.: Low voltage ride through (LVRT) control strategy of grid-connected variable speed Wind Turbine Generator System. In: *IEEE 8th International Conference on Power Electronics and ECCE Asia (ICPE & ECCE)* (2011)
34. Karbouj, H., Rather, Z.H., Flynn, D., Qazi, H.W.: Non-synchronous fast frequency reserves in renewable energy integrated power systems: a critical review. *Electr. Power Energy Syst.* **106**, 488–501 (2019)
35. https://www.rte-france.com/sites/default/files/rte_ra2006_2.pdf
36. https://www.entsoe.eu/fileadmin/user_upload/_library/publications/ce/otherreports/Final-Report-20070130.pdf
37. Office National de l'Electricité (ONE), rapport pour COP22 For a sustainable future (2016). http://www.one.org.ma/FR/pdf/Brochure_ONEE_COP22_FR.pdf
38. Ziping, W.U., Wenzhong, G.A.O., Tianqi, G.A.O., Weihang, Y.A.N., Zhang, H., Yan, S., Wang, S.: State-of-the-art review on frequency response of wind power plants in power systems. *J. Mod. Power Syst. Clean Energy* **6**(1), 1–16 (2018). <https://doi.org/10.1007/s40565-017-0315-y>
39. Energinet, Wind Turbine Connected to Grids with Voltage Above 100 kV, “Technical regulation for the properties and the regulation of wind turbines”. Technical Regulation TF 3.2.5 (2004)
40. Elyalaoui, K., Ouassaid, M., Cherkaoui, M.: Primary frequency control using hierarchal fuzzy logic for a wind farm based on SCIG connected to electrical network. *Sustain. Energy Grids Netw.* **16**, 188–195 (2018)
41. Elyalaoui, K., Ouassaid, M., Cherkaoui, M.: Dispatching and control of active and reactive power for a wind Farm considering fault ride-through with a proposed PI reactive power control. *Renew. Energy Focus* **28**, 56–65 (2019)
42. Elyalaoui, K., Ouassaid, M., et Cherkaoui, M.: Improvement of THD performance of a robust controller for grid-side energy conversion system based on LCL filter without RC sensor. *Int. J. Electr. Power & Energy Syst.* **121** (2020). <https://doi.org/10.1016/j.ijepes.2020.106143>

43. Elyaaoui, K., Labbadi, M., Ouassaid, M., Cherkaoui, M.: Optimal fractional order based on fuzzy control scheme for wind farm voltage control with reactive power compensation. *Math. Problems Eng.* **2021**, Article ID 5559242, 12 (2021). <https://doi.org/10.1155/2021/5559242>

Chapter 2

Description and Modeling of Wind Energy Conversion System



2.1 Introduction

The wind turbines (WTs) are aimed to convert the wind energy into mechanical energy and then into electrical energy. The blades of WT transfer the energy captured from the wind to the hub, which is attached to the shaft. This hub then transfers the mechanical energy to the generator, in order to convert it to electrical energy. Wind turbines are considered as variable power generators connected to the electrical grid. The various elements of a wind turbine are designed to maximize this energy conversion. For an optimal energy conversion the designed WT must include:

- A mechanical control system for orientation of blades and nacelle.
- An electrical control system for control of power injected through the power converters.

Most of the manufacturers build wind turbines with power in the megawatt range. These wind turbines operate based on one of the three following generators: The permanent magnet synchronous generator (PMSG) (without gearbox), the double-fed induction generator (DFIG) and the squirrel cage induction generator (SCIG). Compared to DFIG and PMSG the SCIG offers a simple construction, more reliability and more robustness in terms of fault clearing time impact and tripping of WTs during grid fault. In this book, a 3 MW SCIG based wind farm has been considered for wind energy conversion system. The total power produced by SCIG is injected to grid by means of an AC/DC/AC converter parsing through the filter and transformer. The implemented control systems for wind power conversion are divided into two parts: Control of the generator-side converter and control of the grid-side converter. Active power produced is controlled by the torque control with the orientation of the rotor flux providing a decoupling between these two quantities. The mechanical power is regulated and limited to the rated capacity by means of the pitch control strategy. Active and reactive power transferred to the grid are controlled by the grid side converter to follow the requirements imposed by TSO and to maintain the

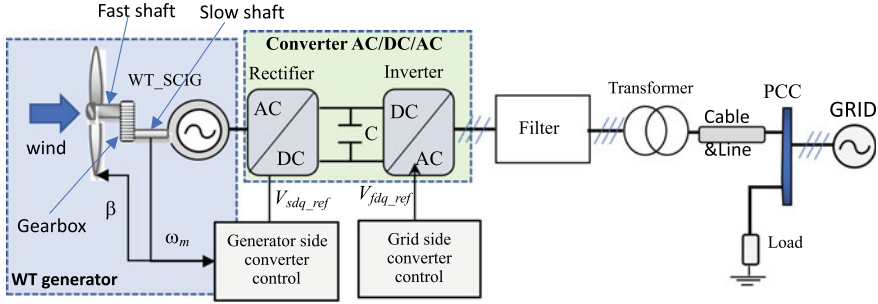


Fig. 2.1 Structure of the wind turbine generator

converter DC bus voltage constant. The connection to the grid is made through passive elements to ensure the smoothing of AC currents and the filtering of DC voltage [1]. The adopted wind generator, consisting of a three-bladed variable speed turbine coupled to an asynchronous generator through a gearbox and connected to grid through converters, is presented in Fig. 2.1. The detailed models of the large wind power conversion system are presented in [2]. The model adopted in this book is a per-unit model. The system of per-unit quantities is a system of parameters in “pu” (Per Unit) which allows the engineer to observe relative quantities of some parameters independently of the voltage and power levels and to compare its values to the same orders in the entire electrical system. To obtain the reduced parameters, the relevant quantities are divided by the base quantities. The two main base quantities chosen are: nominal voltage ($V_{base} = V_{nominal}$) and nominal power ($P_{base} = P_{nominal}$), the other base quantities are the derivations of the latter two.

2.2 Wind Turbine

2.2.1 Modeling of Turbine in Per Unit Notation

Wind turbine model is shown in Fig. 2.2. C_p is the coefficient that characterizes the aerodynamic efficiency of the turbine. It depends on the blade dimensions, the speed ratio λ and the blade orientation angle (β). For this wind turbine, the expression for the power coefficient is given by Heier in the following form:

$$C_p(\lambda, \beta) = C_1 \left(\frac{C_2}{\lambda_i} - C_3 \beta - C_4 \right) \exp \left(\frac{-C_5}{\lambda_i} \right) + C_6 \lambda \quad (2.1)$$

where $\frac{1}{\lambda_i} = \frac{1}{\lambda + 0.08\beta} - \frac{0.035}{\beta^3 + 1}$ and the constants $C_1 = 0.5109$, $C_2 = 116$, $C_3 = 0.4$, $C_4 = 5$, $C_5 = 21$, $C_6 = 0.0068$.

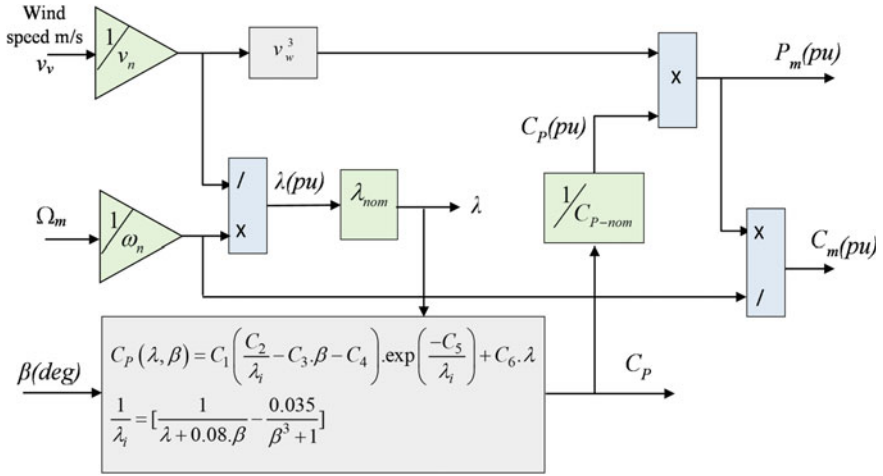
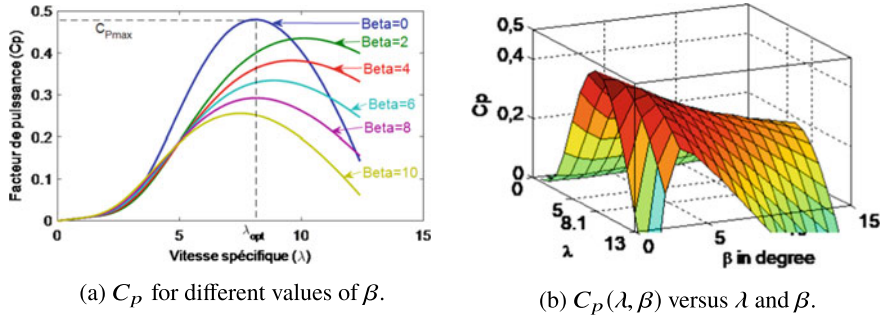


Fig. 2.2 Turbine model implemented in MATLAB/Simulink

Fig. 2.3 Curves of the power coefficient $C_p(\lambda, \beta)$: **a** for different values of β and **b** $C_p(\lambda, \beta)$ versus λ and β

The variation of C_p versus λ , for several values of the blade orientation angle β (deg) is presented in Fig. 2.3a. In Fig. 2.3a, several curves are presented, but we were interested in the one which has the highest maximum value and characterized by the optimal point ($\lambda_{opt} = 8.1$, $C_{pmax} = 0.47$, $\beta = 0^\circ$) corresponding to the maximum of the power coefficient C_p and thus the maximum of the mechanical power extracted from wind by turbine. This single point of maximum operation is confirmed by the three-dimensional graph in Fig. 2.3b.

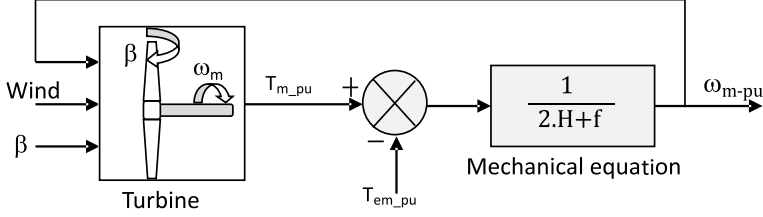


Fig. 2.4 Shaft and wind turbine model

2.2.2 Modeling of the Shaft in Per-unit System

For the modeling in reduced parameters, the fundamental equation of the dynamics is given by:

$$2.H \frac{\Omega_{m-pu}}{dt} = T_{m-pu} - T_{em-pu} - f \Omega_{m-pu} \quad (2.2)$$

With $H = H_p + H_h + H_g$ H_p : Blade inertia constant. H_h : Inertia constant of the hub. H_g : Inertia constant of the generator. f : Coefficient of friction in “pu”. T_{em} : Electromagnetic torque developed by the generator.

The relation between H and J is given by Eq. (2.3).

$$H = \frac{J \Omega_n^2}{2.S_n} \quad (2.3)$$

Ω_n : Nominal mechanical speed. S_n : Nominal apparent power. For per-unit system (without unit) the expression of the aerodynamic power P_a is expressed as:

$$P_a = C_p(\lambda, \beta)_{pu} \cdot V_{vpu}^3 \quad (2.4)$$

The mechanical power at the turbine shaft is expressed as:

$$P_{t_{pu}} = C_p(\lambda, \beta)_{pu} \cdot V_{vpu}^3 \quad (2.5)$$

The model of the Shaft connected to the wind turbine is illustrated in Fig. 2.4.

2.3 Modeling of the Squirrel-Cage Asynchronous Generator in the Park Reference Frame

In the last few years, a structure fully interfaced with the squirrel-cage asynchronous generator and gearbox has been proposed by wind turbine manufacturers. To replace

differential equations, with coefficients dependent on time, by simpler differential equations, with constant coefficients, the Park transformation is used.

2.3.1 Modeling of SCIG in the Park Reference Frame

In order to simplify the dynamic model of the machine, a reference frame change is performed to transform the three stator coils with phase shifts of $\frac{\pi}{3}$ into two equivalent fictive coils with phase shifts of $\frac{\pi}{2}$ (Fig. 2.4).

2.3.2 Electrical Equations of Generator in Park Reference Frame

The stator and rotor of the generator rotate at the same speed therefore the fluxes and currents are related by a time independent expression in park reference frame. By applying the Park transformation to the equations of the asynchronous machine in the (abc) reference frame, a model of the machine in the generator convention (where the currents flow out of the stator) is obtained with units in the international system without taking into account the homopolar components [2–4]:

– For the stator:

$$\begin{cases} V_{sd} = -R_s \cdot i_{sd} - \omega_s \cdot \phi_{sq} + \frac{d\phi_{sd}}{dt} V_{sq} = -R_s \cdot i_{sq} + \omega_s \cdot \phi_{sd} + \frac{d\phi_{sq}}{dt} \end{cases} \quad (2.6)$$

– For the rotor:

$$\begin{cases} 0 = -R_r \cdot i_{rd} - g \cdot \Omega_s \cdot \phi_{rq} + \frac{d\phi_{rd}}{dt} \\ 0 = -R_r \cdot i_{rq} + G \cdot \Omega_s \cdot \phi_{rd} + \frac{d\phi_{rq}}{dt} \end{cases} \quad (2.7)$$

Through the derivation of the relation linking the stator angle to the rotor angle $\theta_s = \theta_r + \theta$, the relationship between the stator pulsation ω_s and the rotor pulsation ω_r is defined as:

$$\omega_r = \omega_s - p \cdot \Omega_m \quad (2.8)$$

The slip is given by: $g = \frac{\omega_r}{\omega_s}$ note that $e_{sd} = -\omega_s \cdot \phi_{sq}$ and $e_{sq} = \omega_s \cdot \phi_{sd}$.

2.3.3 Per-unit System for Modeling

Firstly, a single equation is converter into a per-unit system, then the other equations of the model are deduced. Then, the d-axis stator equation given by:

$$V_{sd} = -R_s \cdot i_{sd} - \omega_s \cdot \phi_{sq} + \frac{d\phi_{sd}}{dt} \quad (2.9)$$

By dividing the two sides of the equation on the base quantity V_b , we obtain:

$$\frac{V_{sd}}{V_b} = \frac{1}{V_b} \cdot \frac{d\phi_{sd}}{dt} - \frac{1}{V_b} \cdot R_s \cdot i_{sd} - \frac{1}{V_b} \cdot \omega_s \cdot \phi_{sq} \quad (2.10)$$

Then, V_b is replaced in the second term by $\omega_b \cdot \phi_b$ and $Z_b \cdot I_b$, to obtain:

$$\frac{V_{sd}}{V_b} = \frac{1}{\omega_b \cdot \phi_b} \cdot \frac{d\phi_{sd}}{dt} - \frac{1}{Z_b \cdot I_b} \cdot R_s \cdot i_{sd} - \frac{1}{\omega_b \cdot \phi_b} \cdot \omega_s \cdot \phi_{sq} \quad (2.11)$$

with $\omega_b = 2\pi \cdot f$: the base pulsation of the system. Finally, the system in per-unit is obtained as follows:

$$V_{sd-pu} = \frac{1}{\omega_b} \cdot \frac{d\phi_{sd-pu}}{dt} - R_{s-pu} \cdot i_{sd-pu} - \omega_{s-pu} \cdot \phi_{sq-pu} \quad (2.12)$$

So, it can be seen that there are two possibilities to model the system in per unit in order to ensure the homogeneity of the equation:

- Either all quantities are in “pu”, including also the time, the equations are strictly identical in physical units and in “pu”. The factor $\frac{1}{\omega_b}$ in the term $\frac{1}{\omega_b} \frac{d\phi_{sd-pu}}{dt}$ must be removed from the system model.
- Or it is preferred to keep the time in seconds, then a factor of $\frac{1}{\omega_b}$ is appeared before the derivation operator, this is the case that has been chosen to developed the system model and the machine study. Then, in the model per-unit, it can replace V_{sd-pu} by V_{sd} , ϕ_{sd-pu} by ϕ_{sd} , R_{s-pu} by R_s , i_{sd-pu} by i_{sd} , ω_{s-pu} by ω_s et ϕ_{sq-pu} by ϕ_{sq} to reduce the sizes of the expressions as shown in the following equation:

$$V_{sd} = -R_s \cdot i_{sd} - \omega_s \cdot \phi_{sq} + \frac{1}{\omega_b} \cdot \frac{d\phi_{sd}}{dt} \quad (2.13)$$

From Eqs. (2.6) and (2.7), the fluxes and currents, when applying the Laplace transformation, are expressed by (2.14)–(2.19). To facilitate the modeling in Matlab/Simulink the fluxes are considered as intermediate quantities between the voltage (Inputs) and the currents (Outputs). Thus, the transient model of the squirrel cage asynchronous generator (generator convention), according to per-unit (pu) notation in park rotating reference frame (d, q), is presented in Fig. 2.5 [5, 6].

– For the stator:

$$\begin{cases} \phi_{sd} = \frac{1}{s} \cdot (\omega_b \cdot (V_{sd} + R_s \cdot i_{sd} + \omega_s \cdot \phi_{sq})) \\ \phi_{sq} = \frac{1}{s} \cdot (\omega_b \cdot (V_{sq} + R_s \cdot i_{sq} - \omega_s \cdot \phi_{sd})) \end{cases} \quad (2.14)$$

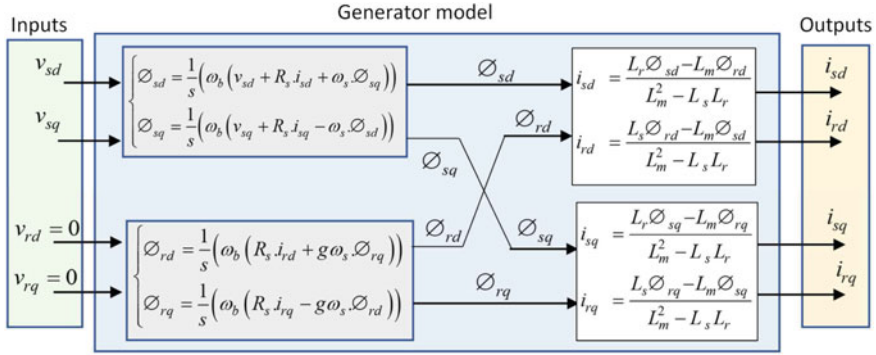


Fig. 2.5 Block diagram of the generator model

– For the rotor:

$$\begin{cases} \phi_{rd} = \frac{1}{s} \cdot (\omega_b \cdot (R_r \cdot i_{rd} + g \cdot \omega_s \cdot \phi_{rq})) \\ \phi_{rq} = \frac{1}{s} \cdot (\omega_b \cdot (R_r \cdot i_{rq} - g \cdot \omega_s \cdot \phi_{rd})) \end{cases} \quad (2.15)$$

where s is the Laplace operator. The equations of the currents versus the fluxes can be expressed as follows:

$$i_{sd} = \frac{L_r \phi_{sd} - L_m \phi_{rd}}{L_m^2 - L_s \cdot L_r} \quad (2.16)$$

$$i_{rd} = \frac{L_s \phi_{rd} - L_m \phi_{sd}}{L_m^2 - L_s \cdot L_r} \quad (2.17)$$

$$i_{sq} = \frac{L_r \phi_{sq} - L_m \phi_{rq}}{L_m^2 - L_s \cdot L_r} \quad (2.18)$$

$$i_{rq} = \frac{L_s \phi_{rq} - L_m \phi_{sq}}{L_m^2 - L_s \cdot L_r} \quad (2.19)$$

where $L_s = l_s + L_m$ and $L_r = l_r + L_m$; l_s : stator leakage inductance, l_r : rotor leakage inductance and L_m : mutual inductance.

2.3.4 Electromagnetic Torque and Power

The electromagnetic torque (in generator convention) can be given as a function of the rotor quantities by the following expression:

$$T_{em} = \frac{L_m}{L_r} (\phi_{rd} \cdot i_{sq} - \phi_{rq} \cdot i_{sd}) \quad (2.20)$$

This expression of the electromagnetic torque leads to the development of vector control, so-called “rotor flux-oriented control”. The expressions for the active power P and reactive power Q are given by:

$$\begin{cases} P = v_{ds} i_{ds} + v_{qs} i_{qs} \\ Q = v_{qs} i_{ds} - v_{ds} i_{qs} \end{cases} \quad (2.21)$$

2.4 Modeling of the RL Filter in pu System

The single-phase diagram in Fig. 2.6 shows that the connection to the electrical network is made via an input filter, a transformer and a transmission line. The filter inductances are designed to reduce the current ripples sufficiently. R_f and L_f are the filter resistance and inductance, respectively. v_1 , v_2 and v_g are respectively the voltages at the output of the filter, the transformer and the PCC. “ i_f ” is the current flowing through the filter. Applying the Kirchhoff’s Voltage Law to the filter terminals and using the per-unit system, allow to obtain (2.22):

$$\begin{cases} v_{ma} = R_f \cdot i_{fa} + \frac{L_f}{\omega_b} \frac{di_{fa}}{dt} + v_{1a} \\ v_{mb} = R_f \cdot i_{fb} + \frac{L_f}{\omega_b} \frac{di_{fb}}{dt} + v_{1b} \\ v_{mc} = R_f \cdot i_{fc} + \frac{L_f}{\omega_b} \frac{di_{fc}}{dt} + v_{1c} \end{cases} \quad (2.22)$$

By applying Park’s transformation to Eq. (2.22), we can easily find the representation of the voltages and currents in the rotating d-q frame (2.23), which is synchronized with the power network.

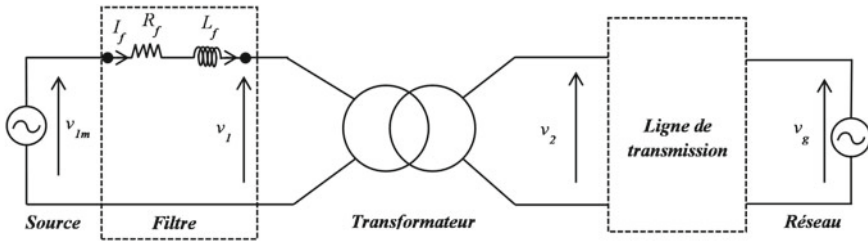


Fig. 2.6 Scheme of the electrical system linking source to the grid

$$\begin{cases} v_{md} = R_f \cdot i_{fd} + \frac{L_f}{\omega_b} \frac{di_{fd}}{dt} - L_f \omega_g i_{fq} + v_{1d} \\ v_{mq} = R_f \cdot i_{fq} + \frac{L_f}{\omega_b} \frac{di_{fq}}{dt} + L_f \omega_g i_{fd} + v_{1q} \end{cases} \quad (2.23)$$

Avec ω_g : la pulsation du réseau électrique. v_{1d} et v_{1q} sont les composantes de la tension du réseau des axes d et q .

Where ω_g : the pulsation of the electrical network. v_{1d} and v_{1q} are d-axis and q-axis components of grid voltage. v_{md} and v_{mq} are d-axis and q-axis components of voltage at the output of the converter. i_{fd} and i_{fq} are d and q axis components of current flowing through filter.

2.5 Modeling of Transformer and Transmission Line

2.5.1 Transformer Model

The model of the transformer brought back to the primary, based on equivalent circuit of a single-phase, is presented in Fig. 2.7. In this model, the iron losses are modeled by a resistor in parallel with the magnetizing inductance (see Fig. 2.7).

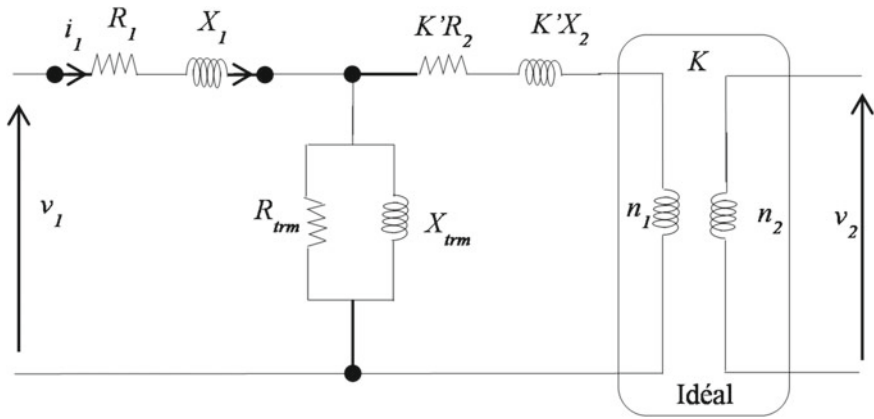


Fig. 2.7 Equivalent simplified electrical scheme of a single phase of the transformer brought back to the primary

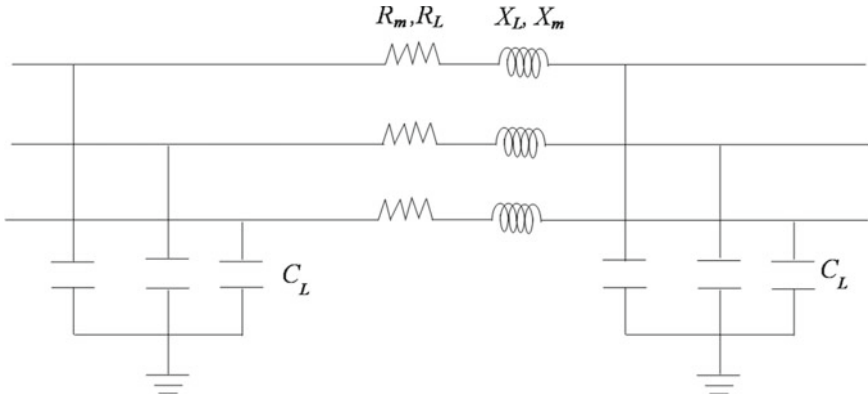


Fig. 2.8 Electrical scheme of the three-phase transmission line

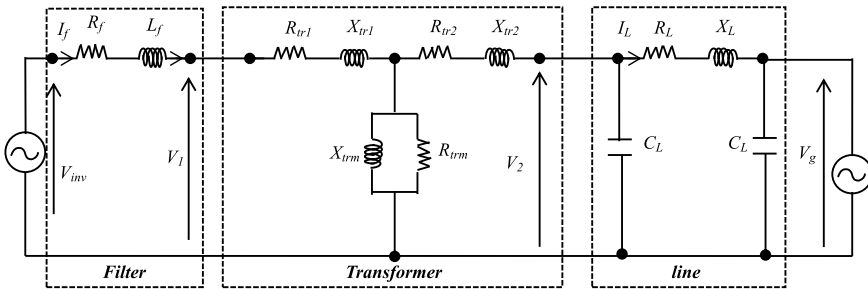


Fig. 2.9 Electrical scheme of filter, transformer and transmission line

2.5.2 Transmission Line Model

Unlike distributed parameters line model with an uniform distribution of parameters (resistance R_L , reactance X_L , and capacitance C_L) along transmission line, the model of line PI section focuses the line parameters in a short section transmission line, as shown in Fig. 2.8, where R_m and X_m are the mutual resistance and reactance, respectively.

Figure 2.9 shows the single-phase electrical scheme of the grid-connected inverter system, which includes the RL filter, transformer and transmission line.

2.6 Modeling of the LCL Filter

The connection to the power network is achieved through passive elements to ensure smoothing of the voltages and the AC currents [1]. Therefore, an LCL filter must be used to minimize the current ripples generated by PWM modulator. The comparison

between standard RL, L and LCL filters, shows that the LCL filter has a smaller size and less expensive and a level of ripple attenuation better than the other filters [7–9]. But the damping solutions are needed to stabilize the conversion system based on the LCL filter. References [10, 11] give an overview of passive damping (PD) and active damping (AD). The PD method is easy for understanding with a simple design. It is widely used in several applications, but its disadvantage is the damping resistance losses, which reduces the system efficiency [12]. PD approaches offer a simple control algorithms with better dynamic performance and a large bandwidth. AD method reduces the power loss problem by adding an extra terms to the control laws, but it is very sensitive to parameter variation [13–16], requires multiple sensors, and increases the complexity of the algorithm. It offers a short bandwidth, which gives a poor dynamic response performance. This comparative study discovers also that with some improvement of the LCL filter topology, the losses in the damping resistors can be reduced to be identical to those of AD methods, while they preserve the inherited advantages of PD methods.

2.6.1 Model of LCL Filter in (abc) Reference Frame

The equivalent single-phase scheme of symmetrical three-phase LCL filter system is given as shown in Fig. 2.10a. The schematic of the model implemented in Simulink is given in Fig. 2.10b. The mathematical model of single phase LCL filter using Laplace transformation, the expression of grid current (i_G) and inverter current (i_I) can be written as follows:

$$i_I - i_C - i_G = 0 \quad (2.24)$$

$$i_I(s) = \frac{\omega_b}{s.L_G}(u_I - u_C) \quad (2.25)$$

$$i_G(s) = \frac{\omega_b}{s.L_I}(u_C - u_G) \quad (2.26)$$

where L_I is the filter inductance at inverter-side, L_G is the inductance at grid-side and C_F is the capacitance of the filter. The expressions for the voltages at the input u_I and output u_G of the filter can be given by the following equations:

$$u_I(s) = z_{11}i_I + z_{12}i_G \quad (2.27)$$

$$u_G(s) = z_{21}i_I + z_{22}i_G \quad (2.28)$$

where: $z_{11} = R_f + \frac{s.L_I}{\omega_b} + \frac{\omega_b}{s.C_F}$, $z_{12} = -(R_f + \frac{\omega_b}{s.C_F})$, $z_{21} = R_f + \frac{\omega_b}{s.C_F}$ and $z_{22} = -(R_f + \frac{s.L_G}{\omega_b} + \frac{\omega_b}{s.C_F})$

2.6.2 Model of LCL Filter in Park Reference Frame

The LCL filter model developed in park reference frame (d, q) is given by:

$$\begin{cases} i_{Id} = \frac{\omega_b}{s.L_I}(u_{Id} + \omega_g.L_I.i_{Iq} - u_{Cd}) \\ i_{Iq} = \frac{\omega_b}{s.L_I}(u_{Iq} - \omega_g.L_I.i_{Id} - u_{Cq}) \end{cases} \quad (2.29)$$

$$\begin{cases} i_{Gd} = \frac{\omega_b}{s.L_G}(-u_{Gd} + \omega_g.L_G.i_{Gq} + u_{Cd}) \\ i_{Gq} = \frac{\omega_b}{s.L_G}(-u_{Gq} - \omega_g.L_G.i_{Gd} + u_{Cq}) \end{cases} \quad (2.30)$$

$$\begin{cases} i_{Cd} = i_{Id} - i_{Gd} \\ i_{Cq} = i_{Iq} - i_{Gq} \end{cases} \quad (2.31)$$

$$\begin{cases} u_{cap-d} = u_{Cd} - R_f.i_{Cd} \\ u_{cap-q} = u_{Cq} - R_f.i_{Cq} \end{cases} \quad (2.32)$$

$$\begin{cases} i_{Cd} = \frac{s.C_F}{\omega_b}u_{cap-d} - C_F.\omega_g.u_{cap-q} \\ i_{Cq} = \frac{s.C_F}{\omega_b}u_{cap-q} + C_F.\omega_g.u_{cap-d} \end{cases} \quad (2.33)$$

u_{Id} and u_{Iq} are: d-axis and q-axis voltage components at inverter output, respectively.

i_{Id} and i_{Iq} are: d- and q-axis current components of current at inverter output, respectively.

u_{Gd} and u_{Gq} are: d-axis and q-axis components of grid voltage, respectively.

i_{Gd} and i_{Gq} are: d-axis and q-axis current components injected into grid, respectively.

L_I and L_G are: LCL filter-side inductance and grid-side inductance, respectively.

C_F and R_F are: capacitance and resistance of LCL filter, respectively.

u_{cd} and u_{cq} : d-axis and q-axis voltage components across the RC branch, respectively.

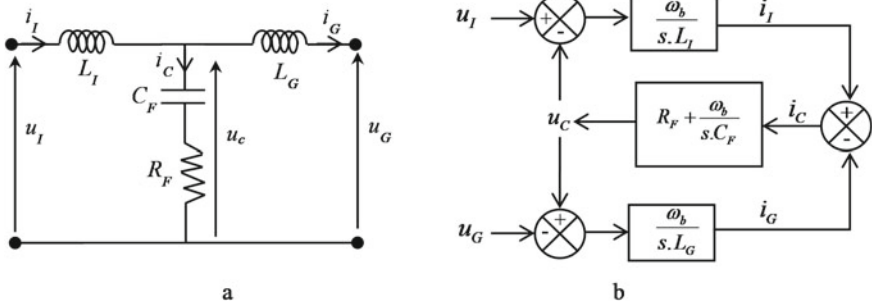


Fig. 2.10 **a** Single-phase equivalent scheme of the LCL filter and **b** Model block of the LCL filter

i_{cd} and i_{cq} : components of the d-axis and q-axis current of the RC branch, respectively.

$\omega_e = 2\pi f$, where f is the grid frequency.

The LCL filter parameters are calculated using an algorithm developed in references [7, 19].

2.7 Electrical Power Network

There are two possibilities to model the power network depending on the control to be tested and the procedure to participate in the auxiliary service.

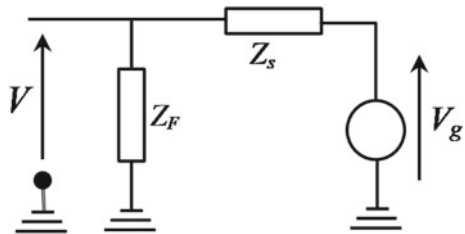
2.7.1 Infinite Grid Model

The grid is modelled using an infinite power source connected in series to an equivalent impedance. It is characterised by a short-circuit power “ S ” of about 10 times the nominal power of the wind farm, a ratio R/X of 0.1 and a short-circuit impedance Z_s (Fig. 2.11) [17, 18]. The effect of voltage drop on wind generators depends on the short-circuit impedance of the grid to which they are connected. The most critical situations are for high impedances (see Danish Grid Code [18]). This type of modeling is used to test non-linear Control Systems such as sliding mode control and their robustness to the variation of the machine parameters.

2.7.2 Dynamic Model of Grid

Regarding the participation in the auxiliary service, the power system model is developed for the possibility of parameterization for voltage control through the injection of reactive power and frequency control through the injection of active power. The power system consists of two synchronous generators (SG1 and SG2) supplying inductive and recitative loads (See Fig. 2.12). Each SG includes a steam turbine with

Fig. 2.11 Single-phase electrical scheme of the infinite power network with short-circuit impedance



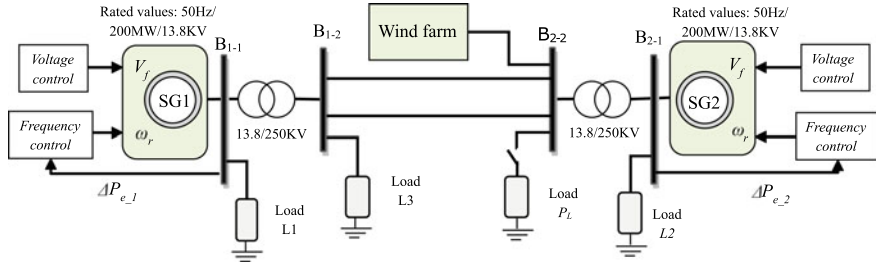


Fig. 2.12 Synoptic scheme of the power network with the possibility of parameterization for participation in the auxiliary service

power control system to provide the required electrical power [4, 20–22]. For power system stability and power flow control, voltage control and frequency control are developed (see Fig. 2.12) [21].

2.8 Conclusion

This chapter is dedicated to the modeling of the different elements of the variable speed wind power system based on a squirrel cage induction generator, as well as the connection to the grid. The modeling is developed in the (d, q) reference frame, using the Park transformation. The models of the generator, filters, and transformers developed in this chapter will be used in the following chapters to develop the control strategies of the wind power conversion chain. The next chapter will be devoted to the robustness study of the sliding mode and fuzzy sliding mode control with the LCL filter.

References

1. Liserre, M., Blaabjerg, F., Dell'Aquila, A.: Step-by-step design procedure for a grid-connected three-phase PWM voltage source converter. *Int. J. Electron.* **91**(8), 445–460 (2004). Aug
2. An, Haejoon, Ko, Heesang, Kim, Hongwoo, Kim, Hyungoo, Kim, Seokwoo, Jang, Gilsoo, Lee, Byongjun: Modeling and voltage-control of variable-speed SCAG-based wind farm. *Renew. Energy* **42**, 28–35 (2012)
3. Li, H., Yang, C., Zhao, B., Wang, H., Chen, Z.: Aggregated models and transient performances of a mixed wind farm with different wind turbine generator systems. *Electric Power Syst. Res.* **92**, 1–10 (2012)
4. Kundur, P.: *Power System Stability and Control*. McGraw-Hill Professional, New York (1994)
5. Elyalaoui, K., Ouassaid, M., Cherkaoui, M.: Low voltage ride through for a wind turbine based SCAG. In: *Third International Conference on Renewable and Sustainable Energy (IRSEC'15)*, pp. 1–6, 10–13, 2015, IEEE, Marr., Morocco
6. Li, H., Zhao, B., Yang, C., et al.: Analysis and estimation of transient stability for a grid-connected wind turbine with induction generator. *Renew. Energy* **36**(5), 1469–1476 (2011)

7. Liserre, M., Blaabjerg, F., Hansen, S.: Design and control of an LCL-filter-based three-phase active rectifier. *IEEE Trans. Ind. Appl.* **41**(5), 1281–1291 (2005). Oct.
8. Massing, J.R., Stefanello, M., Grundling, H.A., Pinheiro, H.: Adaptive current control for grid-connected converters with LCL filter. In: *IEEE Transactions On Industrial Electronics*, vol. 59, no. 12 (2012)
9. Yoon, D.-K., Jeong, H.-G., Lee, K.-B.: The design of an LCL-filter for the three-parallel operation of a power converter in a wind turbine. In: *Energy Conversion Congress and Exposition (ECCE)*, 2010 IEEE, pp. 1537–1544. IEEE (2010)
10. Wei, S., Xiaojie, W., Peng, D., Juan, Z.: An over view of damping methods for three-phase PWM rectifier. In: *IEEE International Conference on Industrial Technology*, 2008. ICIT 2008, pp. 1–5. IEEE (2008)
11. Zhao, W., Chen, G.: Comparison of active and passive damping methods for application in high power active power filter with LCL-filter. In: *International Conference on Sustainable Power Generation and Supply, SUPERGEN'09*, pp. 1–6. IEEE (2009)
12. Said-Romdhane, M.B., Naouar, M.W., Belkhouja, I.S., et al.: Simple and systematic LCL filter design for three-phase grid-connected power converters. *Math. Comput. Simul.* **130**, 181–193 (2016)
13. Dannehl, J., Fuchs, F.W., Hansen, S., Thøgersen, P.B.: IEEE investigation of active damping approaches for PI-based current control of grid-connected pulse width modulation converters with LCL filters. *IEEE Trans. Ind. Appl.* **46**(4) (2010)
14. Gullvik, W., Norum, L., Nilsen, R.: Active damping of resonance oscillations in LCL-filters based on virtual flux and virtual resistor. In: *2007 European Conference on Power Electronics and Applications*, pp. 1–10. IEEE (2007)
15. Malinowski, M., Kazmierkowski, M.P., Szczygiel, W., Bernet, S.: Simple sensorless active damping solution for three-phase PWM rectifier with LCL filter. In: *Industrial Electronics Society, IECON 2005. 31st Annual Conference of IEEE* (pp. 5–pp). IEEE (2005)
16. Rockhill, A.A., Liserre, M., Teodorescu, R., Rodriguez, P.: Grid-filter design for a multi-megawatt medium-voltage voltage-source inverter. *IEEE Trans. Ind. Electron.* **58**(4), 1205–1217 (2011)
17. Allagui, M., Hasnaoui, O.B., Belhadj, J.: Grid support capabilities of direct drive wind turbines during faults for uninterrupted operation mode. In: *International Conference on Electrical Sciences and Technologies in Maghreb (CISTEM)* (2014)
18. Energinet, Wind Turbine Connected to Grids with Voltage Above 100 kV, Technical regulation for the properties and the regulation of wind turbines. Technical Regulation TF 3.2.5 (2004)
19. Júnior, V.P.B., Jacomini, A.S.F.R., Filho, A.S.: Simulation study of squirrel cage induction generator fed by a back-to-back converter and by using a LCL filter (2013)
20. Bevrani, H.: *Robust Power System Frequency Control*, Power Electronics and Power Systems. Springer International Publishing, Berlin (2014)
21. Elyaaoui, K., Ouassaid, M., Cherkaoui, M.: Primary frequency control using hierarchical fuzzy logic for a wind farm based on SCIG connected to electrical network. *Sustain. Energy Grids Netw.* **16**, 188–195 (2018)
22. Elyaaoui, K., Ouassaid, M., Cherkaoui, M.: Dispatching and control of active and reactive power for a wind Farm considering fault ride-through with a proposed PI reactive power control. *Renew. Energy Focus* **28**, 56–65 (2019)

Chapter 3

Power Quality Improvement of Wind Energy Conversion System Using a Fuzzy Nonlinear Controller



3.1 Introduction

In this chapter we propose a fuzzy sliding mode control (Fuzzy-SMC). The proposed control algorithm is used, on the one hand, to regulate power injected into grid using a LCL filter and on the other hand to reduce the harmonics due to the chattering phenomenon. Some reference in the literature [1] employees a sensor for RC branch voltage measurement. This added sensor increases the system cost and does not bring any benefit. To prove that, this system studied is controlled using the sensor and without taking into consideration the RC branch sensor. Therefore, in this work effects of the sensor and the power loss are studied in terms of harmonic's reduction, DC bus voltage and power responses. The simulation results are developed to validate the proposed control system, which also experimentally validated using a test bench based on DSPace Board and three-phase inverter. The complete system model is used including model of DC bus, converters and LCL filter such as given in the diagram presented in Fig. 3.1.

The rest of this chapter is structured as follows. Mathematical modeling of grid-side system was presented in Sect. 3.2. Fuzzy sliding mode control is developed in Sect. 3.3. Simulation results are discussed to validate the proposed control in Sect. 3.4. Then, Experimental validation approach is presented in Sect. 3.5. Conclusion of this chapter is given in the last Sect. 3.6.

3.2 Modeling of Grid-Side System

3.2.1 Modeling of DC Bus

Several papers in the literature present an ideal DC bus model similar to the one given in [2]. To control DC bus voltage, a mathematical model is developed using the scheme diagram shown in Fig. 3.1 gives:

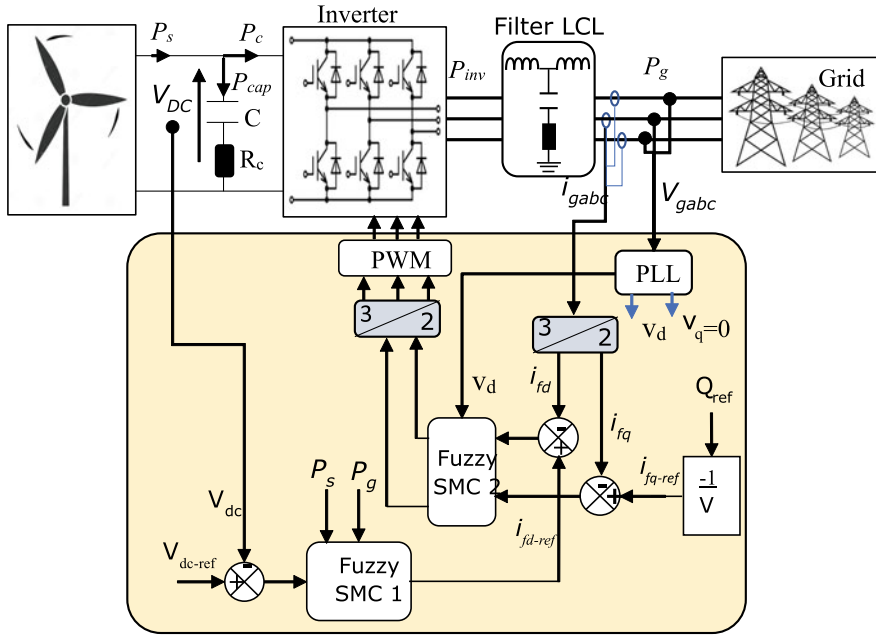


Fig. 3.1 Block diagram of the studied system with LCL filter and converter control

$$C_{dc} V_{dc} \frac{dV_{dc}}{dt} + \frac{V_{dc}^2}{R_C} = P_{dc} \quad (3.1)$$

where $P_{dc} = P_s - P_c$ and $P_c = \Delta P_f + \Delta P_c + \Delta P_{inv} + \Delta P_{ca} + \Delta P_r$.

The voltage and current sensors for data acquisition are placed at DC bus input and filter output, so the new DC bus model takes into account power loss (ΔP), generated active power (P_s) and injected active power into grid (P_g) is obtained by [3]:

$$C_{dc} V_{dc} \frac{dV_{dc}}{dt} = P_s - P_g - \Delta P \quad (3.2)$$

where $\Delta P = \Delta P_f + \Delta P_c + \Delta P_{inv} + \Delta P_{ca}$, $\Delta P_c = \frac{V_{dc}^2}{R_C}$, ΔP_{inv} and ΔP_{ca} are power losses due to filter, DC bus and cable, respectively. C , R_C , V_{dc} and P_{dc} are the capacitance, resistance, voltage and power of DC bus, respectively. These elements dissipate a part of the generated power, which demand taking into account of this eliminated power loss in controller design to ensure a stable operation. To ensure the stability of the dc bus voltage V_{dc} , the SMC should be designed with a equivalent control law versus the total power loss ΔP . Substituting active power expression of grid ($P_g = i_{Gd} v_{Gd}$) into (3.2) gives:

$$\frac{dV_{dc}}{dt} = \frac{P_s - \Delta P - i_{Gd}v_{Gd}}{C_{dc}V_{dc}} \quad (3.3)$$

The implementation of the dc bus voltage control using SMC is developed following the steps described in [3, 7]. The sliding surface, used to control the variable V_{dc} , is defined as follows:

$$s_{dc} = e_{dc} = V_{dc-ref} - V_{dc} \quad (3.4)$$

Where $e_{dc} = V_{dc-ref} - V_{dc}$ is the error and V_{dc-ref} is the reference of the variable. The equivalent control U_{eq} is calculated during the sliding surface and under steady state operation. This condition is obtained if $s_{dc} = 0$, therefore $\frac{ds_{dc}}{dt} = 0$ and $U_n = 0$. The derivation of S_{dc} is given by:

$$\frac{ds_{dc}}{dt} = \frac{dV_{dc-ref}}{dt} - \frac{dV_{dc}}{dt} \quad (3.5)$$

During the sliding surface reaching and steady state, $S(V_{dc}) = 0$. Then, the derivative of the sliding surface is expressed by:

$$\frac{dS_{dc}}{dt} = \frac{dV_{dc-ref}}{dt} - \frac{dV_{dc}}{dt} \text{ and } \frac{dV_{dc-ref}}{dt} = 0 \quad (3.6)$$

From (3.4) and (3.6), the derivative of sliding surface is written as:

$$\frac{dS_{dc}}{dt} = C_{dc}V_{dc}(P_s - \Delta P - i_{Gd-eq}v_{Gd}) = 0 \quad (3.7)$$

Therefore, the d-axis component of the current reference is expressed by:

$$i_{Gd-eq} = \frac{P_s - \Delta P}{v_{Gd}} \quad (3.8)$$

The discontinuous current is given by:

$$i_{Gd-n} = -k_{dc}sgn(S_{dc}) \quad (3.9)$$

The inner loop current reference is given by (3.10).

$$i_{Gd-ref} = \frac{P_s \Delta P}{v_{Gd}} - k_{dc}sgn(S_{dc}) \quad (3.10)$$

where k_{dc} is a positive constant and “ sgn ” is the sign function adopted to reduce the ripples due to chattering phenomena. During steady state and sliding surface reaching, the amount of power loss is equal to difference between generated power and that measured at filter output.

3.2.2 Model of Filter

The model of adopted LCL filter is developed in park reference frame (d, q) as follows:

$$\begin{cases} i_{Id} = \frac{\omega_b}{s.L_I}(u_{Id} + \omega_g.L_I.i_{Iq} - u_{Cd}) \\ i_{Iq} = \frac{\omega_b}{s.L_I}(u_{Iq} - \omega_g.L_I.i_{Id} - u_{Cq}) \end{cases} \quad (3.11)$$

$$\begin{cases} i_{Gd} = \frac{\omega_b}{s.L_G}(-u_{Gd} + \omega_g.L_G.i_{Gq} + u_{Cd}) \\ i_{Gq} = \frac{\omega_b}{s.L_G}(-u_{Gq} - \omega_g.L_G.i_{Gd} + u_{Cq}) \end{cases} \quad (3.12)$$

$$\begin{cases} i_{Cd} = i_{Id} - i_{Gd} \\ i_{Cq} = i_{Iq} - i_{Gq} \end{cases} \quad (3.13)$$

$$\begin{cases} u_{cap-d} = u_{Cd} - R_f.i_{Cd} \\ u_{cap-q} = u_{Cq} - R_f.i_{Cq} \end{cases} \quad (3.14)$$

$$\begin{cases} i_{Cd} = \frac{s.C_F}{\omega_b}u_{cap-d} - C_F.\omega_g.u_{cap-q} \\ i_{Cq} = \frac{s.C_F}{\omega_b}u_{cap-q} + C_F.\omega_g.u_{cap-d} \end{cases} \quad (3.15)$$

where:

u_{Id} and u_{Iq} are d-axis and q-axis inverter voltage components, respectively.

i_{Id} and i_{Iq} are d- and q-axis inverter current components, respectively.

u_{Gd} and u_{Gq} are d-axis and q-axis grid voltage components, respectively.

i_{Gd} and i_{Gq} are the d-axis and q-axis grid current components, respectively.

L_I and L_G are the LCL filter-side inductance and the grid-side inductance, respectively.

C_F and R_F : Capacitance and resistance of LCL filter, respectively.

u_{cd} and u_{cq} : d-axis and q-axis voltage components of RC branch of LCL filter, respectively.

i_{cd} and i_{cq} : components of the d-axis and q-axis current passing through RC branch, respectively.

$\omega_e = 2\pi f$, where f is the grid frequency.

The LCL filter parameters are calculated using an algorithm developed in references [4, 5].

3.3 SMC of Grid-Side Converter

3.3.1 SMC of Grid-Side Current

Sliding mode control guarantees good performance regarding the tracking of the desired values, robustness against parameter variations [6, 7] and sudden load change [8]. However, it increases harmonics due to the chattering phenomenon. To attenuate the current ripples and reducing harmonics, an LCL filter should be used. This last is chosen because of the small size, low cost and better attenuation of ripples [9, 10]. The model of LCL filter developed in (d, q) reference frame in the first chapter is investigated in this chapter.

The RC sensor is used to measure the current i_C flowing through the RC branch of the filter. Therefore, the d-axis and q-axis RC branch current equations (i_{Cd} , i_{Cq}) are introduced into the control system.

Using filter model equations in (d, q) reference, the new model expressions versus (i_{Cd} and i_{Cq}) are obtained as follows [3]:

$$\begin{cases} i_{Gd} + i_{Cd} = \frac{\omega_b}{L_1 s} u_{Id} + \frac{\omega L_L}{\omega_b} (i_{Gq} + i_{Cq}) - u_{Cd} \\ i_{Gq} + i_{Cq} = \frac{\omega_b}{L_1 s} u_{Iq} - \frac{\omega L_L}{\omega_b} (i_{Gd} + i_{Cd}) - u_{Cq} \end{cases} \quad (3.16)$$

$$\begin{cases} i_{Gd} = \frac{\omega_b}{L_1 s} u_{Id} + \frac{\omega}{s} i_{Gq} + \frac{\omega}{s} i_{Cq} - \frac{\omega_b}{L_1 s} u_{Cd} - i_{Cd} \\ i_{Gq} = \frac{\omega_b}{L_1 s} u_{Iq} - \frac{\omega}{s} i_{Gd} - \frac{\omega}{s} i_{Cd} - \frac{\omega_b}{L_1 s} u_{Cq} - i_{Cq} \end{cases} \quad (3.17)$$

From Eq.(3.3), the obtained expressions of u_{Cd} and u_{Cq} are:

$$\begin{cases} u_{Cd} = \frac{L_G s}{\omega_b} i_{Gd} + u_{Gd} - \frac{\omega L_G}{\omega_b} . i_{Gq} \\ u_{Cq} = \frac{L_G s}{\omega_b} i_{Gq} + u_{Gq} + \frac{\omega L_G}{\omega_b} . i_{Gd} \end{cases} \quad (3.18)$$

The substitution of u_{Cd} and u_{Cq} in Eq.(3.17) gives

$$\begin{cases} i_{Gd} = \frac{\omega_b}{L_1 s} u_{Id} + \frac{\omega}{s} i_{Gq} + \frac{\omega}{s} i_{Cq} - \frac{\omega_b}{L_1 s} \left(\frac{L_G s}{\omega_b} i_{Gd} + u_{Gd} - \frac{\omega L_G}{\omega_b} . i_{Gq} \right) - i_{Cd} \\ i_{Gq} = \frac{\omega_b}{L_1 s} u_{Iq} - \frac{\omega}{s} i_{Gd} - \frac{\omega}{s} i_{Cd} - \frac{\omega_b}{L_1 s} \left(\frac{L_G s}{\omega_b} i_{Gq} + u_{Gq} + \frac{\omega L_G}{\omega_b} . i_{Gd} \right) - i_{Cq} \end{cases} \quad (3.19)$$

$$\begin{cases} \left(1 + \frac{L_G}{L_1} \right) i_{Gd} = \frac{\omega_b}{L_1 s} u_{Id} + \frac{\omega}{s} i_{Gq} + \frac{\omega}{s} i_{Cq} - \frac{\omega_b}{L_1 s} u_{Gd} + \frac{\omega L_G}{L_1 s} . i_{Gq} - i_{Cd} \\ \left(1 + \frac{L_G}{L_1} \right) i_{Gq} = \frac{\omega_b}{L_1 s} u_{Iq} - \frac{\omega}{s} i_{Gd} - \frac{\omega}{s} i_{Cd} - \frac{\omega_b}{L_1 s} u_{Gq} - \frac{\omega L_G}{L_1 s} . i_{Gd} - i_{Cq} \end{cases} \quad (3.20)$$

After the simplification of (3.20), the expression of the current injected into the network is given by:

$$\begin{cases} i_{Gd} = \frac{\omega_b}{(L_I+L_G)s} u_{Id} + \frac{L_I}{(L_I+L_G)s} [\omega(1 + \frac{\omega_b L_G}{L_I}).i_{Gq} + \omega i_{Cq} - \frac{\omega_b}{L_I} u_{Gd}] \\ \quad - \frac{L_I}{(L_I+L_G)} i_{Cd} \\ i_{Gq} = \frac{\omega_b}{(L_I+L_G)s} u_{Iq} + \frac{L_I}{(L_I+L_G)s} [-\omega(1 + \frac{\omega_b L_G}{L_I}).i_{Gd} - \omega i_{Cd} - \frac{\omega_b}{L_I} u_{Gq}] \\ \quad - \frac{L_I}{(L_I+L_G)} i_{Cq} \end{cases} \quad (3.21)$$

The derivation of the currents i_{Gd} and i_{Gq} is given by:

$$\begin{cases} \frac{di_{G_d}}{dt} = \frac{\omega_b}{(L_I+L_G)} u_{I_d} + e_d \\ \frac{di_{G_q}}{dt} = \frac{\omega_b}{(L_I+L_G)} u_{I_q} + e_q \end{cases} \quad (3.22)$$

where

$$e_d = \frac{L_I}{(L_I + L_G)} \left(\omega \left(1 + \frac{\omega_b L_G}{L_I} \right) i_{G_q} + \omega i_{C_q} - \frac{\omega_b}{L_I} u_{G_d} \right) - \frac{L_I}{(L_I + L_G)} \frac{di_{C_d}}{dt} \quad (3.23)$$

$$e_q = \frac{L_I}{(L_I + L_G)} \left(-\omega \left(1 + \frac{\omega_b L_G}{L_I} \right) i_{G_d} - \omega i_{C_d} - \frac{\omega_b}{L_I} u_{G_q} \right) - \frac{L_I}{(L_I + L_G)} \frac{di_{C_q}}{dt} \quad (3.24)$$

The sliding surfaces of i_{G_d} and i_{G_q} are expressed by:

$$S_{G_d} = e_{G_d} = i_{G_d_ref} - i_{G_d} \quad (3.25)$$

$$S_{G_q} = e_{G_q} = i_{G_q_ref} - i_{G_q} \quad (3.26)$$

where i_{Gd-ref} and i_{Gq-ref} are the desired values of i_{Gd} and i_{Gq} , respectively. i_{Gd-ref} is generated directly from DC bus voltage control loop, while i_{Gq-ref} is calculated using reactive power expression.

The derivative of the sliding surfaces are defined by

$$\frac{dS_{Gd}}{dt} = \frac{di_{Gd-ref}}{dt} - \frac{di_{Gd}}{dt} \quad (3.27)$$

$$\frac{dS_{Gq}}{dt} = \frac{di_{Gq-ref}}{dt} - \frac{di_{Gq}}{dt} \quad (3.28)$$

Therefore

$$\frac{dS_{Gd}}{dt} = \frac{di_{Gd-ref}}{dt} - \frac{\omega_b}{(L_I + L_G)} u_{Id} - e_d \quad (3.29)$$

$$\frac{dS_{Gq}}{dt} = \frac{di_{Gq-ref}}{dt} - \frac{\omega_b}{(L_I + L_G)} u_{Iq} - e_q \quad (3.30)$$

During the reaching of sliding surface and steady state, $S_{Gd} = 0$ and $S_{Gq} = 0$. Where u_{Id-eq} and u_{Iq-eq} are the voltages of the equivalent control.

$$\frac{dS_{Gd}}{dt} = \frac{di_{Gd-ref}}{dt} - \frac{\omega_b}{(L_I + L_G)} u_{Id-eq} - e_d = 0 \quad (3.31)$$

$$\frac{dS_{Gq}}{dt} = \frac{di_{Gq-ref}}{dt} - \frac{\omega_b}{(L_I + L_G)} u_{Iq-eq} - e_q = 0 \quad (3.32)$$

Therefore, the equivalent control voltages (u_{Id-eq} and u_{Iq-eq}) are expressed by:

$$u_{Id-eq} = \frac{L_I + L_G}{\omega_b} \left(\frac{di_{Gd-ref}}{dt} - e_d \right) \quad (3.33)$$

$$u_{Iq-eq} = \frac{L_I + L_G}{\omega_b} \left(\frac{di_{Gq-ref}}{dt} - e_q \right) \quad (3.34)$$

Finally, the converter control voltages (u_{Id-ref} and u_{Iq-ref}) are expressed as:

$$u_{Id-ref} = \frac{L_I + L_G}{\omega_b} \left(\frac{di_{Gd-ref}}{dt} - e_d \right) - k_{Gd} \cdot \text{sgn}(S_{Gd}) \quad (3.35)$$

$$u_{Iq-ref} = \frac{L_I + L_G}{\omega_b} \left(\frac{di_{Gq-ref}}{dt} - e_q \right) - k_{Gq} \cdot \text{sgn}(S_{Gq}) \quad (3.36)$$

3.3.2 Analysis of System Stability

Theorem 3.1 *The system, including equations of filter and dc bus models, is developed to ensure regulation of dc bus voltage and control of d-axis and q-axis current components.*

According to change of variable, the equilibrium point $S_e = x_{ref} - x = 0$ is interesting to ensure the asymptotic convergence of the variable x to the desired value. x represents V_{dc}, i_{Gd} or i_{Gq} and x_{ref} represents V_{dc-ref}, i_{Gd-ref} or i_{Gq-ref} .

Proof To ensure stability of system studied, the derivative of Lyapunov candidate function positive definite (3.37) must be negative or strictly negative.

$$\frac{d\gamma_2}{dt} = S_{dc} \frac{dS_{dc}}{dt} + S_{Gd} \frac{dS_{Gd}}{dt} + S_{Gq} \frac{dS_{Gq}}{dt} \quad (3.37)$$

The derivatives of the sliding surfaces ((3.7), (3.29) and (3.30)) are substituted in (3.37) to obtain:

$$\begin{aligned} \frac{d\gamma}{dt} = & e_{Gd} \frac{di_{Gd-ref}}{dt} - e_{Gd} \frac{\omega_b}{L_I + L_G} u_{Id} - e_d e_{Gd} + e_{Gq} \frac{di_{Gq-ref}}{dt} \\ & - e_{Gq} \frac{\omega_b}{L_I + L_G} u_{Iq} - e_q e_{Gq} + e_{dc} \frac{dV_{dc-ref}}{dt} - e_{dc} \frac{P_s - i_{Gd} V}{V_{dc} C_{dc}} \end{aligned} \quad (3.38)$$

When replacing the references of the current and the voltage by (3.10), (3.35) and (3.36), taking into account $\frac{dV_{dc-ref}}{dt} = 0$ and after simplification, the Eq. (3.37) becomes:

$$\begin{aligned} \frac{d\gamma}{dt} = & e_{Gd} \frac{di_{Gd-ref}}{dt} - e_{Gd} \frac{\omega_b}{L_I + L_G} \frac{L_I + L_G}{\omega_b} \left(\frac{di_{Gd-ref}}{dt} - e_d \right) \\ & - e_{Gd} \frac{\omega_b}{L_I + L_G} k_{Gd} \text{sgn}(S_{Gd}) - e_d e_{Gd} + e_{Gq} \frac{di_{Gq-ref}}{dt} \\ & - e_{Gq} \frac{\omega_b}{L_I + L_G} \frac{L_I + L_G}{\omega_b} \left(\frac{di_{Gq-ref}}{dt} - e_q \right) - e_{Gq} \frac{\omega_b}{L_I + L_G} k_{Gq} \cdot \text{sgn}(S_{Gq}) \\ & - e_q e_{G-q} + e_{dc} \frac{dV_{dc-ref}}{dt} - e_{DC} \frac{P_s - V \frac{P_s}{v_{Gd}} + V k_{Ld} \text{sgn}(S_{dc})}{V_{dc} C_{dc}} \end{aligned} \quad (3.39)$$

After simplification:

$$\begin{aligned} \frac{d\gamma}{dt} = & e_{Gd} \frac{di_{Gd-ref}}{dt} - e_{Gd} \frac{di_{Gd-ref}}{dt} + e_{Gd} e_d - e_{Gd} \frac{\omega_b}{L_I + L_G} k_{G-d} \text{sgn}(S_{G-d}) \\ & - e_d e_{Gd} + e_{Gq} \frac{di_{Gq-ref}}{dt} - e_{Gq} \frac{di_{Gq-ref}}{dt} + e_{G-q} e_q \\ & - e_{Gq} \frac{\omega_b}{L_I + L_G} k_{Gq} \text{sgn}(S_{Gq}) - e_q e_{Gq} + e_{dc} \frac{dV_{dc-ref}}{dt} \\ & - e_{dc} \cdot \text{sgn}(S_{dc}) \frac{V \cdot k_{Ld}}{V_{dc} C_{dc}} \end{aligned} \quad (3.40)$$

Then:

$$\begin{aligned} \frac{d\gamma_2}{dt} = & - \frac{\omega_b}{L_I + L_G} k_{Gd} e_{Gd} \cdot \text{sgn}(S_{Gd}) - \frac{\omega_b}{L_I + L_G} k_{Gq} e_{Gq} \cdot \text{sgn}(S_{Gq}) \\ & - e_{dc} \cdot \text{sgn}(S_{dc}) \frac{V \cdot k_{Ld}}{V_{dc} C_{dc}} \end{aligned} \quad (3.41)$$

Finally:

$$\frac{d\gamma_2}{dt} = -\frac{\omega_b}{L_I + L_G} k_{Gd} |e_{Gd}| - \frac{\omega_b}{L_I + L_G} k_{Gq} |e_{Gq}| - \frac{V \cdot k_{Ld}}{V_{dc} C_{dc}} |e_{dc}| \leq 0 \quad (3.42)$$

where $||$ indicates the absolute value.

From Eq. 3.42 it can be seen that the derivative of Lyapunov function is negative, Therefore, the stability criteria of SMC is guaranteed.

3.3.3 Sliding Mode Control of Grid Current Without RC Sensor

The three impedances of LCL filter can be computed as follows:

- Inverter-side impedance Z_I (L_I): $Z_I = L_I \cdot 2\pi \cdot 50 = 0.0511 \Omega$.
- Grid-side impedance Z_G (L_G): $Z_G = L_G \cdot 2\pi \cdot 50 = 0.0029 \Omega$.
- Impedance of RC branch Z_{RC} (R_F , C_F):

$$Z_{RC} = \sqrt{R_F^2 + \frac{1}{(100\pi \cdot C_F)^2}} = 9.684 \Omega$$

It can see that Z_{RC} is higher than that Z_I and Z_G . Then, current passing through RC branch is lower compared to the others. Then, the RC branch can be neglected during the filter modelling and controller design. Therefore, the filter model, taking into account the orientation of the grid voltage on the d-axis, becomes:

$$\frac{di_{G_d}}{dt} = \frac{\omega_b}{L_I + L_G} [u_{I_d} + (L_I + L_G)\omega_e i_{G_q} - V] \quad (3.43)$$

$$\frac{di_{G_q}}{dt} = \frac{\omega_b}{L_I + L_G} [u_{I_q} - (L_I + L_G)\omega_e i_{G_d}] \quad (3.44)$$

Using this approximation and following the steps for SMC design such that described in Sect. 3.2, the SMC laws for grid current control are developed as follows:

$$u_{I_d-ref} = \frac{(L_I + L_G)}{\omega_b} \frac{di_{G_d-ref}}{dt} - (L_I + L_G)\omega_e i_{G_q} + V - k_{G_d} \text{sgn}(S_{G_d}) \quad (3.45)$$

$$u_{I_q-ref} = \frac{(L_I + L_G)}{\omega_b} \frac{di_{G_q-ref}}{dt} + (L_I + L_G)\omega_e i_{G_d} - k_{G_q} \text{sgn}(S_{G_q}) \quad (3.46)$$

3.3.4 Fuzzy Smooth Function of FSMC

In this chapter, fuzzy logic has been applied for developing a smooth discontinuous control of SMC. This smooth fuzzy function reduces the output oscillations and

participates in system stability. The output is discontinuous control and input is error “e”. This input is converted into adequate linguistic values by means of fuzzification function.

The linguistic notations for input and output are given as: Big Negative (BN), Small Negative (SN), Equal to Zero (EZ), Small Positive (SP) and Big Positive (BP). The Gaussian membership for input and output are shown in Fig. 3.2a and b. The control strategy is based on an algorithm in the form of “If condition, then conclusion” “IF-THEN”, according to the expert knowledge of error control [3, 11].

- If (S is BN) then (u is BP).
- If (S is SN) then (u is SP).
- If (S is EZ) then (u is EZ).
- If (S is SP) then (u is SN).
- If (S is BP) then (u is BN).

The surface of the output versus the input is given in Fig. 3.2c. The output is generated by defuzzification using center of gravity approach to convert linguistic variables into real output values [12].

3.3.5 FSMC Stability Analysis

Theorem 3.2 *The fuzzy rules which ensure the stability and the condition of existence of SMC are given by [3]:*

- If $S > 0$ then $U_{sw} < 0$ (must be negative).
- If $S < 0$ then $U_{sw} > 0$ (must be positive).

Whatever S and U_{sw} are, their values satisfy the condition $S \cdot U_{sw} < 0$. Where U_{sw} must be replaced by $i_{Gd-Fuzzy}$, $u_{Iq-Fuzzy}$ or $u_{Id-Fuzzy}$.

For V_{dc} control: $S_{dc} \cdot i_{Gd-Fuzzy} < 0$.

For current control: $S_{Id} \cdot u_{Id-Fuzzy} < 0$ and $S_{Iq} \cdot u_{Iq-Fuzzy} < 0$.

Proof To demonstrate Theorem 3.2 and system stability, the Lyapunov function is defined by:

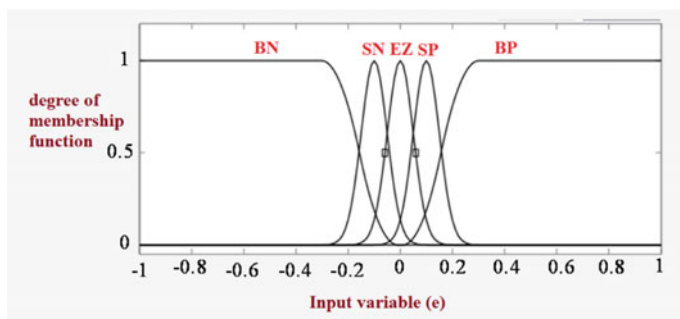
$$\gamma = \frac{1}{2}S_{dc}^2 + \frac{1}{2}S_{Gd}^2 + \frac{1}{2}S_{Gq}^2 \quad (3.47)$$

The time derivative of Lyapunov candidate function is expressed as:

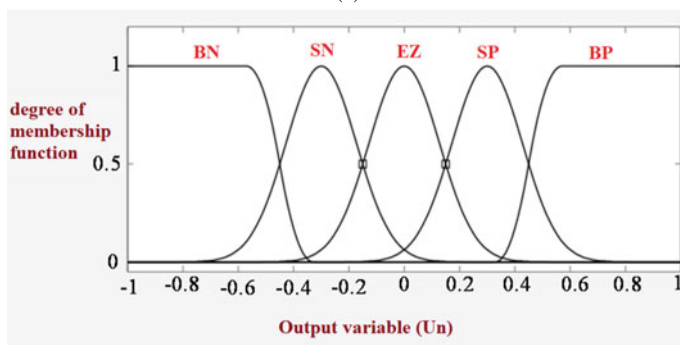
$$\dot{\gamma} = \dot{\gamma}_{dc} + \dot{\gamma}_{Gd} + \dot{\gamma}_{Gq} = s_{dc}\dot{s}_{dc} + s_{Gd}\dot{s}_{Gd} + s_{Gq}\dot{s}_{Gq} \quad (3.48)$$

Concerning V_{dc} control, derivative of γ is expressed as:

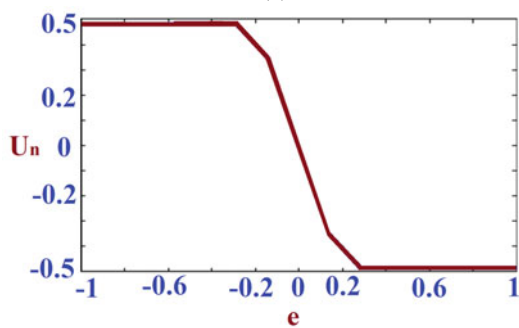
$$\dot{\gamma}_{dc} = s_{dc}(\dot{V}_{dc-ref} - \dot{V}_{dc}) = s_{dc} \left(\dot{V}_{dc-ref} - \frac{P_s - \Delta P - i_{Gd} \cdot v_{Gd}}{C_{dc} V_{dc}} \right) \quad (3.49)$$



(a)



(b)



(c)

Fig. 3.2 The Gaussian membership functions: **a** Input membership functions **b** Output membership functions and **c** Surface of output versus input

$$\dot{v}_{dc} = S_{dc} \cdot \left(\dot{V}_{dc-ref} + \frac{-P_s + \Delta P}{C_{dc} V_{dc}} + \frac{v_{Gd}}{C_{dc} V_{dc}} i_{Gd} \right) \quad (3.50)$$

$$\dot{v}_{dc} = S_{dc} \cdot \left(\dot{V}_{dc-ref} + \frac{-P_s + \Delta P}{C_{dc} V_{dc}} + \frac{v_{Gd}}{C_{dc} V_{dc}} (i_{Gd-equ} + i_{Gd-Fuzzy}) \right) \quad (3.51)$$

$$\dot{v}_{dc} = S_{dc} \cdot \left(\dot{V}_{dc-ref} + \frac{-P_s + \Delta P}{C_{dc} V_{dc}} + \frac{v_{Gd}}{C_{dc} V_{dc}} \left(\frac{P_s - \Delta P}{v_{Gd}} + i_{Gd-Fuzzy} \right) \right) \quad (3.52)$$

$$\dot{v}_{dc} = S_{dc} \cdot \left(\dot{V}_{dc-ref} + \frac{v_{Gd}}{C_{dc} V_{dc}} i_{Gd-Fuzzy} \right) \quad (3.53)$$

$\dot{V}_{dc-ref} = 0$ because V_{dc-ref} is constant.

$$\dot{v}_{dc} = -\frac{v_{Gd}}{C_{dc} V_{dc}} S_{dc} \cdot i_{Gd-Fuzzy} = -\frac{v_{Gd}}{C_{dc} V_{dc}} |S_{dc} \cdot i_{Gd-Fuzzy}| < 0 \quad (3.54)$$

Following the same steps, the derivatives $\dot{v}_{Gd} < 0$ and $\dot{v}_{Gq} < 0$.

Therefore, $\dot{v}_{dc} + \dot{v}_{Gd} + \dot{v}_{Gq} < 0$.

From previous analysis study, it is clearly evident that the FSMC stability condition is achieved.

3.4 Simulation Validation

The simulation results are carried out using physical model developed by Matlab/Simulink environment in Fig. 3.3 and system control configured in Fig. 3.1. Parameters for simulation are given in the appendix (Tables A.1 and A.2). Switching frequency is 10 KHz and sampling time of “Discrete Powergui” is $T_s = 10^{-5}$ s. The objective of simulation is to evaluate current THDi, responses of active and reactive powers, as well as V_{dc} response.

3.4.1 Comparative Study of Filters and Their Control Systems

The comparative study is developed, on one hand, between LCL filter and RL filter and, on other hand, between SMC, Fuzzy-SMC control with/without RC sensor. From Figs. 3.4, 3.5 and 3.6 it can be seen that the THDi given by SMC with LCL is lower than that of SMC with RL filter. Therefore the LCL is considered as the best solution to overcome problem of harmonics. Figure 3.5c reveals that the RC-branch current of LCL filter is very small and oscillates around zero. Then, this current has no effect on control system, but bring a high cost. In Fig. 3.7b the PI controller ensure

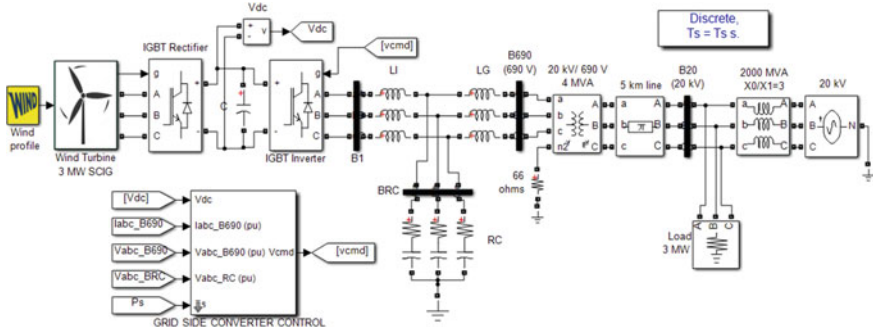


Fig. 3.3 Modeling scheme in MATLAB/Simulink used to obtain the simulation results

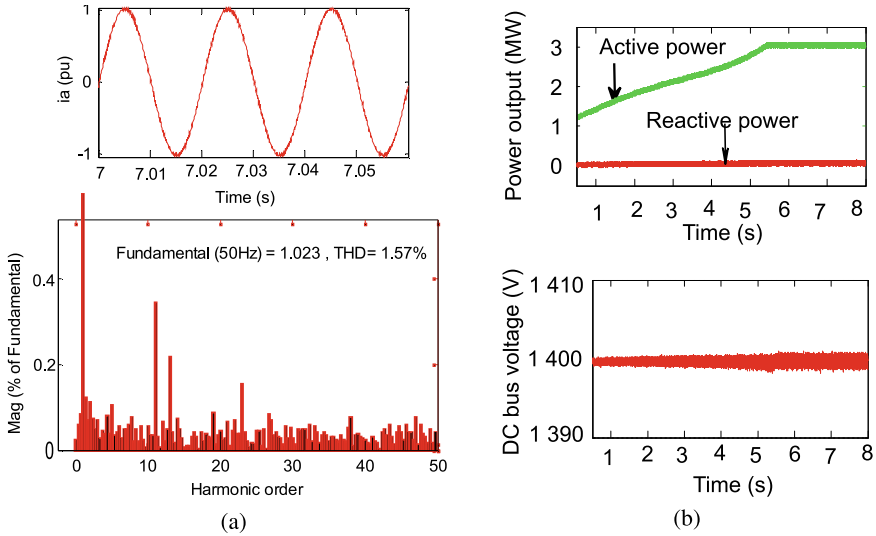


Fig. 3.4 Simulation results of SMC using LCL filter and without RC sensor

the control of V_{dc} to track its reference precisely. But introducing SMC, without power loss, for V_{dc} control lead to system instability. Figure 3.6b shows that deleting of term including power loss for compensation, influence on stability of SMC for V_{dc} control. Therefore, the DC bus voltage does not track desired value. To solve this problem the power loss should be taking into account as shown in Figs. 3.8b and 3.7b shows that the replacement of the PI controller by SMC has no effect on harmonics, power regulation, and DC bus voltage.

The data presented in Table 3.1 are extracted from Fig. 3.4, 3.5, 3.6, 3.7, 3.8 and 3.9. From this table, it can be concluded that the best response is obtained by using the proposed controller (Fuzzy-SMC) with power loss compensation, adopting the LCL filter without using any sensor in the RC branch. This proposed control offers

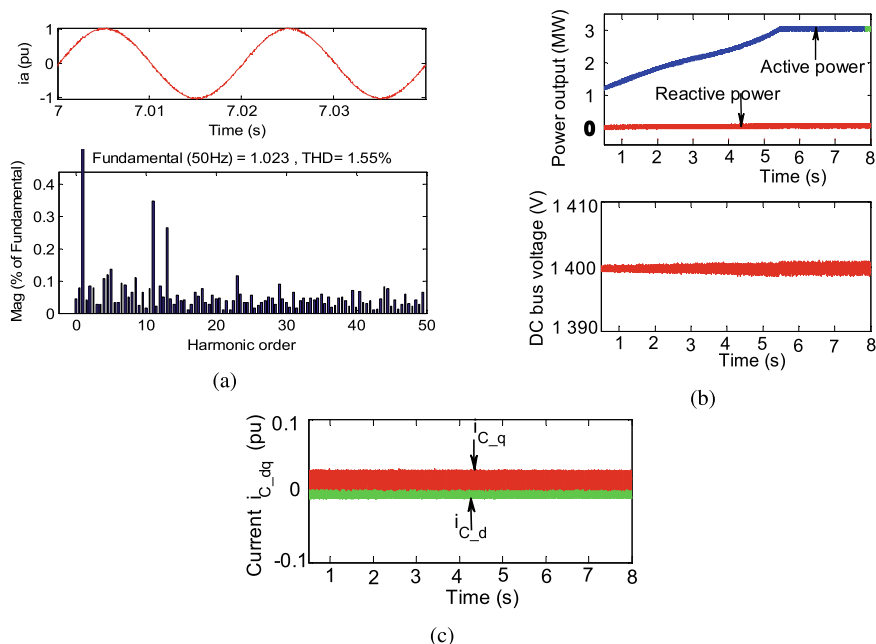


Fig. 3.5 The simulation results of SMC with the LCL filter and the use of sensors at the RC branch. **a** THD of the current, **b** Power and DC bus voltage and **c** Current passing through RC branch of the filter

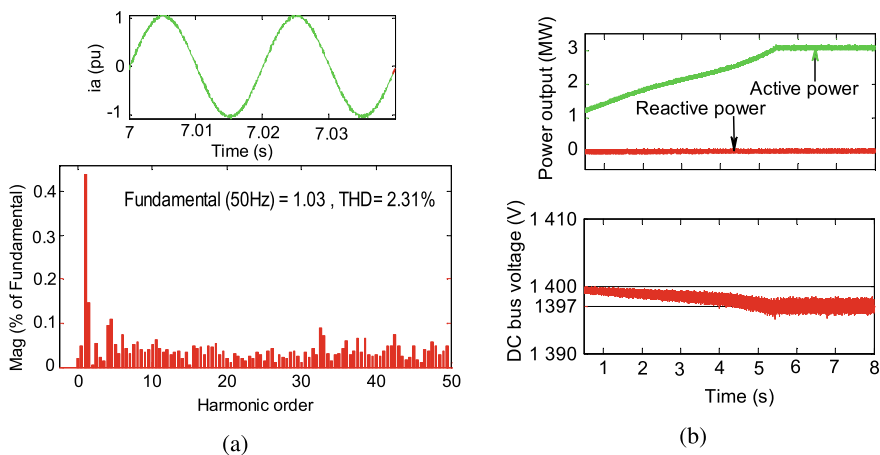


Fig. 3.6 Simulation results of SMC with the RL filter without taking into account the power loss: **a** Current THDi and **b** Power and voltage of DC bus

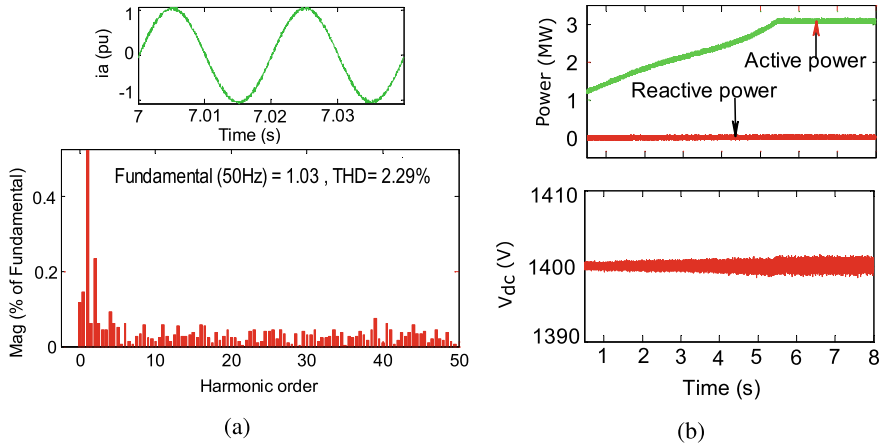


Fig. 3.7 Simulation results of SMC used for current control with the RL filter and the PI controller used for V_{dc} control: **a** Current THDi and **b** Power and voltage of DC bus

Table 3.1 Comparison between the performance of the filters and their proposed controls

Figures	Filter	Control	RC sensor	Power loss compensation	THDi%
Fig. 3.12	LCL	SMC	With	With	1.55
Fig. 3.11	LCL	SMC	Without	With	1.57
Fig. 3.16	LCL	FSMC	Without	With	1.51
Fig. 3.13	RL	SMC	Without	Without	2.31
Fig. 3.15	RL	SMC	Without	With	2.24
Fig. 3.14	RL	SMC for current and PI for V_{dc} control	Without	Without	2.29

the following advantages: (i) voltage V_{dc} is regulated to track 1400 V, (ii) Measured active power follows its reference very well, (iii) Measured reactive power follows its reference ensuring unity power factor, and (iv) THDi is reduced and complies with IEEE [13] recommendations (Table A.3 in Appendix A) and the ICE standards adopted by the Office National of Electricity (ONEE) (Table A.4 in Appendix A) [14–16].

3.4.2 Robustness Test Against Variation of Parameters

Robustness test of control system against parameter variations of inductance, damping resistance and capacitor of LCL filter, and capacitor value of DC bus. The sce-

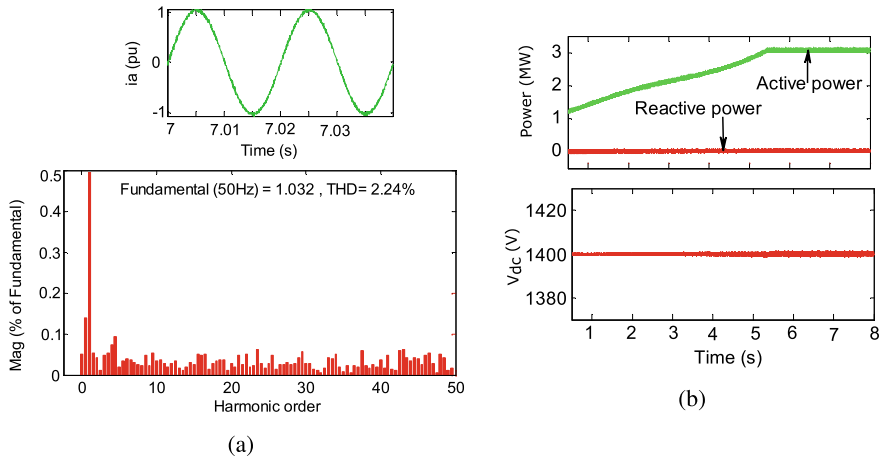


Fig. 3.8 Simulation results of SMC for RL filter taking into account power loss: **a** THD of the current and **b** Power and voltage of DC bus

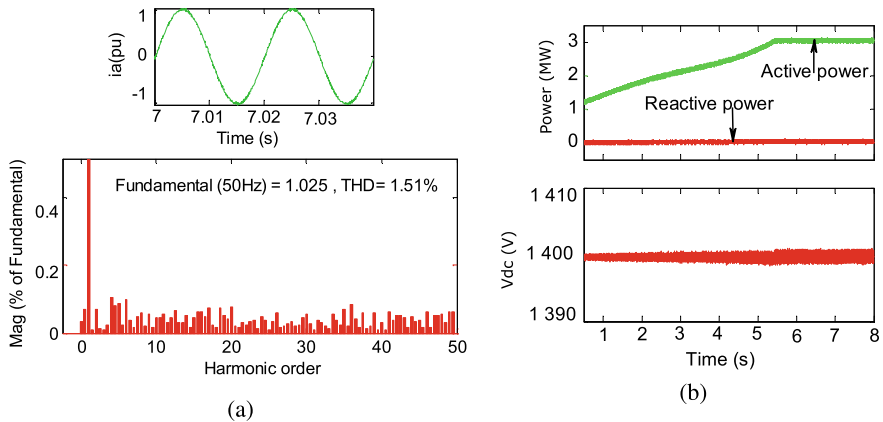


Fig. 3.9 Simulation results of fuzzy SMC for the LCL filter taking into account the power loss and without using sensor in the RC branch: **a** THD of current and **b** Power and voltage of the DC bus

nario aims to vary parameters of LCL filter and DC bus capacitance from 4 to 8 s. The parameters vary to a value of -50% for LCL filter and -60% for DC bus capacitance, respectively. The robustness of SMC for DC bus voltage control with power loss compensation against parameter variations is proved in Fig. 3.10. This control method is more robust than the conventional PI controller. Figure 3.11 presents the simulation results for robustness test of proposed Fuzzy-SMC against parameter variations of LCL filter and DC bus capacitance of -60% . The DC bus voltage, active power and reactive power present identical responses during the operation with/without varia-

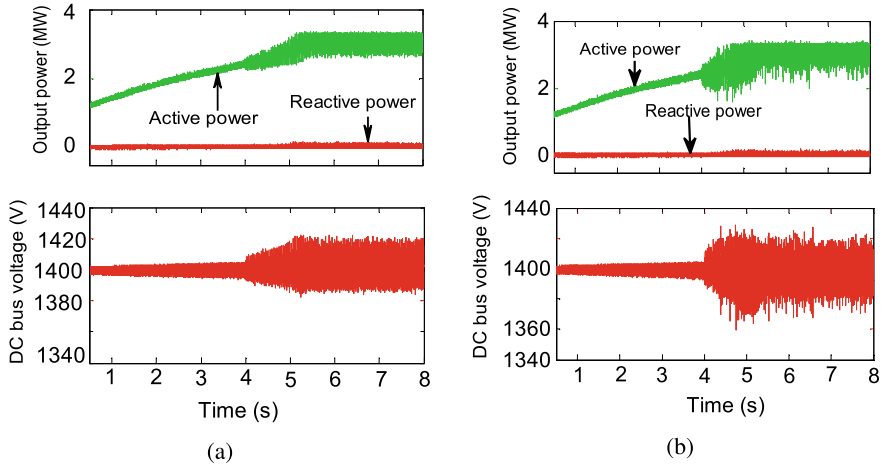


Fig. 3.10 Simulation results of robustness test against parameter variation of -60% of DC bus capacitance value (using RL filter and SMC for current control). **a** DC bus voltage control using SMC and **b** V_{dc} voltage regulation using PI controller

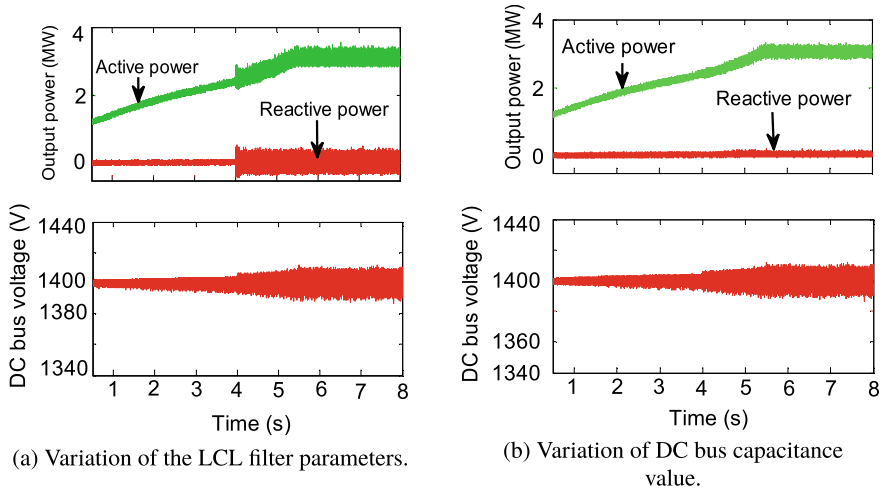


Fig. 3.11 Simulation results of robustness test of the proposed Fuzzy-SMC control against parameter variations of -60% : **a** variation of the LCL filter parameters and **b** variation of the DC bus capacitance value

tion of the parameters. Therefore, robustness of the proposed Fuzzy-SMC against parameter variations is convincingly proven.

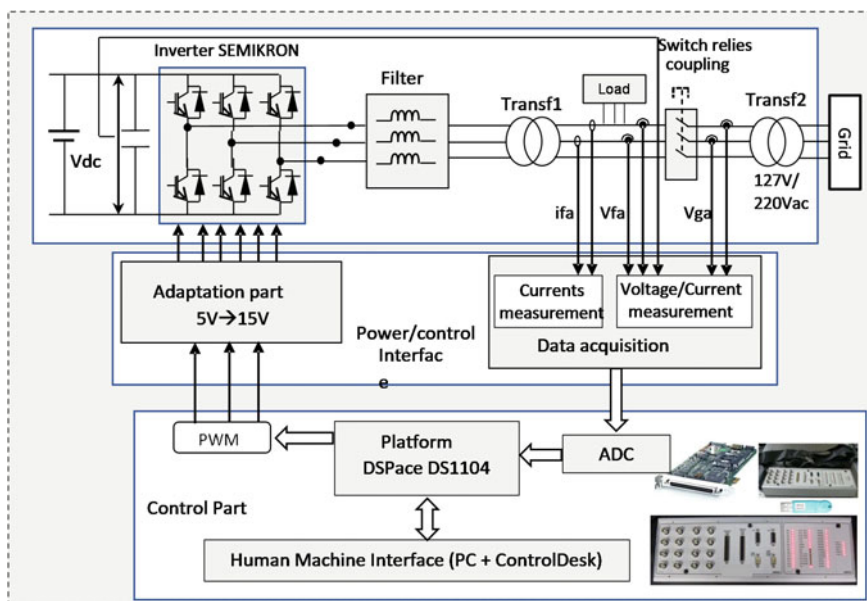


Fig. 3.12 Synoptic diagram of the experimental platform

3.5 Experimental Validation Approach

In order to validate the control methods experimentally, a comparison between the LCL filter and the RL filter on the one hand, and between the vector control, SMC and Fuzzy-SMC on the other hand, has been developed. The control system is implemented on DSPACE DS1104 board using the experimental platform presented by the synoptic block diagram Fig. 3.12 and the flow chart for coupling inverter to grid in Fig. 3.13.

3.5.1 Comparative Study Between RL Filter and LCL Filter

The Figs. 3.14 and 3.15 present THDi and THDv using LCL and RL filters and also their maximum values (THDi-max, THDv-max).

For RL filter: THDv-max = 5.8%f and THDi-max = 8.9%f.

For LCL filter: THDv-max = 2.9%f and THDi-max = 7.5%f.

From this comparative study it can conclude that LCL filter attenuates harmonics better than RL filter, which demonstrate the effectiveness of the adopted LCL filter.

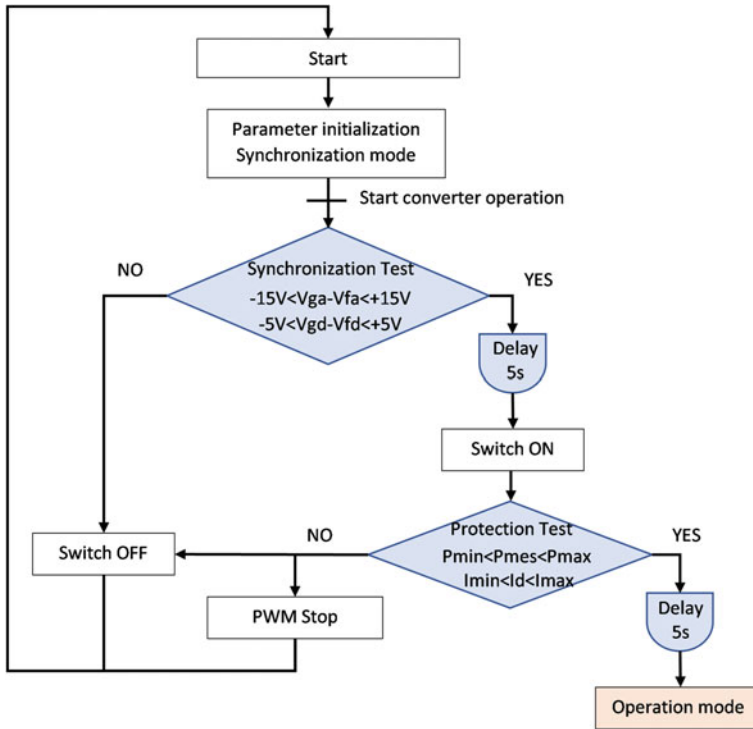


Fig. 3.13 Flow chart for coupling inverter to grid

3.5.2 Comparative Study for Control Methods Using LCL Filter

Figures 3.16 and 3.17 show that the THDs of SMC, with/without RC sensor addition, are almost identical. From an economic point of view the control case without RC sensor is the best choice.

In Figs. 3.17 and 3.18, the THD maximum values of LCL filter are:

For SMC Fig. 3.17: $THD_{v-max} = 3.4\% f$ and $THD_{di-max} = 12.4\% f$. Because of chattering effect the THDs given by SMC are higher than that given by vector control with PI controller.

For Fuzzy-SMC Fig. 3.18: $THD_{v-max} = 2.6\% f$ and $THD_{di-max} = 8.6\% f$. The THD are reduced considerably using the proposed Fuzzy-SMC.

Thus, these experimental results demonstrates that Fuzzy-SMC strategy with LCL filter is the most effective method can be chosen for control and harmonic mitigation. These comply with the ICE standards adopted by the Office National de l'Electricité (ONEE) (Tables A.3 and A.4 in Appendix A) [14–16]. As shown in Fig. 3.19, the good transient active power response is obtained with SMC and Fuzzy-SMC methods with low overshoot of power response. While response of vector control depends

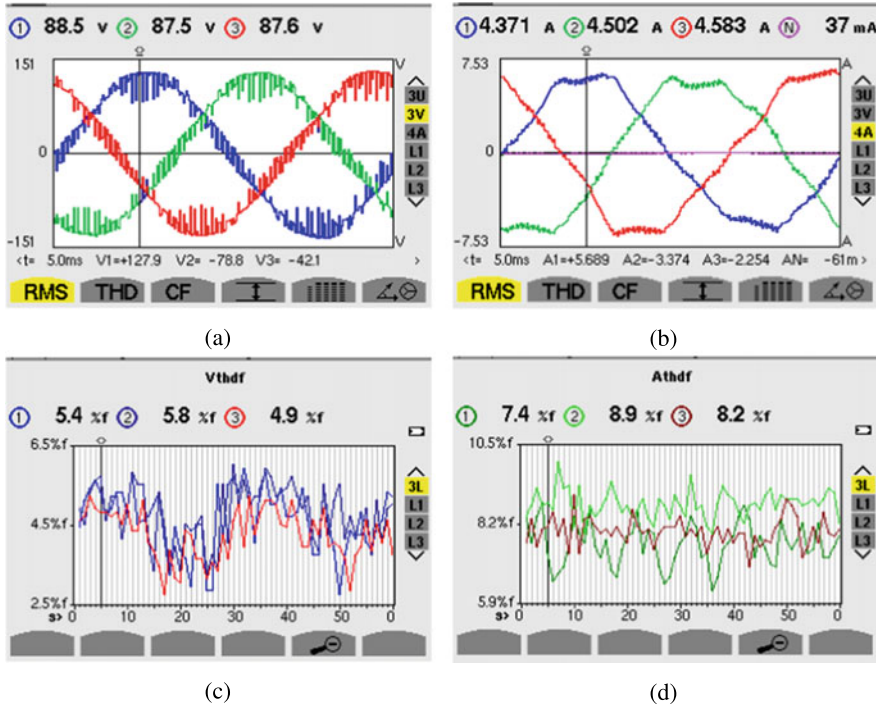


Fig. 3.14 Experimental results of three phases at output of RL filter, **a** three-phase voltages, **b** three-phase currents, **c** THDv of voltage and **d** THDi of current

mostly on parameters of PI controller, it obviously has a long settling time and larger overshoot.

3.5.3 Robustness Test

To connect and disconnect the platform elements, two connection circuits are made, as shown in Fig. 3.20. Each circuit is made using a model of 4 relays controlled manually and automatically with DSpace through optocouplers. The grid connection circuit (Rel1) is designed to connect the system to the grid during synchronization.

The Rel2 circuit is realized to decrease the filter inductance by connecting two identical inductances in parallel, in order to study the impact of parameter variation on system and test robustness of the adopted controls. Figure 3.21 shows THD of current and voltage, using DATView software for data analysis and C.A 8331 power analyzer. These results demonstrate that the robustness of Fuzzy-SMC against inductance variation (L_f) of LCL filter is convincingly verified.

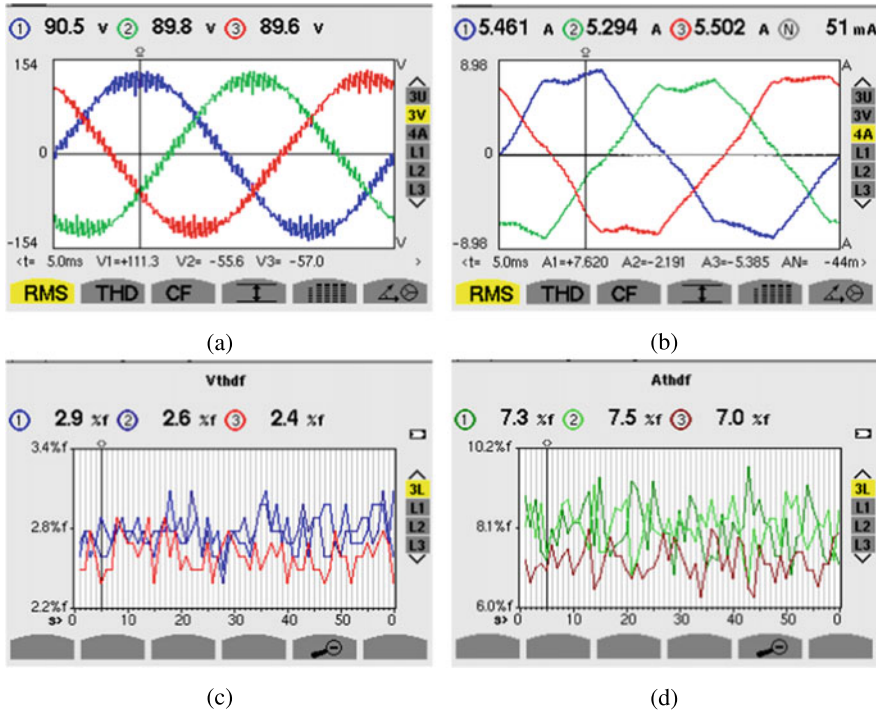


Fig. 3.15 Experimental results of three phases at output of LCL filter, **a** three-phase voltages, **b** three-phase currents, **c** THDv of voltage and **d** THDi of current

3.6 Conclusion

In this chapter the nonlinear Fuzzy-SMC, with LCL filter and power loss compensation without current sensor in RC branch, has been proposed. Indeed, LCL filter attenuates harmonics better than RL filter and current THDi of Fuzzy-SMC is lower compared to that given by conventional SMC. The robustness test of the system proves the effectiveness and robustness of the Fuzzy-SMC nonlinear control. Therefore, the proposed fuzzy-SMC is capable to provide improved transient performance similar to that of SMC, and maintain the harmonic spectrum at the same level as that of vector control (VC). It can be seen that the advantage of the current sensor is not very significant. On the other hand, the control without current sensor provides a low cost of the equipment. Therefore, the proposed control guarantees good performances in terms of current THD reduction, DC bus voltage regulation, active and reactive powers and robustness against filter parameters variation and DC bus capacitance value. The experimental results are almost similar to the obtained simulation results. This demonstrates the good operation of the system and the validation of the proposed and implemented control laws.

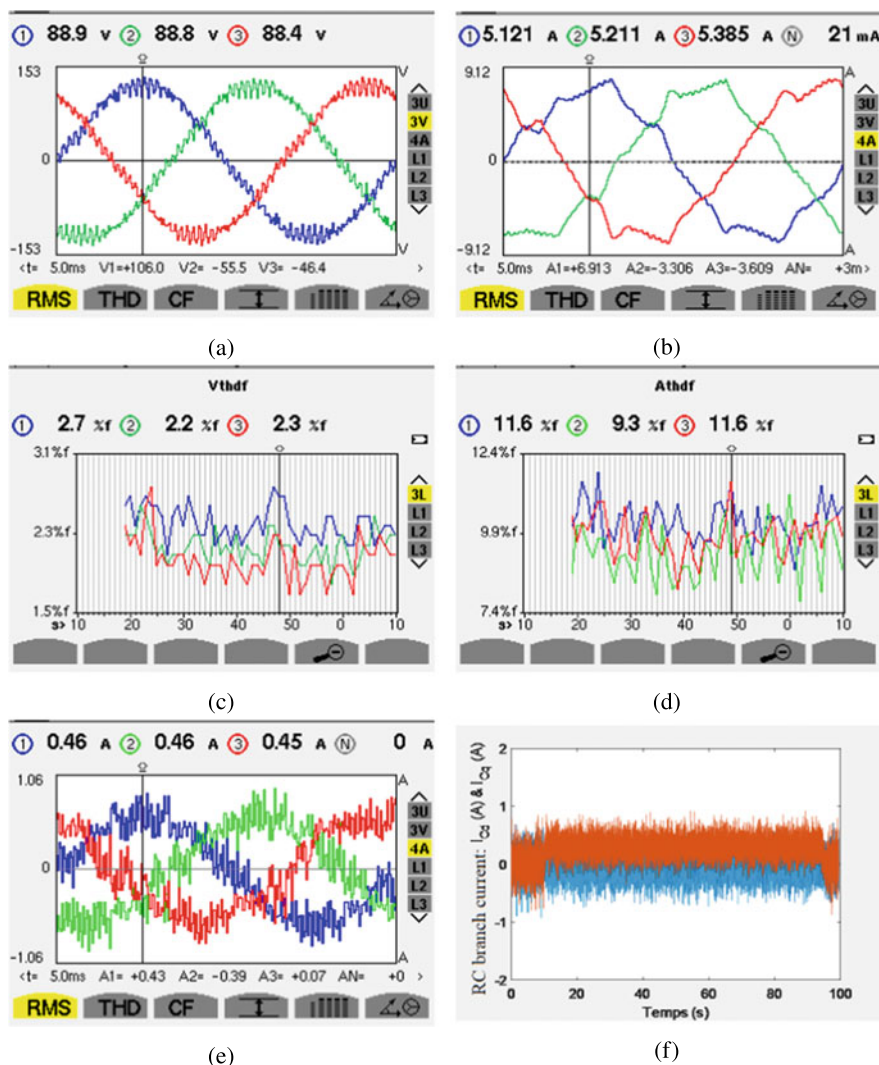


Fig. 3.16 Experimental results of SMC with LCL filter and RC sensor, **a** three-phase voltages, **b** three-phase currents **c** THDv with maximum values, **d** THDi with maximum values, **e** three-phase currents of RC branch and **f** currents of 'd' and 'q' axes of RC branch of LCL filter

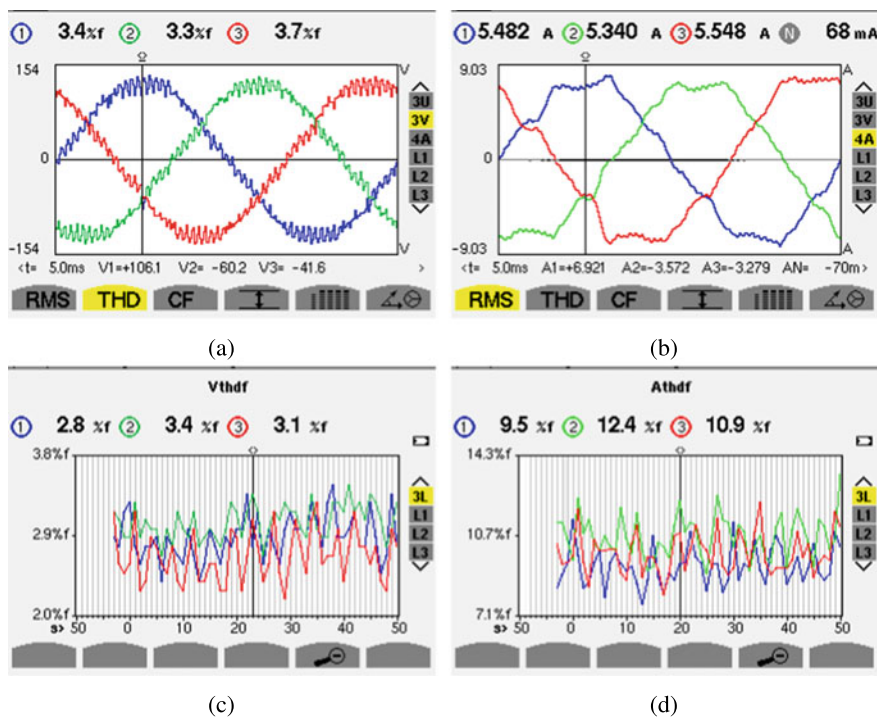


Fig. 3.17 Experimental results of the sliding mode control with LCL filter and without RC sensor, **a** Three-phase voltages, **b** Three-phase voltages **c** THDv with maximum values, **d** THDi with maximum values

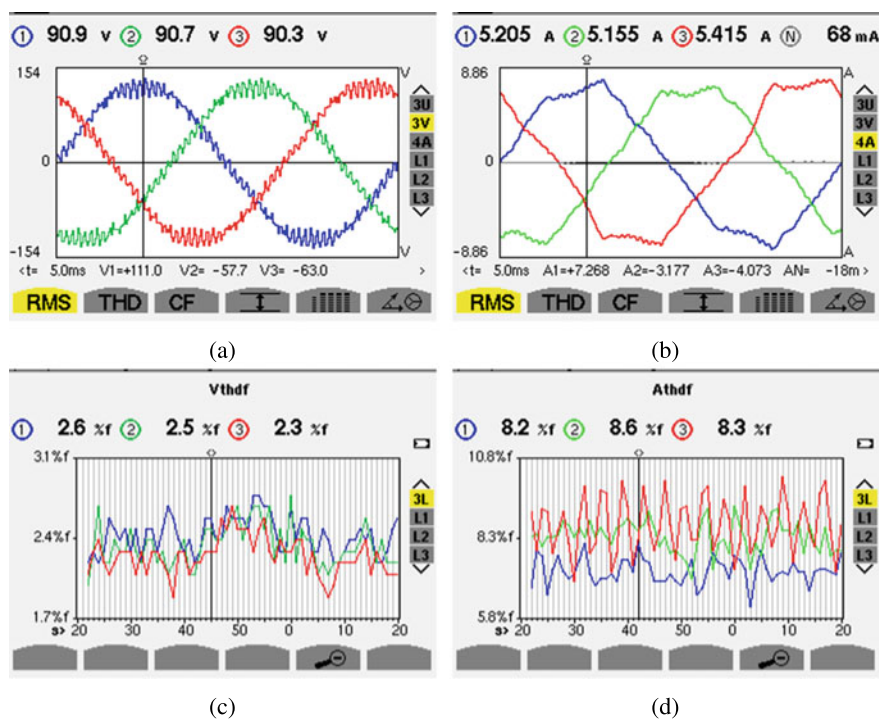
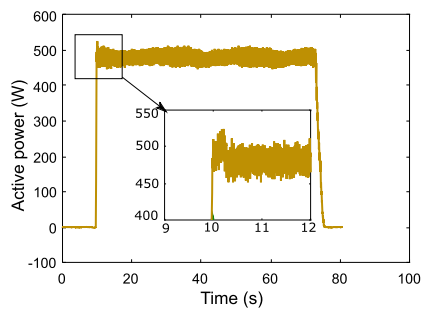
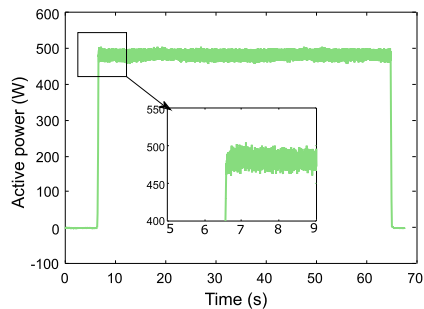


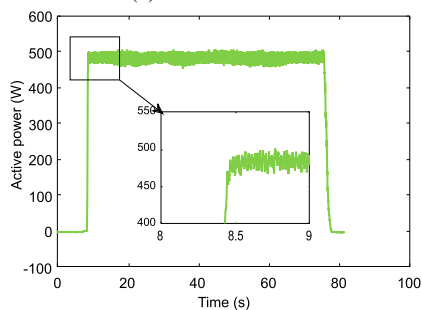
Fig. 3.18 Experimental results of the fuzzy sliding mode control with LCL filter and without RC sensor, **a** Three-phase voltages, **b** Three-phase currents, **c** THDv with maximum values, **d** THDi with maximum values



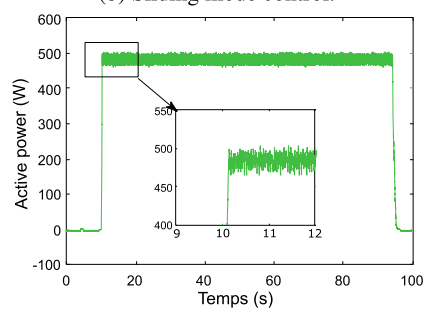
(a) Vector control.



(b) Sliding mode control.



(c) Fuzzy sliding mode control without RC sensor addition.



(d) Sliding mode control with RC sensor addition.

Fig. 3.19 Experimental results of active power at the LCL filter output using: **a** Vector control, **b** Conventional SMC, **c** Fuzzy-SMC, and **d** SMC with RC sensor addition

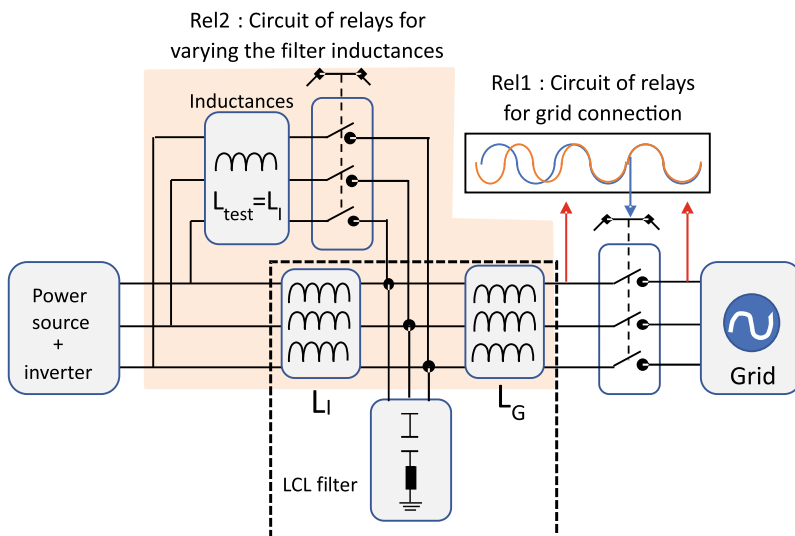
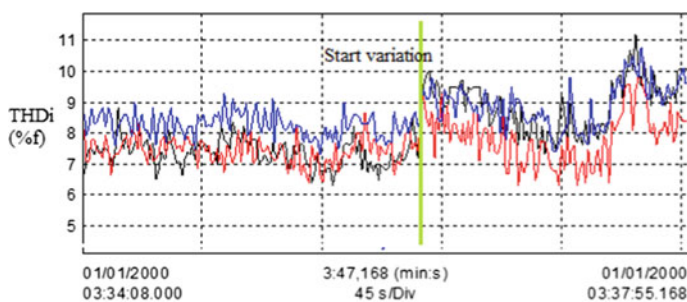
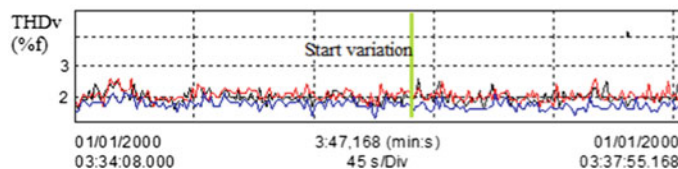


Fig. 3.20 The two circuits of the switching relays for connection to the grid and variation of the filter inductance



(a) THDi during filter inductance variation.



(b) THDv during filter inductance variation.

Fig. 3.21 THD of current and voltage for robustness test of proposed Fuzzy-SMC during LCL filter inductance variation of -50%

References

1. Hao, X., Yang, X., Liu, T., Huang, L., Chen, W.: A sliding-mode controller with multi-resonant sliding surface for single-phase grid-connected VSI with an LCL-filter. *IEEE Trans. Power Electr.* **28**(5), 2259–2268 (2013)
2. Abo-Khalil, A.G., Lee, D.-C.: DC-link capacitance estimation in AC/DC/AC PWM converters using voltage injection. *IEEE Trans. Ind. Appl.* **44**(5), 1631–1637 (2008)
3. Elyalaoui, K., Ouassaid, M., Cherkaoui, M.: Improvement of THD performance of a robust controller for grid-side energy conversion system based on LCL filter without RC sensor. *Int. J. Electr. Power & Energy Syst.* **121**, 123 (2020). <https://doi.org/10.1016/j.ijepes.2020.106143>
4. Liserre, M., Blaabjerg, F., Hansen, S.: Design and control of an LCL-filter-based three-phase active rectifier. *IEEE Trans. Ind. Appl.* **41**(5), 1281–1291 (2005)
5. Júnior, V.P.B., Jacomini, A.S.F.R., Filho, A.S.: Simulation study of squirrel cage induction generator fed by a back-to-back converter and by using a LCL filter (2013)
6. Wang, P., Liu, L., Han, Z., Cai, X.: Sliding mode control for wind energy grid-connected converter with LCL filter. *Wind Eng.* **35**(6), 703–714 (2011)
7. Ouassaid, M., Elyalaoui, K., Cherkaoui, M.: Sliding mode control of induction generator wind turbine connected to the grid. *Advances and Applications in Nonlinear Control Systems*, pp. 531–553. Springer International Publishing Switzerland (2016)
8. Guzman, R., Vicuña, L.G.d., Morales, J., Castilla, M., Matas, J.: Sliding-mode control for a three-phase unity power factor rectifier operating at fixed switching frequency. *IEEE Trans. Power Electr.* **31**(1), 758–769 (2016)
9. Biel, D., Dòria-Cerezo, A., Fossas, E.: Sliding mode control of a three-phase four-wire LCL rectifier. In: 2014 13th International Workshop on Variable Structure Systems (VSS). IEEE (2014)
10. Lekhchine, S., Bahi, T., Abadlia, I., Bouzeria, H.: PV-battery energy storage system operating of asynchronous motor driven by using fuzzy sliding mode control. *Int. J. Hydrog. Energy* (9) (2016)
11. Liu, H., Chen, Z.: Aggregated modelling for wind farms for power system transient stability studies. In: 2012 Asia-Pacific Power and Energy Engineering Conference, pp. 1–6. IEEE (2012)
12. Duong, M.Q., Francesco, G., Sonia, L., Mussetta, M., Emanuele, O.: Pitch angle control using hybrid controller for all operating regions of SCIG wind turbine system. *Renew. Energy* **70**, 197–203 (2014)
13. IEEE519-1992, IEEE Recommended Practices and Requirements for Harmonics Control in Electric Power Systems (ANSI), p. 73. IEEE, New York (1992)
14. McGranaghan, M., Beaulieu, G.: Update on IEC 61000-3-6: Harmonic Emission Limits for Customers Connected to MV, HV, and EHV (2006)
15. Office National de l'Electricité (ONE), Conditions for connecting wind turbines and PV-based solar plants to the national transmission grid (2014)
16. Halpin, S.M.: Comparison of IEEE and IEC harmonic standards. In: IEEE Power Engineering Society General Meeting, pp. 2214–2216. IEEE (2005)

Chapter 4

Supervisory and Power Control Systems of a WF for Participating in Auxiliary Services



4.1 Introduction

Wind farms are increasingly requested to provide active and reactive power control capabilities, either for system service participation or to keep a unit power factor and produce maximum power (Fig. 4.1). In this context, many researchers in control and management of wind power plant system focus on the design of supervisory systems. For dispatching active and reactive power references on wind turbines one of three supervision algorithms can be used: The first algorithm is based on the Integral Proportional Controller (PI) [1]. The second is the proportional distribution algorithm [2, 17, 18]. The third is based on the optimization method with the objective function [3–5]. The central supervisory unit is configured to control active and reactive power (P_F , Q_F) generated by the farm and inject it into grid. Local supervisory units are configured to estimate maximum power (active and reactive powers) of each wind turbine and then send the required information about wind turbines to central supervisory unit. These local units calculate also active power references for inverter operation adopting one of three operating modes, MPPT control mode, PQ control mode or fault control mode. According to transmission system operator, these control systems should satisfy the demand of active and reactive power at Point of Common Coupling (PCC). In order to overcome problem of reactive power control at PCC, a Reactive Power Control method by PI controller (CPR-PI) is proposed. Power distribution strategy based on proportional distribution algorithm is implemented, to ensure that the injection of active and reactive power to grid satisfies the requirements defined by TSO. A PI-Fuzzy-PI hierarchical controller is developed to compensate voltage drop (LVRT) and satisfy GCR. To evaluate the proposed control technique performances, simulation results of WF are carried out using three operating modes under variable wind speeds and adopting a scenario for grid code test. The rest part of this chapter is organized as follows. In Sect. 4.2, the wind farm supervisory system

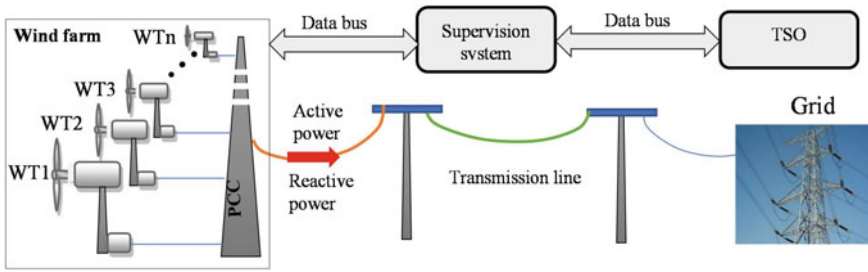


Fig. 4.1 Block diagram of the wind farm connected to the power network

is presented. Wind turbines operating modes are illustrated in Sect. 4.3. Fault control strategy using the fuzzy hierarchical controller is developed in Sect. 4.4. Finally, the conclusion highlights the main contributions in Sect. 4.5.

4.2 Wind Farm Supervision System

The supervision system comprises a set of devices and techniques for the control and monitoring of industrial processes, either under normal operating conditions or in the presence of failures and grid faults. The main activities handled by the wind farm supervision systems are the management and control of active and reactive powers, monitoring of energy production in real time, fault detection, diagnosis and protection of equipment, control of different parts of wind energy conversion system and transmission of data between the TSO and wind farm (4.1).

4.2.1 Power Dispatching Using Proportional Distribution Algorithm

The Proportional distribution algorithm aims to dispatch references of active ($P_{WT-ref-i}$) and reactive ($Q_{WT-ref-i}$) power for wind turbines. These references are developed using references of total active (P_{F-ref}) and total reactive (Q_{F-ref}) imposed by transmission system operator for wind farm. P_{F-ref} and Q_{F-ref} are divided by maximum active power (4.1) and reactive power (4.2), respectively, to obtain $P_{WT-ref-i}$ and $Q_{WT-ref-i}$, respectively. The maximum active power of WT is the optimal power generated by MPPT algorithm and the maximum capacity of farm active power is computed by sum of all maximum available active powers (4.1) [6].

$$P_{F-max} = \sum_{i=1}^n P_{WT-max-i} \quad (4.1)$$

Similarly, maximum reactive power of WF (4.2) is sum of all maximum reactive powers available in WTs.

$$Q_{F-max} = \sum_{i=1}^n Q_{WT-max-i} \quad (4.2)$$

$P_{WT-max-i}$, $Q_{WT-max-i}$ are active and reactive powers of wind turbine “i”, respectively. P_{F-max} , Q_{F-max} are defined as the total active and reactive powers of the farm, respectively. “n” is number of WTs in WF. Maximum active power is equal to optimal power ($P_{WT-max-i} = P_{opt-i}$) and Maximum reactive power is computed by (4.3).

$$Q_{WT-max} = \sqrt{S_n^2 - P_{WT}^2} - Q_s \quad (4.3)$$

where S_n is nominal apparent power and Q_s is reactive power required for magnetization of machine. References $P_{WT-ref-i}$ and $Q_{WT-ref-i}$ are generated using the proportional distribution algorithm. Using this algorithm the wind turbine which has the largest active power generation capacity will receive largest reference. Similarly, the WT which has largest reactive power generating capacity or consumption capacity will receive highest reference, as shown in Eqs. (4.4) and (4.5).

$$P_{WT-ref-i} = \frac{P_{WT-max-i}}{P_{F-max}} P_{F-ref} \quad (4.4)$$

$$Q_{WT-ref-i} = \frac{Q_{WT-max-i}}{Q_{F-max}} Q_{F-ref} \quad (4.5)$$

The advantage of this strategy is to ensure that all wind turbines are operating far enough from their maximum available capacity to not be saturated. If a WT is saturated, the missing power is compensated by others still able to produce more power, i.e., distribute their contribution fairly according to their capacity [2]. In order to implement the proportional distribution algorithm, Algorithm 1 must be followed. This algorithm can be described as shown in Fig. 4.2.

4.2.2 Supervisory System Configuration

The TSO shall manage and control powers of entire WF at all times through central supervisory unit and local supervisory units. The overall supervisory diagram for WTs is illustrated in Fig. 4.3.

Algorithm 1 Proportional distribution algorithm.

Require: $n = 3, i = 1 : n, P_{opt}(i), Qs(i), S_n$ ▷ n : numbers of WTs

while $P_{opt}(i) \geq 10\% \text{ of rated power}$ **do**

$P_{WT-max}(i) = P_{opt}(i)$

$Q_{WT-max}(i) = \sqrt{S_n^2 - (P_{WT-max}(i))^2} - Qs(i)$

$P_{F-max} = \sum_{i=1}^n (P_{WT-max}(i))$

$Q_{F-max} = \sum_{i=1}^n (Q_{WT-max}(i))$

if $P_{F-max} \geq P_{F-ref}$ & $Q_{F-max} \geq Q_{F-ref}$ **then**

$P_{WT-ref-i} = (P_{WT-max-i} \cdot P_{F-ref}) / P_{F-max}$

$Q_{WT-ref-i} = (Q_{WT-max-i} \cdot Q_{F-ref}) / Q_{F-max}$

else

while $P_{F-ref} \geq P_{F-max}$ **do**

$P_{F-ref} = P_{F-ref} - 1000$ ▷ decrease the reference

end while

while $Q_{F-ref} \geq Q_{F-max}$ **do**

$Q_{F-ref} = Q_{F-ref} - 1000$ ▷ decrease the reference

end while

end if

end while

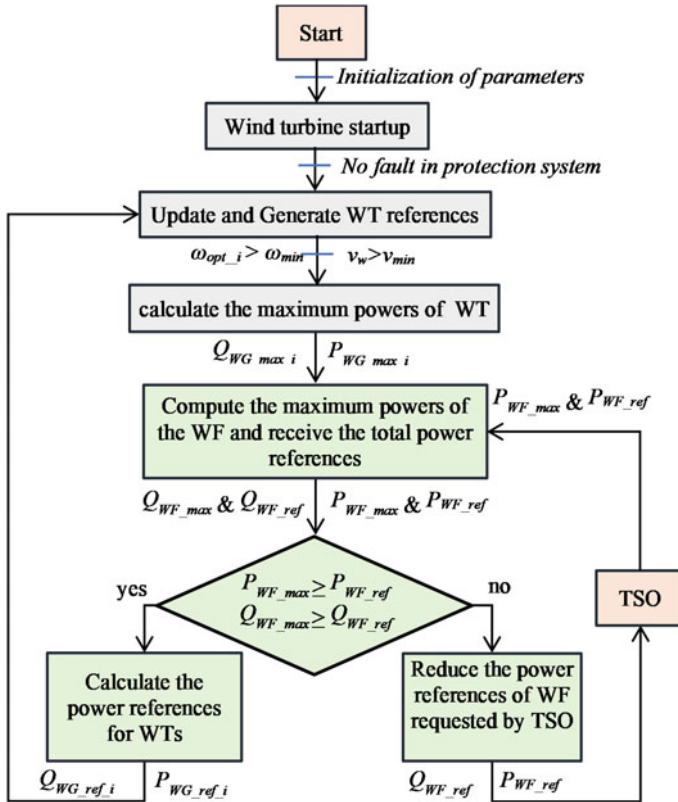


Fig. 4.2 Diagram of the adopted proportional distribution algorithm

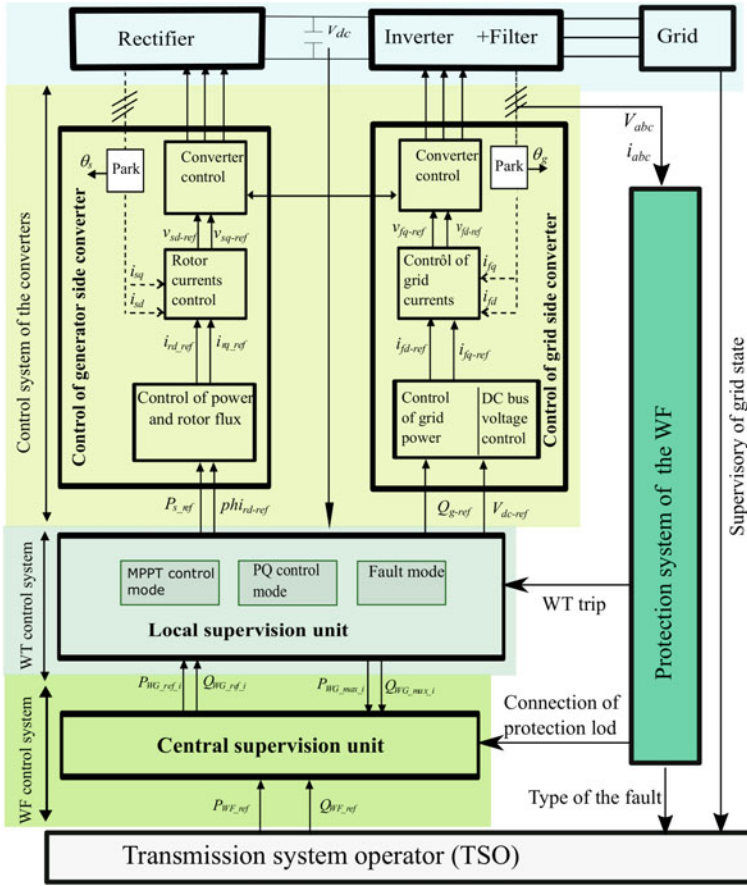


Fig. 4.3 Schematic of the supervision system configuration

4.2.2.1 Central Supervisory Unit of WF

One of main objectives of WF central supervisory unit is to control the total active and reactive power and to respect the power production plan given by TSO. Therefore, WF behaves as a conventional power plant. This central unit receives required information about power amount requested by TSO (P_{F-ref} , Q_{F-ref}). It sends the information about energy production capacity (P_{F-max} , Q_{F-max}) to TSO. The references of power ($P_{WT-ref-i}$, $Q_{WT-ref-i}$) generated by proportional distribution algorithm for each WT are sent in real time to local supervisory units.

4.2.2.2 Local Supervision Unit of WT

The local supervisory unit is configured to generate power references according to one of the three following operating modes: MPPT, PQ or fault mode. Each mode is selected based on power demand and TSO decision. As shown in Fig. 4.1b, the local supervisory unit of WT “i” receives active ($P_{WT-ref-i}$) and reactive ($Q_{WT-ref-i}$) power references from central supervisory unit, information about mechanical power P_{m-i} of WT and power at inverter output P_{WT-i} . It also calculates, in real time, $P_{WT-max-i}$ and $Q_{WT-max-i}$ generated by each WT in order to send it to central supervisory unit. The mechanical power P_{m-i} is investigated to obtain optimal power and ten maximum available power.

4.2.2.3 Automatic Protection System

The system for protection is developed to protect WTs and their equipment against unsupportable grid faults. This system aims to detect the location and type of fault and also disconnects the wind turbines from the grid if necessary, depending on the level of voltage drop, fault persistence time, location, and fault type [7]. The protection loads (LP1) should be connected at output of each disconnected wind turbine in order to dissipate the power underproduction. It also indicates type of problem and sends this information to the TSO (Fig. 4.3). Limits, period, and type of faults are listed in Table 4.1.

Table 4.1 Types of protection

Type of protection	Limits	Duration (s)
AC Instantaneous overcurrent	1.2 pu	
AC Overcurrent (positive sequence)	1.1 pu	5
AC Unbalanced current	0.4 pu	0.2
AC Under voltage (Positive sequence)	0.95 pu	1.5
AC Overvoltage (Positive sequence)	1.05 pu	1.5
AC Voltage unbalance V2/V1 (Negative sequence)	0.05 pu	0.2
AC Voltage unbalance V0/V1 (Zero sequence)	0.05 pu	0.2
DC Overvoltage	1600 (V)	0.001
Under/over frequency (Hz)	[49.8, 50.2]	2
Under/over speed (pu)	[0.3, 1.5] pu	5
Under/over wind speed (m/s)	[4, 14] m/s	

4.3 Transient Control Modes of Wind Turbines

The design of control system is developed based on proportional integral (PI) controllers. Overall system diagram of WF and its control systems are shown in Fig. 4.4.

Where, i_{fd-ref} and i_{fq-ref} are desired values of i_{fd} and i_{fq} . The reference i_{fd-ref} is derived directly from control loop of DC bus voltage, while is derived from reactive power control loop. v_{fd-ref} and v_{fq-ref} are the control voltages.

4.3.1 MPPT Control Mode

The MPPT operating mode is activated during absence of faults $V_g \geq 95\% V_n$, to generate active power reference and extract maximum power from the wind (4.6). During this control mode the reference of reactive power is equal to zero ensuring a unit power factor.

$$P_{ref} = P_{opt} = K_{opt} \cdot \omega_{opt}^3 \quad (4.6)$$

For parameters in “per unit” $K_{opt} = 1$ and $\omega_{opt} = \frac{v}{v_{nom} \lambda_{opt}}$. Where v is the wind speed (m/s), v_{nom} is nominal wind speed and $\lambda_{opt} = 1 pu$ is the optimal tip speed ratio.

4.3.2 PQ Control Mode

The TSO requires the farm to produce the requested power. Reference [8] gives examples of the reactive capacity PQ diagrams of different transmission operators in Europe. The Alberta Electric System Operator (AESO) indicates reactive power requirements for WTs with a limit of 0.484 pu for generation and 0.328 pu for consumption [8]. For WT based on SCIG, the control of generator-side converter aims to generate active power. These active power is converted into active and reactive power by means of grid-side converter as illustrated in Fig. 4.4.

If WT does not meet reactive power demand, a quantity of active power must be sacrificed to generate more reactive power. whereas, the reference is limited to the maximum value Q_{WT-max} (4.3) [9]. The active power reference P_{ref} is defined as a function of reactive power reference Q_{ref} , grid voltage V_g and maximum current (I_{max}) (4.7). the expression (4.7) ensures that the apparent power does not exceed its rated value and current does not exceed maximum value.

$$P_{ref} = \sqrt{(V_g I_{max})^2 - (Q_{ref})^2} \quad (4.7)$$

4.3.3 Fault Control Mode

When a WT is subjected to grid fault causing a voltage dip less than 0.95 pu, the MPPT and PQ control modes should be deactivated and fault mode is activated to compensate this voltage fault ($V_g \leq 0.95$ pu). The large voltage drop leading to a large current in converter [10]. To solve problem of voltage regulation, the grid code imposes for WT to generate an amount of reactive current proportional to magnitude of voltage drop. The relationship between grid voltage and reactive current, in unit notation, is expressed by (4.8), where $V_0/V_n = 1$ pu and $I_{q0}/I_n = 0$ pu.

$$I_q > -2(1 - V_g) \quad (4.8)$$

Therefore, the expression of the reactive current injected into the network versus the magnitude of the network voltage drop is expressed as :

$$I_q = K(1 - V_g) \quad (4.9)$$

Where k is a constant and $k \geq -2$ and $(1 - V_g) \geq 0$. Using rated value of reactive current $I_n = 1$ pu and maximum voltage drop obtained at $V_g = 0$ pu, $k = 1$. Then reactive current can be defined by the following expression:

$$I_q = 1 - V_g \quad (4.10)$$

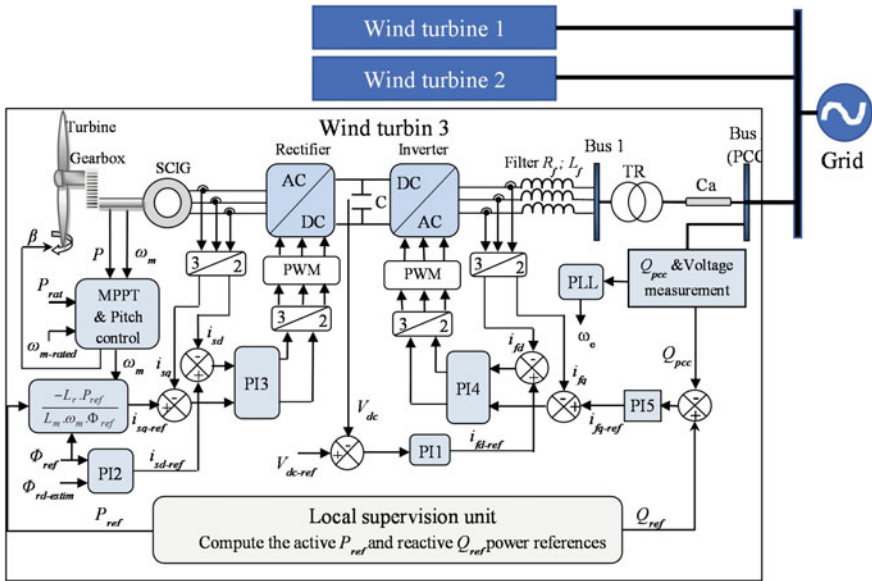


Fig. 4.4 Overall diagram of wind farm and converter control

The orientation of voltage V_g on d-axis allows to obtain $V_q = 0$ and $V_d = V_g$. The reactive power equation given in (2.21) can be expressed as follows:

$$Q = I_q \cdot V_g \quad (4.11)$$

Therefore, according to Eq. (4.10) and the reactive power expression (4.11), the expression for reactive power versus voltage magnitude during the fault is expressed as:

$$Q_{ref} = V_g(1 - V_g) \quad (4.12)$$

Adopting this fault control mode gives possibility to inject power into grid, but does not give the possibility to control the turbine speed during fault. The voltage fault duration is short (maximum of 1.5 s) and the turbine speed vary slowly because of inertia. Therefore, the speed does not deviate too much from initial value during voltage fault that can be supported by WT [11]. Hence, there is no threat to mechanical structure of WT.

4.3.4 Validation and Discussion

The system studied, including grid-connected WF and control system, as well as supervisory systems, are modeled and implemented using Matlab/Simulink software and Simscape tools as shown in Fig. 4.5. The WF is composed of three variable speed wind turbines connected to PCC. The WF rated power capacity is 9 MW and the WTs operating under different variable wind speeds. The simulation results aims to demonstrate the effectiveness the WF control and supervisory systems. The system parameters are given in Appendix A (Sect. A.2, Table A.5).

Two simulation scenarios are performed. Each scenario is divided into three periods; In period 1, MPPT control mode is activated, in period 2 PQ control mode is activated, while the fault control mode is activated automatically in period 3 when a grid fault causes a voltage drop.

Scenario 1: The results of this scenario are given in Figs. 4.6 and 4.7 under variable wind speeds presented in Fig. 4.6b and voltage drop of 40% at $t = 9$ s, as shown in Fig. 4.6a. Despite grid fault, current value does not exceed its nominal value as shown in Fig. 4.7a and DC bus voltage of first wind turbine follows the reference $V_{dc-ref} = 1400$ V as illustrated in Fig. 4.7b. But, a peak less than 7% of V_{dc} nominal value appeared without any risk to the DC bus capacitor, because the DC bus is oversized to support this over-voltage.

The system operation during three periods of scenario 1 is presented as follows:

- Period 1 [0–4s]: During this period the MPPT operating mode is activated. The simulation results shown in Figs. 4.8 and 4.9 show that the active power (4.8) is the sum of the optimal powers of the three wind turbines displayed in Fig. 4.9a,

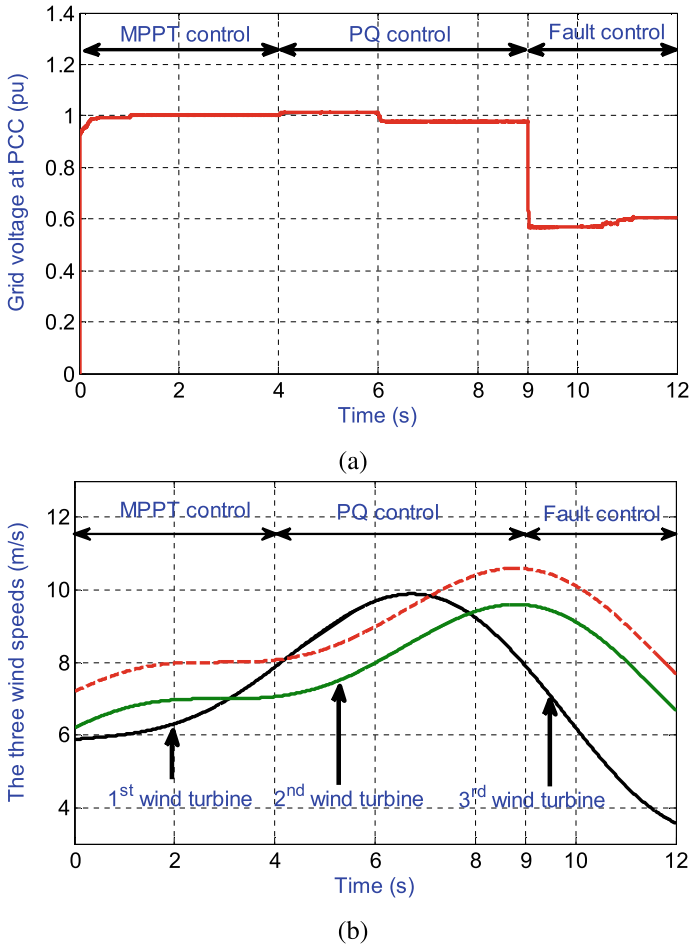
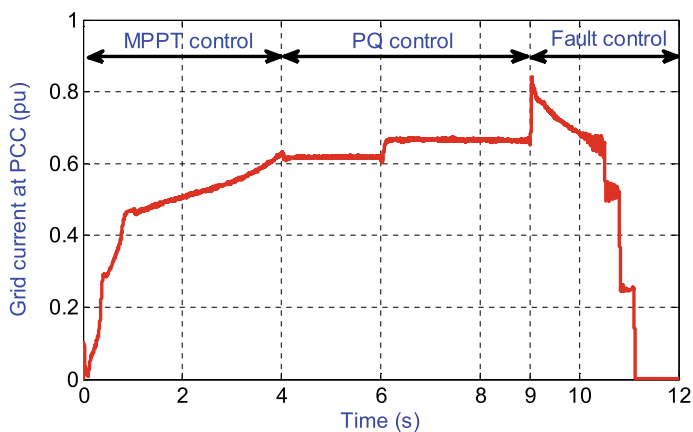


Fig. 4.6 Simulation results for scenario 1: **a** Grid voltage, **b** Three wind profiles

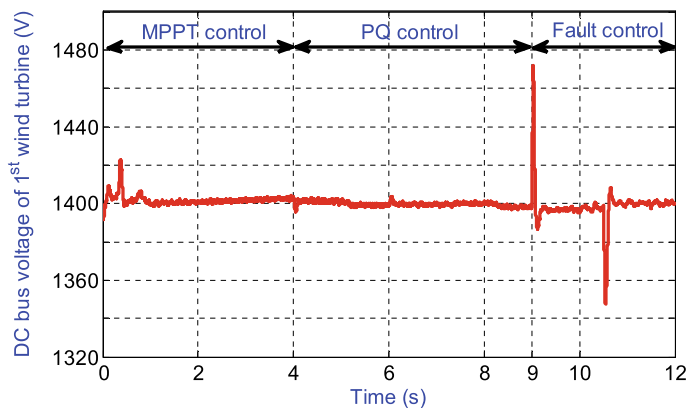
- Verify the WF operation during voltage drop (LVRT) according to grid code requirements.
- Study and analysis the behaviors of the WF and the interactions of WTs.

In this scenario the fault mode is activated automatically for LVRT control when a voltage drop of 0.7 pu happens during period of 0.6 s [from 9 to 9.6 s]. The voltage dip is presented in Fig. 4.10a. The WF operate under constant wind speeds presented in Fig. 4.10b.

The LVRT control is automatically activated during a 70% voltage drop at time 9 s within a period of 0.6 s [from 9 to 9.6 s] (Fig. 4.10a). A constant wind speed profile is adopted (Fig. 4.10b).



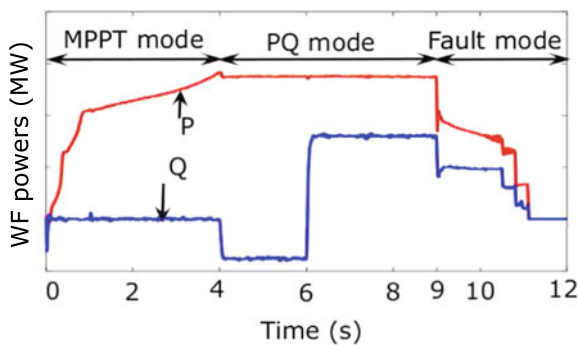
(a)



(b)

Fig. 4.7 Simulation results for scenario 1: **a** Reactive current at PCC (pu), **b** Voltage V_{dc} of 1st wind turbine

Fig. 4.8 Simulation results for scenario 1: Active and reactive powers of Wind farm



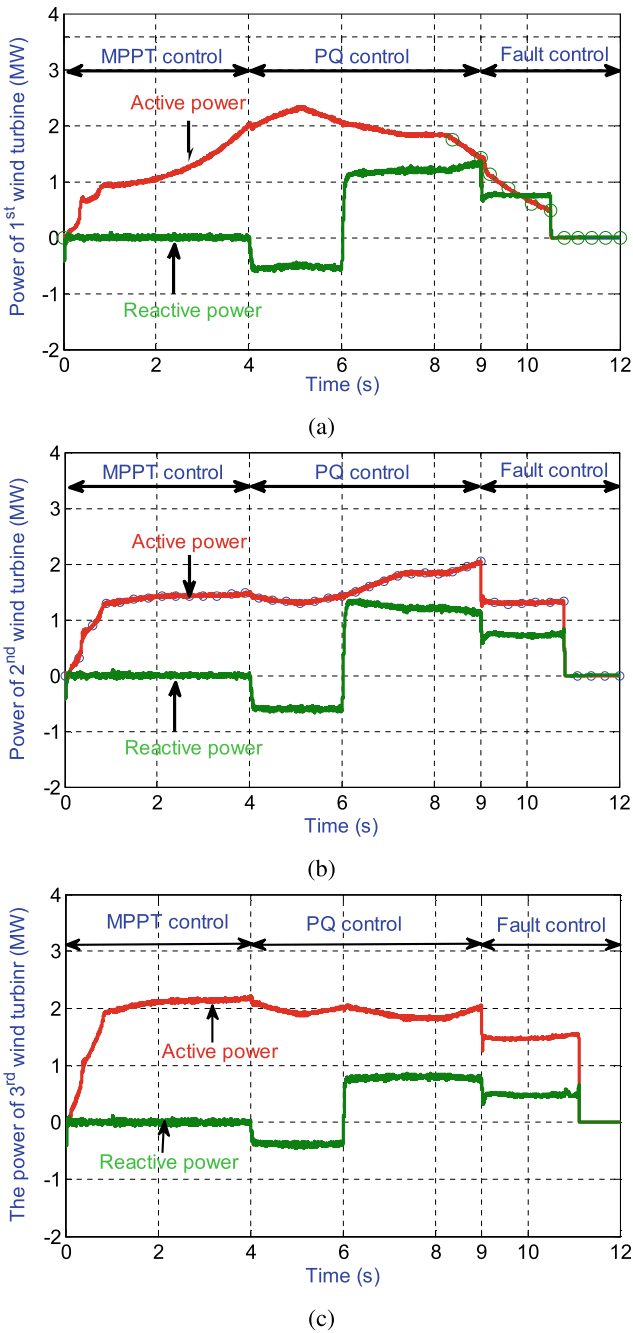


Fig. 4.9 Simulation results for scenario 1: **a** 1st wind turbine power, **b** 2nd wind turbine power and **c** 3rd wind turbine power

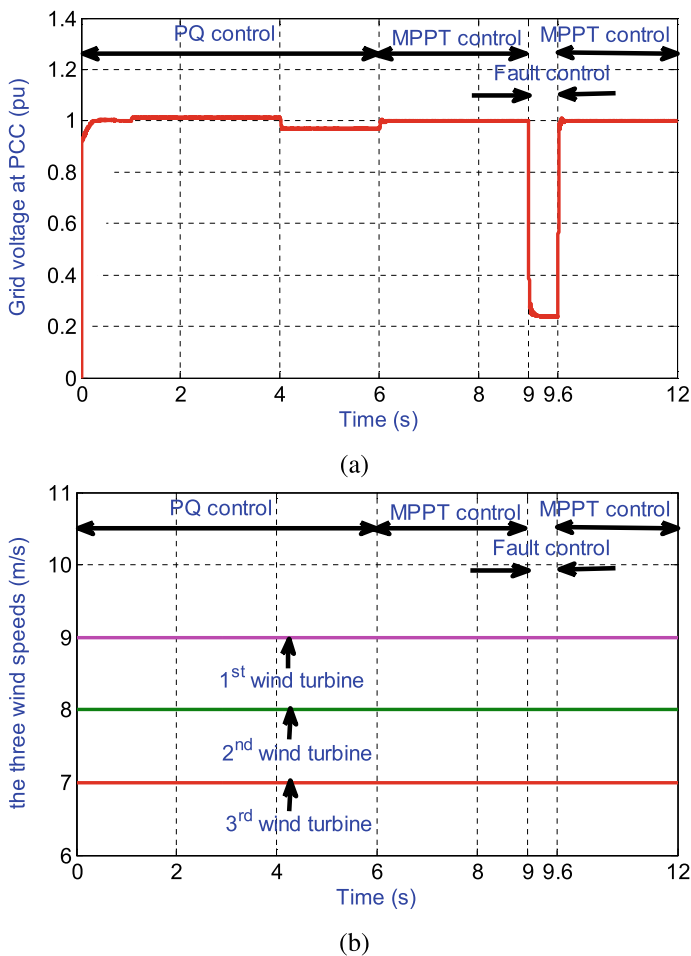
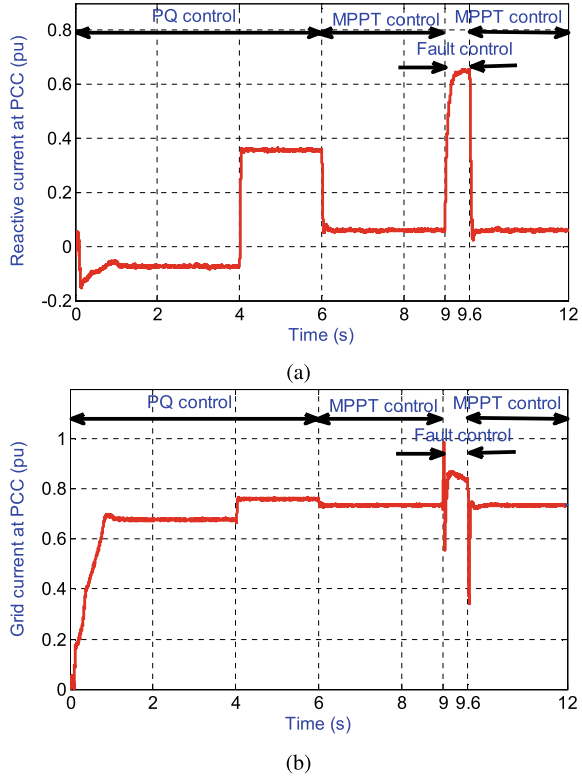


Fig. 4.10 Simulation results for scenario 2: PQ control from 0 to 6 s, MPPT control from 6 to 12 s and voltage drop from 80% to 9 s: **a** grid voltage, **b** the three wind profiles

In Fig. 4.11a, it can be seen that reactive current is generated to compensate the voltage drop according to grid code recommendations. This reactive current is considered as the component of the reactive power that participates in voltage drop compensation. Figure 4.11a and b show that the current fed into the grid and the reactive current are limited to nominal value.

As shown in Fig. 4.12a the WF active and reactive powers follow their references during activation of three operating modes. The WF power is the sum of the all powers of WTs given in Figs. 4.12b, 4.13a and b). During the MPPT control mode the WF generate just active power. While, during fault control and PQ control modes,

Fig. 4.11 Simulation results for scenario 2: PQ control from 0 to 6 s, MPPT control from 6 to 12 s and voltage drop from 80% to 9 s: **a** Reactive current at PCC (pu), **b** current at PCC (pu)



WF can generate reactive power. From analysis of above results, it can be concluded that the proposed control and the supervisory system offer better performances with greater robustness, in terms of participation in voltage stability.

4.4 Fault Control Strategy Using Hierarchical Fuzzy Controller

4.4.1 Dynamic Model of Grid for Voltage-Reactive Power Control

The power system model is developed with possibility of parameterization for voltage-reactive power control. The grid model consists of two synchronous generators (SG1 and SG2) supplying loads, as illustrated in Fig. 4.14. Each SG includes a steam turbine controlled by a power controller to satisfy the demanded load power

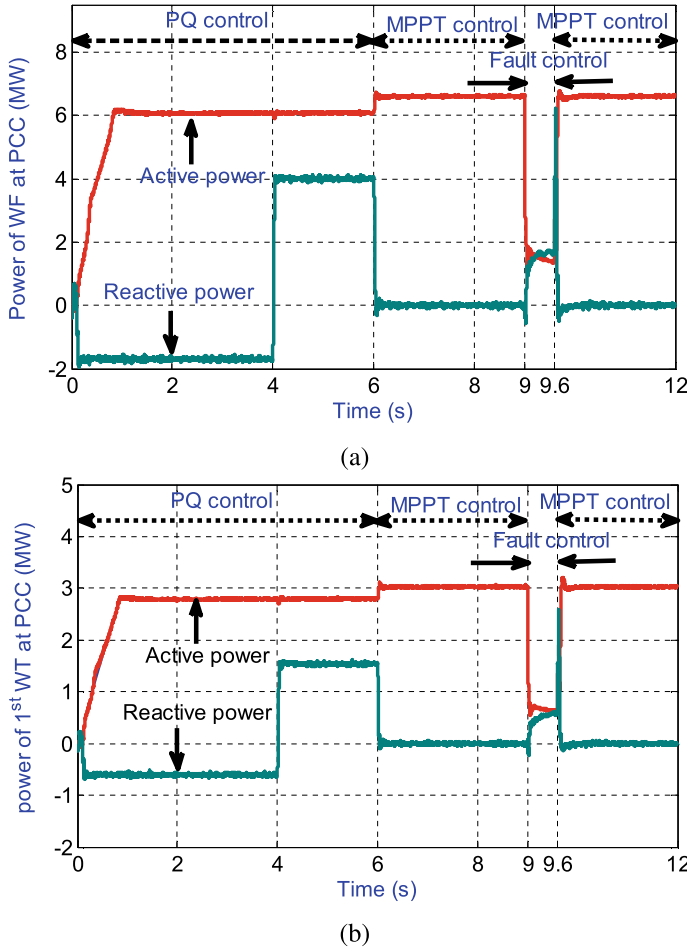
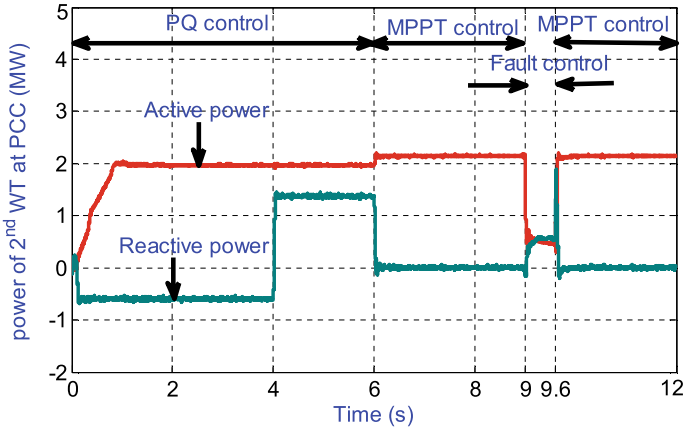


Fig. 4.12 Active and reactive power at PCC for scenario 2: **a** wind farm and **b** 1st wind turbine

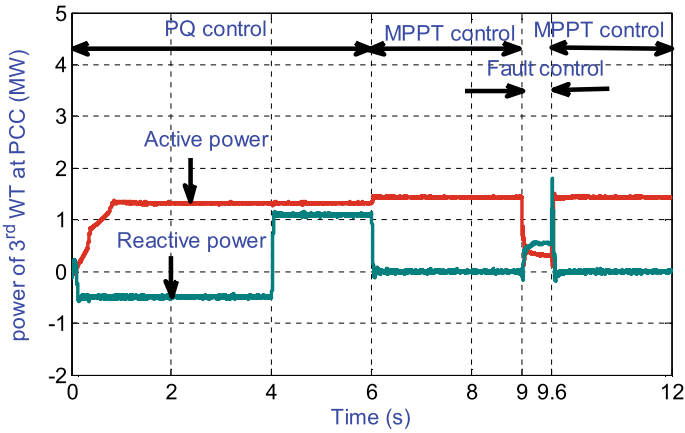
[12–14, 18]. To ensure system stability and power flow control, the voltage control and frequency control system are developed as shown in Fig. 4.14 [14].

The excitation system regulates the terminal voltage of synchronous generators during normal operation [15]. However, when reactive demand increase (an inductive load Q_L is connected) and voltage control is deactivated (SW switch is in position 2, $V_f = 1.36$ in Fig. 4.14), a voltage drop occurs on the grid. In this case, the farm starts to take part for voltage control at PCC, and for reactive power control. Then fault control mode is activated. The level of voltage drop and the time of fault resolution are imposed by WT protection system taking into account location and type of fault.

The parameters noted in Fig. 4.14 are given in Appendix A. Where prefix Δ indicates deviation from initial value. “s” is Laplace operator. ω_{r-1} and ω_{r-2} are



(a)



(b)

Fig. 4.13 Active and reactive power at PCC for scenario 2: **a** 2nd wind turbine wind turbine and **b** the 3rd wind turbine

Rotor speeds of two generators SG1 and SG2, respectively. “y” is position of valve gate and R is a parameter for percent speed regulation.

4.4.2 Voltage Control at PCC

During grid fault presence ($V_g < 95\%V_n$), inverter can be controlled to obtain a non-unity power factor in order to provide a non-zero reactive power and also participate in voltage fault compensation. Voltage drop is caused, in most cases, by the exces-

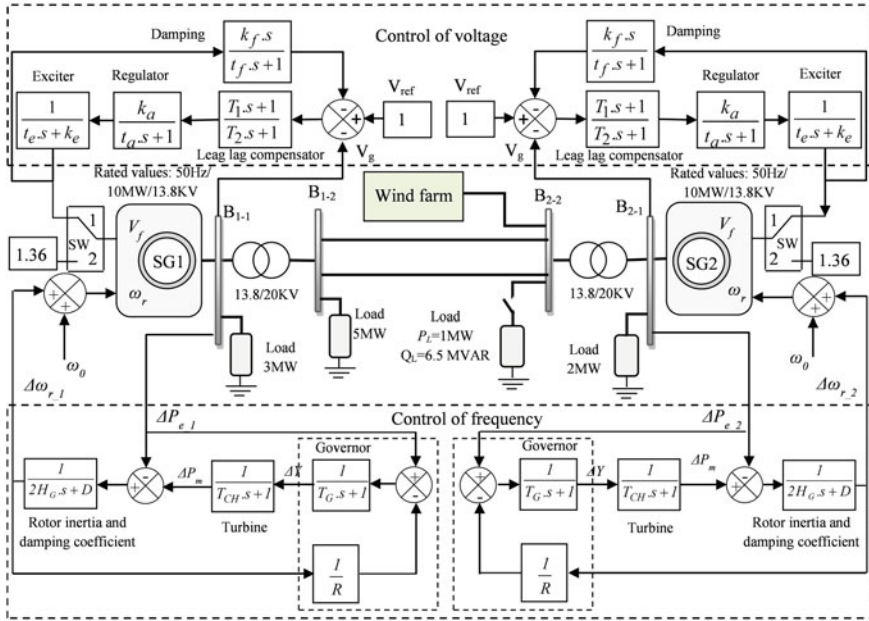


Fig. 4.14 Overall structure of the test system of the electrical power network with the possibility of parameterization of voltage-reactive power control $Q(V)$ of the power network

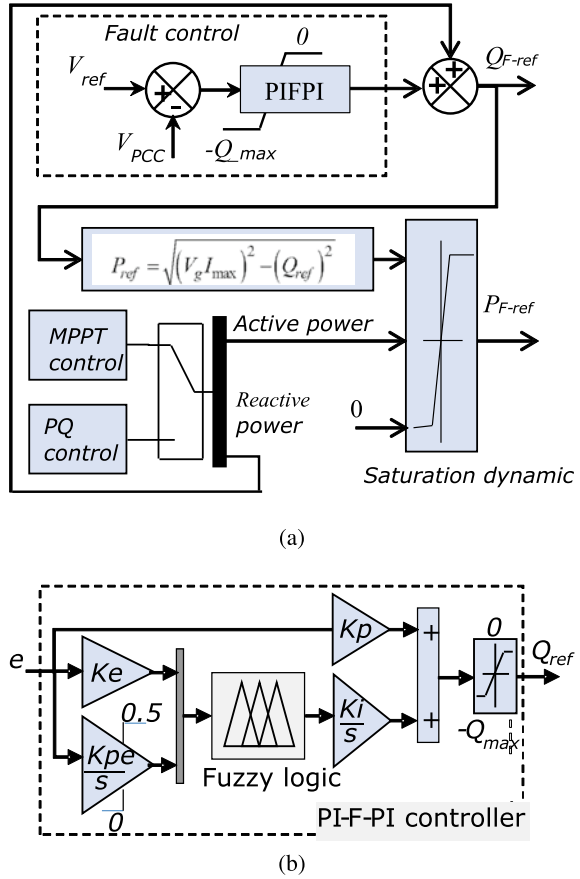
sive reactive power increase when a large inductive load is connected near PCC bus. In order to avoid ripples in reactive power reference, it is preferable to use block sum instead of block switch when switching between fault control mode and other modes as illustrate in Fig. 4.15a. The voltage control scheme is shown in Fig. 4.15a. The active power reference (Q_{ref}) is computed using Eq. (4.13) to not exceed nominal value of apparent power and maximum current. Where, Q_{ref} is reactive power reference, V_g is grid voltage and I_{max} is maximum current.

$$P_{ref} = \sqrt{(V_g \cdot I_{max})^2 - (Q_{ref})^2} \quad (4.13)$$

4.4.3 Proposed Fuzzy Hierarchical Controller

The hierarchical PI-Fuzzy-PI (PIFPI) controller proposed in Fig. 4.15b brings together fuzzy logic and PI controllers in one structure to enhance responses of voltage and reactive power. The inputs are error $e = V_{nom} - V_{pcc}$ and integral of the error ($\int e$). The generated output value (U) is reactive power reference (Q_{F-ref}) [14].

Fig. 4.15 The proposed control strategy: **a** Schematic of the voltage control at the PCC and references for the active and reactive power generation, **b** Block diagram of the hierarchical PIFPI controller



- **Fuzzification:** The input and output variables are transformed to fuzzy quantities using the Gaussian membership functions presented in Fig. 4.16a and b, where LN is Large Negative, SN is Small Negative, EZ is Equal to Zero, SP is Small Positive and LP is Large Positive.
- **Fuzzy logic rules:** The fuzzy logic rules for the voltage controller are expressed as a form of “IF-THEN”, to describe the control knowledge presented in Table 4.2.
- **Defuzzification:** The centroid defuzzification method converts output linguistic variables to real values [14].

Fig. 4.16 Shapes of fuzzy membership functions: **a** Input variables, **b** Output variable

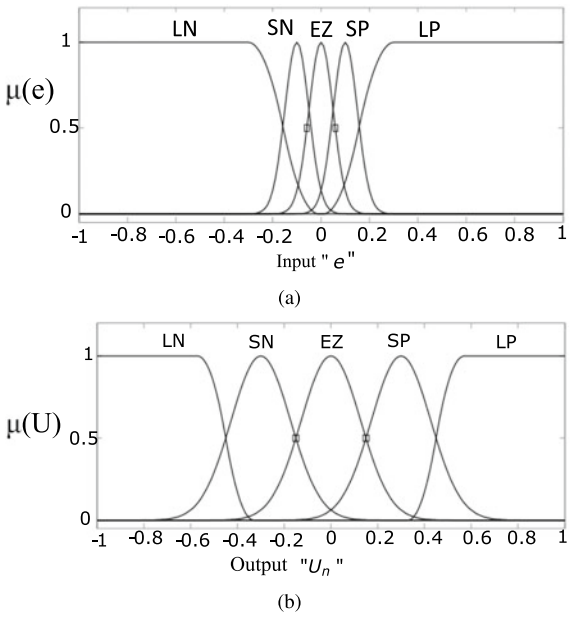


Table 4.2 Fuzzy logic rules for the voltage controller

Integral of error ($\int e$)	Error (e)				
	LP	SP	EZ	SN	LN
LP	LP	LP	SP	SP	EZ
SP	LP	SP	SP	EZ	LN
EZ	LP	SP	EZ	SN	LN
SN	SP	EZ	SN	SN	LN
LN	EZ	SN	SN	LN	LN

4.4.4 Validation and Discussion

The simulation results are generated using the wind farm model and control system developed and simulated using Matlab/Simulink software. The wind farm shown in Fig. 4.4 connected to the grid, aims to control the voltage drop created in the dynamic grid when the inductive load (Q_L) of 6.5 MVAR is connected to bus B_{2-2} in grid. The connection of the inductive load (Q_L) at time $t = 10$ s leads to an increase of the consumed reactive power which has to be compensated. The system parameters of the wind farm are listed in Appendix A (see Tables A.6 and A.5).

The simulation results aim to prove effectiveness of proposed PI-Fuzzy-PI controller employed to ensure LVRT control. This proposed controller is compared to PI controller and constant reactive power control (CRPC) [16] (Ratio for CRPC is K_q

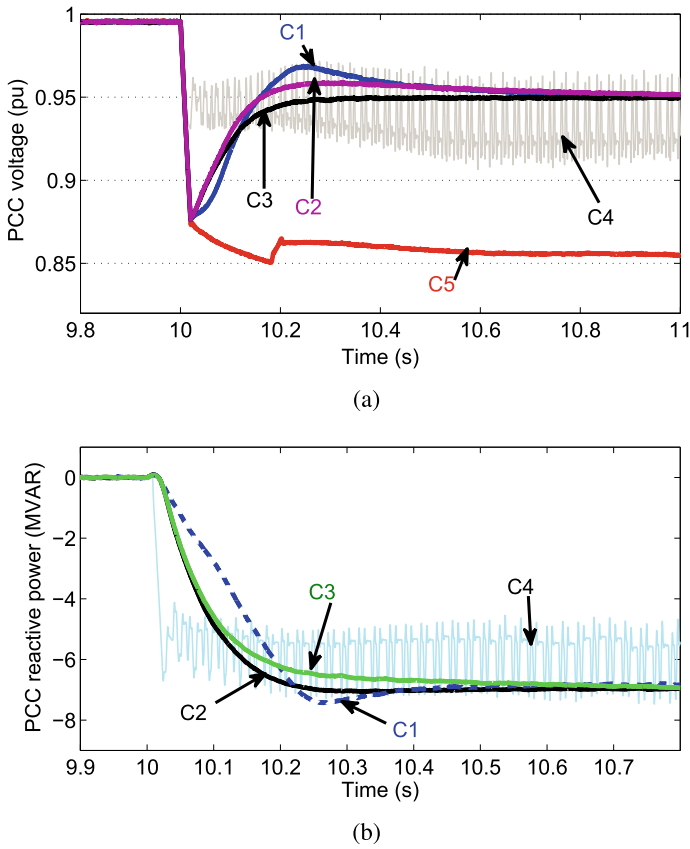


Fig. 4.17 Reactive power and voltage response for different controllers: **a** voltage at PCC, **b** reactive power response

= 0.7). The behavior of WF supervisory system and interactions between WTs under different wind speeds should be illustrated. As shown in Fig. 4.17a when inductive load increases, grid voltage drops to a value below 0.95 pu. The robustness of LVRT control based on the CRPC (C4) method is low which generates more severe oscillations during voltage faults. For a more efficient system of voltage control through reactive power injection, two controllers should be chosen, one for voltage and one for reactive power. These combinations of voltage and reactive power controllers have been presented in Table 4.3. In this table the C2 combination includes the PIFPI controller for voltage control and PI for reactive power control. Figure 4.17 and 4.18 show that the dynamics of C1 and C3 are very poor compared to the proposed combination (C2). But the combination C1 which uses PIFPI controller based on fuzzy logic in all controllers, increases the complexity of the structure (4 blocks of fuzzy logic are added and executed simultaneously) which leads to poor performance.

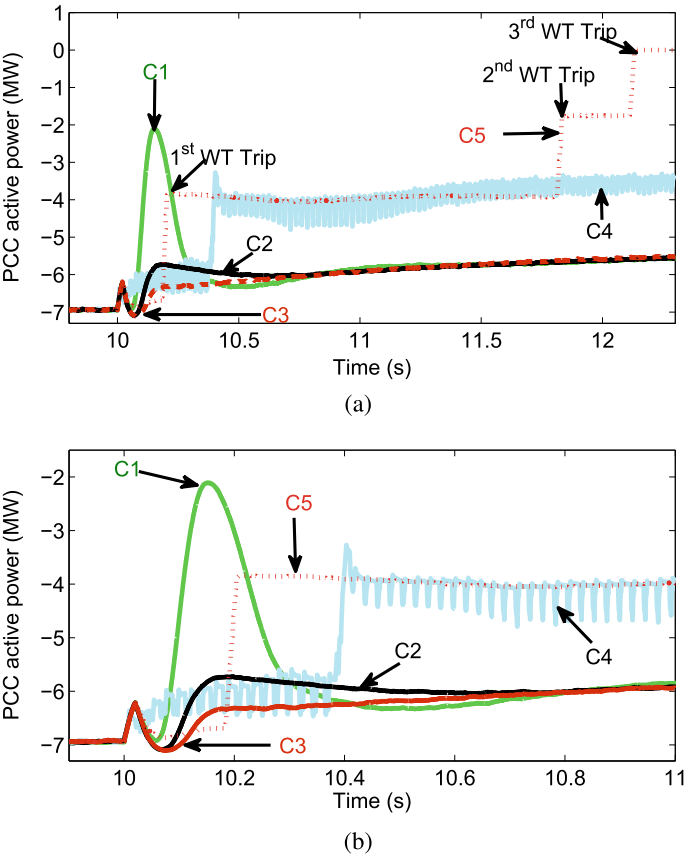


Fig. 4.18 Reactive power and voltage response for different controllers: **a** active power response, **b** zoom of active power response

Table 4.3 Combination of voltage and reactive power controllers Reactive power controller

		Reactive power controller:		
		PIFPI	PI	Without control
Voltage control	PIFPI	C1	C2 (proposed)	0
	PI	0	C3	0
	CCPR	0	0	C4 [16]
	Without control	0	C5	0

Figure 4.17 and 4.18 show that the best responses in terms of time response, deviation from desired values and meeting the requirements of the grid code (fault clearing time less than 0.2 s) are obtained using the proposed PIFPI controller for voltage control and the PI controller for reactive power control. It can be seen in Fig. 4.18a that the absence of the voltage control gives permission to the automatic protection system to disconnect one third of the WT's from the grid in different times. The first turbine was disconnected at 10.2 s, the second at 11.8 s and the third at 12.1 s. This disconnection leads to a gradual decrease in power to reach 0 MW. From the above discussion, it can be concluded that the proposed control system ensures the best performance in terms of voltage stability and power generation.

Figure 4.17 shows that the best voltage and power responses are obtained using the proposed PIFPI controller for LVRT control and the PI controller for reactive power control in terms of time response, deviation from desired values and satisfaction of grid code requirements (fault clearance time less than 0.2 s). As shown in Fig. 4.18a, during the absence of the voltage control, the automatic protection system disconnects one-third of the farm generators from the grid at 10.2, 11.8, and 12.1 s, respectively. The power at the PCC gradually decreases to reach 0 MW. From the above analysis, it can be concluded that the adopted control system guarantees best performance in terms of voltage stability and power generation.

4.5 Conclusion

To ensure optimal integration of a WF based on squirrel cage induction generator into power network, a system of management and control of reactive power has been developed. To achieve this objective a supervision system based on a proportional distribution algorithm for power dispatching using three operating modes (MPPT control mode, PQ control mode and fault control mode). To satisfy a global production plan required by grid operator a central supervisory unit of WF is configured. This unit send information to the local supervisory units in order to control the wind turbines. The effectiveness of combination of supervisory system, proportional distribution algorithm and proposed reactive power control at PCC has been demonstrated and has lead to the development of a fuzzy hierarchical PIFPI controller and a PI controller for the control of voltage and reactive power during voltage drop in an uncompensated power system. The simulation results show that with proposed control approach: (i) settling time is significantly reduced, (ii) deviations from the nominal values are limited and oscillations are damped faster than others. The combination of the supervision system, proportional distribution algorithm, PIFPI for voltage controller and PI controller for reactive power control, allows the wind farm to support the voltage and behaves as a conventional power plant. The proposed supervision system allows WT's to operate under variable wind speeds and far enough from maximum operating point to avoid saturation of WT's.

References

1. Benlahbiband, B., bouchafaa, F.: Centralized algorithm for wind farm supervision. In: *Chez International Conference on Control, Engineering and Information Technology (CEIT'14) Proceedings* (2014)
2. B. Benlahbib, F. bouchafaa and E. Berkouk, Proportional Distribution Algorithm for Wind Farm Supervision, *Internationale conference of renewable energies (CIER'13)*, 2013
3. Dai, C., Chen, W., Zhu, Y., Xuexia, Z.: Seeker optimization algorithm for optimal reactive power dispatch. *IEEE Trans. Power Syst.* **24**(13), 1218–1231 (2009)
4. Dai, C., Chen, W., Zhu, Y., Xuexia, Z.: Reactive power dispatch considering voltage stability with seeker optimization algorithm. *Electr. Power Syst. Res.* **79**(110), 1462–1471 (2009)
5. De Almeida, R.G., Castronuovo, E.D., Lopes, J.: Optimum generation control in wind parks when carrying out system operator requests. *IEEE Trans. Power Syst.* **21**(12), 718–725 (2006)
6. Elyalaoui, K., Ouassaid, M., Cherkaoui, M.: Supervision system of a wind farm based on squirrel cage asynchronous generator. In: *Chez Fourth International Conference on Renewable and Sustainable Energy (IRSEC'16)*, IEEE, Marrakech, Morocco (2016)
7. Alsmadi, Y.M., Xu, L., Blaabjerg, F., Ortega, A.J., Abdelaziz, A.Y., Wangand, A., Albataineh, Z.: Detailed investigation and performance improvement of the dynamic behavior of grid-connected DFIG-based wind turbines under LVRT conditions. *IEEE Trans. Ind. Appl.* (2018)
8. Sandia, N.L.: Reactive power interconnection requirements for PV and wind plants (SAND2012-1098) (2012). [Available online 2020]
9. Haejoon, An., Heesang, Ko., Hongwoo, Kim, Hyungoo, Kim, Seokwoo, Kim, Gilsoo, Jang, Byongjun, Lee: Modeling and voltage-control of variable-speed SCAG-based wind farm. *Renew. Energy* **42**, 28–35 (2012)
10. Benchagra, M., Maaroufi, M., Ouassaid, M.: Study and analysis on the control of SCIG and its responses to grid voltage unbalance. In: *International Conference on Multimedia Computing and Systems*, IEEE ICMCS (2011)
11. Luna, A., Rodriguez, P., Teodorescu, R., Blaabjerg, F.: Low voltage ride through strategies for SCIG wind turbines in distributed power generation systems. In: *Chez IEEE, Power Electronics Specialists Conference, PESC 2008* (2008)
12. Kundur, P.: *Power System Stability and Control*. McGraw-Hill Professional (1994)
13. Bevrani, H.: *Robust Power System Frequency Control*. Power Electronics and Power Systems. Springer International Publishing (2014)
14. Elyalaoui, K., Ouassaid, M., Cherkaoui, M.: Primary frequency control using hierarchal fuzzy logic for a wind farm based on SCIG connected to electrical network. *Sustain. Energy, Grids Netw.* **16**, 188–195 (2018)
15. Lee, D.: IEEE recommended practice for excitation system models for power system stability studies (IEEE std. 421.5–1992), Energy Development and Power Generating Committee of the Power Engineering Society, vol. 95, p. 96 (1992)
16. Oon, K.H., Tan, C., Bakar, A., Che, H.S., Mokhlis, H., Illias, H.: Establishment of fault current characteristics for solar photovoltaic generator considering low voltage ride through and reactive current injection requirement. *Renew. Sustain. Energy Rev.* **92**, 478–488 (2018)
17. Elyalaoui, K., Ouassaid, M., Cherkaoui, M.: Dispatching and control of active and reactive power for a wind Farm considering fault ride-through with a proposed PI reactive power control. *Renew. Energy Focus* **28**, 56–65 (2019)
18. Elyalaoui, K., Labbadi, M., Ouassaid, M., Cherkaoui, M.: Optimal fractional order based on fuzzy control scheme for wind farm voltage control with reactive power compensation. *Math. Probl. Eng.* **2021**(5559242), 12 (2021). <https://doi.org/10.1155/2021/5559242>

Chapter 5

LVRT Control Using an Optimized Fractional Order Fuzzy Controller of a Wind Farm



5.1 Introduction

For an optimal integration and secure operation of grid connected wind farms, the transmission system operator imposes for wind farm manager to satisfy Grid Code Recommendations (GCRs) ([1] 2018). These recommendations should be respected to avoid disconnection of wind turbines from grid and ensure participation in Low Voltage Ride-Through (LVRT) control [5, 24] and Primary Frequency Control (PFC) [26]. To achieve the forementioned objectives and distributing power references among wind turbines a supervision system and its related algorithms are developed in many works [2–6]. In a weakly grid-connected wind power plant, the transportation of the reactive power over a long distance should be avoided for power loss minimization in transmission line. Therefore, the reactive power must be generated near the bus of consumers utilization to ensure minimal grid transportation of reactive power, as recommended by the European Network of Transmission System Operators for Electricity (ENTSO-E) (Policy 3: Operational Security) [7]. These requirements indicate that LVRT should be compensated by reactive power to ensure voltage stability and satisfy GCRs [5]. For compensating the reactive power and ensure the LVRT control, many works in the literature propose a sophisticated control methods such as nonlinear controller, controller based on fuzzy logic [26], combination of fuzzy logic and nonlinear controller [8] and utilization of Fractional Order Controller (FOC) in the control system [9, 25]. This chapter deals with a new control approach based on combination of Fractional-order and PI Fuzzy PI controller in one optimized structure to ensure LVRT control of a WF based on squirrel cage induction generator and satisfy recommendations imposed by TSO. The proposed Fractional-order PI Fuzzy PI (FOPI-fuzzy-FOPI) controller is optimized using Particle Swarm Optimization (PSO) algorithm for better tracking performances and faster convergence of the variables. These performances are demonstrated by numerical simulation results to discuss advantages of proposed control approach. The rest sections of this chapter are organized as follows: Sect. 5.2 is devoted to the wind farm

studied system and the configured supervision system with the algorithm for power dispatching. Some grid code requirements associated to the WF control modes are given in Sect. 5.3. The proposed control technique for voltage fault is developed in Sect. 5.4, and controller performances are validated by simulation results in Sect. 5.5. The last Sect. 5.6 is devoted to conclude the main contributions of the chapter.

5.2 Wind Farm Management According to Grid Code Recommendations

The supervision system is divided into central supervision unit, local supervision unit and protection system as shown in Fig. 5.1 [5].

5.2.1 Central Supervision Unit

The central supervision unit is the TSO side-unit and configured for data exchange between TSO and WF. The main objective of this unit is to control the total active and reactive powers according to a production plan requested every hour by TSO and to satisfy the other orders imposed by the TSO. It is also receives a power (P_{ref} , Q_{ref}) request from grid operator and maximum power of each wind turbine (P_{WT-max_i} , Q_{WT-max_i}) from local units and sends information about maximum power generation capacity (P_{max} , Q_{max}) and references of powers ($P_{WT-ref-i}$, $Q_{WT-ref-i}$) to local units.

5.2.2 Local Supervision Unit

The local supervision unit inside each wind turbine must generate the active and reactive power references ($P_{WT-ref-i}$, $Q_{WT-ref-i}$) of each WT system using the total reference received from the central supervision unit. Moreover, this unit calculates in real time the maximum (P_{WT-max_i} , Q_{WT-max_i}) power that can be produced by each WT in order to send them to central supervision unit. It generates and sends references necessary to produce active and reactive powers, to WTs, according to MPPT or PQ control mode and fault control mode.

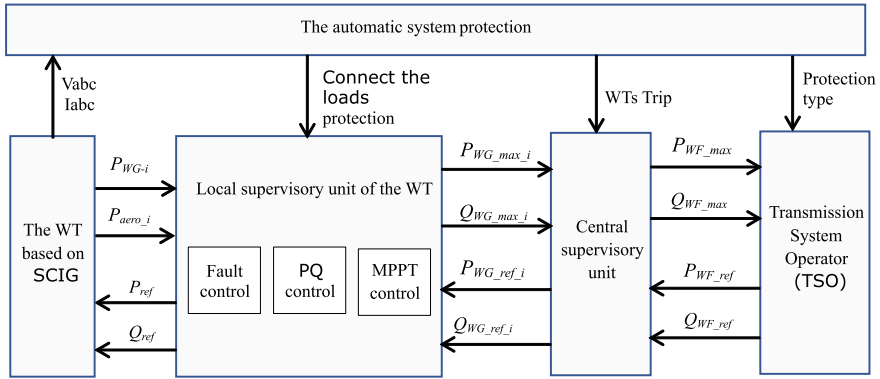


Fig. 5.1 Structures of the configured supervisory system and its main units

5.2.3 System Protection

The WT protection system ensures the safety and automatic protection of all circuits and elements essential for the normal operation of the system to avoid damage to its equipment. The protection procedure is based on real-time fault detection and evaluation of the level of danger that the wind turbines cannot withstand, then automatic disconnection of wind turbines from grid and connection of load of protection (LP1) to dissipate the under-generation power. The information about the type of fault will be sent to the TSO (see Fig. 5.1). The system makes decision based on information about voltage drop level, fault clearing time, location and fault type. The limits, period and types of the fault are listed in Table 4.1 [10].

5.3 Power System Modeling

5.3.1 Objectives of the Study and Choice of Model Type

In order to study the voltage stability of a network hosting generators equipped with power controllers, a mathematical model must be determined. The relevance of obtained results depend directly on quality of proposed model. Thus, the modeling of the system is not the core of this work, but if the modeling is close to reality, it is still a necessary step for the correct evaluation of the proposed control systems. A suitable choice of model is based on a compromise between the precision of the model and its complexity. Indeed, a model that is too simple may lead to results that are far from reality, and a model that is too complex will be difficult to manipulate and may require a calculation time that is incompatible with the purpose of the study.

This is why, before detailing the developed models, the objectives of the study and the studied system should be clearly defined.

5.3.1.1 Objectives

In this work, we want to study the compensation of the voltage drop by injection of the reactive power. The model must represent the behavior of the electricity network and of the producers connected to it. Therefore, the model developed must provide the following characteristics: if there is a power balance the voltage is equal to the nominal voltage. if the inductive load connected to the grid, the reactive power increases, leading to the voltage drop to a value that exceeds the recommended limits. if the capacitive load connected to the network, the reactive power decreases leading to an increase in voltage.

5.3.1.2 Choice of Model Type

In the literature, it is common to classify the models illustrating the operation of electrical networks into two main categories according to the dynamics of the phenomena they allow to study. We can distinguish between the infinite network model and the dynamic network model. The infinite network model gives the possibility to generate the required power whatever the size of the load connected to the network. This does not give the possibility to vary the voltage according to the variation of reactive power [23, 24]. This model is adequate to study the robustness of the developed controller but not adequate to test performance of proposed control system participating in service system, which demand the use of the dynamic model. The dynamic grid model, adopted in this work, is developed to obtain a characteristic that gives the possibility to control the voltage by reactive power and variation of reactive power through connection/disconnection of inductive loads. The power is generated using two synchronous generators (SG1 and SG2) to supply loads, as shown in Fig. 5.2 [25]. The two generators are connected to two steam turbines controlled by two power control systems. The turbines produce mechanical power that will be converted into electrical power consumed by the loads [11, 12, 26]. As shown in Fig. 5.2 [26], the stability of power system is ensured by controlling power flow in two cases:

In normal operation, the excitation system regulates voltage across generators, in order to maintain voltage at its nominal value [13].

In unbalanced operation, where the voltage control is deactivated (SW switch is on position 2, $V_f = 1.36$ in Fig. 5.2) and the load power increases (P_L and Q_L are connected), the grid voltage drops to a value lower than its nominal value. In this case the fault control mode must be activated so that the farm starts to take part in the compensation of the voltage drop by injecting reactive power. The frequency is controlled by the active power control as shown in Fig. 5.2 [26].

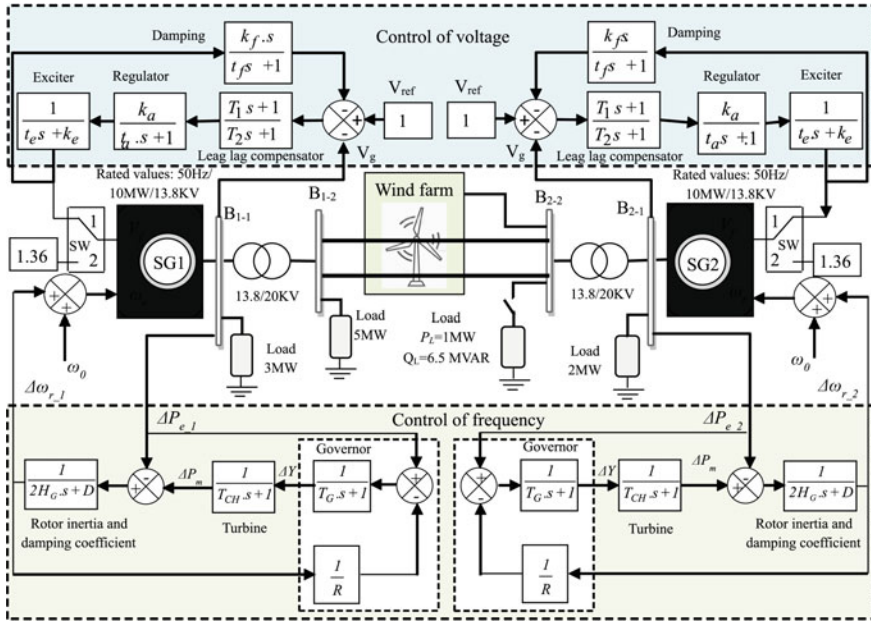


Fig. 5.2 The block diagram of the dynamic power system test Q(V) for voltage control through reactive power injection

The parameters of the power system are given in appendix A. In Fig. 5.2, the prefix Δ represents the difference between the current value of the variable and the initial value. “s” is the Laplace operator. ω_{r-1} and ω_{r-2} are the angular speeds of the two generators in the two areas SG1 and SG2, respectively. y is the position of valve gate, and R is the droop for speed regulation and frequency regulation.

5.4 Wind Farm Management According to Grid Code Requirements

5.4.1 Grid Code Requirements

TSOs have established specific recommendations and standards for controlling and managing the WF like a conventional power plant. The European grid operator ENTSO-E imposes certain requirements for connecting wind farms to grid. The WF must be stable and remain connected to grid during some faults such as voltage drop to a value less than 95% of the nominal value [14, 25]. The WF must react within 20 ms of fault beginning and compensate the drop within 500 ms of fault beginning in order not to exceed the dead zone of $\pm 5\% V_n$ [14–16]. The references

employed to produce the active and reactive power are generated by MPPT operating mode, fault mode or PQ control mode [5].

5.5 Proposed Fault Control Strategy

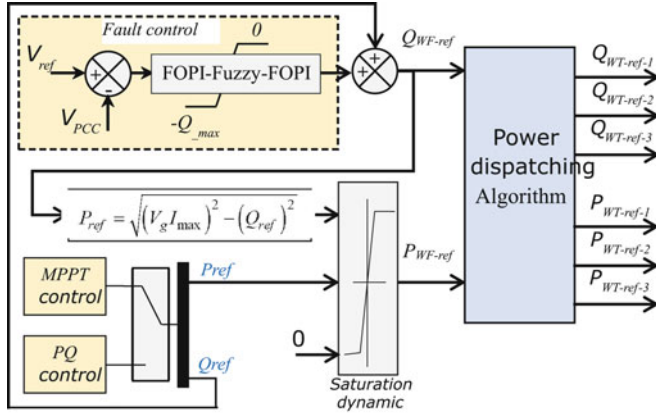
The two control modes MPPT and PQ are activated manually during the absence of voltage drop or $95\%V_n < V_g < 105\%V_n$, while the fault control is activated automatically during the presence of voltage fault.

5.5.1 Voltage Control

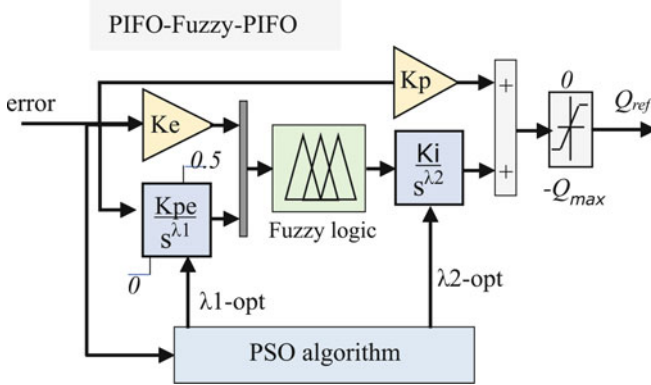
During the existence of voltage fault ($V_g \leq 95\%V_n$), the grid-side converter is controlled to provide a non-unity power factor by producing reactive power to compensate voltage drop due to the inductive load connected near PCC bus. Figure 5.3a illustrates the strategy for generating active and reactive power references to control the voltage at the PCC. The sum block is used to switch from the fault mode to the other mode of operation instead of the switch block which generates oscillations in the power references. This technique is based on adding the reference generated by the fault mode to the references generated by the other modes (MPPT and PQ), not switching between the modes as shown in Fig. 5.4a where I_{max} is the maximum current value.

5.5.2 Design of Fractional Order PIFO-Fuzzy-PIFO Controller

The fractional order PIFO-Fuzzy-PIFO controller is developed using a structure based on PI controller, the fractional order integrator and fuzzy logic: firstly, the PI controller is chosen to generate voltage control references, as shown in Fig. 5.3a. the gains of the PI controller are calculated using trial-and-error method. But the constant gains of the controller do not give a better response. This requires the use of an intelligent control system. The intelligent system based on fuzzy logic should be adopted to ensure the variation of the integrator gain. This increases the flexibility of the controller and obtains a better dynamic response than the PI [26]. The PIFPI controller offers two additional parameters (k_e , k_{pe}) (Fig. 5.3b), which should be determined by means of a Simulink optimization tool “check step response characteristics”. The superiority of the proposed controller has been increased considerably by replacing the integrator operator by the fractional order operator in order to obtain a FOPI-Fuzzy-FOPI controller based on the fractional order operator with two addi-



(a)



(b)

Fig. 5.3 Proposed control system: **a** Diagram block for power references generation according to the three operating modes, **b** Design layout of fractional order PIFO-Fuzzy-PIFO controller with PSO parameter optimization

tional degrees of freedom λ_1 and λ_2 as shown in Fig. 5.3b. The parameters λ_1 and λ_2 of the fractional operator has been optimized by PSO algorithm, which gives good performance with the optimal parameters λ_1 and λ_2 and the structure given in Fig. 5.3. The flow chart of the PSO algorithm adopted for the optimization of fractional order operators is presented in Fig. 5.4.

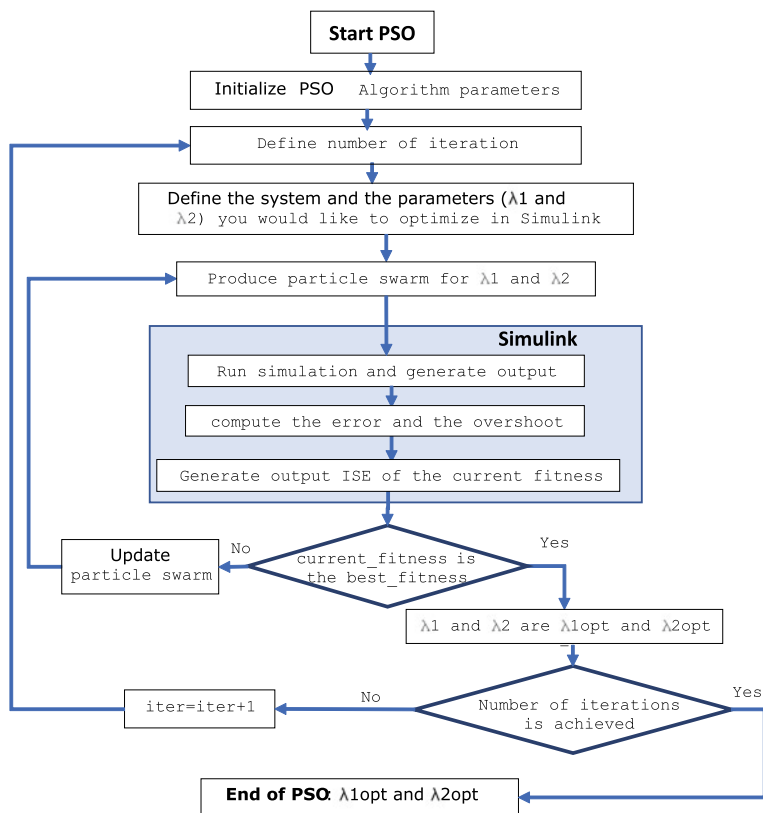


Fig. 5.4 Flowchart of PSO algorithm for optimization the fractional order operators using Matlab/Simulink model

5.5.3 Fractional Order Preliminaries

Fractional-order (FO) controller takes more attention by researcher, scientific and engineers in the engineering fields in the last decades. The notions of differentiation and integration of non-integer order represent an efficient tool to characterize the behavior of an important class of dynamical systems. There are many applications, whether in electricity, thermic, chemistry or signal processing. Using the FO operators for the electrical system control offers two degrees of freedom compared with controller based on integer order. The derivative and integral operator fractional can be defined as follows:

$$D_t^\lambda = \begin{cases} \frac{d^\lambda}{dt^\lambda} \\ 1 \\ \int (dt)^\lambda \end{cases} \quad (5.1)$$

Where the real number λ is the FO operator.

In recent years, several researchers in the literature have been oriented towards the use of derivatives and integrals based on fractional order (FO) operator. Fractional order operator is used in controllers of electrical systems to improve responses. The Riemann-Liouville method is used for the design of the controller proposed in this chapter. For a given function $f(t)$, the fractional order derivative is expressed as [17, 18]:

$$D_t^\lambda f(t) = \frac{1}{\Gamma(m-\lambda)} \frac{d^m}{dt^m} \int_{t_0}^t \frac{f(\tau)}{(t-\tau)^{\lambda-m+1}} d\tau \quad (5.2)$$

where $m-1 < \lambda < m$, $m \in \mathbb{N}$, t_0 is the initial time, and $\Gamma(\cdot)$ is the Gamma function.

The fractional order integral is expressed as:

$$I_t^\lambda f(t) = \frac{1}{\Gamma(\lambda)} \int_{t_0}^t \frac{f(\tau)}{(t-\tau)^{1-\lambda}} d\tau \quad (5.3)$$

The fractional PID controller ($PI^\lambda D^\mu$) was proposed by Podlubny in [18, 19], where λ is an integrator order and μ is a differentiator order. In the Laplace domain the parallel form of the FOPID controller is given by:

$$C_{PID} = k_p + k_i s^{-\lambda} + k_d s^\mu \quad (5.4)$$

For a control loop with a fractional-order system, this fractional order controller is more efficient compared to an integer-order one. Recently many works in the literature confirm the superiority of nonlinear and intelligent controllers based on the fractional order controller [20, 21].

For the implementation of the fractional order controllers, the CRONE toolbox has been employed [22]. The fractional order operator of the controller is approximated with a modified 5th order Oustaloup filter and a frequency band between 0.01 and 100 rad/s.

5.5.4 Proposed FOPI-Fuzzy-FOPI Fractional Order Controller

The hierarchical fractional order controller FOPI-fuzzy-FOPI combines fuzzy logic and FO-PI controller in one designed layout presented in Fig. 5.3b. This controller aims to enhance the responses of both, voltage and reactive power. The fuzzy logic

Table 5.1 Fuzzy logic rules for the proposed controller the voltage controller

$I_t^\lambda(e)$	Error (e)				
	LP	SP	EZ	SN	LN
LP	LP	LP	SP	SP	EZ
SP	LP	SP	SP	EZ	LN
EZ	LP	SP	EZ	SN	LN
SN	SP	EZ	SN	SN	LN
LN	EZ	SN	SN	LN	LN

inputs are error “e” and fractional order integral of error ($I_t^\lambda(e)$). The output (U) generated by the fuzzy controller using the center of gravity method for defuzzification. The output corresponds to reference of the reactive power (Q_{WF-ref}) [8]. Table 5.1 presents the fuzzy rules in “if-then” form to generate the output as a function of the input. Fuzzification is endured using the Gaussian membership functions given in [8].

Where: NB is Negative Big, NM is Negative Medium, EZ is Equal Zero, PM is Positive Medium and PB is Positive Big.

5.6 Validation and Discussion

The simulation results are obtained using Matlab/Simulink software tools, the power system model shown in Fig. 5.2 3 and a wind farm with a total capacity of 9 MW consisting of three WTs connected into PCC. Most of the industrial systems use PID controller because of the facility of implementation and its simple structure with minimum parameters. But, the PID controller used to control voltage, does not give good performance which requires the use of control methods with fractional order PI controller and fuzzy control to improve the voltage and power response. However, with the advanced technology in power electronics and control boards in recent years, the difficulties of implementing controllers based on fuzzy logic and fractional order have been resolved [27]. The introduction of PI controller in the comparison of the obtained results is considered as a reference to the industrial practical results that widely use this type of controller. The overall objective of the present study is based on the comparison of the fractional order fuzzy PI controller with other controllers already presented in the literature, such as the hierarchical fuzzy controller (PIFPI) [26] and the FOFPID controller [28]. The parameters of wind farm and control system are listed in the appendix.

The results obtained aim to demonstrate the effectiveness of the proposed FOPI-Fuzzy-FOPI controller. The performance of the proposed controller has been compared with the PI-Fuzzy-PI controller [26], the PI controller, and a constant reactive power control (CRPC) [29]. These results are analyzed to evaluate the operation of

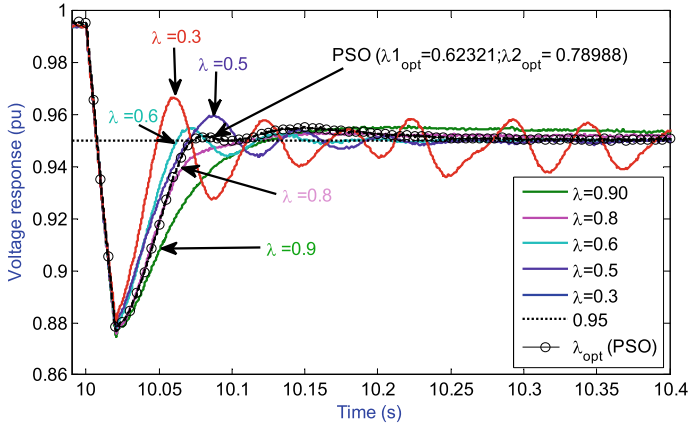


Fig. 5.5 The impact of fractional order parameter λ on the voltage response

the adopted WF supervisory system and the interaction between the WTs under voltage fault and variable wind speed. From Fig. 5.5, which shows the voltage response of the proposed controller for different values of λ_1 and λ_2 , it can be seen that the system response varies with the values of fractional order parameters λ_1 and λ_2 . Through tests using trial and error method, the obtained optimal value of λ is equal to 0.8 (i.e. $\lambda_1 = \lambda_2 = 0.8$). For more precision the optimal values of λ_1 and λ_2 requires an optimization algorithm such as the particle swarm optimization (PSO) algorithm. The optimization strategy follows almost the same steps that are used to optimize a system modeled in Simulink and controlled by a PID controller [31], replacing the parameters of the PID controller by the fractional order parameters (λ_1 and λ_2) of the proposed controller. The parameters are optimized by a program developed using MATLAB commands applied to a system model in Simulink by defining λ_1 and λ_2 as the variable parameters of the simulation that should be to be adjusted. The “sim” command in the MATLAB script executes the SIMULINK model and generates the model output (the variable to be controlled). The PSO optimization process is based on the integral square error index (ISE) [30], defined by the following function:

$$F = \beta \int e^2 + \alpha(overshoot) \quad (5.5)$$

Where α and β are the constant number. The error $e = y - 1$, y is the system variable to tune and $overshoot = Max(y) - 1$. The results given in Fig. 5.5 shows that the use of PSO algorithm to generate the optimal parameters ($\lambda_{1opt} = 0.62321$ and $\lambda_{2opt} = 0.78988$) gives an improved voltage response to obtain the best time response and small overshoot.

5.6.1 Comparative Study of Voltage and Reactive Power Responses

The proposed system for voltage control is shown in Fig. 4.1. To simulate the grid voltage fault scenario, the block diagram in Fig. 5.2 has been converted into Matlab/Simulink program. The voltage was decreased during the lack of reactive power consumed by the inductive load (Q_L) of 6.5 MVAR connected to the B2-2 bus at time $t = 10$ s. In this case the voltage drops to a value below 95% of the nominal voltage, as shown in Fig. 5.6a. To understand the combination of controllers of voltage and reactive power, Table 5.2 presents the notations C1–C7.

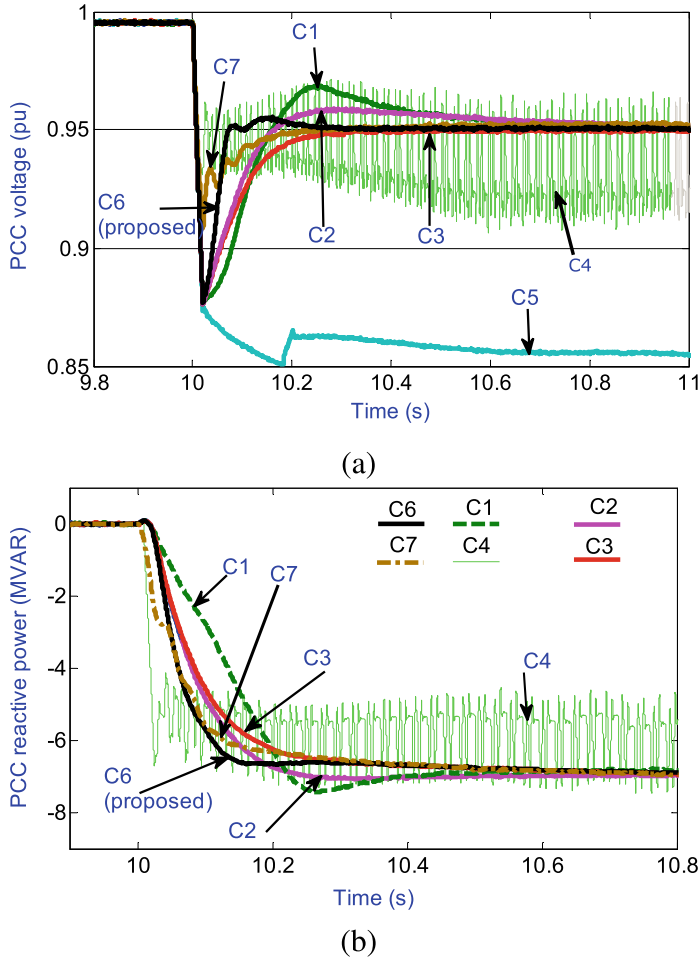
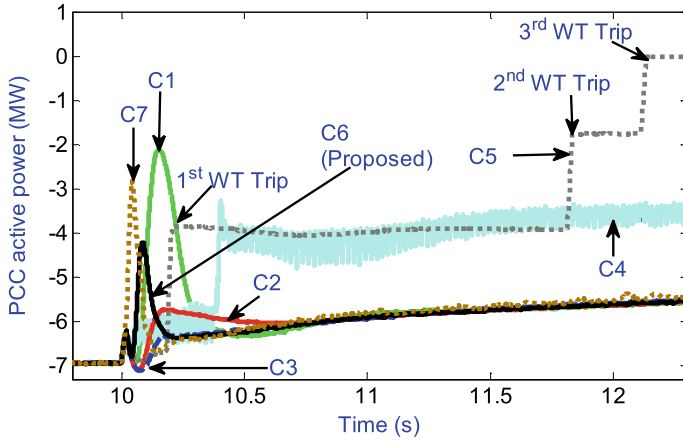
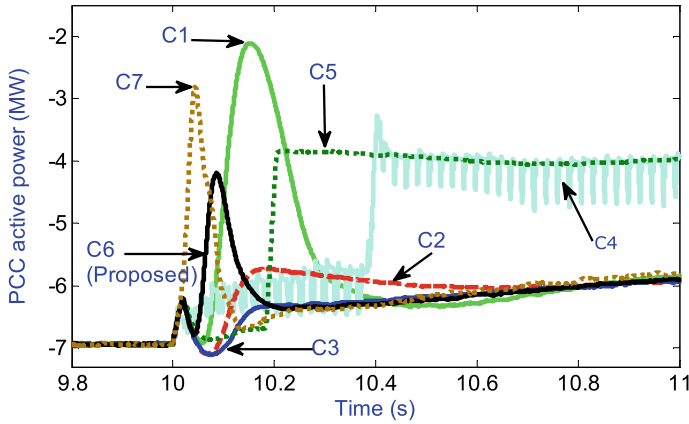


Fig. 5.6 Simulation results of different reactive power and voltage controllers: **a** voltage at the PCC, **b** reactive power response



(a)



(b)

Fig. 5.7 Simulation results of the different reactive power and voltage controllers: **a** active power response, **b** zoom of the active power response

- C1: Two PIFPI controllers are used for LVRT control and reactive power control.
- C2: PIFPI is used for LVRT control and PI for reactive power control.
- C3: Two PI controllers were used for LVRT and reactive power control.
- C4: Use of CRPC for LVRT control without reactive power control.
- C5: Use of PI for reactive power control without voltage control.
- C6: Use of PI for reactive power control and FOPI-F-FOPI controller (proposed) for voltage control.
- C7: Use of PI for reactive power control and the FOFPID controller for voltage control.

Table 5.2 Combination of controllers for voltage and reactive power control

		Reactive power controller:		
		PIFPI	PI	No control
Voltage control	PIFPI	C1	C2	0
	PI	0	C3	0
	CCPR	0	0	C4 [29]
	No control	0	C5	0
	FOPI-F-FOPI (proposed)	0	C6	0
	FOFPID [28]	0	C7	0

The LVRT control method based on CRPC (C4) shows high oscillations, which means that this type of controllers is not efficient to participate in the system service and it is not performing well. From voltage and power responses given in Figs. 5.6 and 5.7, it can be seen that the controllers C1 and C3 have slow dynamics and lower performance than the proposed combination of controllers in C2. The use of fuzzy logic in both voltage and power controllers, results in a more complex control system with the execution of four blocks of fuzzy logic leading to a reduction of efficiency. Therefore, the acceptable voltage response is obtained using Fuzzy PI, which offers the minimum settling time and the minimum deviation [26]. To obtain better performance and increase the superiority of the control system the integer order operators of the PIFPI controller will be replaced by fractional order operators. These additional degrees of freedom increase the flexibility of the FOPI-Fuzzy-FOPI controller which gives better performance than the PIFPI controller. Fig. 5.6a and b show that the use of the proposed FOPI-Fuzzy-FOPI controller (C6) and the optimization of the fractional order parameters (λ_1 and λ_2) by the PSO algorithm, give much improved voltage and reactive power responses compared to the C7 combination (FOFPID [28]). Figures 5.6 and 5.7 show that the best voltage and power responses are obtained by using the FOPI-Fuzzy-FOPI controller for LVRT control and PI controller for reactive power control (C6). This combination ensures fast response, minimal deviation from the reference value and ensures a fault clearing time of less than 0.2 s (satisfying grid code regulations). Without voltage control where the fault mode is deactivated, the automatic protection system starts to disconnect one third of the WTs from the power grid at the times 10.2, 11.8 and 12.1 s, in order to decrease the power gradually until the production stops completely as shown in Fig. 5.7.

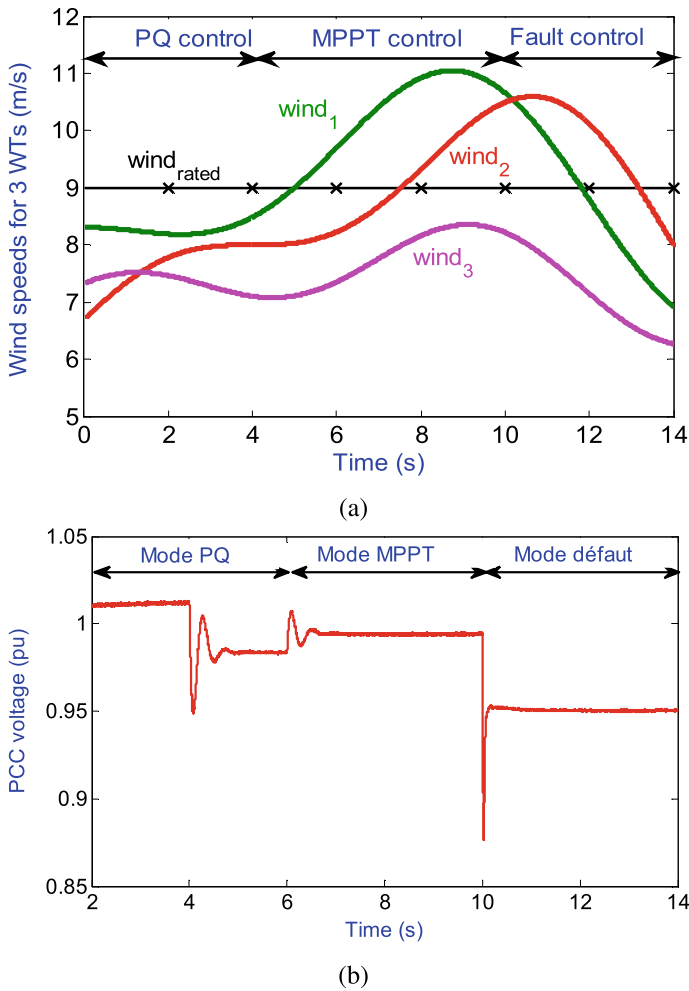


Fig. 5.8 Simulation results of a scenario that includes PQ control [2, 6 s], MPPT control [6, 10 s] and voltage fault control activated at time 9 s. **a** PCC voltage, **b** the three wind profiles

5.6.2 Performance of the Supervision System

The supervision system aims to control and dispatch the references of total WF power using MPPT, PQ and fault control modes. The effectiveness of the system is demonstrated through the development of a scenario divided into three periods. In period 1, PQ control mode is activated, followed by activation of MPPT mode in period 2 and finished by activation of fault control mode which starts at time 10 s when an inductive load of 6.5 MVAR connected near PCC causing a voltage drop, as shown in Fig. 5.6b. The three modes are operated under variable wind speed (Fig.

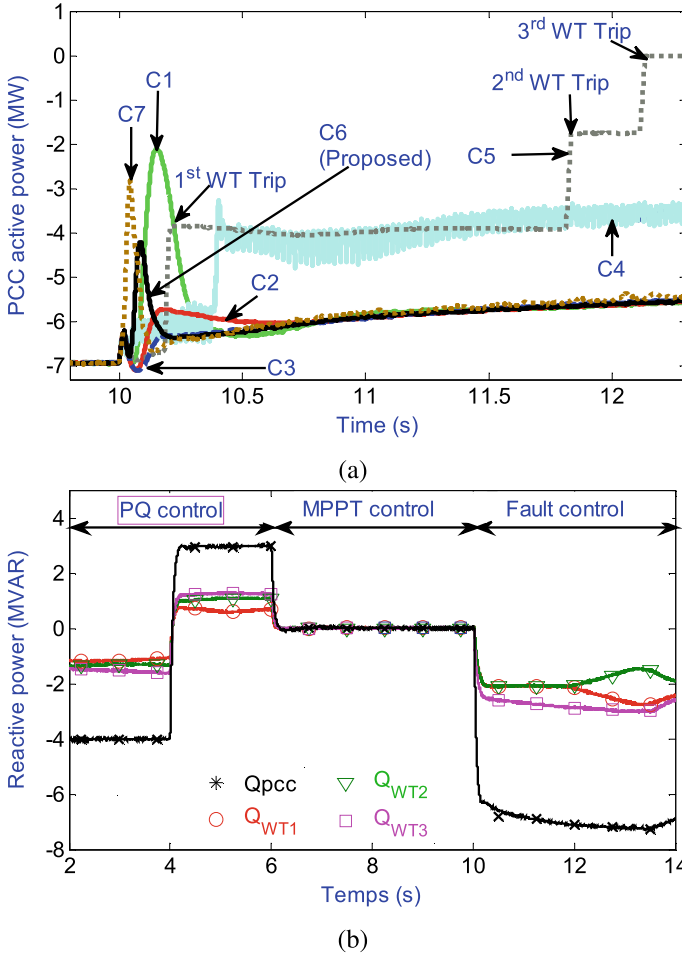
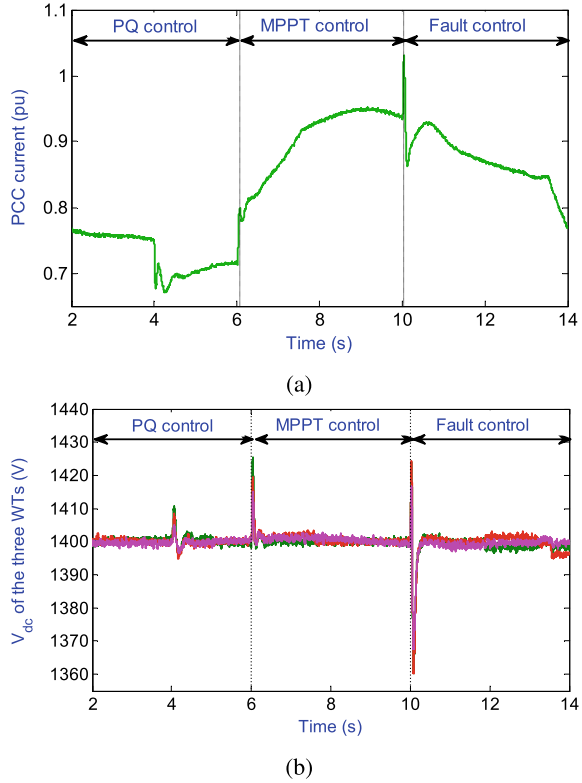


Fig. 5.9 Simulation results of a scenario that includes PQ control [2, 6 s], MPPT control [6, 10 s] and voltage fault control activated at time 9 s. **a** Active power **b** Reactive power

5.8a). During the period between 2 and 6 s of this scenario, the control mode “PQ” is activated under a variable wind speed. The results presented in Fig. 5.9a and b show that the proposed controller with the proposed supervision system allows the active and reactive power of the farm at the point of connection to follow accurately their references (P_{WF-ref} , Q_{wf-ref}). The WF consumes an amount of reactive power equal to 3 MVAR and produce an amount of active power equal to 4 MVAR imposed by the requested production plan in order to behave like a conventional power plant. The power references are distributed among the WTs in a proportional way and each WT participates with an amount of power depending on their maximum available powers as shown in Fig. 5.9a. The third WT is not capable of providing power

Fig. 5.10 Simulation results of a scenario including PQ control [2, 6 s], MPPT control [6, 10 s] and voltage fault control activated at time 9 s. **a** PCC current, **b** the DC bus voltages of the 3 WTs



demand, which allows first and second WTs to take action and increase their power using inertial power reserve. This strategy is applicable during the activation of MPPT mode between 6 and 10 s for an optimal power extraction from wind, which is the maximum active power. While reactive power at connection point is set to zero in order to obtain a unity power factor during the activation of MPPT control mode, as shown in Fig. 5.9b.

During the third period of this scenario, the fault control mode is activated in order to compensate voltage drop at PCC due to the excessive increase of reactive power. The connection of inductive load to grid at time 10 s leads to an imbalance between demand and consumption of reactive power, and at the same time causes a voltage drop (Fig. 5.6a). Unlike the other periods, during the third period the WF sacrifices a large amount of active power to generate reactive power for compensation. The supervision system increases the reactive power reference Q_{wf-ref} and decreases the active power reference P_{wf-ref} , as shown in Fig. 5.9a and b. Each wind turbine in the farm participates according to its maximum available power. In general cases, the voltage drop leads to an increase of current and instability of DC bus voltage. But it can be seen that in this scenario, despite voltage fault, the proposed system ensures that the maximum current value does not exceed the allowable limit, as shown

in Fig. 5.10a. The voltages V_{dc} of the three WTs follow perfectly their references (V_{dc-ref}) (Fig. 5.10b), while there is a peak of less than 5% of the minimal voltage that does not cause any problem to DC bus capacitor. However, the manufacturers design capacitors to support more than 5% of voltage variation. In addition, the DC bus capacitor must ensure a constant voltage at a value of $\pm 5\%$ of nominal voltage value, to ensure controllability and improved power quality. Finally, from the above analysis, it can be concluded that the supervision system with adoption of fractional order fuzzy controller, guarantees better performance in terms of reference tracking, fast response and stability of WF, as well as voltage compensation and power management of all wind turbines.

5.7 Conclusion

In this chapter, the three axes that represent the field of study of wind energy production systems have been examined: the design of the wind energy conversion system to be modeled and controlled, the design of the control system, and the configuration of a farm supervision system. Through these three axes, the structure of a wind farm and the development of an advanced controller (FOPI-F-FOPI) were presented. The supervisory system ensures the cooperation between the different parts of the controlled system and the optimal interaction between the wind turbines of the farm. This chapter deals with LVRT control for a grid-connected WF and the management of active and reactive power. The main advantages of the proposed wind farm control scheme are:

- Compensation of voltage drop in an uncompensated power system using a proposed fractional order fuzzy controller (FOPI-Fuzzy-FOPI) to enhance responses of voltage and reactive power.
- Optimization of fractional order operator parameters using the PSO algorithm.
- Supervision of the WF and distribution of power references using the proportional distribution algorithm associated with the MPPT operating mode, PQ mode and fault control mode.

Simulation results show that the use of proposed voltage and reactive power control system with FOPI-Fuzzy-FOPI controller offers a lower response time, a reduced settling time and a minimum deviation from the nominal value. The validation scenario, which introduces the three operating modes, shows that the supervisory system with DP algorithm provides a very good power management of WF and ensures that WF behave like a conventional power plant.

References

1. Global Wind Energy Council (GWEC), GWEC Global Wind Report (2018)
2. Ghennam, T., Francois, B., Berkouk, E.M.: Local supervisory algorithm for reactive power dispatching of a wind farm. In: *Chez 13th European Conference on Power Electronics and Applications EPE* (2009)
3. Dai, C., Chen, W., Zhu, Y., Xuexia, Z.: Seeker optimization algorithm for optimal reactive power dispatch. *IEEE Trans. Power Syst.* **24**(13), 1218–1231 (2009)
4. Benlahbib, B., Bouchafaa, F.: Centralized algorithm for wind farm supervision. *Chez International Conference on Control, Engineering and Information Technology (CEITâĀĹ14) Proceedings* (2014)
5. Elyaaloui, K., Ouassaid, M., Cherkaoui, M.: Dispatching and control of active and reactive power for a wind farm considering fault ride-through with a proposed PI reactive power control. *Renew. Energy Focus* **28**(100), 56–65 (2019)
6. Elyaaloui, K., Ouassaid, M., Cherkaoui, M.: Supervision system of a wind farm based on squirrel cage asynchronous generator. In: *Chez Fourth International Conference on Renewable and Sustainable Energy (IRSEC'16)*. IEEE, Marrakech, Morocco (2016)
7. ENTSO-E, Entso-e network code for requirements for grid connection applicable to all generators, [En ligne]. <https://www.entsoe.eu>. [Accessed 02 Dec 2016]
8. Elyaaloui, K., Ouassaid, M., Cherkaoui, M.: Improvement of THD performance of a robust controller for grid-side energy conversion system based on LCL filter without RC sensor. *Int. J. Electr. Power Energy Syst.* **121** (2020)
9. ValĂĀrio, D., Costa, J.S.D.: Introduction to single-input, single-output fractional control. *IET Control Theory Appl.* **5**(18), 033–1057 (2011)
10. Alsmadi, Y.M., Xu, L., Blaabjerg, F., Ortega, A.P., Abdelaziz, A.Y., Wang, A., Albataineh, Z.: Detailed investigation and performance improvement of the dynamic behavior of grid-connected DFIG-based wind turbines under LVRT conditions. *IEEE Trans. Ind. Appl.* (2018)
11. Kundur, P.: *Power System Stability and Control*. McGraw-Hill Professional (1994)
12. Bevrani, H.: *Robust Power System Frequency Control*, *Power Electronics and Power Systems*. Springer International Publishing (2014)
13. Lee, D.: IEEE recommended practice for excitation system models for power system stability studies (IEEE std. 421.5–1992). In: *Energy Development and Power Generating Committee of the Power Engineering Society*, Vol. 95, p. 96 (1992)
14. Florin, I., Daniela, H.A., Poul, S., Antonio, C.N.: Mapping of Grid Faults and Grid Codes. RisĂĀ National Laboratory, Technical University of Denmark, Roskilde, Denmark (2007)
15. Shin, H., Jung, H.-S., SUL, S.-K.: Low voltage ride through (LVRT) control strategy of grid-connected variable speed wind turbine generator system. In: *2011 IEEE 8th International Conference on Power Electronics and ECCE Asia (ICPE & ECCE)* (2011)
16. ON Netz GmbH, B.E.: Requirements for Offshore Grid Connections in the Grid of TenneT TSO GmbH, 21 Dec 2012
17. Das, S.: *Functional Fractional Calculus for System Identification and Controls*. Springer, Heidelberg (2008)
18. Podlubny, I.: *Fractional Differential Equations*. Academic, New York (1999)
19. Podlubny, I.: Fractional-order systems and $PI^{\lambda}D^{\mu}$ controllers **44**(11), 208–214 (1999)
20. Elyaaloui, K., Labbadi, M., Ouassaid, M., Cherkaoui, M.: A Continuous nonlinear fractional-order PI controller for primary frequency control application. *Math. Probl. Eng.* (2021)
21. Labbadi, M., Boukal, Y., Cherkaoui, M.: Path following control of quadrotor UAV with continuous fractional-order super twisting sliding mode. *J. Intell. Robot. Syst.* **100**(13), 1429–1451 (2020)
22. Tepljakov, A., Petlenkov, E., Belikov, J.: FOMCON: fractional-order modeling and control toolbox for MATLAB. In: *Proceedings of the 18th International Conference Mixed Design of Integrated Circuits Systems*, pp. 684–689 (2011)

23. Elyaaalaoui, K., Ouassaid, M., Cherkaoui, M.: Non-linear control and transient stability of SCAG connected to unbalanced AC network. In: 2014 International, Renewable and Sustainable Energy Conference (IRSEC). IEEE (2014)
24. Elyaaalaoui, K., Ouassaid, M., Cherkaoui, M.: Low voltage ride through for a wind turbine based SCAG. In: Third International Conference on Renewable and Sustainable Energy (IRSEC'15), pp. 1–6, 10–13. IEEE, Marrakech, Morocco (2015)
25. Elyaaalaoui, K., Ouassaid, M. and Cherkaoui, M.: Optimal fractional order based on fuzzy control scheme for wind farm voltage control with reactive power compensation. *Math. Probl. Eng.* **2021**(5559242), 12 (2021). <https://doi.org/10.1155/2021/5559242>
26. Elyaaalaoui, K., Ouassaid, M., Cherkaoui, M.: Primary frequency control using hierarchal fuzzy logic for a wind farm based on SCIG connected to electrical network. *Sustain. Energy, Grids Netw.* **16**, 188–195 (2018)
27. Pan, I., Das, S.: Fractional order fuzzy control of hybrid power system with renewable generation using chaotic PSO. *ISA Trans.* 1–11 (2016)
28. Pathak, D., Gaur, P.: A fractional order fuzzy-proportional-integral-derivative based pitch angle controller for a direct-drive wind energy system. *Comput. Electr. Eng.* **78**, 420–436 (2019)
29. Oon, K.H., Tan, C., Bakar, A.H.A., Che, H.S., Mokhlis, H., Illias, H.A.: Establishment of fault current characteristics for solar photovoltaic generator considering low voltage ride through and reactive current injection requirement. *Renew. Sustain. Energy Rev.* **92**, 478–488 (2018)
30. Gharghory, S., Kamal, H.: Optimal tuning of PID controller using adaptive hybrid particle swarm optimization algorithm. *Int. J. Comput., Commun. Control* **7**(1), 101–114 (2012)
31. W. M. Korani, “Bacterial foraging oriented by particle swarm optimization strategy for PID tuning,” in Proceedings of the 2008 GECCO Conference Companion on Genetic and Evolutionary Computation, Daejeon, Republic of Korea, 2008

Chapter 6

Primary Frequency Control for Wind Farm Using a Novel PI Fuzzy PI Controller



6.1 Introduction

The primary frequency control takes a lot of attention in last decades and adopted for a secure operation ensuring the stability of the power system connected wind energy conversion system. According to some European grid codes, main cause of frequency deviation is unbalance between demand and supply of active power, which demand the participation of wind power plants must. The kinetic energy of wind power plants is investigated to compensate frequency deviations, which required a sophisticated control system. Fuzzy logic control is used in many applications to solve, on one hand, problems related to nonlinearity of systems, and on other hand, to improve response, attenuate ripples and obtain a faster transient behavior compared to that obtained with classical PI and PID controllers [1–6]. The Fuzzy Logic Controller (FLC) and classical controllers (such as PI, PD, and PID) can be combined together in one structure called Hierarchical Fuzzy Controller (HFC). The PIDFLC hierarchical structure consists of a PD-Fuzzy controller (PDF) added to the PI-Fuzzy controller (PIF) to remedy some problem of PD-Fuzzy, PI-Fuzzy, or PI controller [6–8]. This structure gives good performance than the PD-Fuzzy and PD-Fuzzy + PI controllers. For a faster and a more accurate responses of frequency and power, this chapter deals with primary frequency control using inertial power reserve and proposes PI-Fuzzy-PI Hierarchical Fuzzy Controller (PIFPI) for a better response. To prove that the proposed controller is superior demonstrate its effectiveness, a comparative study is developed between fuzzy hierarchical controllers [6]. For testing performances of proposed controllers an aggregate model of WF should be adopted instead of detailed model is developed. The WF is connected dynamic model of power network consists of two areas supplied by two synchronous generators. The rest sections of this chapter are organized as follows: Aggregate model of the wind farm system for frequency-power response study is illustrated in Sect. 6.2. Full model of the power network is developed in Sect. 6.3. The primary frequency control using a new structure of fuzzy

logic controller is proposed in Sect. 6.4. Simulation results are discussed in Sect. 6.5. The last section is devoted to a conclusion.

6.2 Aggregate Model for Frequency-Power Response Study

To study the effect of power imbalance between grid demand and wind farm production, an aggregate model is adopted for simulating and testing the control system, instead of reduced model based on mechanical part only. However, most of works in literature use reduced model to study frequency control without taking into account the effect of electrical devices, frequency deadband non-linearity, generated power slope constraint and delay time. These effects have been modelled and introduced into a system that includes the aggregate model called the multi-machine model (MMM) and the dynamic grid model [6, 9]. This system is adopted to obtain the real characteristics of the studied system (WF and grid). The complete detailed system of WF is shown in Fig. 6.1 as a cluster. The farm consists of 30 wind turbines based on squirrel-cage induction generators (SCIG). It is aggregated in equivalent multi-machine model (MMM).

6.2.1 Aggregate Model of the Wind Farm

The detailed model is a full model of all wind turbines and their interconnections [10]. However, due to large number of wind turbines, it requires a longer execution time

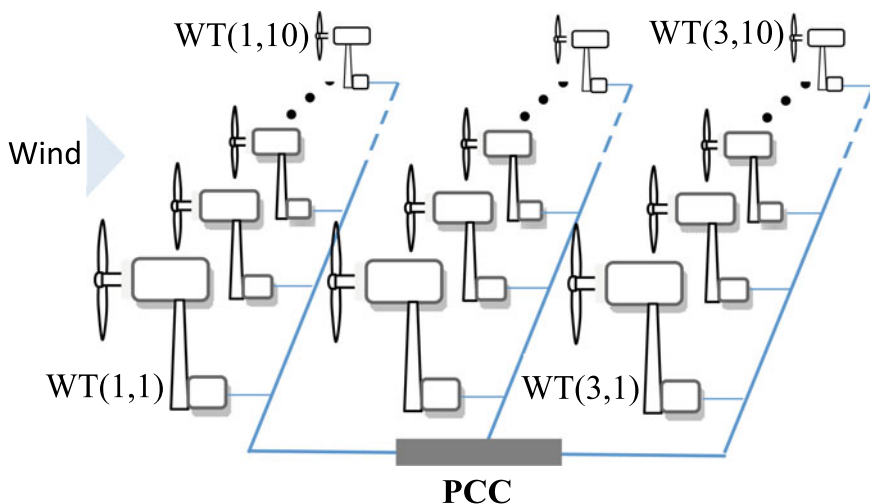


Fig. 6.1 Model of the wind farm as a cluster of 30 wind turbines

and increases system complexity. To solve this problem, the WF model can be aggregated into an equivalent model. In the papers [11, 12] different aggregation methods for WFs are studied, such as Full Aggregated Model (FAM), Semi-Aggregated Model (SAM) and Multi-Machine Model (MMM) were simulated under different operating conditions such as wind fluctuations and grid voltage disturbances at the PCC (see Fig. 6.2). The discussion of these aggregation methods is elaborated with the conditions under which they are valid:

- (a) The CAM model is efficient and appropriate when all wind turbines in the farm have the same parameters, similar operating point and receive identical wind speeds (uniform wind distribution in the farm). In this case, all wind turbines and their interconnections are combined into a single equivalent wind turbine with an equivalent internal power system.
- (b) The SAM model is used when the wind turbines in the farm receive different wind speeds, which avoids the aggregation of the turbines. But the generators will be aggregated into a single equivalent generator driven by several turbines. It aims to study the effect of wind speeds.

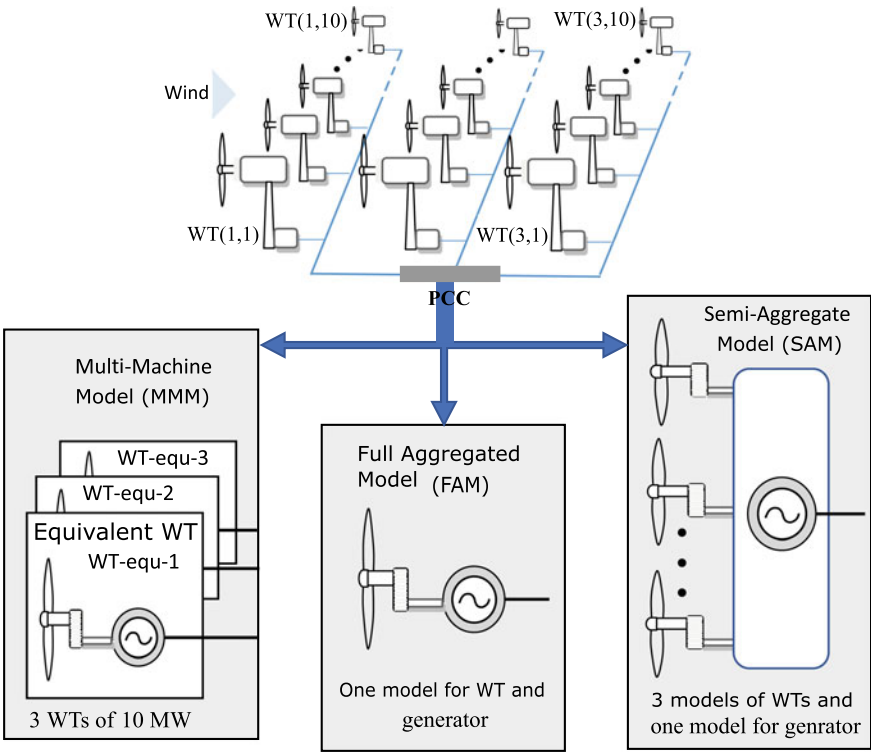


Fig. 6.2 Aggregate models of the wind farm

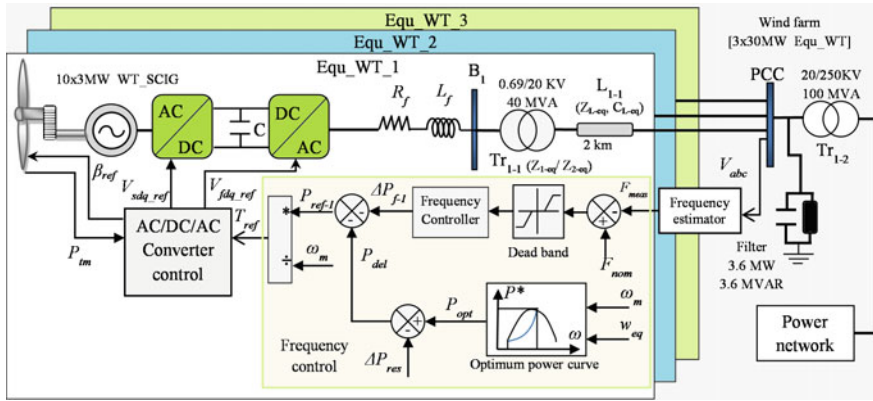


Fig. 6.3 Overall diagram of the farm connected to the electrical grid

- (c) The MMM model is an efficient method for a group of wind turbines with irregular wind distribution. In this technique, the wind turbines of the farm can be divided into several aggregated models, the wind turbines have the same operating point and receive identical wind speeds are grouped together in an equivalent machine. Usually, the wind turbines in the same column of the cluster receive different wind speeds, due to the shadow effect of these turbines. But, the wind turbines in same row of the cluster are aggregated together into same equivalent model [9].

The comparison, under grid disturbance, between aggregate model and detailed model, shows that the equivalent model allows to obtain voltage and power responses identical to those obtained with detailed model [13] during simulation of WF. The active power response is identical in detailed model and multi-machine model (MMM) [11, 12, 14]. Therefore, MMM is considered as good choice for primary frequency control application [6, 9]. In this chapter, adequate aggregate model should be chosen for WF under study is MMM. The form of WF is considered as a group of three rows and ten columns. The wind turbines in same row are grouped together and modeled in an equivalent wind turbine (WT-equ). Each WT-equ is connected to PCC via back-to-back converter, a RL filter, a transformer and a transmission line of 5 km. Therefore, by adopting MMM technique the modeled WF is consisting of three equivalent wind turbines such as presented Fig. 6.3. The control voltages ($V_{sdq-ref}$ and $V_{fdq-ref}$) are generated to control the back-to-back converter. The equivalent wind speed v_{equ-i} of a WT for each row (i) is equal to average wind speed of WT in same column (j), as shown in (6.1) [13].

$$v_{equ-i} = \frac{1}{n} \sum_{j=1}^n v_{i,j} \quad (6.1)$$

where v_{eq-i} is the incoming wind speed for $WT - equ - i$, $v_{i,j}$ is the wind velocity for the turbine “ i, j ” and n is number of aggregated WTs. The equivalent wind speed must satisfy condition $v_{eq-1} > v_{eq-2} > v_{eq-3}$, because the shadow effect is reduced with distance between rows. It is decreased from row 1 to others.

6.2.2 Equivalent Parameters of Aggregated Model

The parameters of $WT - equ$ is obtained using re-scaled power capacity technique. Apparent (S_{eq}), active (P_{eq}) and reactive (Q_{eq}) power of WT-equ are equal to the sum of apparent (S_j), active (P_j) and reactive (Q_j) power of aggregated wind turbines, respectively, as shown in (6.2), (6.3) and (6.4). Mechanical torque of $WT - equ$, in per-unit notation “ pu ”, is equal to mechanical torque of each wind turbine (6.5) [12, 13].

$$S_{equ} = \sum_{j=1}^n S_j = n.S_j \quad (6.2)$$

$$P_{equ} = \sum_{j=1}^n P_j = n.P_j \quad (6.3)$$

$$Q_{equ} = \sum_{j=1}^n Q_j = n.Q_j \quad (6.4)$$

$$T_{m-equ} = T_{m-j} \quad (6.5)$$

The equivalent reactance of capacitor X_{eq} (6.6) and impedance of transformer Z_{eq} (6.7) of $WT - eq$ are equal to reactance X_C and impedance Z_T of a WT divided by the number of wind turbines “ n ”, respectively [12, 15].

$$X_{eq} = \frac{X_c}{n} \quad (6.6)$$

$$Z_{eq} = \frac{Z_T}{n} \quad (6.7)$$

6.2.3 Power System Model for Frequency Control

The frequency stabilization of the power system depends on the balance between power generation and consumption. The variation in active power demand is reflected throughout the system by the frequency variation, because the power system is based

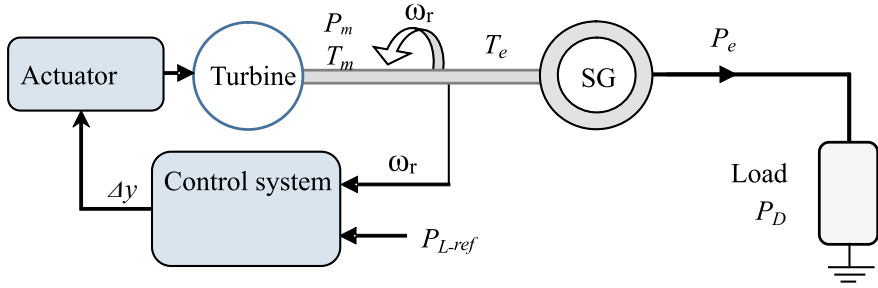


Fig. 6.4 Turbine connected to a synchronous generator supplying an isolated load

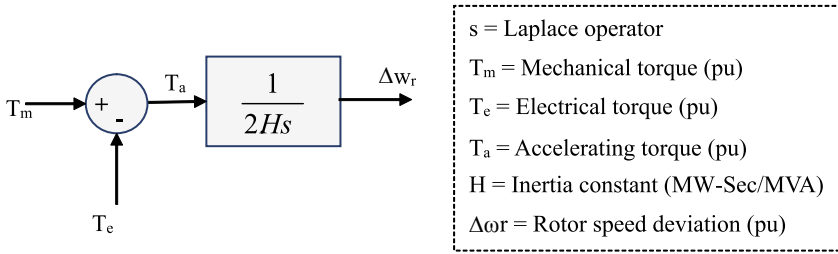


Fig. 6.5 Transfer function relating speed and torques

on many generators feeding the loads (Fig. 6.4). The power generation unit in the power network comprises a steam turbine driven by a power control system designed to produce the required power with a specific droop [16]. When power consumed by loads increases, the electromagnetic torque (T_e) of generator varies leading instantaneously to a difference between mechanical torque (T_m) and T_e . This change in torque leads to a variation in speed as shown in Fig. 6.5.

Where P_D is the power demanded by the load, P_e is the electrical power supplied by the generator, T_m is the mechanical torque, T_e is the electrical torque, ω_r is the generator rotor speed, Δy is the valve position, P_m is the mechanical power, and P_{L-ref} is the active power reference of the load.

6.2.3.1 Transfer Function Linking Mechanical Speed and Power

In the case of load frequency control using active power, the mechanical and electrical torques of the fundamental dynamic equation must be replaced by the mechanical and electrical powers. The relation between the power P and the torque T is given by:

$$P = \omega_r \cdot T \quad (6.8)$$

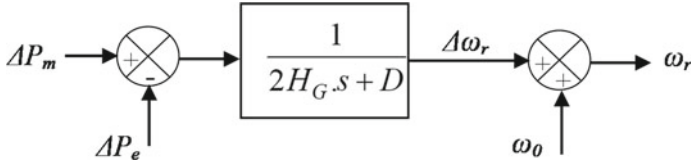


Fig. 6.6 Transfer function linking mechanical speed and power in “per unit” notation

Adopting small deviation (noted prefix Δ) from initial values (noted index 0), applied to (6.8), we can obtain:

$$P = P_0 \cdot \Delta P \quad (6.9)$$

$$T = T_0 \cdot \Delta T \quad (6.10)$$

$$\omega_r = \omega_0 \cdot \Delta \omega_r \quad (6.11)$$

Using (6.9), (6.10) and (6.11), Eq. (6.8) is written as:

$$P_0 \cdot \Delta P = (\omega_0 \cdot \Delta \omega_r)(T_0 \cdot \Delta T) \quad (6.12)$$

Considering $P_0 = \omega_0 \cdot T_0$ and neglecting the higher order terms, the relationship between the perturbed quantities is given by:

$$\Delta P = \omega_0 \cdot \Delta T + T_0 \Delta \omega_r \quad (6.13)$$

Therefore,

$$\Delta P_m - \Delta P_e = \omega_0 \cdot (\Delta T_m - \Delta T_e) + \Delta \omega_r (\Delta T_{m0} - \Delta T_{e0}) \quad (6.14)$$

During steady state operation, electrical and mechanical torques are equal, $T_{m0} = T_{e0}$ and $\omega_0 = 1 pu$. Therefore, these simplifications lead to the following expression [16]:

$$\Delta P_m - \Delta P_e = \Delta T_m - \Delta T_e \quad (6.15)$$

The block diagram of the system and the transfer function relating speed and power (ΔP_m and ΔP_e) are illustrated in Fig. 6.6, with D the damping coefficient of the system. For an acceptable range of speed (or frequency) variation, the position of the valve gate is controlled to obtain the required mechanical power.

6.2.3.2 Proposed Grid Model

As shown in Fig. 6.7, the two areas of power system model is designed using two synchronous generators (SG1 and SG2) supplying the loads. Each area consists of a steam turbine controlled by governor system and connected to synchronous

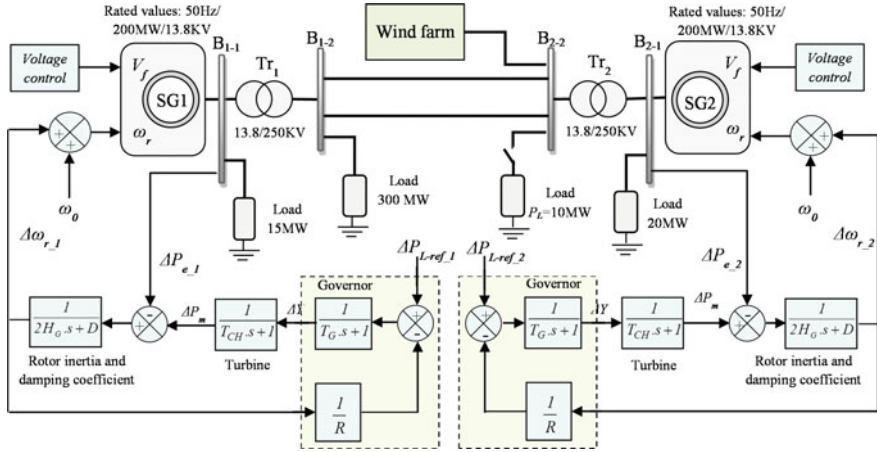


Fig. 6.7 Global electrical grid diagram including generators and loads with the possibility to control the frequency and active power

generator to generate power demanded by loads with a specific droop (R) [16, 17]. The power control system aims to convert mechanical power (ΔP_m) into electrical power (P_e) requested by loads (ΔP_D) to obtain $\Delta P_e = \Delta P_{L-ref}$ and frequency is equal to its nominal value. The reference values of load are $\Delta P_{L-ref-1} = 0.674 pu$ and $\Delta P_{L-ref-2} = 0.6739 pu$. But, when load power increases (P_L is connected), the generators decelerate leading to frequency deviation [6].

Where:

- $\Delta\omega_r$: Speed deviation.
- Δf : Frequency deviation.
- Δy : Change in valve/gate position.
- ΔP : Power output change.

6.2.3.3 Characteristics of Percent Speed Regulation or Droop

The droop value (R) determines the steady state characteristic of the speed control system with respect to the generated power, as shown in Fig. 6.8. It depends on inertia and damping constant of load. It is equal to the ratio between percentage of frequency deviation and percentage of output power change. The value of R is defined in percentage as shown in (6.16).

$$R(\%) = \frac{\text{speed change (\%)} \text{ or } \text{frequency (\%)}}{\text{Power output change (\%)}} \cdot 100 = \frac{\omega_{NL} - \omega_{FL}}{\omega_0} \quad (6.16)$$

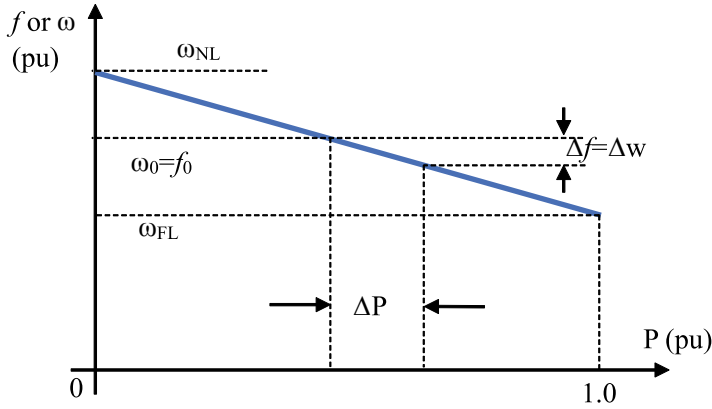


Fig. 6.8 Ideal steady-state characteristics of a governor with speed droop

where:

ω_{NL} is the steady-state speed at no load.

ω_{FL} is the steady-state speed at full load.

ω_0 is the nominal or rated speed.

For example, 5% of droop means that 5% of frequency deviation causes 100% of output power change.

The power-frequency characteristic depends on frequency deviation of all controllers and loads in power system. For studied system, with two generators and load damping constant D , the steady-state frequency deviation (Δf_{ss}) due to the load change ΔP_L can be expressed by [16, 17]:

$$\Delta f_{ss} = \frac{-\Delta P_L}{\frac{1}{R_{eq}} + D} \quad (6.17)$$

$$\frac{1}{R_{eq}} = \frac{1}{R_1} + \frac{1}{R_2} = \frac{2}{R} \quad (6.18)$$

where R_1 , R_2 are droop parameters of generators 1 and 2, respectively. R_{eq} is the equivalent value of R_1 and R_2 , which define the frequency response characteristic of the global system. $R = R_1 = R_2$, because the two generators are identical.

6.2.4 Adaptation of Power System Model to Grid Code Recommendations

To adjust power system model to frequency control according to the requirements of grid code, a term βf , which indicates the frequency response characteristic taking into account the load damping constant, is used. According to the ENTSO-E rec-

ommendations given in Fig. 1.8, a droop “ d ” of 10% means that a 100% change in the output power of the wind farm causes a frequency deviation of 10% from the nominal value (9MW causes 0.5 Hz). The grid frequency will be deviated by 0.5 Hz when the load power changes by 10% of the wind farm’s nominal power ($S_{nF} = 90$ MW). The value of βf is calculated using (6.19). It depends on the rated power of the wind farm, the rated power S_G of the grid generator, the desired frequency deviation and the rated frequency [16].

$$\rho_f = \frac{-\Delta P_L}{\Delta f_{ss}} = \frac{\frac{d \cdot S_{nF}}{S_G}}{\frac{\Delta f}{f_n}} \quad (6.19)$$

Therefore, from (6.18) and (6.19), the value of R is given by:

$$R = \frac{2}{\rho_f - D} \quad (6.20)$$

6.3 Proposed Hierarchical Fuzzy Logic Controller for Primary Frequency Control

Primary Frequency Control (PFC) for WF is divided into two control methods:

- Control of power reserve stored in WTs as inertial power reserve and created in a deloaded operation.
- Frequency control, activated to compensate frequency deviation using inertial power reserve.

In this section, proposed Hierarchical Fuzzy Controller (HFC) allows each wind turbine to reserve a deloaded active power using a simple deload method and participating in PFC.

6.3.1 Power Reserve Control

The power reserve (ΔP_{res}), which is required to meet PFC objective, is created by wind turbines in a deloaded operation. Deloaded operation is obtained when wind turbine operates to extract less power than 10% of maximum available power. If each wind turbine participates in the frequency control with same amount of its available power, the power reserve (ΔP_{res}) of WF is the sum of power stored in all “ m ” WT-equs (6.21).

$$\Delta P_{res} = \sum_{i=1}^m \Delta P_{res-i} \quad (6.21)$$

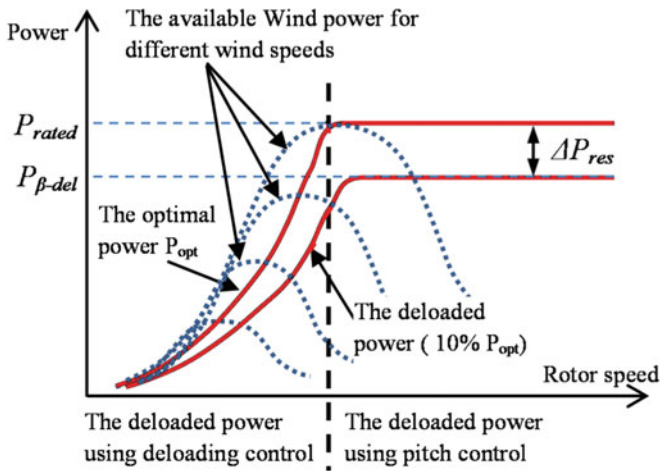
Wind turbines are deloaded using the pitch control and the deloaded control.

6.3.1.1 Pitch Control Method

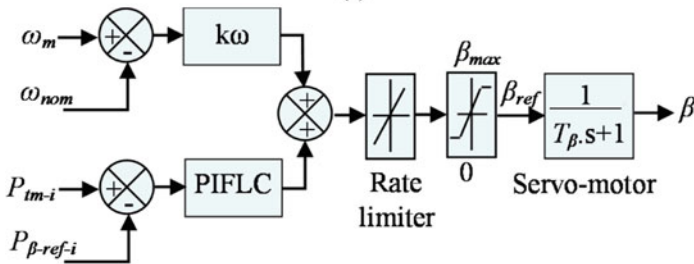
The purpose of using pitch control is to limit the extracted power to a value below the maximum. The stored active power is used during frequency drop by decreasing blade orientation angle, in order to increase mechanical power (P_{tm-i}) and then the injected electrical power. The power delayed by the blade orientation ($P_{\beta-del-i}$) of the WT-equ- i is given in (6.22) (See also Fig. 6.9a).

$$\Delta P_{\beta-del-i} = \Delta P_{n-i} - \Delta P_{res-i} \quad (6.22)$$

The control of blade orientation angle is achieved by hierarchical fuzzy PI controller (HFPI) [1] and proportional controller to limit the WT mechanical power and speed at nominal values, respectively, as shown in Fig. 6.9b.



(a)



(b)

Fig. 6.9 Power reserve control, **a** Optimal and delayed power curves, **b** Block diagram for generating the pitch angle. Where T_{β} is the time constant of the pitch system servo motor. The speed and range of the pitch angle variation are set to $\pm 10^\circ/\text{s}$ and 0° to 90° , respectively

The pitch control is activated during frequency deviation to generate power the stored power, when the wind speed exceeds the maximum value. The power reference for pitch angle control loop is equal to power deloaded by “pitch control” plus power necessary for frequency control (ΔP_{f-i}), (6.23).

$$\Delta P_{\beta-ref-i} = \Delta P_{\beta-del-i} + \Delta P_{f-i} \quad (6.23)$$

The amount of WF power (ΔP_f) required to control frequency and compensate unbalance power, is given by:

$$\Delta P_f = \sum_{i=1}^m \Delta P_{f-i} \quad (6.24)$$

6.3.1.2 Wind Turbine Deloading Control

The other deloading method of wind turbine is activated to generate power less than maximum power, which is optimal power (P_{opt}) given by the MPPT strategy (see Fig. 6.9a). This stored energy is injected into grid during the frequency deviation. To achieve this objective, the power is controlled to follow reference (P_{ref-i}) given in (6.25).

$$P_{ref-i} = -(P_{opt-i} - \Delta P_{res-i} + \Delta P_{f-i}) \quad (6.25)$$

6.3.2 Frequency Control

The power reference for frequency control is dispatched among all the WT-equs using a distribution algorithm. All generators in WF receive same reference. But, if one of them is disconnected, the controller increases power of others to replace missing power (6.26).

$$\Delta P_{f-i} = \frac{\Delta P_f}{m} \quad (6.26)$$

In the per-unit notation (pu), the percentages of reserved power and control power are identical for WF and WT-equ. Torque and power references are generated by frequency control loop as shown in Fig. 6.10.

6.3.2.1 Fuzzy Logic

In this chapter, fuzzy logic is used to ensure best performance, smooth pitch angle and generate desired references. The inputs of fuzzy logic are error $e = (F_{nom} - F_{meas})$ and error derivative (d_e) or error integral ($\int e$). The output (U) is the active power

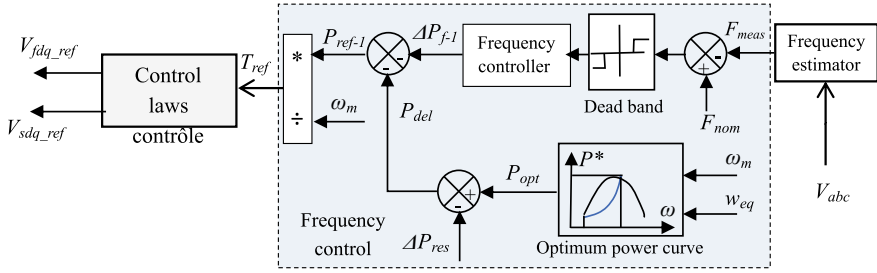


Fig. 6.10 Generation of power and torque references for frequency control

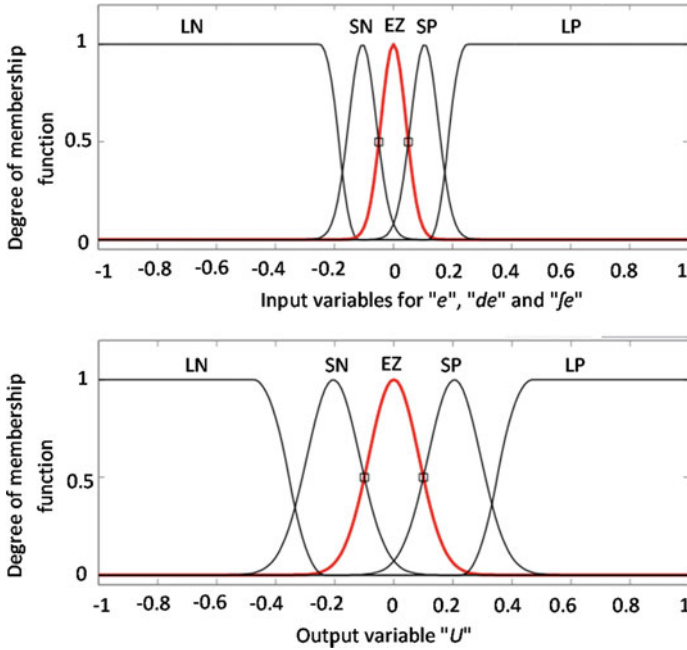


Fig. 6.11 Gaussian membership functions for the inputs and the output

reference (P_f) for frequency control. But for pitch control the output is the pitch angle (β_{ref}). The fuzzy logic rules and Gaussian membership functions are presented in Fig. 6.11. Following same strategy such as shown in previous chapter for fuzzy logic design, the function of fuzzification and fuzzy logic rules are presented in Table 6.1. The values of output variable is computed by the center of gravity method defined by the expression (6.27) [1].

$$U(x) = \frac{\sum_j^N w_{e_j} \cdot \mu_j(x)}{\sum_j^N \mu_j(x)} \quad (6.27)$$

Table 6.1 Fuzzy logic rules for primary frequency control

Derivative (de) and integra of error ($\int e$)	Error (e)				
	LP	SP	EZ	SN	LN
LP	LP	LP	SP	SP	EZ
SP	LP	SP	SP	EZ	LN
EZ	LP	SP	EZ	SN	LN
SN	SP	EZ	SN	SN	LN
LN	EZ	SN	SN	LN	LN

6.3.2.2 Proposed Hierarchical Fuzzy Controller

The design layouts of proposed hierarchical fuzzy controllers are presented in Fig. 6.12. The structures employee PI and or PD at input and output of fuzzy logic block to enhance response of variables.

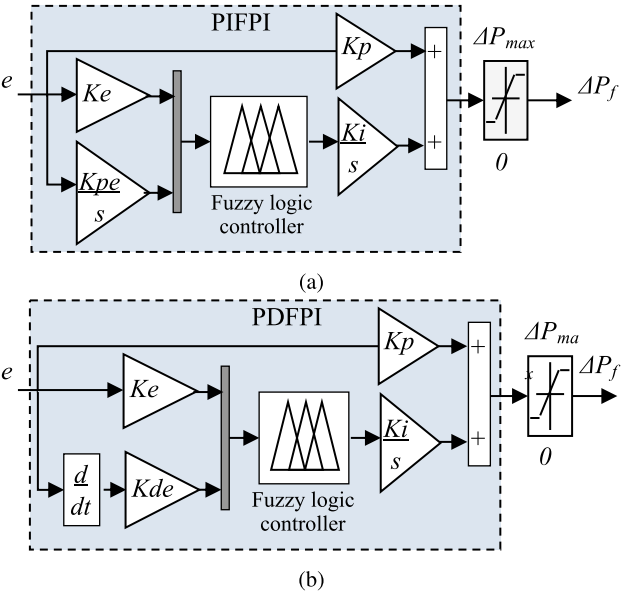


Fig. 6.12 Block diagram of the proposed hierarchical fuzzy controllers: **a** PIFPI controller, **b** PDFPI controller

6.4 Simulation Results and Discussion

The simulation is performed using MATLAB/Simulink environment. The three WT-equs are subjected to different wind speeds ($V_{eq-1} = 10$, $V_{eq-2} = 8.5$ and $V_{eq-3} = 8$ m/s). The system parameters are given in Appendix A (Sect. A.3, Tables A.7 and A.8).

6.4.1 Comparative Study of the Frequency and Power Responses

The simulation results are developed using (i) proposed PIFPI controller, (ii) PI controller, (iii) PIDFLC hierarchical structure proposed as best one in [7], (iv) PDFPI and (v) Inertial Controller (IC) given in [18, 19], with an improved layout shown in Fig. 6.13. The objective of this comparative is to demonstrate superiority of proposed controller and primary frequency control system using test system shown in Fig. 6.3. The unbalance power and frequency deviation below 49.8 Hz are created at time 25 s, when resistive load (PL) of 10 MW is connected to grid at bus B4, as illustrated in Fig. 6.14.

During drop, the CI for PFC present a poor robustness and then produces a lot of oscillations for frequency and power, compared to proposed PIFPI, controllers PI, PDFPI, and PDFLC, as shown in Figs. 6.14 and 6.15a.

The frequency responses for a dead band of 0.01 Hz, presented in Table 6.2, are extracted from Fig. 6.14. Table 6.2 and Fig. 6.15a show that the best responses are obtained using proposed PIFPI controller, which provide a minimum deviation from deadband, minimum settling time and better satisfaction of GCRs (initial activation delay < 2 s and full activation time < 30 s). The proposed control system keep reac-

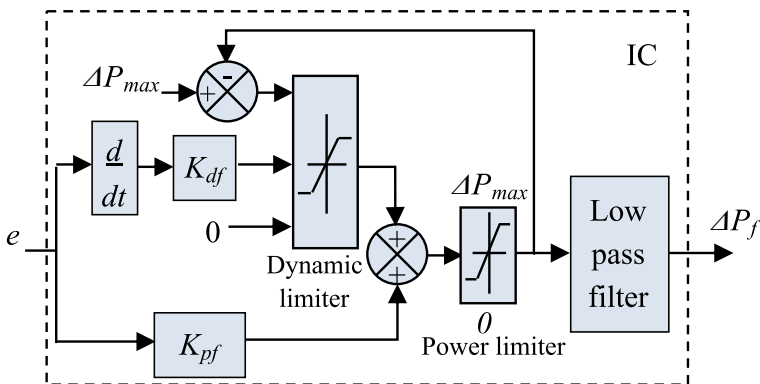
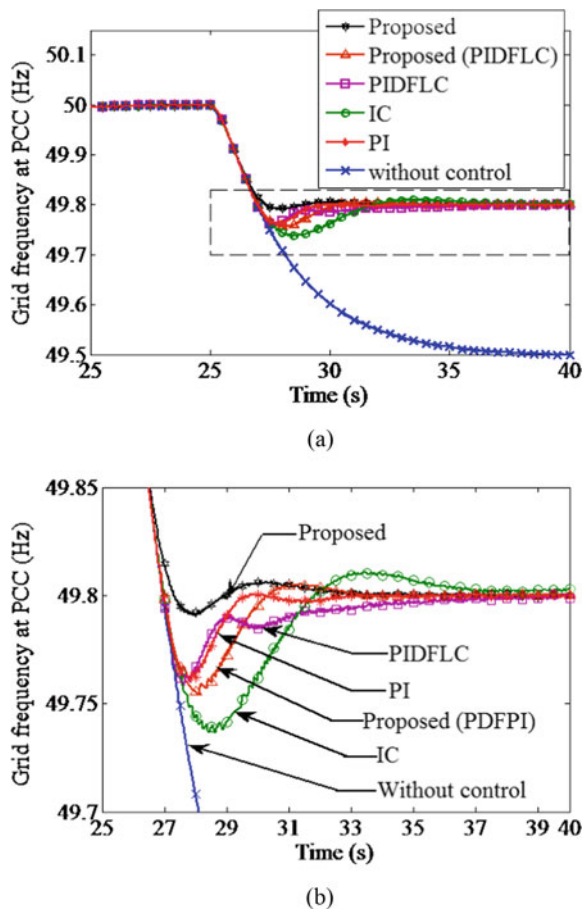


Fig. 6.13 Block diagram of inertial controller for frequency control

Fig. 6.14 Frequency responses (Hz) at the PCC:
a using the five controllers,
b their zoom



tive power stable despite fault with a small deviation, as shown in Fig. 6.15b. Based on the above analysis, it can be seen that the proposed controller offers best responses of frequency and power compared to others proposed in literature.

6.4.2 Dynamic Behavior of WTs

Dynamic behaviors of WT-equs are given in Fig. 6.16 Using proposed PIFPI and PIDFLC controllers for frequency for pitch angle control, respectively. These results are carried out to show influence of “Pitch control” on WTs and demonstrate operation deloading method using “Pitch control”. During frequency deviation, pitch control of WT-equ-1 is activated ($v_{eq1} > v_n$) to decrease pitch angle (Fig. 6.16a) to inject power

Fig. 6.15 The power response: **a** Active power (MW) and **b** Reactive power (MVAR) at PCC

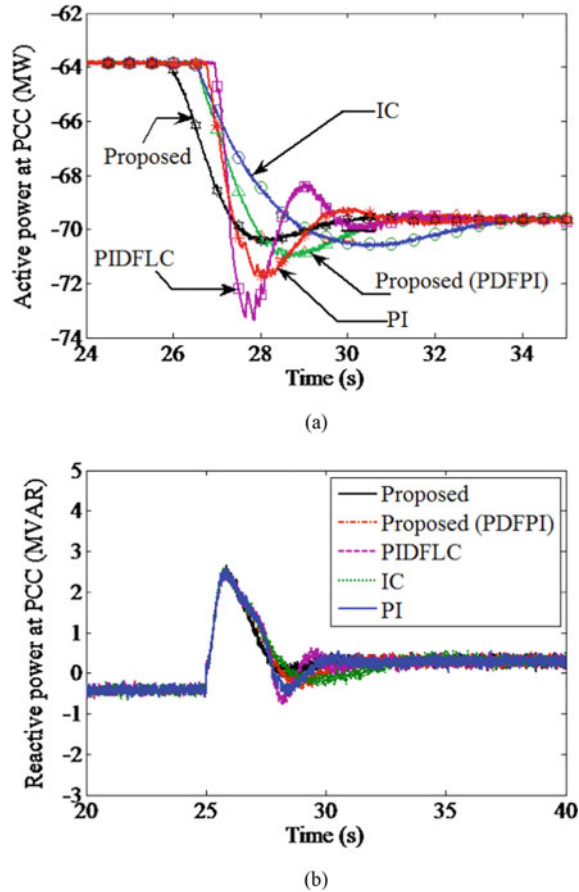


Table 6.2 Frequency responses for an acceptable deviation from deadband of 0.01 Hz

Controller	Maximum deviation (Hz)	Settling time (s)
CI [18, 19]	-0.06	9
PI	-0.04	4
PIDFLC [7]	-0.04	6
PDFPI	-0.045	4.7
PIFPI [proposed]	-0.01	2.5

(Fig. 6.16b). For WT-equ-2 and WT-equ-3, pitch control is deactivated ($v_{eq2} < v_n$ and $v_{eq3} < v_n$) and pitch angle is equal to zero, which activates the deloading control method to create power reserve and participate in frequency control.

The V_{dc} voltages of 3 WT-equs follow their references (1400 V) as shown in Fig. 6.17.

Fig. 6.16 Behaviours of the 3 WT-equs: **a** pitch angle response (degrees) and **b** active power response at the PCC (MW)

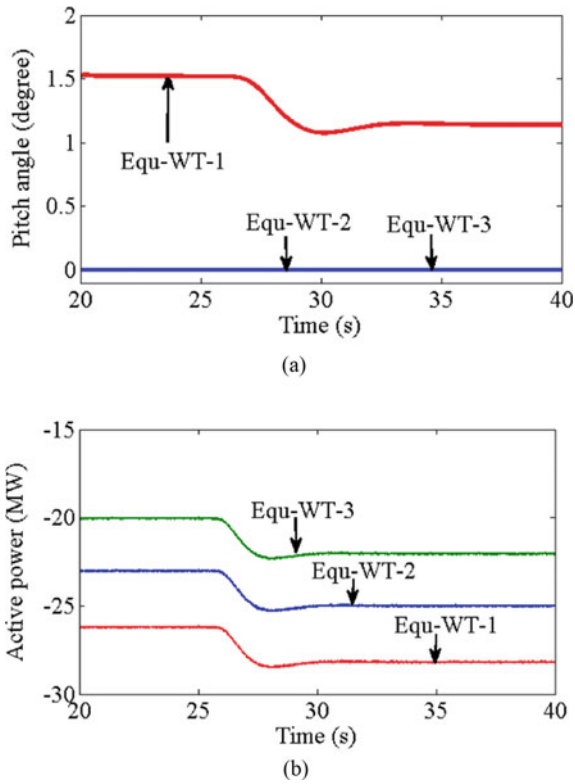
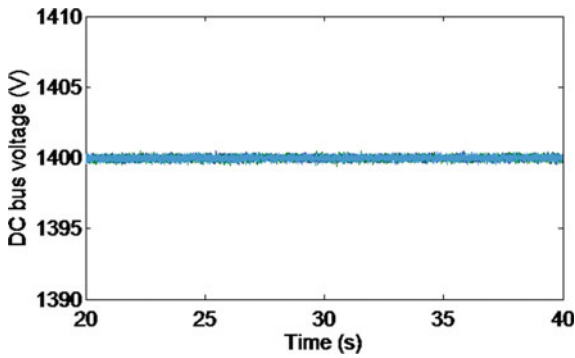


Fig. 6.17 DC bus voltage responses of the three equivalent wind turbines



6.5 Conclusion

In this chapter, a proposed PI-Fuzzy-PI (PIFPI) controller for primary frequency control with inertial power reserve of WF supported by pitch control strategy is developed. The main objective is participating in PFC and ensuring a balance between power demand and production. The WF of 90 MW capacity is aggregated into multi-machine model. It consists of 3 equivalent wind turbines based on squirrel cage induction generator and connected to two grid areas. The comparison with other controllers, shows that the proposed controller provides high performance in terms of:

- Immediate response: low deviation from the nominal value and short stabilization time.
- Meeting grid code requirements: initial activation delay < 2 s and full activation time < 30 s.
- Improved attenuation of power and frequency ripples.

In addition, the obtained results show efficiency of unloaded operation method and effect of activation of pitch control on WTs.

References

1. Duong, M.Q., Francesco, G., Sonia, L., Mussetta, M., Emanuele, O.: Pitch angle control using hybrid controller for all operating regions of SCIG wind turbine system. *Renew. Energy* **70**, 197–203 (2014)
2. Hasanien, H.M., Mahmoud, M.: A fuzzy logic controller for autonomous operation of a voltage source converter-based distributed generation system. *IEEE Trans. Smart Grid* **6**(1), 158–165 (2015)
3. Ikhe, A., Kulkarni, A., Anant, K.: Load frequency control using fuzzy logic controller of two area thermal-thermal power system. *Int. J. Emerg. Technol. Adv. Eng.* **2**(10), 425–428 (2012)
4. Sambariya, D.K., Vivek, N.: Load frequency control using fuzzy logic based controller for multi-area power system. *Br. J. Math. Comput. Sci.* **13**(5), 1–19 (2016)
5. Shengqi, Z., Yateendra, M., Shahidehpour, M.: Fuzzy-logic based frequency controller for wind farms augmented with energy storage systems. *IEEE Trans. Power Syst.* **31**(2), 1595–1603 (2016)
6. Elyalaoui, K., Ouassaid, M., Cherkaoui, M.: Primary frequency control using hierarchal fuzzy logic for a wind farm based on SCIG connected to electrical network. *Sustain. Energy Grids Netw.* **16**, 188–195 (2018)
7. Obaid, Z.A., Cipcigan, L.M., Muhssin, M.T.: Fuzzy hierarchal approach-based optimal frequency control in the Great Britain power system. *Electr. Power Syst. Res.* **141**, 529–537 (2016)
8. Elyalaoui, K., Labbadi, M., Ouassaid, M., Cherkaoui, M.: Optimal fractional order based on fuzzy control scheme for wind farm voltage control with reactive power compensation. *Math. Probl. Eng.* **2021**, Article ID 5559242, 12 pp. (2021). <https://doi.org/10.1155/2021/5559242>
9. Elyalaoui, K., Labbadi, M., Ouassaid, M., Cherkaoui, M.: A continuous nonlinear fractional-order PI controller for primary frequency control application. *Math. Probl. Eng.* **2021** (2021)
10. Elyalaoui, K., Ouassaid, M., Cherkaoui, M.: Dispatching and control of active and reactive power for a wind farm considering fault ride-through with a proposed PI reactive power control. *Renew. Energy Focus* **28**(100), 56–65 (2019)

11. Liu, H., Chen, Z.: Aggregated modelling for wind farms for power system transient stability studies. In: 2012 Asia-Pacific Power and Energy Engineering Conference, IEEE, pp. 1–6 (2012)
12. Al-bayati, A.M.S., Mancilla-David, F., Dominguez-Garcia, J.L.: Aggregated models of wind farms: current methods and future trends. In: North American Power Symposium (NAPS), IEEE, Denver, CO, USA (2016)
13. Fernández, L., García, C., Saenz, J., Jurado, F.: Equivalent models of wind farms by using aggregated wind turbines and equivalent winds. *Energy Convers. Manag.* **50**, 691–704 (2009)
14. Conroy, J., Watson, R.: Aggregate modelling of wind farms containing full-converter wind turbine generators with permanent magnet synchronous machines: transient stability studies. *IET Renew. Power Gener.* **3**(1), 39–52 (2009)
15. Shafiu, A., Anaya-Lara, O., Bathurst, G., Jenkins, N.: Aggregated wind turbine models for power system dynamic studies. *Wind Eng.* **30**(3), 171–186 (2006)
16. Kundur, P.: *Power System Stability and Control*. McGraw-Hill Professional (1994)
17. Bevrani, H.: *Robust Power System Frequency Control, Power Electronics and Power Systems*. Springer International Publishing (2014)
18. Mauricio, J.M., Marano, A., Gomez-Exposito, A., Ramos, J.M.: Frequency regulation contribution through variable-speed wind energy conversion systems. *IEEE Trans. Power Syst.* **24**(1), 173–180 (2009)
19. Morren, J., Haan, S.W.H.d., Kling, W.L., Ferreira, J.A.: Wind turbines emulating inertia and supporting primary frequency control. *IEEE Trans. Power Syst.* **21**(1), 433–434 (2006)

Part II
Modeling, Optimization and Sizing of
Hybrid PV-CSP Plants PV-CSP Hybrid
Plants

Chapter 7

Hybridization PV-CSP: An Overview



7.1 Introduction

Recently, PV-CSP hybridization has received considerable global attention. Indeed, this chapter provides a general overview of hybrid PV-CSP systems.

First of all, the global energy context will be presented to better understand the issues related to the production and the consumption of electrical energy. In this context, renewable energies are shown to be a growing ecological and economic alternative to replace fossil fuels.

Then, the context and the challenges related to the integration of renewable energies resources will be addressed: their intermittent nature is a limiting factor in their development. Hybridization between renewable energy sources and the integration of energy storage systems appear to be relevant solutions for strengthening the integration of renewable energies into mixed electricity supply. Particular interest will be paid to solar energy, which is the most abundant source of energy. Photovoltaic and concentrated solar power are two main technologies that allow better exploitation of solar energy.

Finally, the concept of PV-CSP hybridization as well as the possible types of PV-CSP hybridization will be discussed. A literature review will be also presented, based on the state of art of the hybrid PV-CSP systems.

7.2 Global Energy Context

In the last decade, global energy demand has been growing steadily due to rapid population growth, improved standards of living and industrialisation [1]. In 2020, global energy demand fell by 4%, the largest decline since World War II, due to the impacts of the pandemic on global energy use [1]. Based on first quarter data, projections for 2021 indicate that with the lifting of Covid restrictions and economic recovery, energy demand is expected to rebound by 4.6%, bringing global energy

© The Author(s), under exclusive license to Springer Nature Switzerland AG 2022

129

M. Labbadi et al., *Modeling, Optimization and Intelligent Control Techniques in Renewable Energy Systems*, Studies in Systems, Decision and Control 434, https://doi.org/10.1007/978-3-030-98737-4_7

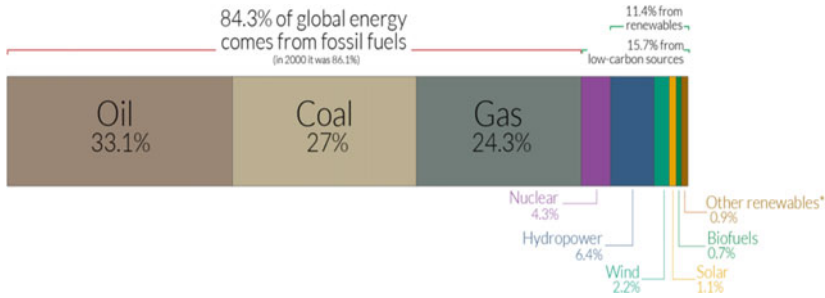


Fig. 7.1 The breakdown of energy demand by source for the year 2020 [1]

consumption in 2021 to 0.5% above pre-Covid-19 levels [1, 2]. According to the International Energy Agency (IEA), global energy demand continues to grow by 2030 [2].

Figure 7.1 shows the breakdown of global energy demand by source for the year 2020. It can be seen that it is mainly supplied by fossil fuels (27% coal, 33.1% oil, and 24.3% natural gas) [1, 2], which contributes to environmental problems linked to climate change due to greenhouse gas emissions, and economic problems linked to the increase in the cost of fossil fuels due to the rapid depletion of their reserves [3, 4].

The world economy is facing a major energy challenge, which involves meeting the growing demand for energy while minimising greenhouse gas emissions [4, 5]. Indeed, an energy transition is needed [4, 5].

Energy resources are consumed in different forms: fuels for transport, thermal comfort and electricity [2]. On a global scale, 17% of fossil energy resources are consumed in the form of electrical energy [2, 6]. Electricity is not a major consumer of these energy resources, yet it is an important energy carrier [7]. This consumption is likely to increase in the future with the development and use of electric vehicles. The IEA forecasts that electricity demand will rise from 23 million GWh in 2018 to 34.5 million GWh in 2040 [8, 9].

According to Fig. 7.2, low carbon technologies exceeded coal as a primary source of electricity generation in 2019 [1]. However, the world's electricity production was still carbon-based (In 2020, 61% was produced by using fossil fuels) [1]. Requiring the implementation of a “low carbon” energy transition. This transition is based on reducing energy demand and developing non-greenhouse gas-emitting electricity production sources [5, 10].

This is how the era of energy transition begins: reducing the use of fossil energy resources and switching to green energy [5].

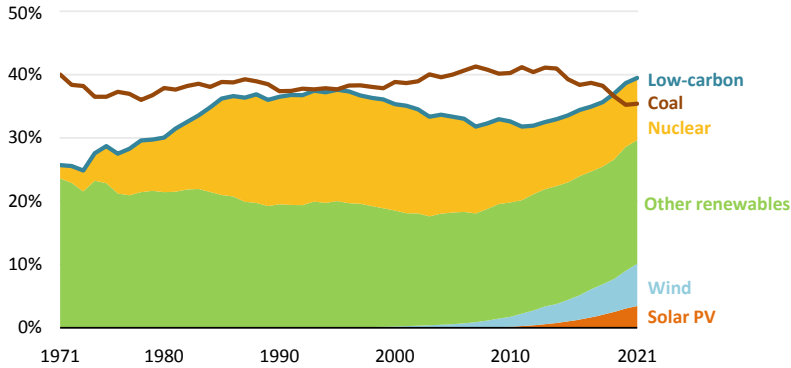


Fig. 7.2 Energy breakdown of world electricity production, 1971–2021 [1]

7.3 Renewable Energies Sources (RES)

7.3.1 *The Context of Integration of Renewable Energies Sources in the Electrical Grid*

Renewable energies (RE) are useful and inexhaustible sources of energy on a human timescale; they are constantly regenerated and recreated [11]. Unlike fossil resources, the current use of RE sources does not limit future availability [11]. The main sources of renewable energy are the sun, wind, rivers, the sea, the earth's heat, and biomass. We then speak of solar, wind, hydraulic, geothermal, marine and biomass energy.

RE sources allow electricity to be produced from a system:

- Grid-connected power system [12]: In such a system, all of the electricity generation will be sold to the distributor or used to supply a load with only the surplus sold.
- Stand-alone power system [13]: all the production will be used to meet the required load. This type of plant is a good alternative in areas not connected to the power grid.

7.3.2 *Issues Related to the Integration of Renewable Energies Sources*

The main challenges of power generation presented by some RE (solar and wind) are [14]:

Non-schedulable: the main rule of an electrical system is that production must always be equal to demand. Some RE sources do not allow this adjustment because their production is not scalable [14].

Intermittent: electricity production varies continuously with weather conditions [14].

Difficult to predict: some RE sources, such as solar and wind, are difficult to predict, as they vary according to location and time of measurement [15].

Not guaranteed: unlike conventional resources (fossil and fissile fuels), the presence of natural resources (sun and wind) cannot be guaranteed. The production profile is difficult to predict [14, 15].

Fluctuating: some RE are subject to variations in production, which makes the electricity grid unstable (fluctuation in production and frequency) [14].

7.3.3 *Proposed Solutions*

The massive integration of RE sources in the energy mix poses challenges. Currently, researchers are interested in finding relevant solutions to overcome these challenges [14].

The use of advanced weather forecasting: Effective forecasting of RE resources (solar and wind) is crucial to increase their penetration rate in the energy mix. Forecasting allows for better prediction of power generation and planning of shut-downs/starts of RE power plants, thus adjusting the supply-demand balance and mitigating grid reliability issues [15]. Advanced forecasting involves exploiting artificial intelligence and Big Data techniques to improve the accuracy of weather forecasts significantly [15–17].

The development and integration of storage systems: the intermittency of RE can only be overcome by integrating storage devices, allowing a quantity of energy to be stored in a form that can be easily reused later [18]. The storage system must be efficient, economical and have adequate autonomy to ensure the continuity of production in a reliable way with a reduced cost [19]. Currently, energy storage can be carried out in different forms: mechanical storage (steps and flywheels), electrochemical storage (batteries), thermal storage (latent heat, sensitive heat and phase change), chemical storage and magnetic storage [20].

For many years, energy storage has been the subject of various research activities. This research work is either part of:

- The experimental component: developing new storage technologies with new processes and materials to improve technical performances (efficiency, durability, autonomy, response time, etc.) [20, 21].
- The modeling and simulation component: optimization and sizing of storage systems for each application, depending on the energy supply context and the size of the energy system [20, 21].

The sustained development of storage systems allows for better integration of RE without jeopardising the electricity grid.

The design of smart grids: these grids require the use of an information system to adjust the flow of electricity between suppliers and consumers, thus ensuring a balance between supply and demand. Smart grids are sized to accommodate new RE installations, allowing for their better management [22, 23]. Many research activities are currently being carried out to advance smart grids, to make them more reliable for today's needs. These research works are particularly focused on the insertion of reliable energy management systems to ensure better communication between the different agents of the electrical grid [24].

Hybridization between different RE sources: Hybridization consists in combining several energy sources of different nature in the same system, coupled with a storage device to improve the quality of the production [25, 26]. This solution is the subject of this chapter and will be detailed in the following sections.

7.4 Solar Energy

In this chapter, particular interest will be paid to solar energy, as it is the most abundant source of energy in the world, inexhaustible and very promising for the production of clean electricity [27].

Harnessing solar energy can produce electricity or heat, depending on the type of solar radiation used and the technology employed. Figure 7.3 illustrates the different solar technologies that can be used to harness the different types of solar radiation and their applications.

Photovoltaics (PV) and concentrated solar power (CSP) are considered as attractive technologies for the use of solar energy to produce electricity.

7.5 Hybrid Energy Systems (HES)

Hybrid energy systems (HES) refer to multi-source energy systems, including at least one RE source [26]. These systems can be stand-alone or grid-connected. The hybrid system that allows only renewable energy sources (RES) to be combined is called a hybrid renewable energy system (HRES) and is usually coupled to a storage device [28]. The objective of using multiple RE technologies in a single system is to incorporate the advantages and best operational characteristics of each technology, as well as, to minimise the use of fossil fuels [26, 28].

PV and CSP are emerging as promising technologies to be combined with other technologies to produce electricity.

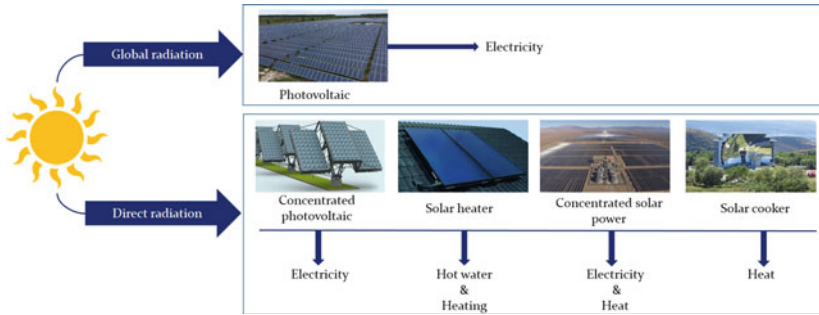


Fig. 7.3 Applications of solar energy

7.5.1 PV Hybrid Systems

7.5.1.1 Hybridization with Wind Power

Regarding ecological and economic development, PV-wind hybridization is very interesting when local conditions are favourable in terms of wind availability and sunshine [29]. Solar and wind energy do not compete with each other due to their different seasonal characteristics. However, they proved to be complementary [26, 29].

PV-Wind systems can be coupled or not to an electrical energy storage system. PV-wind hybrid systems without storage are rarely used, as they do not ensure security of supply [30]. In contrast, PV-wind-battery hybrid systems are shown as an attractive solution for remote locations. In such a hybrid system, the energy produced by the PV or wind system can be used immediately to supply the load or stored in batteries for later use. These installations increase the reliability of the electrical system by meeting the load demand [28–30].

Various research studies have been conducted to develop and evaluate the performance of PV-wind hybrid systems [31]. These research works confirm that using a storage system can improve the performance of these systems and make them more practical [30, 32]. Various optimisation techniques have been applied to define the optimal sizing of such a system according to the load requested and the location of the installation [31].

7.5.1.2 Hybridization with Diesel Generator

The hybridization of PV with fossil fuels has been used mainly to reduce the costs of existing fossil fuel power plants and to reduce greenhouse gas emissions [33].

One example of such hybridization that is currently well studied in various research studies is the hybridization of PV with diesel generators in the presence or absence of an electrical energy storage (EES) system [33, 34]. Diesel generators

are used to meet the electricity needs in many areas not connected to the electricity grid. However, their operating cost is very high [33]. In this context, their hybridization with PV allows high reliability at a low cost of electricity production [34].

7.5.1.3 Hybridization with Wind and Diesel Generator

The use of wind turbines as a complementary agent to PV and diesel generators represents an attractive solution to solar energy intermittency. This type of hybrid systems allows the production of electrical energy during the night in the absence of solar energy at high efficiency [35, 36].

7.5.2 CSP Hybrid Systems

CSP technology offers specific advantages as a RE source, thanks to its ability to integrate a thermal energy storage (TES) system [37].

7.5.2.1 Hybridization with Fossil Fuels

The power block of a CSP plant is similar to that used in conventional power plants, which allows easy hybridization between them [37]. Hybridizing CSP with fossil fuels (coal or natural gas) reduces the overall cost of the hybrid power plant by increasing its technical performance [38]. A research study was conducted in [39]; it indicates that the investment cost of a hybrid CSP-Coal plant is reduced by 28% and the energy production is increased by 25% compared to a CSP plant alone. Another research studies [37–40] confirm that hybrid CSP-fossil fuel systems present an increase in energy efficiency and a reduction in cost of electricity (e.g. CSP-coal 0.05/kWh–0.1/kWh) compared to a CSP plant alone. As well as, the capital cost of the CSP-fossil fuel plant is higher than that of a conventional plant of the same size, due to the high cost of the solar field.

7.5.2.2 Hybridization with Biofuels

Similar to CSP hybridization with fossil fuels, which has shown good synergies. Hybridization of CSP with biofuels has the same advantages (i.e. renewable energy with a fuel to improve flexibility and reliability), but has the potential to provide 100% renewable electrical energy [37, 41].

7.5.2.3 Hybridization with Wind

Wind technology is different from CSP technology. Indeed, the hybridization between them only takes place at the level of the electrical grid. This type of hybridization is the least studied in the literature. Nevertheless, it can satisfy the load demand and contribute to the stability of the power grid [42].

7.6 PV-CSP Hybridization

Hybridization is a solution that could disrupt existing power plants [43]. The types of hybridization already mentioned in the Sects. 7.5.1 and 7.5.2 are relevant solutions for producing electricity. However, hybridization of PV or CSP with fossil fuels does not allow for the generation of 100% renewable energy, as the electricity production still depends on fossil fuels [37]. Also, hybridization of PV with wind requires the availability of a cheaper electrical energy storage device, as the cost of batteries is still high for large-scale applications [37, 43]. In this context and due to the high potential of solar energy, the concept of PV-CSP hybridization has attracted increasing interest in countries with high solar resources [37, 44]. This interest is due to the high decrease in the cost of PV production and the large-scale thermal storage that CSP allows [43, 44].

PV-CSP hybridization allows the competitive advantages of both technologies to be combined. It offers the possibility to develop continuous solar generation at a competitive cost, thus increasing the penetration of solar energy in the energy mix [43, 44].

There are different scenarios for PV-CSP hybridization:

- **The 1st scenario:** (Figure 7.4a) there is a predominance of CSP production. This production is used to produce electricity day and night. The production from PV is negligible compared to that from CSP. In this case, the PV can be used just to power the auxiliaries of the CSP plant. In fact, this is not a true hybridization.
- **The 2nd scenario:** (Figure 7.4b) PV and CSP operate simultaneously during the day, but the CSP continues to operate alone at night, thanks to the energy stored in the storage system.
- **The 3rd scenario:** (Figure 7.4c) All the production from the PV is fed into the grid to meet the demand during the day. The CSP plant stores all the thermal energy produced by the solar array to meet the load during the night.

Hybrid PV-CSP power plants are a hot topic that is now experiencing its first experiments worldwide. Several PV-CSP projects have emerged and others are being developed around the world, particularly in Morocco, Chile and South Africa [43, 45]. The Table 7.1 presents technical informations on PV-CSP projects around the world.

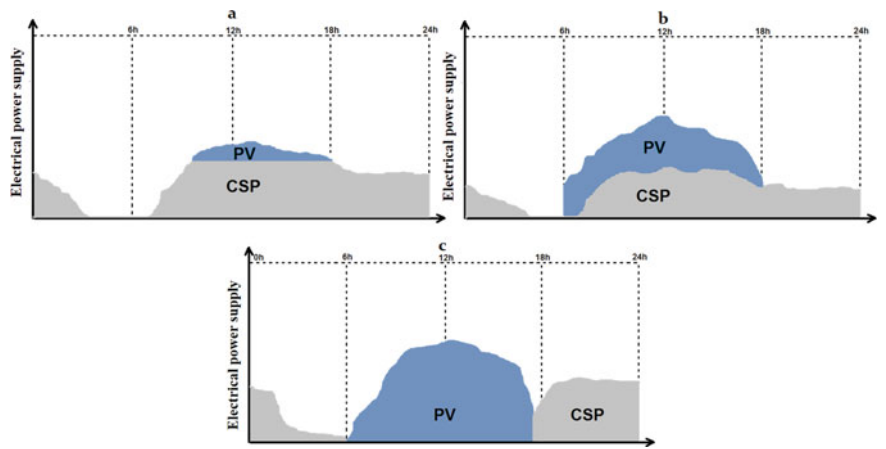


Fig. 7.4 PV-CSP hybridization scenarios

Table 7.1 PV-CSP projects around the world [43, 45–47]

Project	Country	PV installed capacity (MW)	CSP installed capacity (MW)	Storage size (h)	Initial operation
Copiapo	Chili	150	130*2 STP	14	2019
Atacama I	Chili	100	110 STP	17.5	2018
Atacama II	Chili	100	110 STP	15	2018
Redstone&	South	75 + 96	100 STP	12	2019
Lesedi & Jasper	africa				
Noor Midelt I	Morocco	190	210 PTP	5	2022
Noor Midelt II	Morocco	190	210 PTP	5	2022

STP: solar tower plant, PTP: Parabolic-trough plant

7.7 Literature Review on PV-CSP Hybridization

PV-CSP hybridization is a new field of research. Various research studies have been carried out to study the feasibility and confirm the techno-economic performances of PV-CSP hybrid systems for different locations.

The concept of PV-CSP hybridization was introduced by Platzer [48]. His study was based on the combination of a 50 MW PTP with a 12 h of thermal storage and a 75 MW concentrated photovoltaic plant (CPV), in order to extend the operating time of the hybrid plant [48].

In another study [49], platzer investigated a hybrid plant that combines CPV technology with CSP technology based on the use of molten salt Fresnel collectors with direct two-tank thermal storage. The simulation results showed that the capacity

factor can reach 80% for the hybrid plant with a lower energy cost than the CSP plant alone.

The simulation of a hybrid plant that combines a STP (with a capacity of 100 MW and 14 h of thermal storage) with a PV plant (with a capacity of 60 MW) was carried out by Green et al. [50], based on 24-h weather data in Chili. The result indicated that the PV-CSP plant could achieve a capacity factor of around 90%.

Parrado et al. [51], carried out an economic study, based on the calculation of the energy cost until 2050 for solar power plants of the same installed capacity (50 MW): a PV plant, a CSP plant with 15 h of thermal storage, and a PV (20 MW)-CSP (30 MW) hybrid plant with 15 h of thermal storage. The study was conducted using Chilean weather data. The results confirmed the economic profitability of the PV-CSP plant compared to the non-hybridized PV and CSP plant.

Cocco et al. [52] studied a PV-CSP plant (a PTP coupled to a TES system combined with a CPV plant coupled to a battery storage) through the application of two dispatching strategies to satisfy a baseload, using weather data from Ottana (Italy). The first strategy consisted of operating the CSP and CPV system in synergy to provide the requested power. While for the second strategy, the two systems operated independently to meet the required load. The results indicated that the application of the first strategy in the hybrid plant led to better technical performances, both in terms of annual energy production and operating time.

For the two sites of Ouarzazate (Morocco) and Ottana (Italy), the hybridization of a PV (coupled with batteries)—CSP (linear Fresnel reflectors operating with an organic Rankine cycle (ORC)) plant have been studied by Petrollese et al. [53]. The simulation results showed that the hybrid plant could operate for more than 16 h satisfying the load demand, as well as, the sizing of the hybrid plant was highly dependent on the available solar resources; the solar field required less solar collectors and PV modules for the city of Ouarzazate, due to its high solar potential.

Based on meteorological data from the north of Chili, Starke et al. [45] present a techno-economic study of two PV-CSP hybrid plants with two different solar fields (PTC and STP). The simulations were carried out using the TRNSYS (Transient System Simulation Program) software. The simulation results of the PV-CSP hybrid plants were compared with a CSP plant alone, resulting in a reduction of the solar array size by 30–40% and the energy cost by 1.5–7%, while ensuring a capacity factor of over 80%.

Pan and Dinter [54] carried out a technical study based on a STP (100 MW) coupled with a TES system and combined with a PV plant (100 MW), with the objective of meeting a baseload (100 MW) in South Africa. The simulation results indicate that the hybrid plant satisfies 90% of the load with a solar multiple of 2.5 and a storage capacity of 16 h, in contrast to a CSP plant which achieves it with a solar multiple of 3.5 and a storage capacity of 18 h. This confirms the excellent technical performances of the PV-CSP plants.

Zurita et al. [55] carried out a parametric study concerning installed PV capacity, battery capacity, solar multiple and thermal storage capacity, in order to determine the optimal configuration of the PV-CSP plant with minimal cost. The results indicate that the current costs of batteries make their integration into a PV-CSP plant

uneconomical, requiring a reduction in their price from 60 to 90% of the current cost. Thus, for a given battery size, the PV-CSP plant equipped with a single-axis solar tracker for the PV plant requires only a small installed PV capacity compared to a PV-CSP plant with fixed PV modules.

All These research studies has shown that PV-CSP hybrid plants are more efficient than PV or CSP plants alone, both technically and economically [45–55].

The optimisation of hybrid power plants using advanced optimisation algorithms is a current topic. In the literature, various research works address the problem of hybrid power plant CSP optimization. However, the optimisation of hybrid PV-CSP plants is at an early stage.

The optimisation of hybrid PV-CSP systems involves the application of optimisation algorithms, to find an optimal solution(s) to minimisation or maximisation problems. Some researchers have focused on single-objective or multi-objective optimisation of PV-CSP systems using some bio-inspired algorithms.

Zhai et al. [56] developed a single-objective optimisation based on genetic algorithm (GA) for a PV-CSP hybrid plant. The objective was to minimise the leveled cost of electricity (LCOE), considering as decision variables the PV installed capacity, the battery capacity and the TES system capacity. The optimisation was carried out by integrating a dispatching strategy to manage the energy flow in the hybrid plant. The results showed that the integration of the CSP plant into the hybrid system stabilised its production.

In another study [57], the PV-CSP system was optimised into two dispatching strategies by applying a hybrid optimisation algorithm (GA-PSO). The PV capacity and the size of the thermal storage system were the decision variables to be searched for, in order to achieve a minimum cost.

In a study by Wang et al. [58], the parameters of PV-CSP system were carefully optimised using an artificial fish swarm algorithm to achieve a minimum LCOE. The results proved the effectiveness of the optimisation algorithm and the cost-effectiveness of PV-CSP installations.

Another study focused on the multi-objective optimisation approach, Stark et al. [59], developed a multi-objective optimisation of a PV-CSP plant, using the genetic algorithm (GA). The optimisation approach was designed to minimise the LCOE, minimise the initial investment and maximise the capacity factor. The study showed a trade-off between the three objective functions and demonstrated that with hybridization, the initial investment cost and LCOE are minimised, as well as, the capacity factor is improved.

The research works mentioned in this section focus on the feasibility, technical performance and economic profitability of PV-CSP systems. However, this area of research is at an early stage of development. It is expected that this hybridization will be further researched, using other optimization algorithms, and that hybrid PV-CSP plants will soon be implemented in other regions where solar radiation and weather conditions are favourable.

7.8 Conclusion

In this chapter, the energy context related to electricity production was presented, which raised the need for energy transition in this sector. The latter involves increasing the rate of integration of renewable energies into the energy mix. Among the existing renewable energy sources, solar energy is the most abundant source on earth and its better exploitation allows a revolution in the field of electricity production.

PV and CSP are presented as the main technologies for the valorisation of solar energy. as well as, the hybridization between them seems to be an attractive solution to increase the share of solar energy penetration in the energy mix.

The last part of the chapter was devoted to presenting the concept of the PV-CSP hybridization, as well as, a literature review was conducted on the different works related to the technico-economic feasibility and optimization of hybrid PV-CSP plants.

The PV-CSP hybridization is the subject of the next chapters, for its proper elaboration; a detailed modeling of PV-CSP plants is necessary, hence the main objective of the next chapter.

References

1. IEA: Global energy review 2021, IEA, Paris (2021). <https://www.iea.org/reports/global-energy-review-2021>
2. IEA: Key World Energy Statistics 2020, IEA, Paris (2020). <https://www.iea.org/reports/key-world-energy-statistics-2020>
3. Awan, A.B., Zubair, M., Praveen, R.P., Bhatti, A.R.: Design and comparative analysis of photovoltaic and parabolic trough based CSP plants. *Solar Energy* **183**, 551–565 (2019)
4. Zhao, N., You, F.: Can renewable generation, energy storage and energy efficient technologies enable carbon neutral energy transition. *Appl. Energy* **279**, 115889 (2020)
5. Neofytou, H., Nikas, A., Doukas, H.: Sustainable energy transition readiness: a multicriteria assessment index. *Renew. Sustain. Energy Rev.* **131**, 109988 (2020)
6. IEA: Electricity Information: Overview, IEA, Paris (2020). <https://www.iea.org/reports/electricity-information-overview>
7. Liu, Z.: *Global Energy Interconnection*. Academic Press (2015)
8. Cozzi, L.: Global energy perspectives to 2040: the International Energy Agency's scenarios. *Futuribles* **5**, 49–67, 109988 (2020)
9. IEA: World Energy Outlook 2019, IEA, Paris(2019). <https://www.iea.org/reports/world-energy-outlook-2019>
10. Ram, M., Aghahosseini, A., Breyer, C.: Job creation during the global energy transition towards 100% renewable power system by 2050. *Technol. Forecast. Soc. Change* **151**, 119682 (2020)
11. Gielen, D., Boshell, F., Saygin, D., Bazilian, M.D., Wagner, N., Gorini, R.: The role of renewable energy in the global energy transformation. *Energy Strat. Rev.* **24**, 38–50, 119682 (2019)
12. Thopil, M.S., Bansal, R.C., Zhang, L., Sharma, G.: A review of grid connected distributed generation using renewable energy sources in South Africa. *Energy Strat. Revi* **21**, 88–97, 119682 (2018)
13. Abdmouleh, Z., Gastli, A., Ben-Brahim, L., Haouari, M., Al-Emadi, N.A.: Review of optimization techniques applied for the integration of distributed generation from renewable energy sources. *Renew. Energy* **113**, 266–280, 119682 (2017)

14. Sinsel, S.R., Riemke, R.L., Hoffmann, V.H.: Challenges and solution technologies for the integration of variable renewable energy sources—A review. *Renew. Energy* **145**, 2271–2285 (2020)
15. Alkhayat, G., Mehmood, R.: A review and taxonomy of wind and solar energy forecasting methods based on deep learning. *Energy A* **I**, 100060 (2021)
16. Ahmed, R., Sreeram, V., Mishra, Y., Arif, M.D.: A review and evaluation of the state-of-the-art in PV solar power forecasting: techniques and optimization. *Renew. Sustain. Energy Rev.* **124**, 109792 (2020)
17. Wang, H., Lei, Z., Zhang, X., Zhou, B., Peng, J.: A review of deep learning for renewable energy forecasting. *Energy Convers. Manag.* **198**, 111799 (2019)
18. Cho, J., Jeong, S., Kim, Y.: Commercial and research battery technologies for electrical energy storage applications. *Prog. Energy Combust. Sci.* **48**, 84–101, 111799 (2015)
19. Akbari, H., Browne, M.C., Ortega, A., Huang, M.J., Hewitt, N.J., Norton, B., McCormack, S.J.: Efficient energy storage technologies for photovoltaic systems. *Solar Energy* **192**, 144–168 (2019)
20. Rahman, M.M., Oni, A.O., Gemechu, E., Kumar, A.: Assessment of energy storage technologies: a review. *Energy Convers. Manag.* **223**, 113295 (2020)
21. Koohi-Fayegh, S., Rosen, M.A.: A review of energy storage types, applications and recent developments. *J. Energy Storage* **27**, 101047 (2020)
22. Sahbani, S., Mahmoudi, H., Hasnaoui, A., Kchikach, M.: Development prospect of smart grid in Morocco. *Procedia Comput. Sci.* **83**, 1313–1320, 101047 (2016)
23. Azaroual, M., Ouassaid, M., Maaroufi, M.: Optimal control for energy dispatch of a smart grid tied PV-wind-battery hybrid power system. In: 2019 Third International Conference on Intelligent Computing in Data Sciences (ICDS), pp. 1–7. IEEE, Oct. 2019
24. Ourahou, M., Ayir, W., Hassouni, B.E., Haddi, A.: Review on smart grid control and reliability in presence of renewable energies: challenges and prospects. *Math. Comput. Simul.* **167**, 19–31, 101047 (2020)
25. Belgana, S., Dabib, A., Bilil, H., Maaroufi, M.: Hybrid renewable energy system design using multiojective optimization. In: 2013 International Conference on Renewable Energy Research and Applications (ICRERA), pp. 955–960. IEEE, Oct. 2013
26. Ahouar, W., Boussemamti, L., Labbadi, M., Lakrit, S., Cherkaoui, M.: Sizing Optimization of Grid-Connected Hybrid PV-Wind Energy Systems: State of Art Review and Perspectives (2021)
27. Duffie, J.A., Beckman, W.A.: *Solar Engineering of Thermal Processes*. Wiley (2013)
28. Mahesh, A., Sandhu, K.S.: Hybrid wind/photovoltaic energy system developments: critical review and findings. *Renew. Sustain. Energy Rev.* **52**, 1135–1147, 101047 (2015)
29. Belmili, H., Haddadi, M., Bacha, S., Almi, M.F., Bendib, B.: Sizing stand-alone photovoltaic-wind hybrid system: techno-economic analysis and optimization. *Renew. Sustain. Energy Rev.* **30**, 821–832, 101047 (2014)
30. Anoune, K., Ghazi, M., Bouya, M., Laknizi, A., Ghazouani, M., Abdellah, A.B., Astito, A.: Optimization and techno-economic analysis of photovoltaic-wind-battery based hybrid system. *J. Energy Storage* **32**, 101878 (2020)
31. Lian, J., Zhang, Y., Ma, C., Yang, Y., Chaima, E.: A review on recent sizing methodologies of hybrid renewable energy systems. *Energy Convers. Manag.* **199**, 112027 (2019)
32. Mazzeo, D., Oliveti, G., Baglivo, C., Congedo, P.M.: Energy reliability-constrained method for the multi-objective optimization of a photovoltaic-wind hybrid system with battery storage. *Energy* **156**, 688–708 (2018)
33. Mohammed, A., Pasupuleti, J., Khatib, T., Elmenreich, W.: A review of process and operational system control of hybrid photovoltaic/diesel generator systems. *Renew. Sustain. Energy Rev.* **44**, 436–446, 112027 (2015)
34. Jännir, E.D.F.M., Răijther, R.: The influence of the solar radiation database and the photovoltaic simulator on the sizing and economics of photovoltaic-diesel generators. *Energy Convers. Manag.* **210**, 112737 (2020)

35. Bukar, A.L., Tan, C.W., Lau, K.Y.: Optimal sizing of an autonomous photo-voltaic/wind/battery/diesel generator microgrid using grasshopper optimization algorithm. *Solar Energy* **188**, 685–696 (2019)
36. Nsafon, B.E.K., Owolabi, A.B., Butu, H.M., Roh, J.W., Suh, D., Huh, J.S.: Optimization and sustainability analysis of PV/wind/diesel hybrid energy system for decentralized energy generation. *Energy Strat. Rev.* **32**, 100570 (2020)
37. Powell, K.M., Rashid, K., Ellingwood, K., Tuttle, J., Iverson, B.D.: Hybrid concentrated solar thermal power systems: a review. *Renew. Sustain. Energy Rev.* **80**, 215–237, 100570 (2017)
38. Rashid, K., Mohammadi, K., Powell, K.: Dynamic simulation and techno-economic analysis of a concentrated solar power (CSP) plant hybridized with both thermal energy storage and natural gas. *J. Clean. Prod.* **248**, 119193 (2020)
39. Pierce, W., Gauchál', P., von BackstrÄm, T., Brent, A.C., Tadros, A.: A comparison of solar aided power generation (SAPG) and stand-alone concentrating solar power (CSP): a South African case study. *Appl. Therm. Eng.* **61**(2), 657–662, 119193 (2013)
40. Chitakure, M., Ruziwa, W.R., Musadamba, D.: Optimization of hybridization configurations for concentrating solar power systems and coal-fired power plants: a review. *Renew. Energy Focus* **35**, 41–55, 119193 (2020)
41. DomÄnguez, R., Conejo, A.J., CarriÄn, M.: Operation of a fully renewable electric energy system with CSP plants. *Appl. Energy* **119**, 417–430 (2014)
42. Ding, Z., Hou, H., Yu, G., Hu, E., Duan, L., Zhao, J.: Performance analysis of a wind-solar hybrid power generation system. *Energy Convers. Manag.* **181**, 223–234, 119193 (2019)
43. Ju, X., Xu, C., Hu, Y., Han, X., Wei, G., Du, X.: A review on the development of photo-voltaic/concentrated solar power (PV-CSP) hybrid systems. *Solar Energy Mater. Solar Cells* **161**, 305–327, 119193 (2017)
44. Valenzuela, C., Mata-Torres, C., Cardemil, J.M., Escobar, R.A.: CSP+ PV hybrid solar plants for power and water cogeneration in northern Chile. *Solar Energy* **157**, 713–726 (2017)
45. Starke, A.R., Cardemil, J.M., Escobar, R.A., Colle, S.: Assessing the performance of hybrid CSP+ PV plants in northern Chile. *Solar Energy* **138**, 88–97 (2016)
46. Ju, X., Xu, C., Han, X., Zhang, H., Wei, G., Chen, L.: Recent advances in the PV-CSP hybrid solar power technology. In: *AIP Conference Proceedings*, vol. 1850, No. 1, p. 110006. AIP Publishing LLC, June 2017
47. MASEN: <https://www.masen.ma/fr/actualites-masen/noor-midelt-i-le-maroc-construit-une-centrale-solaire-hybride-hors-norme>
48. Platzer, W.: PVÄenhanced solar thermal power. *Energy Procedia* **57**, 477–486 (2014)
49. Platzer, W.J.: Combined solar thermal and photovoltaic power plantsÄan approach to 24h solar electricity. In: *AIP Conference Proceedings*, vol. 1734, No. 1, p. 070026. AIP Publishing LLC, May 2016
50. Green, A., Diep, C., Dunn, R., Dent, J.: High capacity factor CSP-PV hybrid systems. *Energy Procedia* **69**, 2049–2059 (2015)
51. Parrado, C., Girard, A., Simon, F., Fuentealba, E.: 2050 LCOE (Levelized Cost of Energy) projection for a hybrid PV (photovoltaic)-CSP (concentrated solar power) plant in the Atacama Desert, Chile. *Energy* **94**, 422–430 (2016)
52. Cocco, D., Migliari, L., Petrollese, M.: A hybrid CSPÄSCP system for improving the dispatchability of solar power plants. *Energy Convers. Manag.* **114**, 312–323, 100570 (2016)
53. Petrollese, M., Cocco, D.: Optimal design of a hybrid CSP-PV plant for achieving the full dispatchability of solar energy power plants. *Solar Energy* **137**, 477–489 (2016)
54. Pan, C.A., Dinter, F.: Combination of PV and central receiver CSP plants for base load power generation in South Africa. *Solar Energy* **146**, 379–388 (2017)
55. Zurita, A., Mata-Torres, C., Valenzuela, C., Felbol, C., Cardemil, J.M., GuzmÄn, A. M., Escobar, R.A.: Techno-economic evaluation of a hybrid CSP+ PV plant integrated with thermal energy storage and a large-scale battery energy storage system for base generation. *Solar Energy* **173**, 1262–1277 (2018)
56. Zhai, R., Chen, Y., Liu, H., Wu, H., Yang, Y.: Optimal design method of a hybrid CSP-PV plant based on genetic algorithm considering the operation strategy. *Int. J. Photoenergy* (2018)

57. Liu, H., Zhai, R., Fu, J., Wang, Y., Yang, Y.: Optimization study of thermal-storage PV-CSP integrated system based on GA-PSO algorithm. *Solar Energy* **184**, 391–409, 100570 (2019)
58. Wang, X., Wang, Y., Chen, K., Bin, X., Zhou, Z., Peng, H.: Global optimization of CSP-PV Hybrid System using an Artificial Fish-Swarm Algorithm. In: 2019 Chinese Automation Congress (CAC), pp. 5618–5622. IEEE, Nov. 2019
59. Starke, A.R., Cardemil, J.M., Escobar, R., Colle, S.: Multi-objective optimization of hybrid CSP+ PV system using genetic algorithm. *Energy* **147**, 490–503 (2018)

Chapter 8

Detailed Modeling of Hybrid PV-CSP Plant



8.1 Introduction

This chapter presents the modeling of a hybrid PV-CSP system. The proposed model is very useful for simulation of a PV-CSP system in order to supply any requested load. The methodology followed in this chapter consists of combining PV and CSP models, to get a global model of the PV-CSP plant. The PV and CSP mathematical models were established in order to evaluate the power production from each plant using a 1-h time step for a year. The PV plant produces electrical power, whereas the CSP field generates thermal power. To handle these two forms of power with high efficiency, a dispatch strategy is required to be established.

8.2 Solar Position

At a given point above Earth's surface, the amount of solar radiation that reaches the Earth's surface varies according to: the geographic location, the season, the time of day, the solar position and the orientation of the receiving surface [1, 2]. The solar position is expressed as a function of the equatorial coordinates (the solar declination (δ_s), the hour angle (ω_s)) and the horizontal coordinates (the solar altitude (α_s) and the solar azimuth (γ_s)).

The calculation of sun's position is strongly dependent on the earth's geographic coordinates and it is involved in several astronomical and energy calculation processes. For any application of solar energy, a good estimate of the solar position is necessary for carrying out a simulation of a photovoltaic system or a concentrated solar power system [1].

Geographic Coordinate System

The geographic coordinate system is used to determine the position of a location on the Earth's surface. Any location can be referenced by the longitude and the latitude.

Latitude (φ_s) is the angle between the equatorial plane and the straight line that passes through the point of location and through the center of the Earth. Locations of northern hemisphere have positive latitudes that range from 0° to $+90^\circ$, while locations of western hemisphere have negative latitudes that range from 0° to -90° degrees.

Longitude (λ_s) is the angular distance from the prime meridian to another meridian that passes through a point on the Earth's surface. It varies from -180° to 180° . By convention, a sign (+) is assigned to eastern longitudes, and a sign (−) for western longitudes.

Solar Declination (δ_s)

The solar declination is the angle between the lines joining the center of the Earth to the center of the Sun and its projection on the Earth's equatorial plane. Declination angle changes seasonally due to the inclination of Earth's polar axis and the Earth's rotation about its axis of rotation and around the Sun [3]. It varies over the course of the year, from -23.5° to $+23.5^\circ$. Declination angle can be calculated by the following Eq. (8.1) [4].

$$\delta_s = \sin^{-1} \left[0.398 \sin \left(\frac{360}{365} (d - 82) + 2 \sin \frac{360}{365} (d - 2) \right) \right] \quad (8.1)$$

Where d is the number of the day in the year, for example 1 January = 1, 20 February = 51, and so on.

The variation of the solar declination throughout the year is illustrated in the Fig. 8.1. This angle value is null at the vernal and the fall equinox, (March 21 and September 21), maximal at the summer solstice (June 21) and minimal at the winter solstice (December 21).

Equation of Time (E_{time})

The equation of time is an empirical formula that accounts for the eccentricity of the Earth's orbit, as well as, its axial tilt. It is expressed in minutes and can be calculated approximately for any day (d) by the Eq. (8.2).

$$E_{time} = 9.87 \sin \left(2 \frac{360}{365} (d - 81) \right) - 7.53 \cos \left(\frac{360}{365} (d - 81) \right) - 1.5 \sin \left(\frac{360}{365} (d - 81) \right) \quad (8.2)$$

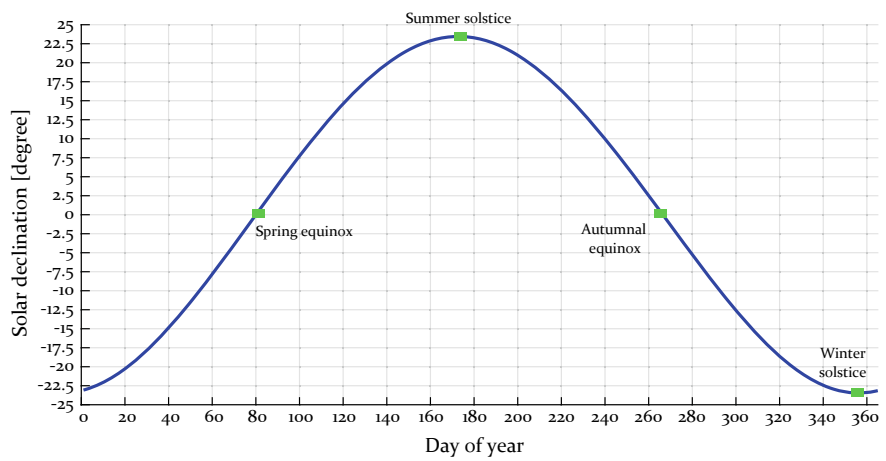


Fig. 8.1 The annual variation of the solar declination (δ_s)

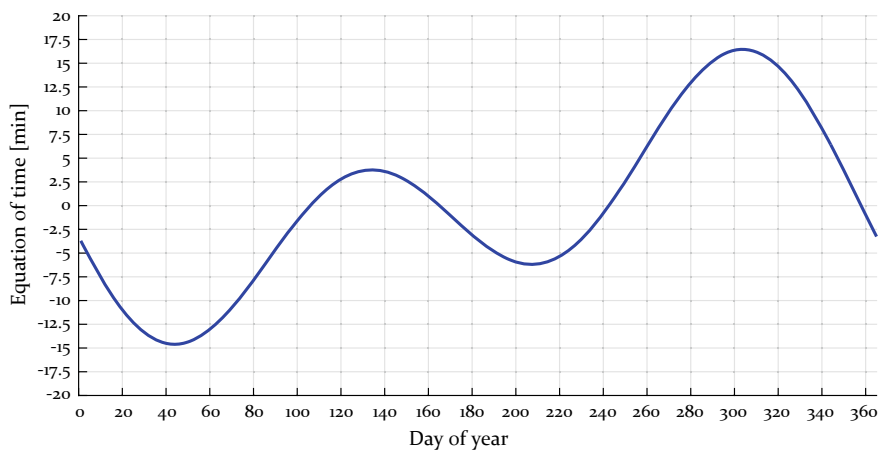


Fig. 8.2 The annual variation of the equation of time (E_{time})

The annual variation of the equation of time is shown in Fig. 8.2.

Hour Angle (ω_s)

The hour angle is the angular distance from the plane of the sun’s direction to the local meridian. Conventionally, the hour angle is zero degree at solar noon, negative before noon and positive after noon. The following Eq. (8.3) can be used to calculate the hour angle in degrees [5, 6].

$$\omega_s = 15 \left(hr + \frac{E_{time}}{60} + \frac{\lambda_s}{15} - T_z - 12 \right) \quad (8.3)$$

Where, hr is the hour and T_z is the time zone.

Solar Altitude (α_s)

Solar altitude refers to the angle formed between the direction of the Sun and the horizontal plane passing through the observation point. Its value varies based on geographic position and time of day. The complement of α_s is the zenith angle (θ_z), it is measured from the vertical direction and the sun's rays ($\alpha_s + \theta_z = 90^\circ$).

Solar altitude varies in range of -90° to $+90^\circ$. It is zero at the sunrise and the sunset, positive in the day and negative in the night. The following Eq. (8.4) can be used to calculate solar altitude [7].

$$\alpha_s = \sin^{-1} \left(\sin(\delta_s) \sin(\varphi_s) + \cos(\delta_s) \cos(\varphi_s) \cos(\omega_s) \right) \quad (8.4)$$

Solar Azimuth (γ_s)

The solar azimuth is the angle formed between the projection of the sun's center onto the horizontal surface and due south direction. It can be calculated as follows in Eq. (8.5) [7].

$$\gamma_s = \cos^{-1} \left(\frac{\sin(\delta_s) \cos(\varphi_s) - \cos(\delta_s) \sin(\varphi_s) \cos(\omega_s)}{\cos(\alpha_s)} \right) \quad (8.5)$$

By performing the following correction:

$$\gamma = \begin{cases} \gamma_s & \text{if } LST < 12 \text{ ou } \omega_s < 0 \\ 360 - \gamma_s & \text{if } LST > 12 \text{ ou } \omega_s > 0 \end{cases} \quad (8.6)$$

Where, LST is the local standard time.

8.3 PV Model

The PV model is mainly sub-divided into two blocks: the PV field and the inverter. The simulation of a PV model requires the development of a detailed mathematical model for each block. Indeed, in the following, the PV models is developed as displayed in Fig. 8.3.

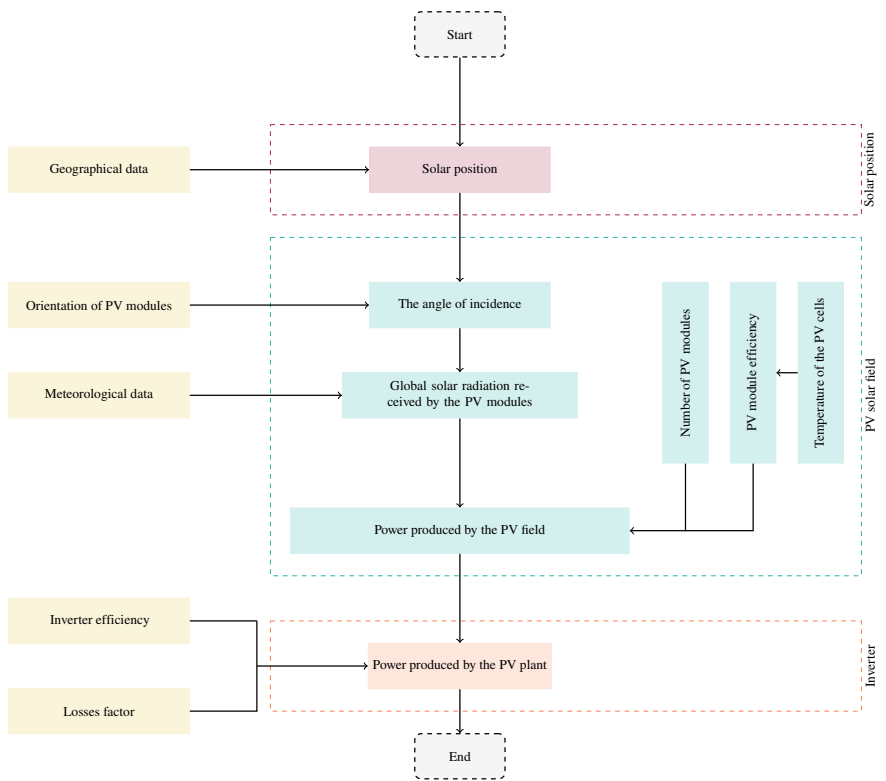


Fig. 8.3 Model of the PV plant

The PV Field

The solar field of a photovoltaic power plant includes a large number of PV modules installed in rows and connected to each other. They capture sunlight and convert it into usable electrical energy using the photo-effect. The performance of the PV system must be as efficiently as possible, its sunlight collection efficiency can be increased by optimizing the orientation of the PV modules. The PV modules orientation can be considered as fixed or variable, when it depends on the sun tracking system (1 axis or 2 axes) [8, 9].

Calculate the Angle of Incidence

The PV module is typically positioned in a direction (Azimuth angle (γ)) and inclination (Tilt angle (i)). An optimal azimuth and tilt setting is important for increasing the annual energy production of a photovoltaic system [8, 9]

For a fixed orientation: the tilt and orientation angle must be set to optimal values (Eq. (8.7)) [10].

$$\begin{cases} i = i_0 \\ \gamma = \gamma_0 \end{cases} \quad (8.7)$$

For a single-axis tracking system: the tilt angle is set to an optimal value while the azimuth angle follows the solar azimuth angle (γ_s) (Eq. (8.8)) [10].

$$\begin{cases} i = i_0 \\ \gamma = \gamma_s \end{cases} \quad (8.8)$$

For a dual-axis tracking system: the tilt angle follows the zenith angle (θ_z) and the azimuth angle follows the solar azimuth angle (γ_s) (Eq. (8.9)) [10].

$$\begin{cases} i = \theta_z \\ \gamma = \gamma_s \end{cases} \quad (8.9)$$

The PV module collects sunlight most efficiently when the sun's rays are always perpendicular to it. Indeed, positioning the PV modules in an optimal orientation will optimize incidence angle at which the PV module receives maximum solar radiation [8, 10]. The incidence angle of a PV module is calculated as shown in Eq. (8.10)) [10].

$$\theta_{PV} = \cos^{-1}(\sin(\alpha_s) \cos(i) - \cos(\alpha_s) \sin(i) \cos(\gamma_s - \gamma)) \quad (8.10)$$

The calculation of the incidence angle is important to estimate the amount of solar radiation incident on the surface of PV panels regardless of their orientation [8].

Estimate the Global Solar Radiation Received by the PV Modules

Solar radiation data has a direct effect on the efficiency of solar power systems. Accurate information of solar radiation data in a particular geographic area is indispensable for the design, the optimization, the investment identification, the projection, the planning and the continuity of solar energy utilization technologies [11–13].

Practical measures of solar radiation are the most accurate data but they are not always available, which is mainly due to the initial investment and maintenance cost of the measuring instruments and corresponding recorders. Therefore, the estimation of solar radiation at the Earth's surface using satellite data is an alternative technique to obtain solar radiation data, when no local measurement record exists [11–13].

Models for estimating solar radiation can be categorized according to different criteria. For instance, type of solar radiation (global, diffuse, direct, or reflected), model input data (meteorological, climatological, or other data), time scale (annual, monthly, daily or hourly), spatial coverage (site-dependent or global

model), approach (physical, semi-physical or empirical), surface tilt (horizontal or sloped surfaces) and sky type (all sky conditions, clear or cloudy sky) [11–14]

The global solar radiation intercepted by an inclined surface (global tilted irradiance (G_{tilted})) is the sum of direct (B_{tilted}), diffuse (D_{tilted}) and reflected (R_{tilted}) irradiation intercepted by the surface (Eq. (8.11)) [10].

$$G_{tilted} = B_{tilted} + D_{tilted} + R_{tilted} \quad (8.11)$$

The estimation of global tilted irradiation can be done at hourly, daily or monthly scale; many models have been proposed and developed according to this viewpoint [14, 15]. Some of these models are mathematical formulas, which are called empirical models, and others are based on artificial intelligence techniques. The estimation of the global tilted irradiation at hourly scale allows recording the detailed change of solar radiation in a day [14, 15].

The direct solar irradiance intercepted by an inclined surface is calculated as follows in Eq. (8.12) [14].

$$B_{tilted} = B_n \cos(\theta_{PV}) \quad (8.12)$$

Where, B_n is the direct normal irradiance.

The reflected radiation is obtained as follows in Eq. (8.13) [16].

$$R_{tilted} = \frac{1 - \cos(i)}{2} \rho G_h \quad (8.13)$$

Where, G_h is the global irradiance on horizontal plane and ρ is the Albedo (The ratio of the reflected incident radiation to the total incident radiation).

Most of solar radiation models cited in the literature estimate the tilted direct and reflected radiation using the same mathematical expressions given in Eqs. (8.12) and (8.13). However, the estimation of the diffuse tilted irradiation differs from one model to another.

The estimation of the solar diffuse radiation involves three components: the diffuse circumference, isotopic and horizon. Indeed, there are many models developed recently to calculate the diffuse radiation, the difference between them consists in the way they develop or neglect one of the components of this radiation [17, 18].

For our proposed model, the solar diffuse irradiance is calculated using the HDKR model [17] that is among the most cited models in the literature [19]. As well as, it can be used for all sky types, different geographical locations and different surface orientations [17, 19].

The diffuse radiation is obtained as follows in Eq. (8.14) [17].

$$D_{tilted} = D_h \left((1 - A_i) \frac{1 + \cos(i)}{2} (1 + f_s) + A_i \frac{\cos(\theta_{PV})}{\sin(\alpha_s)} \right) \quad (8.14)$$

Where: D_h is the diffuse irradiance on horizontal plane.

A_i is the anisotropy index, which is calculated according to the Eq. (8.15)) by introducing the extraterrestrial solar radiation ($I_{radiation}$).

$$A_i = \frac{B_n}{I_{radiation}} \quad (8.15)$$

$$I_{radiation} = 1367(1,00011 + 0,034221 \cos(\frac{2\pi j}{365}) + 0,00128 \sin(\frac{2\pi j}{365}) + 0,000719 \cos(\frac{4\pi j}{365}) + 0,000077 \sin(\frac{4\pi j}{365})) \quad (8.16)$$

f and s are two correction factors, calculated by Eqs. (8.17)) and (8.18)) respectively.

$$f = \sqrt{\frac{B_n \sin(\alpha_s)}{G_h}} \quad (8.17)$$

$$s = (\sin(\frac{i}{2}))^3 \quad (8.18)$$

Estimate the DC Power Produced by the Photovoltaic Field

The power output generated by solar PV field P_{DC} is deeply related to the geographical location of the plant, the solar irradiation received, the orientation and the efficiency of the PV modules, as well as, the type of material and the temperature of the solar cells. It is obtained as follows in Eq. (8.19) [20, 21]

$$P_{DC} = G_{tilted} \eta_{module} N_{module} A_{ref} \quad (8.19)$$

Where, A_{ref} is the area of PV module, N_{module} is the number of module in the PV field and η_{module} is PV module efficiency, which is calculated using the following Eq. (8.20) [20, 21].

$$\eta_{module} = \eta_{module,ref} (1 + \gamma_f (T_c - T_{module,ref})) \quad (8.20)$$

Where, $T_{module,ref}$ and $\eta_{module,ref}$ are the PV module temperature and the PV module efficiency under standard test conditions, respectively. And thus, γ_f is the power temperature coefficient and T_c is the PV cell temperature, which can be calculated as shown in Eq. (8.21) [20, 21].

$$T_c = T_{amb} \left(\frac{G_{tilted}}{G_{noct,ref}} \right) (T_{noct} - T_{noct,ref}) \left(1 - \frac{\eta_{module,ref}}{\tau \alpha} \right) \left(\frac{U l_{noct}}{5.7 + 3.8 V_{wind}} \right) \quad (8.21)$$

Where, T_{amb} is the ambient temperature, $G_{noct,ref}$ and $T_{noct,ref}$ is the nominal solar irradiance under operating conditions (NOCT conditions), V_{wind} is the wind velocity, U_{noct} is the heat transfer coefficients at NOCT conditions and $\tau\alpha$ is the transmittance-absorptance coefficient.

The Inverter

The inverter is the main element in a PV system; it converts the direct current (DC) to alternating current (AC) and feeds this into the electrical grid. PV inverter losses have reduced over time, and their efficiency can exceed 97%, or even higher for central inverters, which is a benefit to PV systems.

Estimate the Electrical Power Produced by the PV System

The output power of a PV system $P^{el,pv}$ can be calculated using Eq. (8.22) [21]. This power produced is strongly affected by the inverter efficiency ($\eta_{inverter}$) and the factor of losses (f_{losses}) considered to account for some PV losses such as mismatch, soiling, wiring losses and other secondary losses [22].

$$P^{el,pv} = P_{DC} \eta_{inverter} f_{losses} \quad (8.22)$$

8.4 CSP Model

The CSP model can be sub-divided into three blocks: the solar field, the power block and the thermal storage. In this section, a detailed optical and thermal model will be presented, as shown in Fig. 8.4.

The Solar Field

The solar field is the starting point of the electricity production process in a CSP plant. The solar field of a parabolic trough collector (PTC) plant is composed of a set of solar collectors, which are installed on a metallic structure and controlled by a sun tracking system. These collectors reflect the incident solar radiation on tubes placed at their focal axes where a heat transfer fluid (HTF) circulates [23, 24].

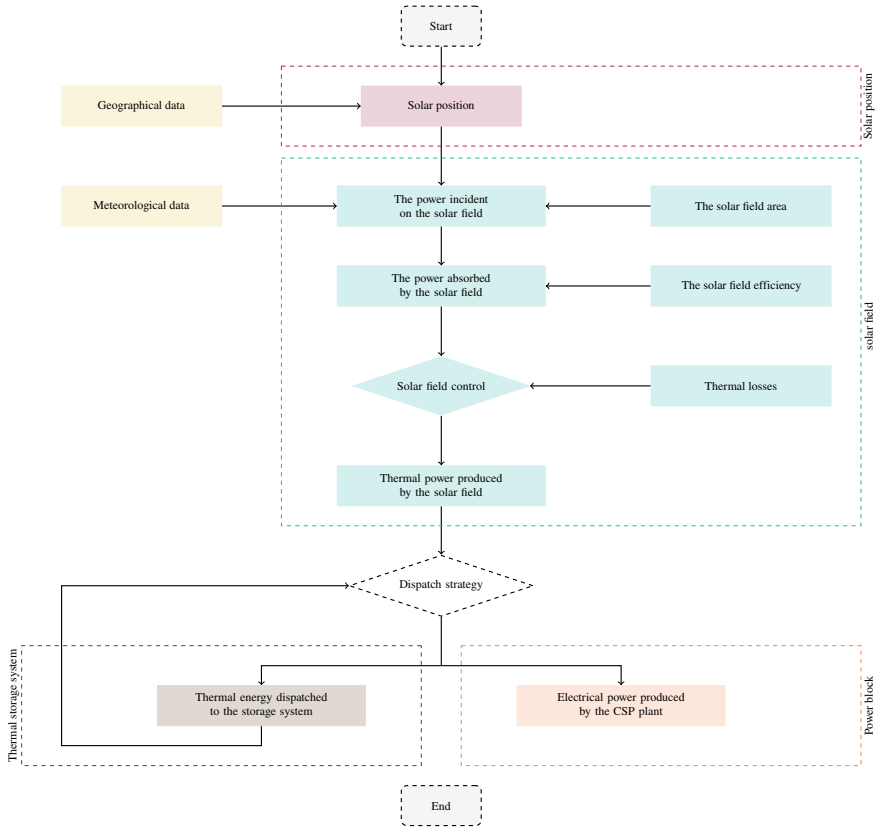


Fig. 8.4 Model of the CSP plant

Estimate the Thermal Power Incident on the Solar Field

The solar field of a PTC power plant is in the form of a chain of loops that usually take the shape of a U. Each loop contains a limited number of solar collector assemblies (SCAs), each SCA contains a limited number of solar collector elements (SCEs), and each SCE contains a specific number of mirrors [23, 24].

All loops in a PTC solar field are connected in parallel and linked by a common cold collector pipe that delivers an equal flow rate of cold HTF to each loop. A second pipe collects the hot HTF and returns it either to the power block for electricity generation or to the thermal storage system for later use [23, 24].

The PTC's solar field is often rectangular in shape, with the alimentation block in the center. This allows for the shortest possible pipe lengths, as well as a reduction in thermal losses throughout the solar field [23, 24].

The thermal power incident on the solar field of a PTC power plant is calculated using the Eq. (8.23) [22].

$$P^{th,incident} = B_n A_{field} \quad (8.23)$$

with, A_{field} is the solar field's area, and B_n is the normal direct radiation.

Estimate the Thermal Power Absorbed by the Solar Field

The thermal power absorbed by the solar field is a fraction of the incident thermal power adjusted with the efficiency of the solar field, according to the Eq. (8.24) [25].

$$P^{th,absorbed} = P^{th,incident} \eta_{sf} \quad (8.24)$$

Calculate the Solar Field Efficiency

The calculation of the solar field efficiency requires the calculation of the various optical and geometrical losses which influence the technical performances of the PTC plant according to the Eq. (8.25) [26].

$$\eta_{sf} = \cos(\theta_{csp}) k(\theta_{csp}) \eta_{shadow} \eta_{end} \eta_{col} \eta_{rec} \quad (8.25)$$

Cosine losses are generated due to the variation of the angle of incidence during the day. As the solar position varies, the sun rays come down to the collector at an incidence angle which will decrease the field efficiency. The equation can be further described as (8.26) [25, 26].

$$\cos(\theta_{CSP}) = \sqrt{1 - \cos^2(\delta) \sin^2(\omega)} \quad (8.26)$$

The incident angle modifier is calculated as follows in Eq. (8.27). It corrects for some additional losses due to absorption and reflection. For each collector type, the incident angle modifier is given as an empirical formula [26].

$$k(\theta_{csp}) = k_0 + k_1 \frac{\theta_{csp}}{\cos(\theta_{csp})} + k_2 \frac{\theta_{csp}^2}{\cos(\theta_{csp})} \quad (8.27)$$

With, k_0 , k_1 and k_2 are experimental parameters related to the type of solar collector chosen.

Shading losses are generated due to the arrangement of solar collectors in parallel rows. To minimize these losses, the spacing between collectors must to be optimized. The shading factor is the ratio between the width of the mirror that is not shaded to its actual width. The factor to calculate the shadow from row to row as written in Eq. (8.28) [27]

$$\eta_{shadow} = \frac{\sin(\alpha_s) L_{spacing}}{A_{col} \cos(\theta_{csp})} \quad (8.28)$$

with, $L_{spacing}$ is the spacing between the collector's rows, A_{col} is the width of the collector.

The value of the shading factor is limited to the range of values between 0.5 and 1, as shown in Eq. (8.29) [27]

$$\eta_{shadow} = \begin{cases} 0 & \text{if } \eta_{shadow} < 0.5 \text{ or } \alpha_s < 0 \\ \eta_{shadow} & \text{if } 0.5 \leq \eta_{shadow} \leq 1 \\ 1 & \text{if } \eta_{shadow} > 1 \end{cases} \quad (8.29)$$

If the shading factor is less than 0.5, the solar field does not work, the geometric efficiency is set to zero. If the shading factor is equal to 0 it explains that the rows are completely shaded, whereas a value of 1 indicates that the rows are not shaded.

The end losses occur naturally when reflected sunlight does not reach the absorption tubes. The factor of end losses is calculated as shown in Eq. (8.30) [6].

$$\eta_{end} = 1 - \frac{L_{focal} \tan(\theta_{CSP})}{L_{col}} \quad (8.30)$$

with, L_{focal} and L_{col} is the length and focal length of the solar collector. The collector efficiency is calculated based on various experimental measurements given by the manufacturer, which are related to material properties and collector performance factors such as, mirror reflectivity (η_{ref}), tracking error losses (η_{track}), geometry defects (η_{geo}), mirror dirt ($\eta_{dirt-col}$), and overall uncaptured errors (η_{opt}). So Eq. (8.31) can be further described as [25].

$$\eta_{col} = \eta_{ref} \eta_{track} \eta_{geo} \eta_{dirt-col} \eta_{opt} \quad (8.31)$$

The receiver efficiency is calculated using different experimental measurements provided by the manufacturer, including the transmissivity of the glass tube (τ_{glass}), the absorption factor (η_{abs}), the interception factor (γ_{rec}) and the losses due to dirt ($\eta_{dirt,rec}$). So Eq. (8.32) can be further described as [25].

$$\eta_{rec} = \tau_{glass} \eta_{abs} \gamma_{rec} \eta_{dirt-rec} \quad (8.32)$$

Calculate the Solar Field Area

The exact area $A_{ref,exact}$ is the area required to provide enough thermal energy to drive the power block under design conditions. It is calculated by the Eq. (8.33).

$$A_{ref,exact} = \frac{P_{CSP}}{\eta_{pb} (B_{n,ref} \eta_{rec} \eta_{col} - P_{ref}^{th,losses})} \quad (8.33)$$

with, P_{CSP} is the CSP installed capacity, η_{pb} is the power block efficiency and $P_{ref}^{th,losses}$ and $B_{n,ref}$ are the heat losses and direct normal radiation at reference conditions, respectively.

The calculation of the surface effectively exploitable by the PTC plant must take into account the solar multiple (SM). (Equation (8.34))

$$A_{field} = A_{ref,exact} SM \quad (8.34)$$

The solar multiple is the degree of oversize of the solar field, it can be also defined as the ratio of the thermal power generated by the solar field to that required by the power block at design conditions.

Calculate the Thermal Losses

The heat losses occur in the solar receivers ($P_t^{th,rec}$) and the pipe system that connects the solar collectors between them ($P_t^{th,pipe}$). These losses are calculated according to the Eq. (8.35) [26]. In order to reduce the complexity of the model, the calculation of these losses is based on an empirical approach.

$$P^{th,losses} = (P^{th,rec} + P^{th,pipe})A_{field} \quad (8.35)$$

The heat losses in the receiver: The solar flux received by the receiver is not totally transmitted to the heat transfer fluid (HTF) because of the various thermal exchanges. These heat losses are calculated according to Eq. (8.36) [28]. They are strongly influenced by the direct radiation, the ambient temperature (T_{amb}), the wind speed (v_{wind}) and the solar field inlet ($T_t^{sf,in}$) and outlet ($T_t^{sf,out}$) temperature.

$$P^{th,rec} = \frac{A_1 + A_2 + A_3 + A_4}{A_{col} (T_t^{sf,out} - T_t^{sf,in})} \quad (8.36)$$

with,

$$\begin{aligned} A_1 &= (a_0 + a_5 \sqrt{v_{wind}}) ((T_t^{sf,out} - T_t^{sf,in})) \\ A_2 &= \frac{1}{2} (a_1 + a_6 \sqrt{v_{wind}}) ((T_t^{sf,out})^2 - (T_t^{sf,in})^2 - 2 T_{amb} (T_t^{sf,out} - T_t^{sf,in})) \\ A_3 &= \frac{1}{3} (a_2 + a_4 B_n \cos(\theta_{csp}) k(\theta_{csp})) ((T_t^{sf,out})^3 - (T_t^{sf,in})^3) \\ A_4 &= \frac{1}{4} a_3 ((T_t^{sf,out})^4 - (T_t^{sf,in})^4) \end{aligned}$$

with, a_0, a_1, a_2, a_3, a_4 et a_5 are experimental parameters that depend on the chosen receiver type.

The heat losses in the pipe system are evaluated as a function of the difference between the average temperature of the solar field and the ambient temperature. (Equation (8.37)) [26].

$$P^{th,pipe} = (H_3 \Delta T^3 + H_2 \Delta T^2 + H_1 \Delta T) P_{design}^{pipe} \quad (8.37)$$

$$\Delta T = \frac{(T_t^{sf,out} + T_t^{sf,in})}{2} - T_{amb}$$

with, P_{design}^{pipe} is the heat losses factor in the pipe system under design conditions.

Calculate the Thermal Power Produced by the Solar Field

The thermal power produced by the solar field is the difference between the thermal power absorbed by the solar field and the different thermal losses. It is calculated according to the Eq. (8.38) [26].

$$P^{th,sf} = P^{th,absorbed} - P^{th,losses} \quad (8.38)$$

The calculation of the heat losses depends on the solar field inlet and outlet temperatures, which are calculated according to the operating mode of the solar field.

The Solar Field Control

the control method of the solar field that shown in Fig. 8.5, represents three operating mode of solar field. Each operating mode requires different equations to calculate the solar field temperatures [27].

Mode 1: HTF Freeze Protection

When the thermal energy produced is zero or less than zero, it implies that the solar field does not operate. In this case, the main concern is to determine if a freeze protection energy is required to prevent the HTF temperature from decreasing below its minimum. The calculation process starts by determining the average temperature of the fluid ($T_t^{sf,moy}$), then calculating the energy needed against freezing (Q_t^{freeze}) and finally determining the exact solar field inlet and outlet temperature [27].

Mode 2: Warm-up

When the thermal energy produced is greater than zero and the average temperature of the solar field is less than the design temperature, the system must warm up to reach its nominal temperature. The energy required for warm-up (Q_t^{warmup}) must be calculated to determine whether or not the solar field can warm up or not [27].

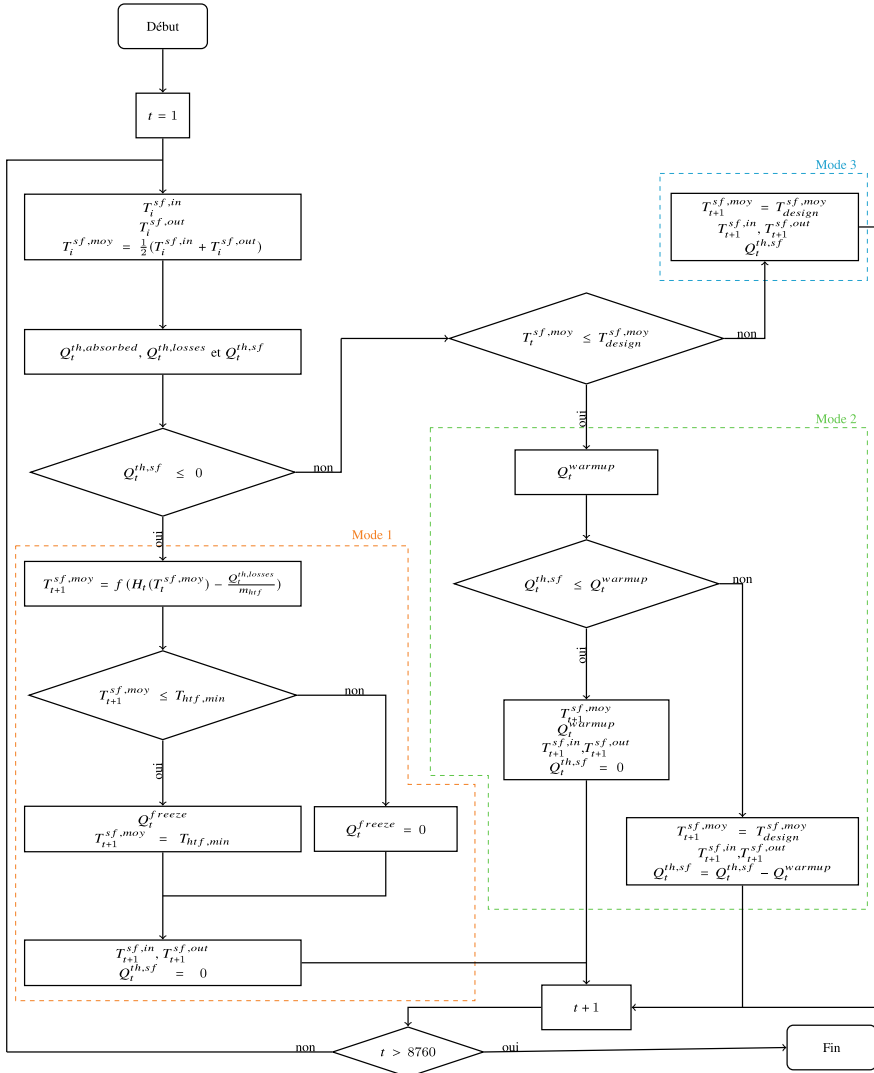


Fig. 8.5 Solar field control Mode 1: HTF freeze protection, Mode 2: Warm-up and Mode 3: Normal operation

Mode 4: Normal Operation

When the thermal energy produced by the solar field is greater than zero and the temperature average of the solar field is greater than design temperature, the solar field operates under normal conditions [27].

The Power Block

The Power Block (PB) is used to produce electrical power from the thermal power supplied by the solar field. It is similar to a power block in a conventional thermal power plant. The power output of PB (P_{out}^{pb}) is expressed as (8.39) by means the PB power input (P_{in}^{pb}) and the PB efficiency (η_{pb}) [28].

$$P_{out}^{pb} = \eta_{pb} P_{in}^{pb} \quad (8.39)$$

The operation of the power block is limited by its maximum and minimum operating power. (Equation (8.40) [28].

$$P_{min}^{pb} \leq P_{in}^{pb} \leq P_{max}^{pb} \quad (8.40)$$

The Thermal Storage System

The capacity of TES system (C_{tes}) is usually depend to the storage duration (h_{tes}), the CSP plant capacity (P_{csp}) and the PB efficiency (η_{pb}). It calculated as shown in (8.41) [28].

$$C_{tes} = \frac{P_{csp} h_{tes}}{\eta_{pb}} \quad (8.41)$$

The heat storage of TES system after the storage and discharge process are both shown as follows (8.42) [28].

$$\begin{cases} TES_{th}^{t+1} = TES_{th}^t + \frac{H_{tes,c}^t}{\eta_{tes,c}} \Delta t \\ TES_{th}^{t+1} = TES_{th}^t - \frac{H_{tes,d}^t}{\eta_{tes,d}} \Delta t \end{cases} \quad (8.42)$$

where TES_{th}^{t+1} and TES_{th}^t are the heat storage of TES in period $t + 1$ and period t , respectively. And thus, $H_{tes,d}$ and $H_{tes,c}$ are the discharge and storage power, respectively. $\eta_{tes,d}$ and $\eta_{tes,c}$ are the discharge and storage efficiency, respectively. And, Δt is time duration.

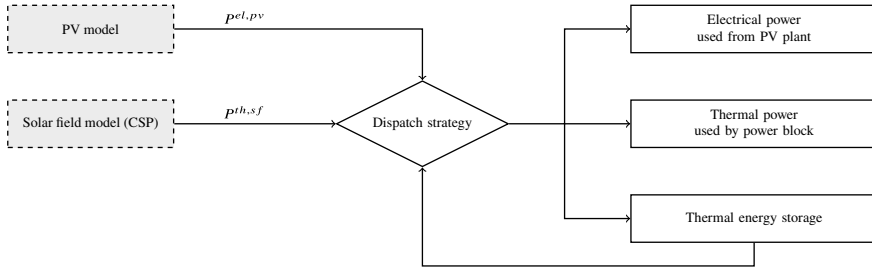


Fig. 8.6 Model of PV-CSP plant

8.5 Dispatch Strategy

To use thermal energy and electrical energy provided by CSP subsystem and PV subsystem respectively in an optimal way in the hybrid PV-CSP system, a strategy of dispatching is obligatory to be implemented based on the operational mode of the plant (start-up mode, day operation mode, night operation mode). The main objective of a dispatch strategy is to manage the power flows in the PV-CSP system and determine whether the subsystem of plant can accurately operate to satisfy the demanded load (Fig. 8.6). Our proposed dispatch strategy takes into account the electricity tariff system to prioritize meeting the load during peak hours and consequently, increasing the revenue of the PV-CSP plant. Its consists of:

- Prioritize load satisfaction during peak hours over base hours.
- Prioritize the operation of the PV plant over the CSP plant, to minimize the dumped energy by the PV plant.
- Operate CSP plant at response to PV production.
- Charge the TES system by the excess energy from SF, if the TES system is fully charged, the surplus energy is spilled.
- Impose operation of the turbine at its minimum of its rated power after its start-up to minimize the number of turbine shutdowns and start-ups (only one start-up per day).

8.6 Conclusion

In this work, we have developed a rigorous mathematical model of the PV and CSP plant, in order to be able to calculate at any time the electrical power produced by the PV plant and the thermal power produced by the solar field of the CSP plant, for any installed capacity of the PV plant and the CSP plant. The mathematical model of hybrid PV-CSP plant is based on PV and CSP models and a dispatch strategy, which is developed in order to manage the power flows to satisfy the requested load.

Our motivation here was to develop a mathematical model of the PV-CSP plant, taking into account the technical plant parameters and meteorological data over a full-year operation. This model will be used later on to study the technico-economic performance of PV-CSP plants.

References

1. Reda, I., Andreas, A.: Solar position algorithm for solar radiation applications. *Sol. Energy* **76**(5), 577–589 (2004)
2. Grena, R.: An algorithm for the computation of the solar position. *Sol. Energy* **82**(5), 462–470 (2008)
3. Vician, P., Palacka, M., Danský, P., Jandačka, J.: Determination of optimal position of solar trough collector. *Procedia Eng.* **192**, 941–946 (2017)
4. Campbell, G.S., Norman, J.: *An Introduction to Environmental Biophysics*. Springer Science & Business Media (2012)
5. Nadia, A.R., Isa, N.A.M., Desa, M.K.M.: Advances in solar photovoltaic tracking systems: a review. *Renew. Sustain. Energy Rev.* **82**, 2548–2569 (2018)
6. Wang, J., Wang, J., Bi, X., Wang, X.: Performance simulation comparison for parabolic trough solar collectors in China. *Int. J. Photoenergy* (2016)
7. Nsengiyumva, W., Chen, S.G., Hu, L., Chen, X.: Recent advancements and challenges in Solar Tracking Systems (STS): a review. *Renew. Sustain. Energy Rev.* **81**, 250–279 (2018)
8. Hafez, A.Z., Soliman, A., El-Metwally, K.A., Ismail, I.M.: Tilt and azimuth angles in solar energy applications-a review. *Renew. Sustain. Energy Rev.* **77**, 147–168 (2017)
9. Awasthi, A., Shukla, A.K., SR, M.M., Dondariya, C., Shukla, K.N., Porwal, D., Richhariya, G.: Review on sun tracking technology in solar PV system. *Energy Rep.* **6**, 392–405 (2020)
10. Gilman, P., DiOrio, N.A., Freeman, J.M., Janzou, S., Dobos, A., Ryberg, D.: SAM photovoltaic model technical reference 2016 Update (No. NREL/TP-6A20-67399). Natl. Renew. Energy Lab. (NREL), Golden, CO (United States) (2018)
11. Chen, J.L., He, L., Yang, H., Ma, M., Chen, Q., Wu, S.J., Xiao, Z.L.: Empirical models for estimating monthly global solar radiation: a most comprehensive review and comparative case study in China. *Renew. Sustain. Energy Rev.* **108**, 91–111 (2019)
12. Bayrakç, H.C., Demircan, C., Keçebaş, A.: The development of empirical models for estimating global solar radiation on horizontal surface: a case study. *Renew. Sustain. Energy Rev.* **81**, 2771–2782 (2018)
13. Li, D.H., Lou, S.: Review of solar irradiance and daylight illuminance modeling and sky classification. *Renew. Energy* **126**, 445–453 (2018)
14. Danandeh, M.A.: Solar irradiance estimation models and optimum tilt angle approaches: a comparative study. *Renew. Sustain. Energy Rev.* **92**, 319–330 (2018)
15. Lahnaoui, A., Stenzel, P., Linssen, J.: Tilt angle and orientation impact on the techno-economic performance of photovoltaic battery systems. *Energy Procedia* **105**, 4312–4320 (2017)
16. Conceição, R., Silva, H.G., Fialho, L., Lopes, F.M., Collares-Pereira, M.: PV system design with the effect of soiling on the optimum tilt angle. *Renew. Energy* **133**, 787–796 (2019)
17. Mousavi Maleki, S.A., Hizam, H., Gomes, C.: Estimation of hourly, daily and monthly global solar radiation on inclined surfaces: models re-visited. *Energies* **10**(1), 134 (2017)
18. Zhang, J., Zhao, L., Deng, S., Xu, W., Zhang, Y.: A critical review of the models used to estimate solar radiation. *Renew. Sustain. Energy Rev.* **70**, 314–329 (2017)
19. Roberts, J.J., Zevallos, A.A.M., Cassula, A.M.: Assessment of photovoltaic performance models for system simulation. *Renew. Sustain. Energy Rev.* **72**, 1104–1123 (2017)
20. Liu, H., Zhai, R., Fu, J., Wang, Y., Yang, Y.: Optimization study of thermal-storage PV-CSP integrated system based on GA-PSO algorithm. *Sol. Energy* **184**, 391–409 (2019)

21. Bousselamti, L., Ahouar, W., Cherkaoui, M.: Multi-objective optimization of PV-CSP system in different dispatch strategies, case of study: Midelt city. *J. Renew. Sustain. Energy* **13**(1), 013701 (2021)
22. Behar, O., Sbarbaro, D., Moran, L.: Which is the most competitive solar power technology for integration into the existing copper mining plants: Photovoltaic (PV), Concentrating Solar Power (CSP), or hybrid PV-CSP. *J. Clean. Prod.* **287**, 125455 (2021)
23. Awan, A.B., Khan, M.N., Zubair, M., Bellos, E.: Commercial parabolic trough CSP plants: research trends and technological advancements. *Sol. Energy* **211**(125455), 1422–1458 (2020)
24. Yuanjing, W., Cheng, Z., Yanping, Z., Xiaohong, H.: Performance analysis of an improved 30 MW parabolic trough solar thermal power plant. *Energy* **213**, 118862 (2020)
25. Rohani, S., Fluri, T.P., Dinter, F., Nitz, P.: Modelling and simulation of parabolic trough plants based on real operating data. *Sol. Energy* **158**, 845–860 (2017)
26. Zhai, R., Chen, Y., Liu, H., Wu, H., Yang, Y.: Optimal design method of a hybrid CSP-PV plant based on genetic algorithm considering the operation strategy. *Int. J. Photoenergy* (2018)
27. Wagner, M.J., Gilman, P.: Technical manual for the SAM physical trough model (No. NREL/TP-5500-51825). Natl. Renew. Energy Lab. (NREL), Golden, CO (United States) (2011)
28. Guo, S., He, Y., Pei, H., Wu, S.: The multi-objective capacity optimization of wind-photovoltaic-thermal energy storage hybrid power system with electric heater. *Sol. Energy* **195**, 138–149 (2020)
29. Bousselamti, L., Cherkaoui, M., Labbadi, M.: Study of hybrid PV-CSP plants considering two dispatching strategies in Ouarzazate. In: 2019 8th International Conference on Systems and Control (ICSC), pp. 449–454. IEEE (2019)

Chapter 9

Techno-economic Parametric Study of Hybrid PV-CSP Power Plants



9.1 Introduction

The parametric assessment outlined in this chapter involves evaluating the impact of the different decision parameters on the techno-economic performances of the PV, CSP, and hybrid PV-CSP solar plants.

Both the electrical annual energy and electricity cost will be assessed for various values of the tilt angle and orientation of the PV modules for the PV plant, and they will be assessed for various values of the solar multiple and the thermal storage size for the CSP plant. The hybrid PV-CSP plant will also be the subject of a techno-economic study by calculating its annual energy, electricity cost, and capacity factor for different scenarios, by varying the solar multiple value, the thermal storage size, and the fraction of hybridization.

Based on this parametric evaluation, the results of various simulations will be examined and discussed in detail, in order to evaluate the behavior of different proposed solar plants according to their decision parameters and to assess the benefits of PV-CSP hybridization.

9.2 Technical and Economic Assessment

The mathematical models developed for the simulation of PV and CSP plants were established in the previous Chapter, and they will be useful for the simulation of PV-CSP power plants.

The simulation model that is proposed for the PV plant enables the calculation of its hourly generated electrical power. This power is calculated for any installed capacity of the PV plant, using the meteorological data of the location and the technical characteristics of the PV modules and the inverters [1].

The proposed simulation model for CSP plant is used to calculate the hourly thermal power generated by its solar field. This power is calculated for any installed capacity of the CSP plant, using the meteorological data of the site and the technical characteristics of the collectors and solar receivers. The generated thermal power will be subject to a dispatching strategy that used to manage the power flows between the thermal energy storage (TES) system and the power block (PB) (depending on the requested load) [1].

The simulation model for the PV-CSP plants has been developed already in the previous Chapter, which enables the calculation of the electrical power, delivered by the hybrid plant for any installed capacity of the PV plant and the CSP plant [1].

The principal objective of this chapter is to develop a parametric assessment for the PV, CSP, and PV-CSP plants. This assessment involves extracting the decision parameters that influence the techno-economic performances of the PV and CSP plants and then evaluating their effects on the optimal sizing of PV-CSP hybrid systems.

9.2.1 Technical Assessment

The technical assessment is based on the calculation of the annual electrical energy produced by the solar power plants (PV, CSP, and PV-CSP), as well as their capacity factor (CF).

The annual electrical energy produced (E_{tot}) by the solar plants (PV, CSP, and PV-CSP) shall be calculated as the sum of hourly electrical energy produced throughout the year.

The capacity factor (CF) is a technical performance indicator that is used to evaluate the ability of the power plants to meet the demanded load. It is calculated using the Eq. (9.1) [2, 3].

$$CF = \frac{E_{tot}}{8760 P_{np}} \quad (9.1)$$

In this context, the CF is calculated based on the assumption that the nominal capacity (P_{np}) of the solar plant is 100MW, given that, the objective is to satisfy a base load of 100MW.

9.2.2 Economic Assessment

Several economic indicators can be calculated in an economical assessment of PV, CSP, or PV-CSP plants. In this chapter, we mainly consider the levelized cost of electricity (LCOE). The LCOE is considered as the main indicator used to study the economic feasibility of a power plant for a specific location [4, 5].

The LCOE was first introduced in 1995 by the national renewable resources laboratory (NREL, USA), in order to evaluate the profitability of solar photovoltaic plants [6]. It has been considered by NREL and the IEA (International Energy Agency) as the best economic indicator for comparing between different power generation technologies, independently of the installation location and installed capacity [7]. The LCOE doesn't give the cost of buying the electricity from the final consumer but it reviews all the costs involved in the production of the electrical energy and represents the minimum cost per kWh of energy that the producer can adopt [7].

According to the literature, the LCOE is a decision-making indicator for investors. It helps to justify the type of technology chosen, the location of the plant, and the capacity to be installed to meet the requested load. The LCOE of a power plant is calculated using the Eq. (9.2) [1, 7].

$$LCOE = \frac{CAPEX + \sum_{t=1}^T \frac{OPEX}{(1+r)^t}}{\sum_{t=1}^T \frac{E_{tot}(1-d)^t}{(1+r)^t}} \quad (9.2)$$

With, $CAPEX$ is the initial investment cost, $OPEX$ is the annual operating cost, E_{tot} is the annual electrical energy produced by the plant, d is the degradation factor, T is the lifetime of plant and r is the inflation factor.

The LCOE of a PV-CSP hybrid plant is calculated according to the Eq. (9.3) [3].

$$LCOE_{PV-CSP} = \frac{CAPEX_{CSP} + \sum_{t=1}^T \frac{OPEX_{CSP}}{(1+r)^t} + CAPEX_{PV} + \sum_{t=1}^T \frac{OPEX_{PV}}{(1+r)^t}}{\sum_{t=1}^T \frac{E_{CSP}(1-d_{CSP})^t + E_{PV}(1-d_{PV})^t}{(1+r)^t}} \quad (9.3)$$

The initial investment cost of a PV or CSP plant involves direct and indirect costs. For the PV power plant the direct costs include the cost of solar modules (c_{mod}), inverters (c_{inv}), installation labor (c_{eng}), installer margin and overhead (c_{str}) and balance of system (c_{elec}). For the CSP power plant, the direct costs include the cost of solar field (c_{col}), power bloc (c_{pb}), storage system (c_{tes}), heat transfer fluid (c_{htf}) and balance of plant (c_{plant}). For both solar plants, the indirect costs ($c_{indirect,pv}$ and $c_{indirect,csp}$) are estimated considering engineering and construction costs. The PV and CSP initial investment costs were obtained using the Eqs. (9.4) and (9.5) [3].

$$CAPEX_{pv} = \overbrace{P_{pv}(c_{mod}c_{eng}c_{str}c_{elec}c_{inv})}^{c_{direct,pv}} + \overbrace{g_{pv}c_{indirect,pv}}^{c_{indirect,pv}} \quad (9.4)$$

$$CAPEX_{csp} = \overbrace{(c_{col} + c_{htf})A_{field} + C_{storage}c_{tes} + P_{csp}(c_{pb} + c_{plant})}^{c_{direct,csp}} + \overbrace{g_{csp}c_{indirect,csp}}^{c_{indirect,csp}} \quad (9.5)$$

The annual operating cost for PV ($OPEX_{pv}$) or CSP ($OPEX_{csp}$) plant includes maintenances and operation costs. It calculated using Eq. (9.6) [3].

$$\begin{cases} OPEX_{pv} = C_{pv}P_{pv} \\ OPEX_{csp} = C_{fixe}P_{csp} + C_{var}E_{csp} \end{cases} \quad (9.6)$$

With, C_{pv} is the annual operation and maintenance cost for PV plant, and C_{fixe} and C_{var} being the fixed and variable operation cost for CSP plant.

The set of economic parameters used to calculate the LCOE for the PV, CSP, and PV-CSP power plants will be defined and listed in Appendix B.

9.3 Site Selection

The study area is located in the atlas of Morocco, exactly in Midelt city. It is considered one of the most appropriate area for implementing solar power plants. The study area belongs to the driest cities in Morocco, it has a typical semi to arid climate with marked seasonal contrasting climate variabilities, which is characterized by high internal-annual variability, very dry between February to November, and wet during December and January. Midelt city also enjoys a high amount of solar radiation, a large available of suited surface area to the implementation of solar power plants, an access to water resources via a barrage which is located near to the studied area, as well as an easy electrical connection and a minimal existence of environmental constraints [3, 8]. Typical meteorological year (TMY) data of the study area was taken from Photovoltaic Geographical Information System (PVGIS) interface based on longitude and latitude [9]. The annual direct normal irradiance (DNI) and global horizontal irradiance (GHI) are both shown in Fig. 9.1a, b. Figure 9.2 illustrates the monthly hourly average of GHI and DNI. As can be seen in figures, Midelt city has an excellent solar resources with a GHI and DNI yearly average of 5.25 KWh/m² day and 5.85 KWh/m² day, respectively [3].

9.4 Parametric Study of Solar Power Plants

9.4.1 The PV Plant

The parametric assessment of the PV plant consists in simulating its technical and economic behaviour under different values of the tilt angle and the orientation of the PV modules. The simulation has been performed, based on the previously suggested model of the PV plant (Chap. 8) and it is done by using the economic and technical data identified in the Appendix B.

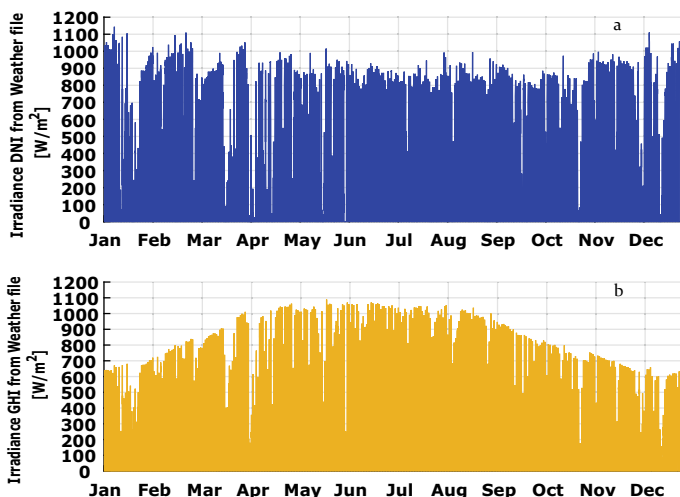
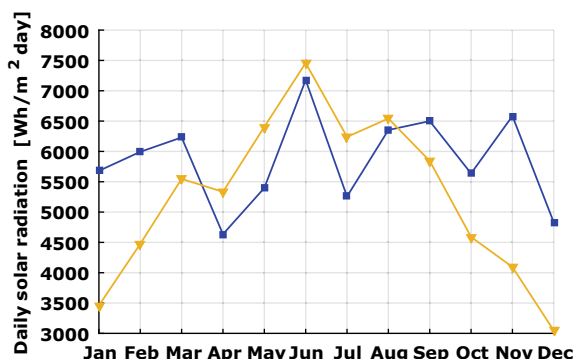


Fig. 9.1 a Annual DNI profile b Annual GHI profile

Fig. 9.2 Daily solar radiation (DNI and GHI)



The PV plant must be able to satisfy a baseload (100MW). Its strategy of operation consist of two cases:

- If the power produced ($P^{el,pv}$) is sufficient to satisfy the load (P^{el}_{load}), then the excess power will be dumped (P^{pv}_{dumped}), as the PV plant does not coupled to an electrical energy storage system.
- If the power produced is less than the power demanded by the load, then the load may not be satisfied or is only partially satisfied.

Influence of tilt and orientation angle on performance of PV plant

The position of the PV modules is described by a tilt angle (i) and an orientation angle (γ). The mounting methods (fixed support, 1-axis or 2-axis tracker), the topography of the landscape, and the geographical coordination are the important factors to consider when determining the optimal tilt and orientation angle of PV modules [1,

[10]. When the PV module follows the path of the sun by changing continuously its tilt angle or/and orientation, which means the PV module is coupled to a sun tracker. A sun tracking system can be either single-axis or dual-axis sun tracker. Connecting the PV system to a solar tracker brings a significant gain in terms of energy production; however, its installation is very costly and complex [10, 11]. Therefore, large-scale PV installations are usually installed with a fixed tilt and orientation. Whereas, residential or small-scale PV installations can be equipped with sun-tracking devices. A fixed PV system is more affordable and requires less maintenance compared to those equipped with a 1-axis or 2-axis solar tracker. In this context, several approaches have been proposed to optimize the position of PV modules for different locations at different latitudes. In this work, we focus on fixed PV systems [12–15].

The current study was carried out for evaluating the techno-economic performance of a PV plant under different tilt and orientation angle and prevailing meteorological data at the location. Figure 9.3 shows the variation of annual electrical energy generated by the PV plant as a function of tilt angle for different orientations (Equation (9.7)). It can be observed that the annual energy generated by orienting the PV modules towards the south ($\gamma = 0$) is higher than that generated in the case of other orientations.

$$\gamma = \begin{cases} 0 & \text{Sud} \\ 180 & \text{Nord} \\ 90 & \text{East} \\ -90 & \text{Ouest} \end{cases} \quad (9.7)$$

Figure 9.4 shows the variation of the annual energy produced and the LCOE for the PV plant as a function of tilt angle for a southern orientation. It can be observed that the annual energy produced increases in the tilt angle range $[0^\circ, 35^\circ]$ from 162 to 182 GWh; once the tilt angle exceeds 35° , the annual energy output decreases significantly. The curve representing the annual energy produced is opposite to that of the LCOE. When the annual energy decreases, the LCOE increases and vice versa. The lowest LCOE is 0.0515/kWh and the highest annual energy output is 182 GWh. The best cost-effectiveness is achieved for a southern orientation and a tilt angle closest to the local geographic latitude.

The result of this case study was expected since the installation is located in the northern hemisphere and the local latitude of such regions is selected as the optimal tilt angle for PV systems [12, 15]. Furthermore, this case study allowed us to validate the proposed mathematical calculation model for the PV plant and to visualize the effect of varying the tilt angle and orientation of the PV modules on the annual energy and the LCOE of the PV plant [1].

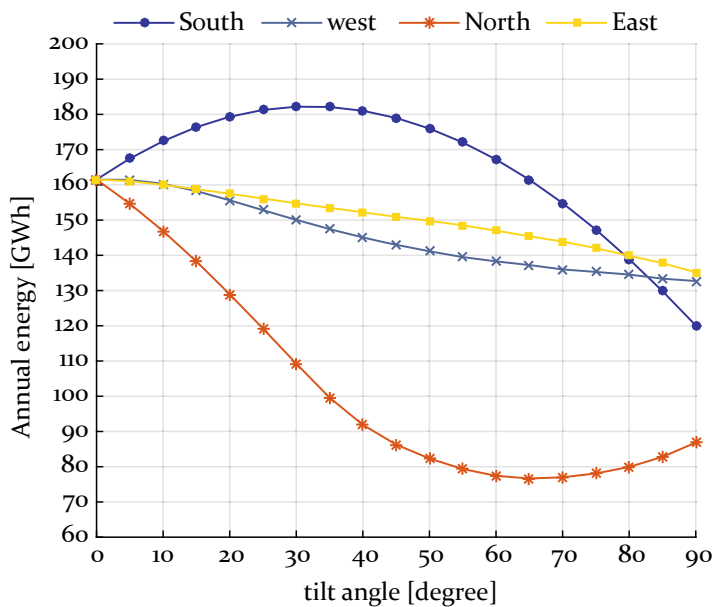


Fig. 9.3 The influence of varying the tilt and orientation angle on the annual energy produced by the PV plant

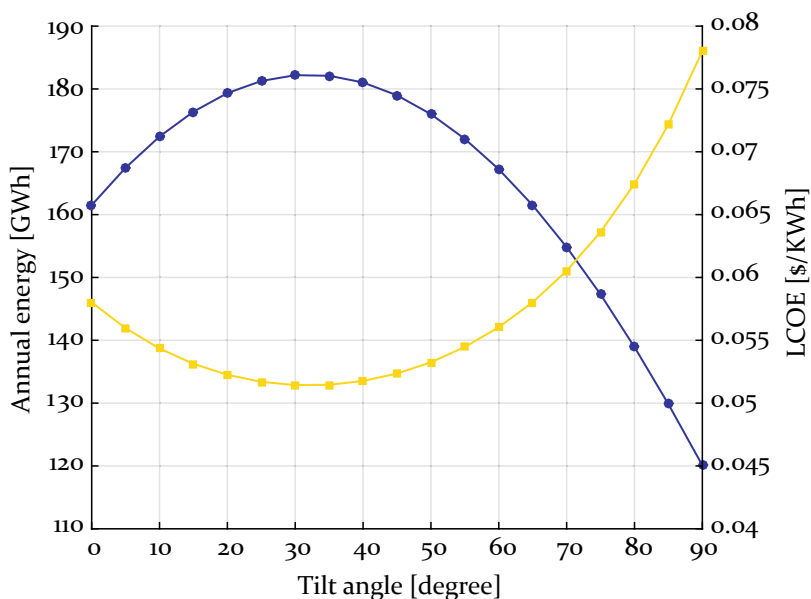


Fig. 9.4 The influence of varying tilt angle on the annual energy and the LCOE of the PV plant (for southern orientation)

9.4.2 The CSP Plant

The parametric evaluation of the CSP plant is similar to that of the PV plant. It consists of simulating the technical-economic behavior of the CSP plant, using the economic and technical parameters defined in Appendix B.

This current section aims to simulate the behavior of a CSP plant based on a parabolic trough technology, by varying the values of the solar multiple and the thermal storage size. The system is designed to supply a baseload (100 MW). The implemented dispatch strategy for the CSP plant gives priority to the operation of the power block over the thermal storage system.

Influence of solar multiple and TES size on performance of CSP plant

To better disclose the impact of solar multiple and TES size on the technical-economic performances of a CSP plant, a parametric analysis is necessary to be presented, which is done by examining the annual energy output and the LCOE of a CSP plant.

Two simulation cases of the CSP plant were performed for a solar multiple equal to 3, considering different value of TES size ($h_{TES} = 6$ h and $h_{TES} = 12$ h) in each simulation case. Figure 9.5 illustrates the variation of the normal direct radiation, the energy generated by the power block, the state of charge of the TES, and the rejected thermal energy for a typical day.

From Fig. 9.5a, it is very clear that from 10pm onwards, the system does not produce any electrical energy even though the power plant has a storage capacity of 6h. Given that during the period between 12 and 5pm, the storage system had achieved its maximum capacity of storage which is about 1780 MWh. Hence, the excess thermal energy that was not used by the power block was dumped.

From Fig. 9.5b, it can be observed that from 10pm onwards, the system continues to produce electricity. This production is ensured from surplus energy that has been stored during the day. Therefore, the energy produced by the solar field is fully utilized by the thermal storage system and the power block.

The CSP plant with the configuration ($SM = 3$, $h_{tes} = 12$ h) provided high daily usable energy than a CSP plant with the same solar multiple value and a smaller storage size ($SM = 3$, $h_{tes} = 6$ h). One can say that, if the TES size is smaller than its optimal value for an installed capacity of the CSP plant, the thermal energy produced by the CSP field and which is not used directly by the power block will be dumped (the storage quickly reaches its maximum capacity).

The choice of solar multiple and TES size value is related to each other and it highly affects the annual performances of CSP plants.

By applying the CSP plant simulation model, the annual electrical energy generated and the LCOE of the CSP plant are calculated for different values of solar multiple and TES size. The results of these different simulations are shown in the Figs. 9.6 and 9.7.

By analysing Figs. 9.6 and 9.7, it can be observed that when the solar multiple is equal to 1, the annual energy produced remains constant for all values of TES size, but the LCOE increases significantly due to the high initial investment cost in storage system. In this case, the solar field can only deliver the thermal energy used during

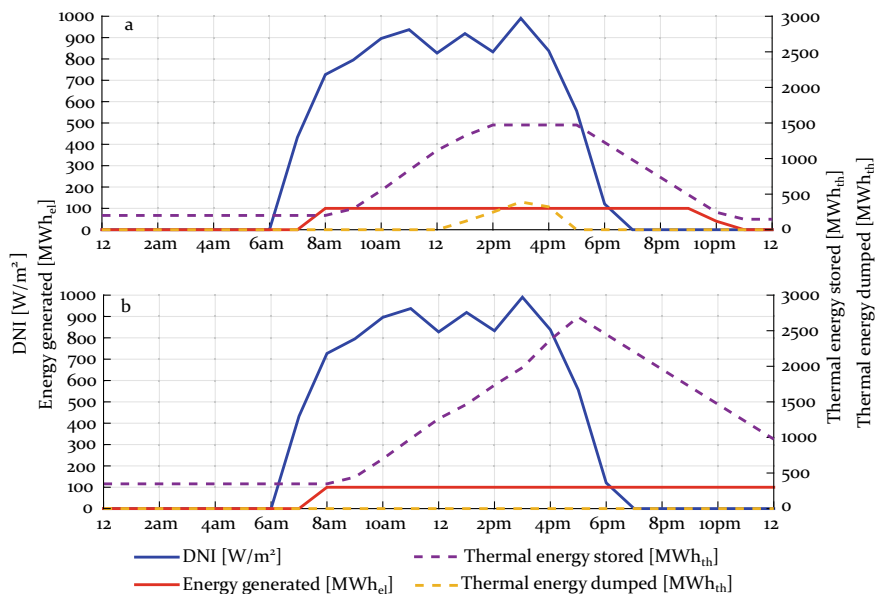


Fig. 9.5 The influence of TES size value on the CSP system energy produced: **a** TES = 6 h, **b** TES = 12 h (CSP plant with 100MW and SM = 3)

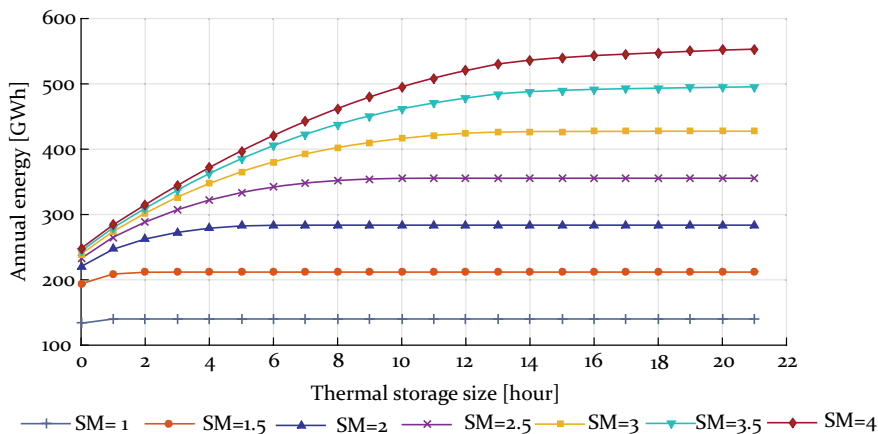


Fig. 9.6 Variation of annual energy as function of TES size for different values of solar multiple

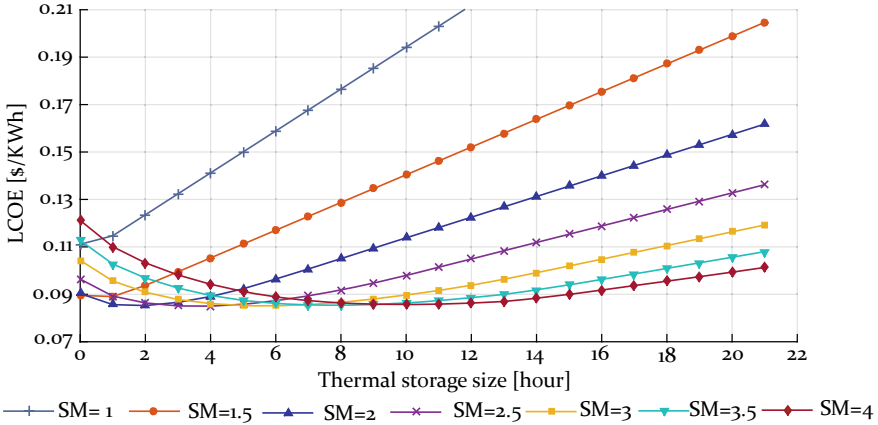


Fig. 9.7 Variation of LCOE as function of TES size for different values of solar multiple

the day; it cannot generate excess energy to be stored. In this case ($SM = 1$), the investment in storage system is not profitable.

When the value of the solar multiple is greater than 1 but the power plant is not coupled to any storage system ($h_{TES} = 0h$), the value of annual energy produced is minimal, while the LCOE is maximal for all values of solar multiple. In this case, the solar field is oversized, as well as there is no storage system to store the excess thermal energy not used directly by the power block. This excess energy will be rejected and therefore some mirrors must be defocused.

A solar multiple equal to 1 is the optimal value for a CSP plant without a storage system.

For a fixed value of thermal storage size, it is clear that with increasing the value of solar multiple, the annual energy produced increases, and the LCOE of the CSP plant decreases. This is because increasing the solar field size increases the number of solar collectors collecting the solar energy, thereby generating more energy and consequently reducing the LCOE.

For all values of solar multiple (except $SM = 1$), the amount of annual energy generated increases with increasing TES size until a certain value of that size is achieved, the annual energy generated remains constant. Simultaneously, the LCOE values decrease with increasing TES size until a certain value of that size is achieved; they start to increase again with the further increase in TES size.

For any given value of the solar multiple, it is not cost-efficient to increase the size of the TES system above a value where the LCOE starts to increase, because the CSP system will be undersized against the defined TES size. This leads to an increase in initial investment cost of the CSP plant.

We can deduce that for each value of solar multiple, we have an optimal value of TES size for which the CSP plant produces a maximum amount of energy at a minimum LCOE value compared to the installed capacity. The solar multiple and

Table 9.1 Simulated configurations

Fraction of hybridization	PV capacity (MW)	CSP capacity (MW)	SM	h_{tes} (h)
Scenario 1	200	0	–	–
Scenario 2	150	50	[1.5 2 2.5 3 3.5 4]	[6 8 10 12]
Scenario 3	100	100	[1.5 2 2.5 3 3.5 4]	[6 8 10 12]
Scenario 4	50	150	[1.5 2 2.5 3 3.5 4]	[6 8 10 12]
Scenario 5	0	200	–	–

TES size are two critical parameters to consider when sizing of CSP plants. The choice of the optimal value of solar multiple and TES size needs to be balanced based on the trade-off between the technical and economic performances of the CSP plant.

9.4.3 The Hybrid PV-CSP Plant

The parametric study of the hybrid PV-CSP plant consists of simulating its annual technical-economic behavior in order to evaluate the impact of key parameters on the selection of the optimal configuration of a PV-CSP hybrid plant.

To perform this parametric study, five scenarios were simulated. Three of them were simulated in the case of a PV-CSP hybrid plant with different values of solar multiple, TES size, and hybridization fraction (Variation of the share of PV and CSP compared to total installed capacity). Table 9.1 provides the parameters of all simulated configurations.

To show the profitability of the PV-CSP plant, the annual energy production and LCOE calculated for each hybridization scenario were compared to the one calculated for a PV (Scenario 1) and CSP (Scenario 5) plant alone.

The results obtained from the various simulations performed are presented in Figs. 9.8 and 9.9 in order to discuss the techno-economic performances of the different solar power plants. Figure 9.8 shows the results related to the annual electrical energy calculated for each simulated configuration, as well as the results of the LCOE calculation are presented in Fig. 9.9.

According to Fig. 9.9, the amount of annual energy produced by all configurations (except scenario 1) increases with increasing solar multiple value. This increase is very significant for configurations of scenarios 3, 4, and 5 and less significant for configuration of scenario 2. In addition, the increase in thermal storage size has a marginal effect on the amount of annual energy produced from configurations of scenarios 2 and 3 and scenarios 4 and 5 when the solar multiple value is less than 2.5, however, this effect becomes very significant for configurations of scenarios 4 and 5 when the solar multiple exceeds 2.5.

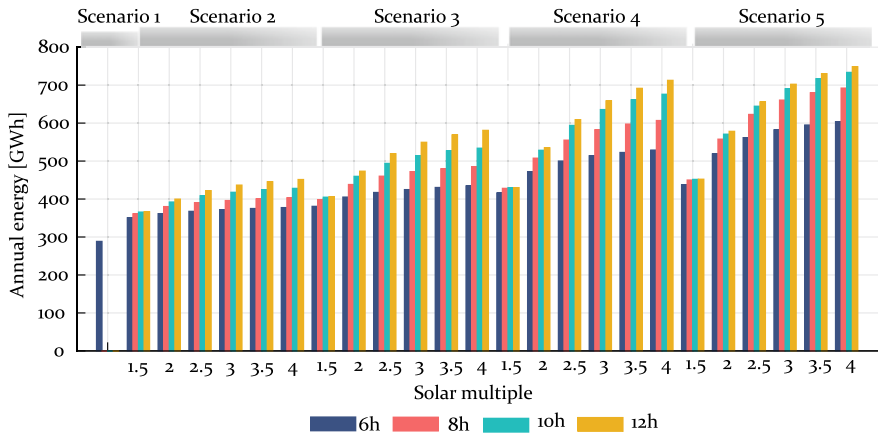


Fig. 9.8 The annual energy generated of all simulated scenarios

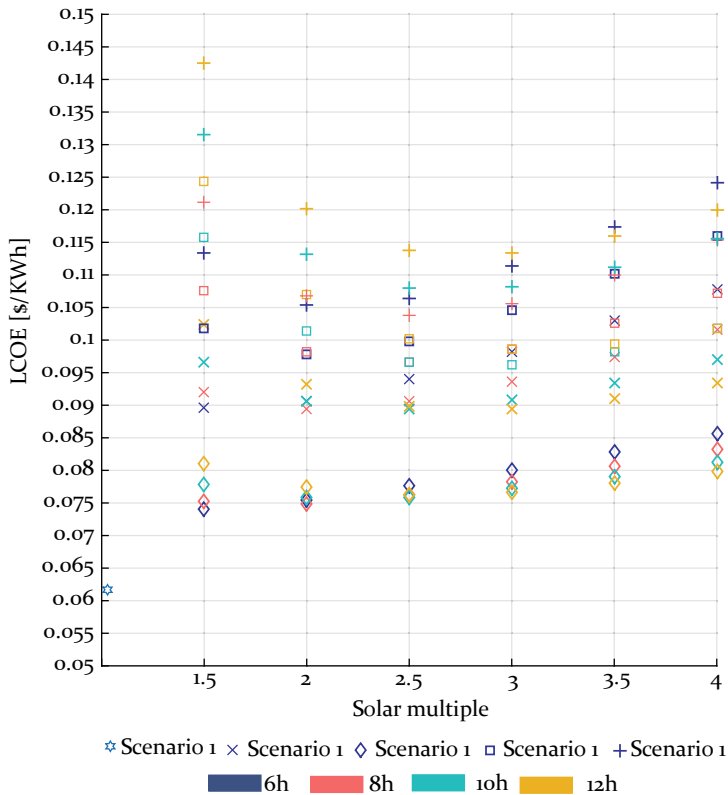


Fig. 9.9 The LCOE of all simulated scenarios

As a result, we can conclude that when the installed capacity of the CSP plant is important (compared to the total installed size of the PV-CSP hybrid plant), the effect of the choice of solar multiple and TES size on the annual energy produced becomes significant.

From Fig. 9.9, we can see that the minimum cost of 0.0617\$/kWh is obtained by scenario 1 (100% PV), due to the low cost of PV technology. The minimum cost obtained for scenarios 2, 3, 4 and 5 is 0.074\$/kWh, 0.09\$/kWh, 0.096\$/kWh and 0.103\$/kWh, respectively. These costs are obtained by the configuration with a small storage size, due to the low initial investment cost in small TES systems.

To further visualize the results already discussed, we used Fig. 9.10 that shows the variation of electrical annual energy, capacity factor and LCOE as a function of solar multiple values specifically for TES size of 12 h.

In Scenario 1, we obtain a minimum amount of energy produced because the PV plant does not coupled to an electrical energy storage system. Therefore, the excess energy generated during the daytime cannot be stored, as well as, the plant cannot supply the load demand during the night, resulting in a minimum capacity factor.

Comparing scenario 1 with the other scenarios (different configurations), this scenario enables us to produce electricity at the lowest cost but its capacity factor remains unsatisfactory.

The vertical analysis of the results allows to compare the simulation results between the different scenarios for the same value of solar multiple (except scenario 1).

In scenario 2, the installed capacity of PV is 3 times the CSP capacity. By comparing the simulation results of scenario 2 and scenario 5, we can deduce that scenario 5 produces more electrical energy than Scenario 2. However, scenario 2 requires a lower cost (LCOE) than scenario 5.

A similar result is obtained when comparing scenario 5 and scenario 3 (In scenario 3, the installed capacity of PV is equal to the CSP capacity). The scenario 3 produces globally less energy than scenario 5 at a low cost.

In scenario 4, the installed capacity of CSP capacity is 75% lower than the CSP capacity in Scenario 5, when comparing scenario 4 and 5 for the same solar multiple values; scenario 4 has a lower cost (LCOE) than scenario 5.

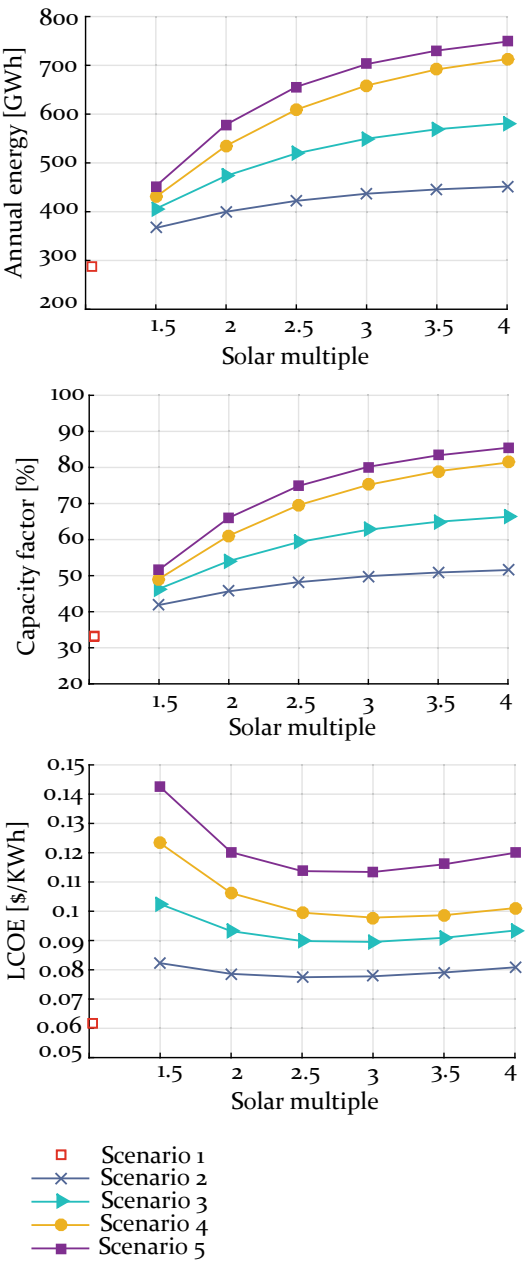
Consequently, Scenario 5 generates a maximum amount of energy (which accounts for a high capacity factor) at the highest cost compared to the other scenarios. The lowest amount of energy is provided by scenario 2, but it has the lowest cost compared to the other scenarios (3, 4, and 5).

For the same value of solar multiple and storage size, the configuration with the largest CSP installed capacity produces more energy, while the configuration with the largest PV installed capacity generates electricity with the lowest cost.

The cross-analysis of the results allows comparing the simulation results between the different scenarios for different values of solar multiple.

While comparing scenario 2 ($P_{pv} = 150$ MW, $P_{csp} = 50$ MW, $SM = 4$, $h_{TES} = 12$ h) and scenario 5 ($P_{pv} = 0$ MW, $P_{csp} = 200$ MW, $SM = 1, 5$, $h_{TES} = 12$ h), we can visualize that both configurations satisfy the demanded load with the same

Fig. 9.10 The variation of electrical annual energy, capacity factor, and LCOE according to solar multiple for $h_{tes} = 12\text{h}$



capacity factor, but the LCOE of scenario 2 is reduced by 43% compared to the scenario 5.

Similarly, for scenario 3 ($P_{pv} = 100$ MW, $P_{csp} = 100$ MW, $SM = 4$, $h_{TES} = 12$ h) and scenario 5 ($P_{pv} = 0$ MW, $P_{csp} = 200$ MW, $SM = 2$, $h_{TES} = 12$ h), the comparison between them showed that the hybrid scenario (scenario 3) produces the same amount of energy (same capacity factor) as the non-hybridized scenario (scenario 5) and thus reducing costs by 22%.

A comparison of scenario 4 ($P_{pv} = 50$ MW, $P_{csp} = 150$ MW, $SM = 3$, $h_{TES} = 12$ h) with scenario 5 ($P_{pv} = 0$ MW, $P_{csp} = 200$ MW, $SM = 2$, $h_{TES} = 12$ h) indicates that both scenarios produce almost the same amount of annual energy but with different costs; scenario 5 satisfies the load with a 16% higher cost than scenario 4.

By comparing the simulated hybrid scenarios with each other, it is shown that scenario 2 ($P_{pv} = 150$ MW, $P_{csp} = 50$ MW, $SM = 3$, $TES = 12$ h) and scenario 4 ($P_{pv} = 50$ MW, $P_{csp} = 150$ MW, $SM = 1$, $TES = 12$ h) satisfy the requested load with a capacity factor of 50% but at different costs; the LCOE obtained by scenario 2 is reduced by 37% compared to scenario 4.

From the vertical analysis, it appears that the CSP plant is capable of generating a large amount of electrical energy, which allows the load to be satisfied with a high capacity factor. On the other hand, the cross-analysis allows us to deduce that the hybrid scenarios can also generate a large amount of electrical energy but at a lower cost than the CSP plant alone. As a result, PV-CSP hybridization is a smart choice.

Regarding the implementation of PV-CSP hybrid plants, choosing the optimal configuration can change depending on the objectives of the decision makers. We would opt for configurations of scenario 4 to satisfy the load at a high capacity factor with a moderate cost. For a much lower LCOE, we would opt for configurations of scenario 2 to satisfy the load at a moderate capacity factor and lowest cost.

The selection of the optimal PV-CSP configuration to satisfy a given load is based on a techno-economic trade-off to be ensured.

9.5 Findings

Based on this parametric assessment we can observe that:

- The tilt angle and orientation of the PV modules have a strong influence on the annual electrical energy and LCOE of the PV plant. The southern orientation with a tilt angle equal to the latitude is considered as the optimal position for the PV modules.
- The strength of the CSP technology over the PV technology is the possibility to be coupled to a thermal energy storage system, which increases its technical and economic performances.

- The selection of solar multiple value and TES size is relatively interrelated; for each solar multiple value, a TES size is appropriate in terms of cost/ profitability ratio (For CSP and PV-CSP plants).
- The variation of the solar multiple values and the storage size affects the production and profitability of PV-CSP hybrid plants. The effect of these two parameters becomes more significant as the share of CSP installed (relative to the total capacity of the hybrid plant) increases.
- Based on the total capacity of the hybrid plant, a PV-CSP hybrid plant can provide the same amount of annual energy as a CSP plant but at a lower cost.
- The hybridization fraction strongly influences the technical-economic performances of PV-CSP hybrid plants. By increasing the PV installed capacity, the LCOE is reduced considerably. Contrary to the increase of the CSP installed capacity, which leads to a significant increase in the annual electrical energy produced for the same total installed capacity.

9.6 Conclusion

The parametric assessment carried out in this chapter, enabled us to identify the decision parameters that influence the techno-economic performances of PV-CSP hybrid plants, which are:

- The installed capacity of the PV plant.
- The installed capacity of the CSP plant.
- The solar multiple.
- The size of the thermal storage.

As a result, the optimal sizing of the hybrid PV-CSP plant is highly dependent on these decision parameters.

Overall, the LCOE and the capacity factor (as well as the annual energy) represent two conflicting functions, which means that a trade-off must be found between them when choosing the decision parameters for the optimal sizing of hybrid PV-CSP plants. Therefore, optimal sizing of PV-CSP hybrid plants requires an optimization approach.

References

1. Bousselamti, L., Cherkaoui, M.: Modelling and assessing the performance of hybrid PV-CSP plants in morocco: a parametric study. *Int. J. Photoenergy* (2019)
2. Pan, C.A., Dinter, F.: Combination of PV and central receiver CSP plants for base load power generation in South Africa. *Solar Energy* **146**, 379–388 (2017)
3. Bousselamti, L., Ahouar, W., Cherkaoui, M.: Multi-objective optimization of PV-CSP system in different dispatch strategies, case of study: Midelt city. *J. Renew. Sustain. Energy* **13**(1), 013701 (2021)

4. Aguilar-Jiménez, J.A., Velázquez, N., Acuña, A., Cota, R., González, E., González, L., Islas, S.: Techno-economic analysis of a hybrid PV-CSP system with thermal energy storage applied to isolated microgrids. *Solar Energy* **174**, 55–65 (2018)
5. Shen, W., Chen, X., Qiu, J., Hayward, J.A., Sayeef, S., Osman, P., Dong, Z.Y.: A comprehensive review of variable renewable energy levelized cost of electricity. *Renew. Sustain. Energy Rev.* **133**, 110301 (2020)
6. Darling, S.B., You, F., Veselka, T., Velosa, A.: Assumptions and the levelized cost of energy for photovoltaics. *Energy Environ. Sci.* **4**(9), 3133–3139 (2011)
7. Kost, C., Shammugam, S., Jeulch, V., Nguyen, H., Schlegl, T.: Levelized Cost of Electricity Renewable Energy Technologies, vol. 144. Fraunhofer Institute for Solar Energy Systems ISE (2013)
8. Bouhal, T., Agrouaz, Y., Kousksou, T., Allouhi, A., El Rhafiki, T., Jamil, A., Bakkas, M.: Technical feasibility of a sustainable Concentrated Solar Power in Morocco through an energy analysis. *Renew Sustain. Energy Rev.* **81**, 1087–1095, 013701 (2018)
9. Photovoltaic Geographical Information System interface. <https://ec.europa.eu/jrc/en/PVGIS/tools/tmy>
10. Awasthi, A., Shukla, A.K., SR, M.M., Dondariya, C., Shukla, K.N., Porwal, D., Richhariya, G.: Review on sun tracking technology in solar PV system. *Energy Rep.* **6**, 392–405 (2020)
11. Salgado-Conrado, L.: A review on sun position sensors used in solar applications. *Renew. Sustain. Energy Rev.* **82**, 2128–2146, 013701 (2018)
12. Abdeen, E., Orabi, M., Hasaneen, E.S.: Optimum tilt angle for photovoltaic system in desert environment. *Solar Energy* **155**, 267–280, 013701 (2017)
13. Dey, S., Lakshmanan, M.K., Pesala, B.: Optimal solar tree design for increased flexibility in seasonal energy extraction. *Renew. Energy* **125**, 1038–1048, 013701 (2018)
14. Jacobson, M.Z., Jadhav, V.: World estimates of PV optimal tilt angles and ratios of sunlight incident upon tilted and tracked PV panels relative to horizontal panels. *Solar Energy* **169**, 55–66 (2018)
15. Al Garni, H.Z., Awasthi, A., Wright, D.: Optimal orientation angles for maximizing energy yield for solar PV in Saudi Arabia. *Renew. Energy* **133**, 538–550, 013701 (2019)

Chapter 10

Optimal PV-CSP System Sizing Using Mono Objective Optimization



10.1 Introduction

Recently, PV-CSP hybridization has received considerable global attention to satisfy requested load. This chapter aims to propose a methodology for optimal sizing of PV-CSP plants using the hybrid PSO-CS (Particle Swarm Optimization-Cuckoo Search) algorithm. The optimization problem aims to minimize the LCOE (Levelized cost of electricity) at a predetermined level of capacity factor value. In this study, two types of load profile were investigated. The optimization problem is solved by the PSO-CS algorithm based on the penalty function, by considering the PV and CSP installed capacity, the solar multiple, and the size of the thermal storage system as decision variables.

The comparisons between different configurations obtained have been carried out to show the influence of the system efficiency and load profile on PV-CSP optimal sizing. As well as a comparative study between the proposed solutions for a PV-CSP hybrid system and a CSP system alone is performed to show the cost-effectiveness of hybrid PV-CSP systems.

10.2 Optimization Problem Statement

10.2.1 Objective Function

Levelized cost of electricity (LCOE): The LCOE is considered as an economic evaluation indicator for the hybrid power systems. It is a key technical element which can allow decision makers to compare different energy technologies even if the installed capacity and the initial investment cost are different [1]. The LCOE of a PV-CSP hybrid plant is calculated according to the Eq. (10.1).

$$LCOE_{PV-CSP} = \frac{CAPEX_{CSP} + \sum_{t=1}^T \frac{OPEX_{CSP}}{(1+r)^t} + CAPEX_{PV} + \sum_{t=1}^T \frac{OPEX_{PV}}{(1+r)^t}}{\sum_{t=1}^T \frac{E_{CSP} f_a (1-d_{CSP})^t + E_{PV} (1-d_{PV})^t}{(1+r)^t}} \quad (10.1)$$

Where, $(CAPEX_{CSP}, CAPEX_{PV})$ are the initial investment, $(OPEX_{CSP}, OPEX_{PV})$ are the annual costs, (E_{CSP}, E_{PV}) are the first-year energy production, (E_{CSP}, E_{PV}) are the annual factors of degradation, (i) is the discount rate, (T) is the system lifetime and (f_a) is the factor disponibility of CSP plant the disponibility factor of CSP plant is calculated according to [2, 3]:

- The number of startups and shutdowns of the turbine.
- The nature of the start (Cold, warm and hot start).
- The total hour operation of the turbine.

10.2.2 Constraint

Capacity factor (CF): To ensure system efficiency, the capacity factor is used as the efficiency index of the hybrid PV-CSP generation system. The PV-CSP system must meet the desired load with a specified capacity factor value [4].

The optimization problem is based on the minimization of the LCOE at a specified level of efficiency identified by the capacity factor.

10.2.3 Decision Variables

The optimized variables are PV plant capacity (P_{pv}), CSP plant capacity (P_{csp}), solar multiple (SM) and TES size (h_{tes}) which subject to the maximum and minimum value as follows (10.2).

$$\begin{cases} P_{pv,min} \leq P_{pv} \leq P_{pv,max} \\ P_{csp,min} \leq P_{csp} \leq P_{csp,max} \\ SM_{min} \leq SM \leq SM_{max} \\ h_{tes,min} \leq h_{tes} \leq h_{tes,max} \end{cases} \quad (10.2)$$

10.3 Optimization Algorithm

One of the most critical engineering problems is to minimizing losses or maximizing benefits of engineering systems. In many fields of research, the optimization problems cannot be easily solved because of the complexity of the engineering systems. For this reason, optimization algorithms are required. To determine the optimal

solution for an optimization problem, several approaches could be investigated. In fact, there are many different optimization algorithms which have been developed to solve maximization or minimization problems. It should be mentioned that each optimization algorithm is able to solve a range of optimization problems [4–6].

The presented chapter aims to show the utilization of the hybrid particle swarm optimization-Cuckoo search (PSO-CS) as an optimization algorithm to solve the PV-CSP sizing problem.

PSO mechanism is generally based on the concept of swarm behavior. The algorithm is initiated by creating population of particles which represents problem solutions in the search space. Each particle tries to improve its position ($x_i(t)$) and velocity ($v_i(t)$) according to its best personal ($P_{i,best}$) experience, as well as the best experience of the swarm (G_{best}) [4, 6].

The position and velocity calculation requires the use of the following mentioned system of Eqs. 10.3. The velocity vector incorporated historical best solution of particle, best global solution and PSO algorithm parameters (c_1 , c_2 and w) [4, 6].

$$\begin{cases} v_i(t+1) = wv_i(t) + c_1r_1(P_{i,best}(t) - x_i(t)) + c_2r_2(G_{best}(t) - x_i(t)) \\ x_i(t+1) = x_i(t) + v_i(t+1) \end{cases} \quad (10.3)$$

Where, w is the coefficient of inertia, c_1r_1 and c_2r_2 are acceleration coefficients.

Cuckoo search (CS) algorithm is introduced by Yang and Deb in 2009. The idea of this metaheuristic mechanism is based on the breeding behavior of some cuckoo birds. Some species of cuckoo lay their eggs on the nests of other birds. The cuckoo's egg faces two situations: Firstly, it is discovered by the host bird and then it will be discarded. Second, it is undetected then the cuckoo's eggs hatch usually earlier than the host eggs and the young cuckoo birds will push host eggs out of the nest. Scientific studies show that female cuckoos are often highly specialized in mimicking color and pattern of the host's eggs selected, as well as, young cuckoo birds can mimic the call of host's bird to access to feeding. Based on this metaphor, the CS algorithm was built with twice times creating new solutions through Levy flight and discovery of strange egg as follows in Eq. (10.4) [7, 8].

$$x_i(t+1) = x_i(t) + \alpha \oplus \text{levy}(\lambda) \quad (10.4)$$

Where, λ and σ are calculated using Eqs. 10.5 and 10.6, respectively [7, 8].

$$\text{levy}(\lambda) = \frac{\sigma \mu}{|\tau|^{\frac{1}{\beta}}} \quad (10.5)$$

$$\sigma = \left(\frac{\Gamma(1+\beta) \sin(\frac{\pi\beta}{2})}{\Gamma(\frac{1+\beta}{2}) \beta 2^{\frac{\beta-1}{2}}} \right)^{\frac{1}{\beta}} \quad (10.6)$$

Particle swarm optimization-cuckoo search (PSO-Cuckoo) is a compound optimization algorithm, the Cuckoo method is investigated to enhance the PSO algorithm. In

this calculation process, the excellent optimization ability of PSO is preserved but the performance and the convergence speed is improved by integrating the effect of levy flight in Cuckoo. Thus, the proposed PSO-CS algorithm is detailed as follows [9, 10].

Step 1: Define the objective function ($f(x)$).

Step 2: Initialize parameters of PSO and CS algorithms (Inertia weight (w), personal learning coefficient (c_1), global learning coefficient (c_2), Probability of discovery of alien egg (pa), maximum number iteration (N), population size (n_{pop}).

Step 3: Generate randomly an initial population of particles, uniformly distributed in the search space, $X_i = (x_1, \dots, x_{N_{pop}})$, each particle x_i is a D dimensional vector.

Step 4: Evaluate the fitness value of each particles, $F_i = (f(x_1), \dots, f(x_{N_{pop}}))$.

Step 5: Initialize randomly the velocity ($v_i(t)$) of each particle.

Step 6: Set the initial position as a personal best position for the particle (P_{best}).

Step 7: Select the particle with minimum fitness value in the swarm (G_{best}).

while ($t \leq N_{iter}$)

Step 8: Update velocity ($v_i(t)$) and position ($x_i(t)$) for each particle according to the Eqs. (10.7).

$$\begin{cases} v_i(t+1) = wv_i(t) + (c_1 \oplus \text{levy}(\lambda))(P_{i,best}(t) - x_i(t)) + (c_2 \oplus \text{levy}(\lambda)) \\ \quad (G_{best}(t) - x_i(t)) \\ x_i(t+1) = x_i(t) + v_i(t+1) \end{cases} \quad (10.7)$$

Step 9: Evaluate the fitness value of each particle.

Step 10: Update the personal best position for each particle (P_{best}).

Step 11: Select the particle with minimum fitness value in the swarm (G_{best}).

Step 12: Generate new solutions ($x_{i,new}$) considering the probability coefficient (pa) and evaluate their fitness value (Eq. 10.8).

$$x_{i,new}(t) = \begin{cases} x_i(t) + \text{rand}(x_{rand1} - x_{rand2}) & \text{rand} > pa \\ x_i(t) & \text{else} \end{cases} \quad (10.8)$$

Step 13: Replace current solutions with new solutions (Eq. (10.9)).

$$x_i(t) = \begin{cases} x_i(t) = x_{i,new} & \text{if } f(x_{new}) \leq f(x_j) \\ x_i(t) & \text{else} \end{cases} \quad (10.9)$$

Step 14: Rank the solutions and find the current best solution.

Step 15: Update the inertia factor.

End while

Step 16: Process results and visualizing.

To evaluate the effectiveness of the PSO-CS algorithm compared to the PSO and CS algorithms, five independent runs were performed for each algorithm using the test functions shown in Table 10.1.

Table 10.1 Mathematical test functions

Test function	Label	dimension (d)	searche space	Global minimum
Ackley	F1	4	$[-32.768, 32.768]$	0
Rastrigin	F2	3	$[-5, 12, 5, 12]$	0
Griewank	F3	2	$[-600, 600]$	0
Sphere	F4	10	$[-5.12, 5.12]$	0

Table 10.2 Statistics for algorithms (PSO, CS et PSO-CS)

Function	Statistics	PSO	CS	PSO-CS
F1	Min	0,00433	0,00051	1,36e-5
	Moyenne	0,00642	0,00160	2,29e-5
	STD.	1,8e-6	4,47e-7	1,13e-10
F2	Min	4,09e-6	1,34e-5	0
	Moyenne	2,07e-4	2,77e-5	1,4e-4
	STD.	4,67e-8	2,66e-9	2,22e-8
F3	Min	3,74e-3	1e-4	2e-5
	Moyenne	6,18e-3	4,14e-4	3,15e-3
	STD.	5,46e-7	2,22e-6	1,2e-5
F4	Min	4,5e-3	6,7e-3	3,19e-6
	Moyenne	5,78e-3	8,36e-3	1,92e-5
	STD.	8,09e-7	7,97e-7	2,79e-11

$$F1(x) = -20 \exp \left(-0, 2 \sqrt{\frac{1}{d} \sum_{i=1}^d x_i^2} \right) - \exp \left(\frac{1}{d} \sum_{i=1}^d \cos(2\pi x_i) \right) + 20 + \exp(1)$$

$$F2(x) = 10d + \sum_{i=1}^d (x_i^2 - 10 \cos(2\pi x_i))$$

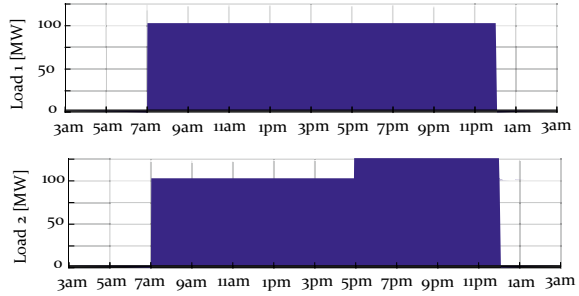
$$F3(x) = \sum_{i=1}^d \frac{x_i^2}{4000} - \prod_{i=1}^d \cos\left(\frac{x_i}{\sqrt{i}}\right) + 1$$

$$F4(x) = \sum_{i=1}^d x_i^2$$

The Table 10.2 shows the basic statistics (minimum, mean and standard deviation) for each algorithm. It is clear that the PSO-CS algorithm has a minimum deviation, which makes it better than the PSO and CS algorithms.

Table 10.3 PSO-CS parameters

N_{pop}	50	N_{iter}	100
c_1	2	c_2	2
w	0.9	pa	0.25

Fig. 10.1 Load profiles

10.4 Result and Discussion

In this chapter, the formulated hybrid PV-CSP system design problem is implemented to be solved with PSO-CS optimization algorithm. Indeed, Table 10.3 presents the parameters fixed in the PSO-CS optimization process.

The optimization case aims to provide an optimal PV-CSP configuration by mean of minimizing the electricity cost (LCOE) at a critical level of capacity factor value (CF). The problem statement in this case study is written as follows (10.10) [4].

$$\begin{cases} f_{obj} = \min(LCOE) \\ CF \geq CF_{min} \end{cases} \quad (10.10)$$

Indeed, the decision variables of the proposed plant was optimized to provide an optimal PV-CSP configuration for the optimization case study.

In this chapter, the PV-CSP system is suggested to satisfy two types of load as illustrated in Fig. 10.1.

10.4.1 Case 1

The optimization of PV-CSP plant is performed at different values of CF in order to determine the optimal PV-CSP system configuration with minimum LCOE to satisfy load 1 (i.e. Baseload).

In this case, optimal configurations of PV-CSP plant performed at different levels of CF (60, 70, 80 and 90%) using the proposed algorithm (PSO-CS) were independently

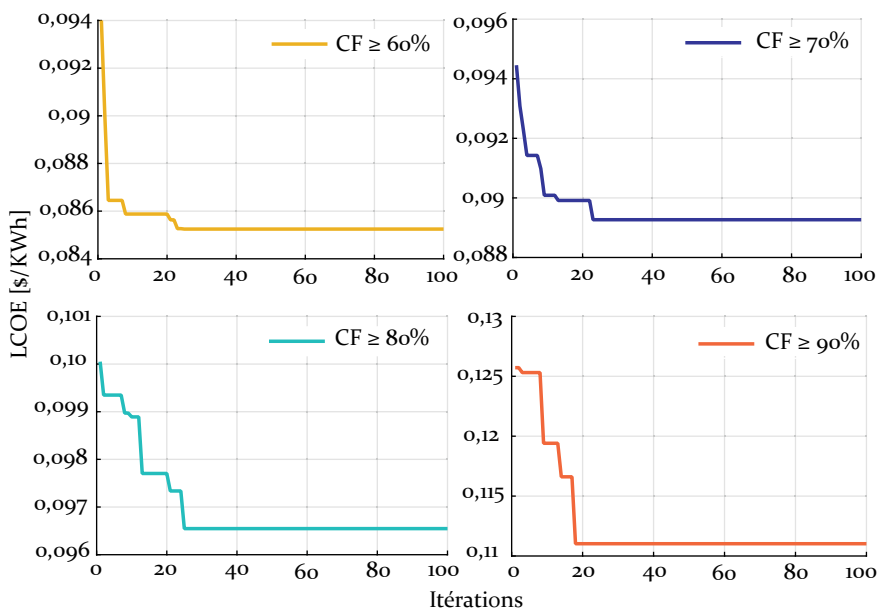


Fig. 10.2 The convergence of PSO-CS algorithm (Case 1, Load 1)

obtained. Figure 10.2 shows the convergence plot of the algorithm for each CF level which is defined by the user.

As can be seen in Fig. 10.2, the minimum LCOE is achieved in each simulation case (CF level) which shows a good convergence of the proposed PSO-CS algorithm. For each CF level, the optimization results were examined individually and presented in Table 10.4.

Careful examination of Table 10.4 reveals that the PV-CSP configuration with high efficiency ($CF \geq 90\%$) is more costly than other configurations. Therefore, the most efficient PV-CSP configuration requests a large solar field size and more hours of thermal storage.

Overall, for each simulation, different value of decision variables (i.e. P_{pv} , P_{csp} , SM and h_{tes}) were obtained. Increasing the value of minimum CF requires a low increase in the PV installed capacity as well as a high increase in the CSP sizing (P_{csp} , SM and h_{tes}), which involves that the LCOE and efficiency of PV-CSP plant increase.

According to these different simulations, the global minimum obtained corresponds to the case where the minimum value of the capacity factor is 60%, due to the reduced size of the PV-CSP plant. In this case, the plant satisfies only 60% of the requested load.

Table 10.4 Optimization results (Load 1)

	$CF \geq 60\%$	$CF \geq 70\%$	$CF \geq 80\%$	$CF \geq 90\%$
	Configuration A	Configuration B	Configuration C	Configuration D
P_{pv} [MW]	147	147	168.5	155.5
P_{csp} [MW]	54	77	86.3	86.7
SM	1.79	2	2.65	4
h_{tes} [h]	11	10	10.7	19
LCOE [\$/KWh]	0.0852	0.0892	0.0965	0.111

10.4.2 Case 2

In this case, the PV-CSP system is optimized using the proposed hybrid PSO-Cuckoo algorithm at $CF \geq 90\%$ in order to meet load 2. Figure 10.3 illustrates the convergence plot of the PSO-CS respecting the CF inequality constraint. The optimal configuration that correspond to $CF \geq 90\%$ is shown in Table 10.5.

To satisfy load 2 with minimum LCOE, the optimal PV-CSP configuration consists of an installed capacity of 152.5MW for PV plant and 105MW for CSP plant with a SM of 3.55 and 18 hours of thermal storage. The PV-CSP system was able to satisfy both loads (load 1: baseload and load 2: base and peak load) which prove that the PV-CSP plant is flexible in varying its hourly production levels with requested demand.

By comparing both configuration (configuration D with configuration E), the value of PV installed capacity presents a slight difference in both configurations, which explain that the PV plant contributes to satisfy load during daytime and didn't in night peak hours due to the absence of a storage system.

The solar field size (P_{csp} , SM) in configuration E is larger than the solar field size in configuration D. This result is expected due to the fact that with increasing the load level requested (the load 1 presents a baseload throughout the day and night whereas, the load 2 presents a baseload throughout the day and a peak load in the night), the solar field must be extended to generate more excess thermal energy to be stored for night use. The solar field extension leads to an increase in the investment cost, which explains the increase of LCOE in configurations E compared to configurations D.

10.4.3 Comparative Study (A PV-CSP Plant and a CSP Plant)

In order to show the performance of the hybrid PV-CSP plants, the PV-CSP configurations (configuration D and E) are compared to configurations of CSP plant based on the same optimization problem statement already described. The optimal CSP configuration obtained by PSO-CS algorithm is reported in Table 10.6 for each load profile.

Fig. 10.3 The convergence of PSO-CS algorithm (Load 2)

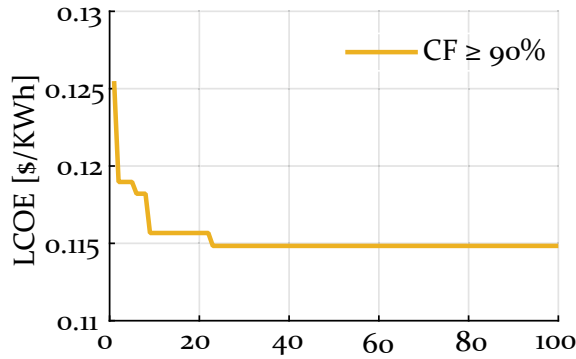


Table 10.5 Optimization results (Load 2)

	$CF \geq 90\%$
	Configuration E
P_{pv} (MW)	152.5
P_{csp} (MW)	105
SM	3.55
h_{tes} (h)	18
LCOE (\$/KWh)	0.1148

Table 10.6 Optimization results for CSP plant alone (Load 1 and 2)

	$CF \geq 90\%$	$CF \geq 90\%$
	Load 1	Load 2
	Configuration F	Configuration G
P_{csp} (MW)	163	173
SM	4	4
h_{tes} (h)	15	15
LCOE (\$/KWh)	0.1445	0.1449

As can be seen in Table 10.6, when the PV-CSP system (configuration D and E) and CSP system (configuration F and G) achieved the same value of capacity factor, the LCOE is higher for CSP plant alone than PV-CSP plant. The configuration F and G show an increase of 30 and 26% in the LCOE compared to the configuration D and E respectively. As a result, the hybrid PV-CSP plant is more efficient and economic than CSP plant alone.

10.5 Conclusions

The current chapter presents a techno-economic optimization of PV-CSP plant for Midelt city located in the atlas of Morocco. The PV installed capacity, CSP installed capacity, solar multiple and thermal storage size were optimized using PSO-CS algorithm to supply two types of load profile. In this chapter, the optimization case study seeks to minimize the electricity cost (LCOE) at a predefined level of efficiency identified by value of capacity factor.

The conclusion made based on discussion can be summarized as follows:

The PSO-Cuckoo algorithm shows its high robustness in term of fast convergence to find the optimal solution.

The minimum LCOE required for PV-CSP plant depends on the system efficiency. Therefore, to meet high efficiency (i.e. high capacity factor), the LCOE of the PV-CSP increase considerably due to the increase of PV-CSP system size.

The economic efficiency and dispatchability of PV-CSP plants are both affected by the ratio of CSP to total capacity.

The PV-CSP plants are flexible in satisfying both baseload and peak load due to the integration of thermal storage system.

The PV-CSP systems are a viable system than the CSP alone.

This optimization approach allows decision-makers to determine the optimal configuration of the PV-CSP that should be installed according to the requested load and specified criteria. This optimization approach can be deployed in every locations by considering only load profile and meteorological data.

References

1. Zurita, A., Mata-Torres, C., Cardemil, J.M., Guédez, R., Escobar, R.A.: Multi-objective optimal design of solar power plants with storage systems according to dispatch strategy. *Energy* **237**, 121627 (2021)
2. Guédez, R., Spelling, J., Laumert, B.: Reducing the number of turbine starts in concentrating solar power plants through the integration of thermal energy storage. *J. Solar Energy Eng.* **137**(1) (2015)
3. Guédez, R., Spelling, J., Laumert, B., Fransson, T.: Reducing the number of turbine starts in concentrating solar power plants through the integration of thermal energy storage. In: ASME Turbo Expo 2013: Turbine Technical Conference and Exposition. American Society of Mechanical Engineers Digital Collection (2013)
4. Bousselamti, L., Ahouar, W., Cherkaoui, M.: Mono-objective optimization of PV-CSP system using PSO algorithm. In: 2020 IEEE 4th International Conference on Intelligent Energy and Power Systems (IEPS), pp. 186–189. IEEE, sept. 2020
5. Yan, Z., Zhang, J., Zeng, J., Tang, J.: Nature inspired approach: An enhanced whale optimization algorithm for global optimization. *Math. Comput. Simul.* **185**, 1–46 (2021)
6. Taleb, M., Cherkaoui, M., Hbib, M.: Using particle swarm optimization to enhance PI controller performances for active and reactive power control in wind energy conversion systems. In: IOP Conference Series: Earth and Environmental Science, vol. 154, No. 1, p. 012015. IOP Publishing, May 2018

7. Yang, X.S., Deb, S.: Engineering optimisation by cuckoo search. *Int. J. Math. Model. Numer. Optim.* **1**(4), 330–343, 121627 (2010)
8. Nadjemi, O., Nacer, T., Hamidat, A., Salhi, H.: Optimal hybrid PV/wind energy system sizing: application of cuckoo search algorithm for Algerian dairy farms. *Renew. Sustain. Energy Rev.* **70**, 1352–1365, 121627 (2017)
9. Ding, J., Wang, Q., Zhang, Q., Ye, Q., Ma, Y.: A hybrid particle swarm optimization-cuckoo search algorithm and its engineering applications. *Math. Probl. Eng.* **2019**, 1–12, 121627 (2019)
10. Wang, F., Luo, L., He, X.-S., Wang, Y.: Hybrid optimization algorithm of PSO and Cuckoo Search. In: 2011 2nd International Conference on Artificial Intelligence, Management Science and Electronic Commerce (AIMSEC), Aug. 2011

Chapter 11

The Multi-objective Optimization of PV-CSP Hybrid System with Electric Heater



11.1 Introduction

In order to reduce dumped energy from PV plant, a PV-CSP coupled to an electric heater (EH) to form a PV-CSP-EH power system is proposed in this chapter. In such a system, the EH permit to recover the dumped energy by the PV plant and transform it into thermal energy to be stored in the TES system and used later. From the perspective of thermal power plant reconstruction, the hybrid system aims to maximize the capacity factor (CF) and minimize the levelized cost of electricity (LCOE) and total dumped energy (DE). The optimization problem is solved by multi-objective NSGA II optimization algorithm.

The optimization results obtained for the PV-CSP-EH plant will be compared to those obtained in the case of a reference PV-CSP plant without EH, in order to evaluate the techno-economic impact of the addition of an electric heater on PV-CSP plants.

11.2 Literature Review

The integration of TES system into a hybrid PV-CSP plant to store the excess thermal energy enables to increase the technical advantages of such a hybrid power plant. However, the TES system is coupled only to the CSP plant. In this chapter, a new equipment called electric heater (EH) is introduced in the PV-CSP hybrid system, enabling optimal use of available energy [1].

The EH converts the excess of electrical energy produced by the PV plant into thermal energy, which will then be stored in the TES system and can be used later to generate electrical energy via the power block. The EH not only allows the use of excess PV energy, but also increases the dispatchability of the hybrid PV-CSP system by adding another additional heat source for the TES system [1].

The use of the electric heater in a hybrid system to convert electrical energy to thermal energy has been proposed in various research studies already cited in the literature.

Yong et al. [2] studied a hybrid Wind-CSP system integrating an EH, to convert excess wind energy into thermal energy, to be used later. This study is focused on the analysis of the effect of integrating an EH on the performance of the hybrid wind-CSP plant under different weather conditions. The results of the evaluation showed that the integration of an EH allows to reduce the generation deviation from 5.15% to 0% for a clear day and from 47.49% to 31.74% for a partly cloudy day. As well as, the wind power reduction rate is also reduced from 52.59% on a clear day and 100% on a partly cloudy day.

Another study was conducted by Xing Gou et al. [3] also confirms that the addition of an EH can reduce the wind power curtailment in a hybrid system containing a CSP plant, a wind plant and a TES system.

Zeyu Ding et al. [4] performed an optimization approach based on the PSO algorithm for a hybrid wind-CSP plant incorporating an EH to maximize the economic performances of the proposed plant. The results showed that the integration of an EH improve the output power stability and reduce the wind power curtailment of the hybrid wind-CSP system.

The optimal sizing of a hybrid wind-CSP plant integrating an EH has been proposed by Rong Li et al. [5] The optimization problem consists in minimizing the LCOE while respecting a constraint related to the reliability of the system. The problem was solved using an optimization algorithm that combines two optimization methods, which are JADE and CPLEX. The simulation results obtained for the hybrid plant with an EH were compared with the simulation results of a similar hybrid plant without an EH. As a result, the LCOE is reduced by 0.004\$/kWh and 0.009\$/kWh when the value of the LPSP is 2% and 5% respectively.

A PV-Wind-CSP hybrid system integrating an EH has been proposed by Xue Han et al. [6] in order to satisfy the requested load. This research work aims to establish a dynamic simulation of the proposed hybrid system to analyze its techno-economic performances. The simulation results showed that the hybrid system fully satisfies the demanded load, as well as, the addition of the EH can allow to reducing the rejected energy.

Su Guo et al. [7] studied a hybrid wind-PV-TES system with an EH, using a multi-objective optimization approach. The optimization problem consists in minimizing the LCOE and maximizing the transmission channel utilization rate. This problem has been solved using PSO algorithm. The results deduced from the Pareto front and the decision making method, allow to confirm the cost effectiveness of the proposed system compared to a PV-wind plant and a PV-wind-Battery plant.

In this chapter, we are interested in integrating an electric heater (EH) into a PV-CSP system.

11.3 System Modeling

In this chapter, the study focuses on the techno-economic performances of a PV-CSP-EH system. The simplified schema of this power system is presented in the Fig. 11.1. It is mainly composed of three subsystems: PV, CSP and EH.

The modeling of the PV and the CSP system will be done according to the models already presented in Chap. 2. While the EH model allows the calculation of the thermal power produced based on the Eq. (11.1).

$$P_{out}^{EH} = \eta_{EH} P_{in}^{EH} \quad (11.1)$$

with, η_{EH} is the conversion efficiency of the EH, P_{in}^{EH} is the input power and P_{out}^{EH} is the output power of the EH.

For normal operation of the EH, its input power should not exceed its maximum capacity C_{EH} . The operation of the hybrid plant must meet the constraint mentioned in Eq. (11.2).

$$0 \leq P_{in}^{EH} \leq C_{EH} \quad (11.2)$$

The implemented dispatch strategy is based on the same principle of the strategy already stated in Chap. 8, by adopting the following assumptions:

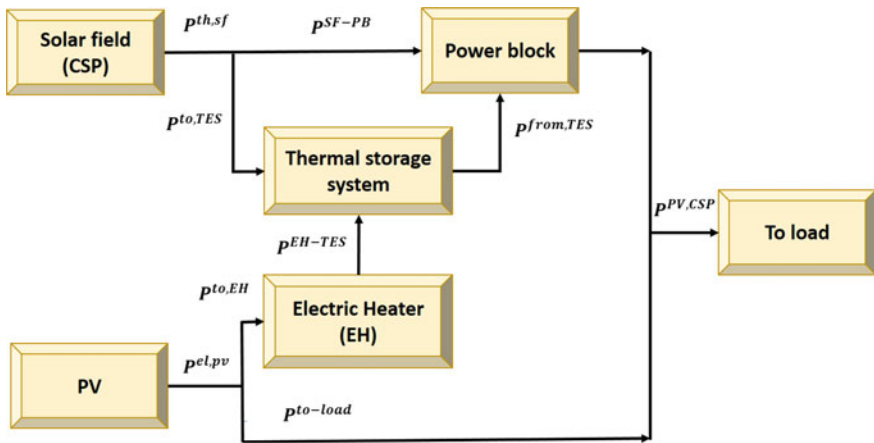


Fig. 11.1 Simplified diagram of the PV-CSP-EH plant $p^{th,SF}$: Thermal power produced by solar field (CSP), $p^{SF,PB}$: Thermal power directly used by the power block from the solar field, $p^{to,TES}$: Thermal power sent to the TES, $p^{from,TES}$: Thermal power used by the power block from the TES system, p^{PV} : Electrical power produced by the PV plant, $p^{to,load}$: Electrical power directly used to satisfy the load from the PV, $p^{to,EH}$: the electrical power rejected by the PV plant and which will be sent to the EH, $p^{EH,TES}$: Dumped electrical power and $p^{PV,CSP}$: Electrical power used to satisfy the load

- The excess electrical energy from the PV plant will be dumped if thermal storage system is full, otherwise it will be converted to thermal energy to be stored.
- If the TES system capacity is less than the excess electrical power, a part of the excess electrical power will be rejected.
- Excess energy from solar field is prioritized in storage over the energy generated by the EH.

11.4 Optimization Problem Statement

The PV-CSP-EH hybrid system aims to minimize the cost of electricity ($LCOE$), the dumped energy (DE) and simultaneously maximize the capacity factor (CF). The problem optimization is solved using a multi-objective optimization approach, in order to determine the trade-off between the three objective functions. The optimization problem is presented in the following mathematical formulation (Eq. (11.3)).

$$\begin{cases} f_{obj}(1) = \min(LCOE) \\ f_{obj}(2) = \min(DE) \\ f_{obj}(3) = \max(CF) \end{cases} \quad (11.3)$$

Five decision variables will be considered: P_{pv} , P_{csp} , C_{EH} , SM and h_{tes} . These decision variables are subject to satisfying the following constraints (Eq. (11.4)).

$$\begin{cases} P_{pv,min} \leq P_{pv} \leq P_{pv,max} \\ P_{csp,min} \leq P_{csp} \leq P_{csp,max} \\ C_{EH,min} \leq C_{EH} \leq C_{EH,max} \\ SM_{min} \leq SM \leq SM_{max} \\ h_{tes,min} \leq h_{tes} \leq h_{tes,max} \end{cases} \quad (11.4)$$

11.5 Multi-objective Optimization Algorithm

In practical, optimization problems can be treated as a single-objective or multi-objective optimization problem. The first optimization case seeks to optimize a single objective function to reach a unique optimal solution. However, complex systems usually involve performance objectives with conflicting characters. In the case, the optimization problem is expanded to a multi-objective framework [8].

In a multi-objective optimization problem, multiple conflicting objective functions must be optimized simultaneously. In this optimization case, the improvement of one objective function will inevitably result in the expense of other objective functions. This conflict arises frequently while attempting to achieve the best feasible technical performance at a low cost. Multi-objective optimization does not allow to find a unique and optimal solution but it introduces the concept of the Pareto front as

optimal solutions. The Pareto front is a set of solutions that correspond to the best trade-off between the different objective functions to be optimized [9, 10].

Bio-inspired metaheuristic algorithms are highly recommended for solving a variety of complex optimization problems. They have shown a high-level adaptability to solve multiple problems in various fields. Furthermore, the majority of these algorithms allow the possibility to modify their control parameters taking into account the complexity of the mathematical problem to be optimized. These metaheuristic algorithms can provide a unique solution or a set of optimal solutions, which allows a better diversification of the search space. Thus, Bio-inspired metaheuristic algorithms can be used to solve both single-objective optimization and multi-objective optimization [11, 12].

Several bio-inspired metaheuristic algorithms have already been developed to solve multi-objective optimization problems, which are classified into swarm intelligence and evolutionary optimization algorithms [10–12].

Evolutionary algorithms are inspired by the biological evolution of living species based on the principles of Darwinian theory (1985) [13]. These optimization algorithms are developed to solve several complex optimization problems. In the literature, many algorithms recently developed are based on evolutionary metaheuristics, such as, evolutionary strategy, genetic algorithms, genetic programming and differential evolution [13].

Genetic algorithms were initially developed by J. Holland in 1975. They are the most popular and widely used evolutionary algorithms [14]. Several versions of genetic algorithm have already been used in the literature. Among them, the Non-dominated Sorting Genetic Algorithm-II (NSGA-II) is the most commonly adopted to solve multi-objective problems. The NSGA-II algorithm is an improved version of the NSGA algorithm proposed in 1994 by Goldberg [15]. According to the literature, this optimization algorithm has been widely used for many global optimization problems [15]. The results reveal that NSGA-II is a robust algorithm in term of performance and fast convergence [14, 15]. As a result, it was chosen as the optimization algorithm used to solve the optimization problem described in this chapter.

11.6 Multi-criteria Decision-Making Method

The resolution of a multi-objective optimization problem based on the Pareto concept, leads to the identification of a set of possible solutions, among them no one can be prioritized. Multi-criteria decision-making (MCDM) method is a useful technique to clarify and justify the decision-maker's choices. It allows decision-makers to select the optimal solution by prioritizing their preferences and requirements. The analysis of a multi-objective optimization problem can be solved using a variety of MCDM techniques [16–18].

Among many MCDM methods that exist, the Technique for order of preference by similarity to ideal solution (TOPSIS) method was chosen due to its high frequency of use and simplicity. In spite of the large number of possible solutions obtained by

multi-objective optimization and displayed on the Pareto front, the TOPSIS method allows decision makers to select an optimal solution according to the importance weight value assigned to each objective function [16–18].

In this context, $G = (g_{ij})$ is the decision matrix, each objective function can be treated as a cost function or a benefit function, as well as, $V = (v_j)$ is the importance weight value according to each criterion function [17, 18].

Step1: Each objective function should be transformed into a non-dimensional variable which can be performed by using the following formula (11.5).

$$r_{ij} = \frac{G_{ij}}{\sqrt{\sum_{i=1}^N G_{ij}^2}} \quad (11.5)$$

Step 2: Using the following Eq. (11.6) to calculate the weighted normalized value.

$$w_{ij} = v_j r_{ij} \quad (11.6)$$

Step 3: Calculate the positive and negative solutions for each objective value using the following formulas (11.7) and (11.8).

$$w_j^+ = \begin{cases} \max(w_{ij}) & \text{if benefit criteria} \\ \min(w_{ij}) & \text{if cost criteria} \end{cases} \quad (11.7)$$

$$w_j^- = \begin{cases} \min(w_{ij}) & \text{if benefit criteria} \\ \max(w_{ij}) & \text{if cost criteria} \end{cases} \quad (11.8)$$

Step 4: calculate the separation of each objective value from the negative and positive solution using Eqs. (11.9) and (11.10) respectively.

$$d_i^+ = \sqrt{\sum_{i=1}^n (w_{ij} - w_j^+)^2} \quad (11.9)$$

$$d_i^- = \sqrt{\sum_{i=1}^n (w_{ij} - w_j^-)^2} \quad (11.10)$$

Step 5: Select the solution with the maximum value obtained by the Eq. (11.11) as an optimal solution.

$$R_i = \frac{d_i^-}{d_i^- + d_i^+} \quad (11.11)$$

11.7 Results and Discussion

In this section, the results obtained by using the multi-objective optimization approach of the hybrid PV-CSP-EH plant will be discussed in detail. The simulation results was generated by considering 150 generations of 50 individuals. Figure 11.2 illustrates the Pareto front obtained by genetic optimization for hybrid PV-CSP-EH. Each solution displayed in the Pareto front presents a trade-off between the three defined objective functions. The Pareto front help decision makers to select the suitable configuration according to their choice criteria. The results of Pareto front can be divided into four regions.

In the A–B region, the LCOE and DE decrease significantly, while the CF decreases slightly from 97.2% to 94.9%.

In the B–C region, a high decrease in the CF, LCOE and DE is observed.

In the C–D region, a moderate reduction in the CF, LCOE and DE is observed.

In the D–E region, a slight decrease in the LCOE and DE with a moderate decrease in the CF is shown.

It should be noted that the points A and E can be taken to be optimal solutions where the CF and the DE are the unique objective functions, respectively.

The B–C region indicates a good trade-off between the three objectives functions (CF, LCOE and DE), since the difference values of the three functions are not very expressive. Thus, it is considered to be the optimal region in the Pareto front.

The following Figs. 11.3, 11.4, 11.5, 11.6 and 11.7 illustrate the optimal Pareto front in terms of LCOE, DE, CF and a decision variable. These curves are constructed

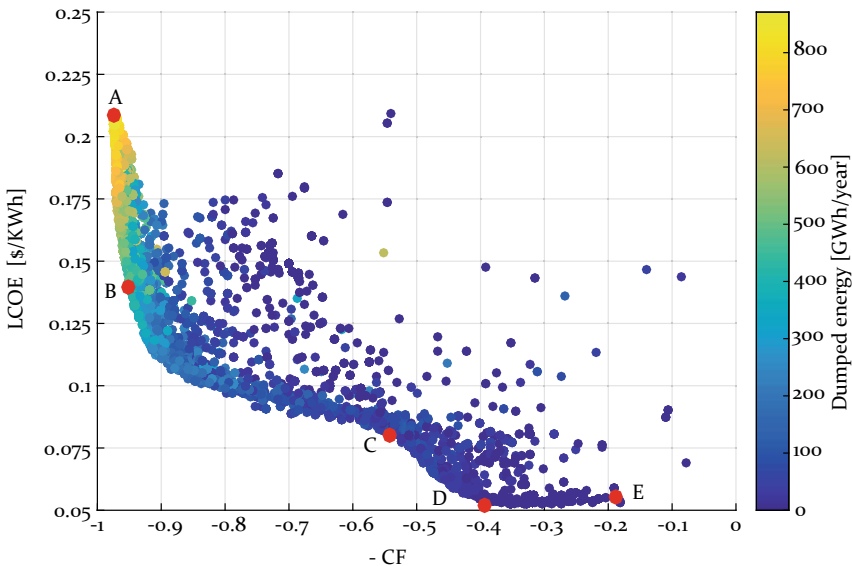


Fig. 11.2 Pareto front obtained by optimization of the PV-CSP-EH

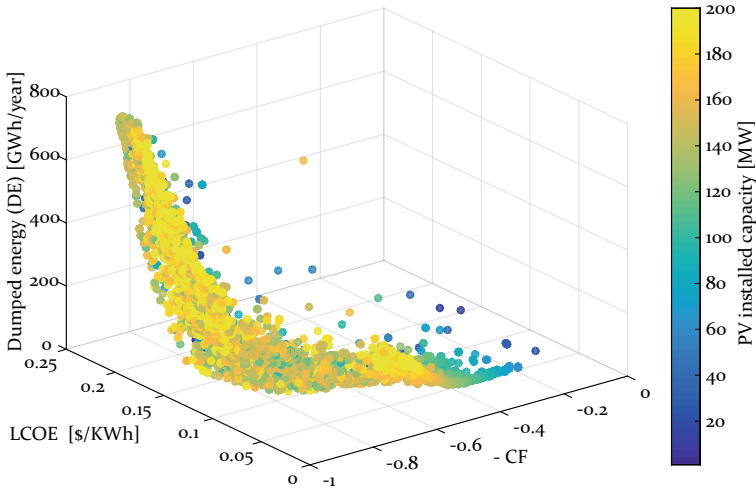


Fig. 11.3 Pareto front in terms of PV installed capacity

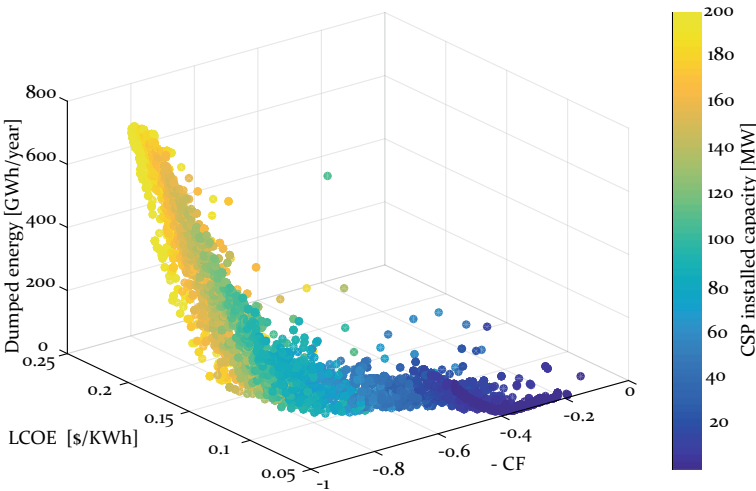


Fig. 11.4 Pareto front in terms of CSP installed capacity

by a large number of points, each one of them represents a particular configuration of the hybrid PV-CSP-EH plant.

The analysis of the above figures shows that each decision variable converges to well-defined value in the optimal region of the Pareto front.

It can be noted that the PV installed capacity converges to the values above 120MW, which leads to satisfy the requested load with a high CF and a low value of LCOE and DE (Fig. 11.3).

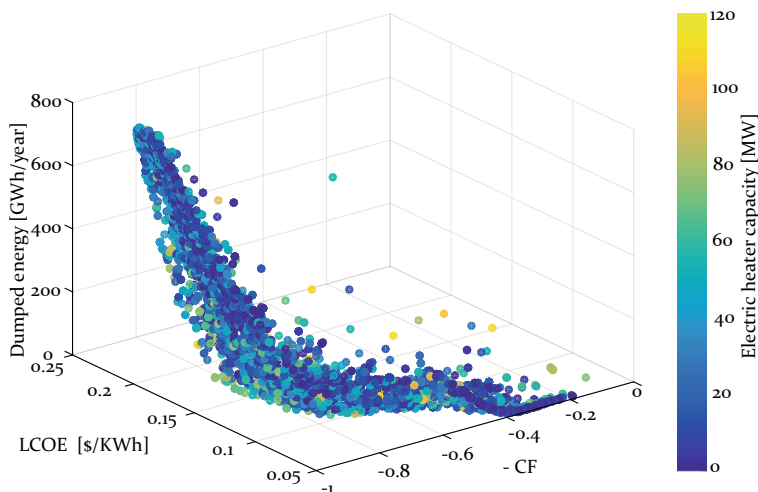


Fig. 11.5 Pareto front in terms of electric heater capacity

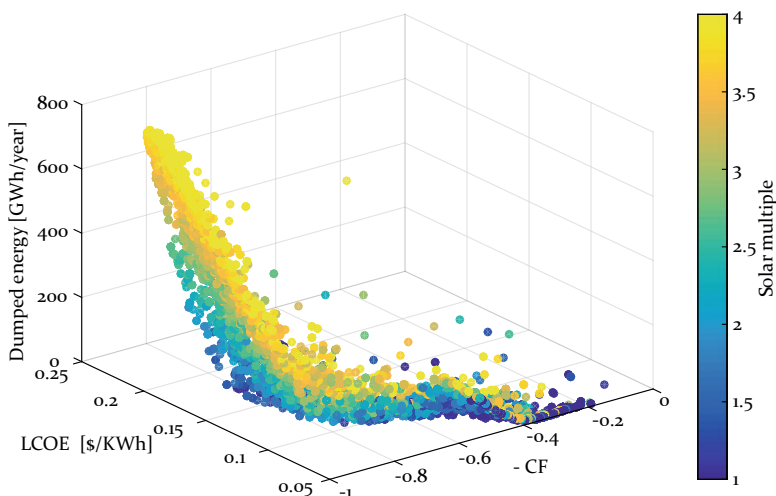


Fig. 11.6 Pareto front in terms of solar multiple

The increase of the CSP installed capacity above 140MW, allows satisfying the load with a high capacity factor but leads to a significant increase in LCOE and DE. Which explained by an oversizing of the PV-CSP-EH hybrid plant compared to the requested load. In the optimal region of the Pareto front, the CSP installed capacity converges to the between 80MW and 120MW (Fig. 11.4). As well as the capacity of the EH (Fig. 11.5) and solar multiple (Fig. 11.6) converge to the values below 70MW and 2.5, respectively.

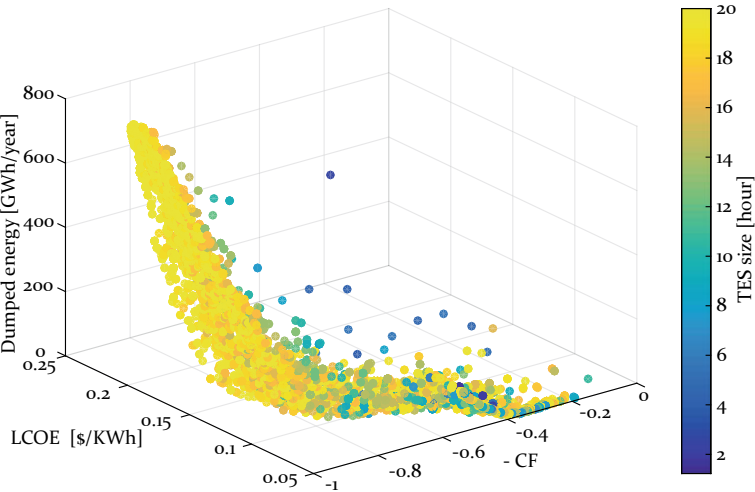


Fig. 11.7 Pareto front in terms of TES size

Table 11.1 Optimization results (PV-CSP-EH power system)

Solution	P_{PV} (MW)	P_{CSP} (MW)	SM	h_{tes} (h)	C_{EH} (MW)	CF (%)	LCOE (\$/KWh)	DE (GWh/year)
	$w_1 = \frac{1}{3}, w_2 = \frac{1}{3}$ et $w_3 = \frac{1}{3}$							
a	183	81.5	1.7	9.54	40.6	75.3	0.0914	54.52
	$w_1 = \frac{1}{2}, w_2 = \frac{1}{4}$ et $w_3 = \frac{1}{4}$							
b	164	67.2	1	11.4	11.88	45.5	0.0625	21.99
	$w_1 = \frac{1}{4}, w_2 = \frac{1}{2}$ et $w_3 = \frac{1}{4}$							
c	200	104	1.65	16	67.63	85.64	0.1123	42.86
	$w_1 = \frac{1}{4}, w_2 = \frac{1}{4}$ et $w_3 = \frac{1}{2}$							
d	167	85.7	1.62	9.6	50.91	74.37	0.0916	36.5

w_1 is the weight assigned to the LCOE function, w_2 is the weight assigned to the CF function and w_3 is the weight assigned to the DE function

In terms of the influence of thermal storage size, it can also be noted that a high TES sizes are requested for optimal configurations due to the large amount of thermal energy to be stored (Fig. 11.7). In order to ensure plant operation during peak hours and to minimize the energy rejected by both PV and CSP plant. A lower TES size would not allow the hybrid plant to guarantee high satisfaction rate of requested load, thus, high TES size are most suitable for base load operation.

To select the final optimal solution from results obtained by the Pareto front, the TOPSIS method has been applied to make this step easier. The optimization results based on different optimization weights assigned to each objective function will be presented in Table 11.1.

Table 11.2 Optimization results (PV-CSP power system)

Solution	P_{PV} (MW)	P_{CSP} (MW)	SM	h_{tes} (h)	CF (%)	LCOE (\$/KWh)	DE (GWh/year)
	$w_1 = \frac{1}{3}, w_2 = \frac{1}{3} \text{ et } w_3 = \frac{1}{3}$						
a	183	81.5	1.7	9.54	74	0.0922	85.9
	$w_1 = \frac{1}{2}, w_2 = \frac{1}{4} \text{ et } w_3 = \frac{1}{4}$						
b	164	67.2	1	11.4	45	0.0627	31.58
	$w_1 = \frac{1}{4}, w_2 = \frac{1}{2} \text{ et } w_3 = \frac{1}{4}$						
c	200	104	1.65	16	83.22	0.1144	109.70
	$w_1 = \frac{1}{4}, w_2 = \frac{1}{4} \text{ et } w_3 = \frac{1}{2}$						
d	167	85.7	1.62	9.6	73.23	0.0921	61.43

According to Table 11.1, when the optimization weight assigned to LCOE function is high (b), the obtained value of the CSP installed capacity and the solar multiple are small. When the optimization weight assigned to CF function is high (c), the CSP installed capacity and the TES size are also high. As results, the increase of the PV installed capacity leads to a high reduction in the LCOE. As well as, the increase of the CSP installed capacity, allows to a significant increase in the CF. To show the techno-economic impact of integrating an EH into a hybrid PV-CSP system, the results obtained in the case of the PV-CSP-EH hybrid plant (Table 11.1) are compared to those obtained by a PV-CSP hybrid plant (Table 11.2) for the same mentioned configurations.

By comparing the performances of PV-CSP-EH and PV-CSP plants, it was found that the LCOE is increased by 0.8%, 0.3%, 2%, and 0.6%, respectively, for configurations a, b, c and d. As well as, The CF is reduced by 1.7%, 1%, 2.7% and 1.4%, respectively. When comparing the DE values, it can be noted that the DE is reduced by 36.5%, 30.4%, 60.8%, and 41%, respectively, for each configurations of PV-CSP-EH compared to PV-CSP plant.

Compared to a PV-CSP plant, the performances of a hybrid PV-CSP-EH plant show a high reduction in dumped energy with a slight difference in the capacity factor and LCOE.

The optimization results show that the addition of an EH to the hybrid PV-CSP plant allows to achieves high dumped energy, high capacity factor and low LCOE compared to PV-CSP without EH. Integrating an EH improve significantly the efficiency of hybrid PV-CSP systems. However, from the economic viewpoint, it is always indispensable to select the most cost-effective EH capacity to make the system always beneficial.

11.8 Conclusions

In this chapter, a PV-CSP hybrid system coupled to an electric heater (EH) has been modeled and optimized to satisfy a requested base-load. The optimization problem is based on three objective functions that include minimizing the LCOE and total dumped energy (DE) while maximizing the capacity factor. The resolution of the optimization problem was performed by the NSGA II algorithm. Final optimal configurations are obtained by the Pareto front and decision-making method.

The performance of the PV-CSP-EH system is analyzed and compared with the PV-CSP system based on the same configurations. The results show that the proposed system effectively decrease the total dumped energy and presents a better efficiency and economy performance.

References

1. Li, J., Qi, W., Yang, J., He, Y., Luo, J., Guo, S.: The capacity optimization of wind-photovoltaic-thermal energy storage hybrid power system. In: E3S Web of Conferences, vol. 118, p. 02054. EDP Sciences (2019)
2. Yang, Y., Guo, S., Liu, D., Li, R., Chu, Y.: Operation optimization strategy for wind-concentrated solar power hybrid power generation system. *Energy Convers. Manag.* **160**, 243–250 (2018)
3. Gou, X., Chen, Q., Hu, K., Ma, H., Chen, L., Wang, X.H., Min, Y.: Optimal planning of capacities and distribution of electric heater and heat storage for reduction of wind power curtailment in power systems. *Energy* **160**, 763–773 (2018)
4. Ding, Z., Hou, H., Yu, G., Hu, E., Duan, L., Zhao, J.: Performance analysis of a wind-solar hybrid power generation system. *Energy Convers. Manag.* **181**, 223–234 (2019)
5. Li, R., Guo, S., Yang, Y., Liu, D.: Optimal sizing of wind/concentrated solar plant/electric heater hybrid renewable energy system based on two-stage stochastic programming. *Energy* **209**, 118472 (2020)
6. Han, X., Pan, X., Yang, H., Xu, C., Ju, X., Du, X.: Dynamic output characteristics of a photovoltaic-wind-concentrating solar power hybrid system integrating an electric heating device. *Energy Convers. Manag.* **193**, 86–98 (2019)
7. Guo, S., He, Y., Pei, H., Wu, S.: The multi-objective capacity optimization of wind-photovoltaic-thermal energy storage hybrid power system with electric heater. *Solar Energy* **195**, 138–149 (2020)
8. Yang, X.S.: *Optimization Techniques and Applications with Examples*. Wiley (2018)
9. Cui, Y., Geng, Z., Zhu, Q., Han, Y.: Multi-objective optimization methods and application in energy saving. *Energy* **125**, 681–704 (2017)
10. Gunantara, N.: A review of multi-objective optimization: methods and its applications. *Cogent Eng.* **5**(1), 1502242 (2018)
11. Kar, A.K.: Bio inspired computing-a review of algorithms and scope of applications. *Expert Syst. Appl.* **59**, 20–32 (2016)
12. Chiroma, H., Herawan, T., Fister, I., Jr., Fister, I., Abdulkareem, S., Shuib, L., Abubakar, A.: Bio-inspired computation: recent development on the modifications of the cuckoo search algorithm. *Appl. Soft Comput.* **61**, 149–173 (2017)
13. Bozorg-Haddad, O., Solgi, M., Loáiciga, H.A.: *Meta-Heuristic and Evolutionary Algorithms for Engineering Optimization*. Wiley (2017)

14. Wang, Z., Sobey, A.: A comparative review between Genetic Algorithm use in composite optimisation and the state-of-the-art in evolutionary computation. *Compos. Struct.* **233**, 111739 (2020)
15. Deb, K., Agrawal, S., Pratap, A., Meyarivan, T.: A fast elitist non-dominated sorting genetic algorithm for multi-objective optimization: NSGA-II. In: *International Conference on Parallel Problem Solving from Nature*, pp. 849–858. Springer, Berlin, Heidelberg (2000)
16. Bousselamti, L., Ahouar, W., Cherkaoui, M.: Multi-objective optimization of PV-CSP system in different dispatch strategies, case of study: Midelt city. *J. Renew. Sustain. Energy* **13**(1), 013701 (2021)
17. Roszkowska, E.: Multi-criteria decision making models by applying the TOPSIS method to crisp and interval data. *Mult. Criteria Decis. Mak./Univ. Econ. Katowice* **6**(1), 200–230 (2011)
18. Balioti, V., Tzimopoulos, C., Evangelides, C.: Multi-criteria decision making using TOPSIS method under fuzzy environment. application in spillway selection. In: *Multidisciplinary Digital Publishing Institute Proceedings*, vol. 2, No. 11, p. 637 (2018)

Chapter 12

Summary and Scope



12.1 Summary of Full Text

The control and supervision of a wind energy conversion system based on squirrel cage induction generator connected to the grid is discussed in the first part of the book. The impact of this connection on the grid and the participation in ancillary services are examined.

A model of the Wind Energy Conversion System based on the squirrel cage induction generator connected to the grid through AC/DC/AC converters has been developed and the stability analysis of the power system has been performed. To improve the power quality and ensure efficient participation in auxiliary services, a fuzzy sliding mode control of the wind energy conversion system is developed. The comparative study is carried out to prove the effectiveness and robustness of the Fuzzy-SMC controller when the sliding surface is subjected to the variation of the LCL filter and DC bus parameters. The experimental results obtained, using the test bench set up in our laboratory, validate the proposed control and demonstrate its effectiveness. The Total Harmonic Distortion (THD) is reduced using the sliding mode control from $[THDV = 3.4\% \text{ f}, THDI = 12.4\% \text{ f}]$ to $[THDV = 2.6\% \text{ f}, THDI = 8.6\% \text{ f}]$ using Fuzzy-SMC. The obtained experimental results are in accordance with that of the simulation using the established model. The LCL filter attenuates harmonics better than the RL filter. The maximum value of THDV, using the RL filter, is $5.8\% \text{ f}$ to the fundamental. While this value is $2.9\% \text{ f}$ using the LCL filter. The THDI value with the LCL filter ($7.5\% \text{ f}$) is reduced compared to the RL filter ($8.9\% \text{ f}$).

Real-time monitoring of the wind farm and participation in frequency and voltage control are developed in this book. Two grid models are adopted, the first one is developed to obtain the possibility of voltage control by reactive power injection and the second one with parameterization possibility for frequency control by active power injection. A fuzzy hierarchical controller is suggested for voltage control and participation in primary frequency control. During voltage drop the controller ensures

a considerably reduced stabilization time. Deviations from the nominal values are limited and oscillations are damped effectively. In the event of power imbalance, this controller ensures better frequency and power response, in terms of fast response and meeting grid code requirements. The initial activation time and the time to full activation are less than the limit values. The fractional-order fuzzy controller (FOPI-Fuzzy-FOPI) for LVRT control for the uncompensated power network is proposed to improve the response of voltage and reactive power. The PSO algorithm is adopted to obtain the optimal parameters of the FO operators. This controller allows the WF to compensate the grid voltage and exhibit a behavior similar to that of the conventional power plant. The adopted supervision system drives all the wind turbine generators to work under different wind velocities and quite far from their saturation zone.

The modeling, optimization and sizing of PV-CSP hybrid systems, are addressed in the second part of the book in order to determine the technical and economic interest of PV-CSP hybridization. These objectives were achieved in several steps. From the literature review presented in the Chap. 7, it can be noted that renewable energy sources are increasingly popular as an alternative to thermal conventional sources to produce electricity. Almost in all examined systems that include the use of more than one alternative and/or conventional energy sources, it can be noticed that they show higher performance than power systems which only include one alternative energy source. In this context, the hybrid PV-CSP systems has attracted increasing interest due to the high potential of solar energy, the high decrease in the cost of PV production and the large-scale thermal storage that CSP allows. Through this chapter, a detailed model of PV system and CSP system based on parabolic trough technology are presented. The models of calcul can be applied for any chosen site based on its geographical and meteorological data, as well as the technical data related to each type of plant. The simulation model proposed for the PV and CSP power plant allow an annual simulation with a time step of 1 h, which is suited for the simulation of hybrid PV-CSP systems. To manage the power flows in the PV-CSP, a dispatch strategy was proposed based on the electricity tariff system to prioritize meeting the load during peak hours. From the parametric evaluation of the PV-CSP plant presented in Chap. 9, it can be conclude that the optimal sizing of PV-CSP hybrid plants is highly depend to decision variable which are; the PV and CSP installed capacity, the solar multiple and TES size. As well as, the best trade-off between its technical and economic performances. Therefore, optimal sizing of PV-CSP hybrid plants requires an optimization approach. Chapter 10 presents an optimal sizing method for PV-CSP hybrid systems based on a constrained mono-objective optimization approach, using hybrid PSO-CS algorithm. The results show that the proposed optimization algorithm is robust due to its ability to find the global optimum solution. As well as, the minimum cost electricity is highly depend on the system efficiency and the load profile to be satisfied. In comparison with CSP plant alone, the hybrid PV-CSP is more flexible and cost-effective in satisfying both load profiles. A multi-objective optimization of PV-CSP system integrating an electric heater is presented in Chap. 11. This optimization approach is based on minimizing the LCOE, the total dumped energy and maximizing the capacity factor. The multi-objective optimization approach has allowed getting the Pareto front, which is helpful for decision makers to

select the optimal configuration according to their selection criteria. The optimization results reveal a trade-off between the three defined objective functions. The final optimal configurations from Pareto front were obtained by implementing the TOPSIS method as a decision-making method. The performance of PV-CSP-EH is analysed and compared to a hybrid PV-CSP without an electric heater. The results show that adding an electric heater will significantly reduce the dumped energy, which improve the profitability of PV-CSP-EH systems.

12.2 Future Research Prospect

Somme directions of the present book will be addressed as future works for the first and second parts of the book. For the first part of the book:

1. The algorithms introduced in the Chaps. 4, 5, and 6 have been validated by simulations. Therefore, an experimental validation must be performed to confirm the results of the simulations.
2. In the first part of the book, all state variables are assumed to be measurable, which could not be the case in real systems. It then becomes necessary to develop a state observer to overcome this problem.
3. The filter LCL should be replaced. Therefore, the active filter Will be designed and implemented to reduce harmonics due to non-linear loads.

For the second part of the book:

1. Use other technical and economic parameters for a more thorough techno-economic evaluation of PV-CSP hybrid plants;
2. Extension of the studies performed in the case of PV-CSP-Wind hybrid systems;
3. Propose a dynamic dispatching strategy for PV-CSP hybrid plants using artificial intelligence techniques.

Appendix A

Part I: Parameters and Preliminaries of Wind Energy Conversion System and Controllers

A.1 Fuzzy Sliding Mode Control with LCL Filter

The parameters of the studied system and the nonlinear controls are given in Tables A.1 and A.2, respectively.

The IEEE Recommended Practices and Requirements for Harmonic Control in Electrical Power Systems are given in Table A.3. Table A.4 gives the limit values for harmonic voltage levels (in percent of nominal voltage) in MV, HV and EHV according to IEC 61000-3-6 standards of INTERNATIONAL ELECTROTECHNICAL COMMISSION (IEC) and adopted by “ONE” in Morocco :

The base parameters for per unit notation are: $\omega_b = 2\pi f_b$; $f_b = 50$ Hz; $V_b = 690$ V; $P_b = 3$ MW; $Z_b = V_b^2/P_b$, $L_b = Z_b/\omega_b$ and $S_b = P_b/0.9$.

The parameters of line, transformer and filter are given in Table A.5.

A.2 Supervisory System and Reactive Power Control

The parameters of reactive power controller are:

PI : $k_i = 12.21$ and $k_p = 0.063$.

PIFPI : $k_e = 0.5$, $k_{pe} = 0.4$, $k_i = 12.21$ and $k_p = 0.063$.

The parameters of the voltage controller are:

PIFPI : $k_e = 0.4$, $k_{pe} = 0.8$, $k_i = 120$ and $k_p = 6$.

PI: $k_p = 120$ and $k_i = 6$ (Table A.6).

Table A.1 Parameters of the inverter, RL filter and LCL filter

Symbol	Quantity	Value
L_I	Inductance of the inverter side of the LCL filter	0.1073 pu
L_G	Inductance of the grid side of the LCL filter	0.0061 pu
R_F	LCL filter resistance	3.404 pu
C_F	LCL filter capacitance	0.05 (pu)
R_{RL}	RL filter resistance	0.0036 (pu)
L_{RL}	RL filter inductance	0.18 (pu)
R_{on}	Internal resistance	10-6 Ohm
R_{snub}	Snubber resistance	106 Ohm
T_f	The fall time	10-6 s
T_t	Tail time	2.10-6 s
V_f	Forward voltage	1 V

Table A.2 Control system parameters in per unit notation

Controller	Parameter	Quantity Value	
SMC1	ε_{Ld}	Width of the sign function	0.15
	k_{Ld}	Amplitude of the sign function	2
SMC2	$\varepsilon_{Gd}, \varepsilon_{Gq}$	Width of the “sign” function	0.1
	k_{Gd}, k_{Gq}	Amplitude of the function “sign”	2
Fuzzy SMC	k_{e-DC}	Error gain at the input of the fuzzy logic block	1.16
	k_{u-DC}	Output gain of the fuzzy logic block	5
Fuzzy SMC2	k_{e-I}	Error gain at the input of the fuzzy logic block	3.5
	k_{u-I}	Output gain of the fuzzy logic block	2.5
PI	k_p	Proportional gain	14. 3781
	k_i	Integral gain	3.2×10^3

Table A.3 IEEE recommended practices and requirements for harmonic control in electrical power systems

INDIVIDUAL HARMONIC ORDER (ODD HARMONICS)						
I_{sc}/I_L	<11	$11 \leq h < 17$	$17 \leq h < 23$	$23 \leq h < 35$	$35 \leq h$	THD
<50	2.0	1.0	0.75	0.3	0.15	2.5
≥ 50	3.0	1.5	1.15	0.45	0.22	3.75
Even harmonics are limited to 25% of the odd harmonic limits above						
Current distortions that result in a dc offset, e.g., half-wave converters, are not allowed						
*All power generation equipment is limited to these values of current distortion, regardless of actual I_{sc}/I_L						
Where: I_{sc} = maximum short-circuit at PCC						
I_L = maximum demand load current (fundamental frequency component) at PCC						

Table A.4 Limit values for harmonic voltage (MV, HV and EHV)

Odd ranks not multiple of 3			Odd ranks multiple of 3			Even ranks		
Rank h	Harmonic voltage (%)		Rank h	Harmonic voltage (%)		Rank h	Harmonic voltage (%)	
	MV	HV, EHV		MV	HV, EHV		MV	HV, EHV
5	5	2	3	4	2	2	1.8	1.5
7	4	2	9	1.2	1	4	1	1
11	3	1.5	15	0.3	0.3	6	0.5	0.5
13	2.5	1.5	21	0.2	0.2	8	0.5	0.4
17	1.7	1	>21	0.2	0.2	10	1.47	0.4
19	1.5	1				12	0.42	0.2
23	1.2	0.7				>12	0.4	0.2
25	1.1	0.7						
>25	1.9×17	$0.2 + 0.5$						
>25	$/h-0.2$	$\times 25/h$						

Total harmonic distortion: THDMV = 6.5% in THDHV-EHV = 3%

Table A.5 Parameters of line, transformer and filter

Symbol	Quantity	Value
R_{ca}	Resistance of line and cable	0.019 (pu)
L_{ca}	Inductance of line and cable	0.016 (pu)
C_{ca}	Capacitor of line and cable	0.055 (pu)
R_{tr}	Resistance of transformer	0.0017 (pu)
L_{tr}	Inductance of transformer	0.05 (pu)
R_f	Resistance of filter	0.027 (pu)
L_f	Inductance of filter	0.186 (pu)

Table A.6 Parameters of the excitation system

Symbol	Quantity	Value
Tr	Low-pass filter time constant	20e-3 s
[K_a, T_a]	Regulator gain and time constant	[200, 0.02 s]
[K_e, T_e]	Exciter	[1, 0 s]
[T_b, T_c]	Transient gain reduction	[0 s, 0 s]
[K_f, T_f]	Damping filter gain and time constant	[0.001, 0.1 s]
[E_{fmin}, E_{fmax}, K_p]	Regulator output limits and gain	[0, 6 pu, 0]
[$V_{t0}(pu), V_{f0}(pu)$]	Initial values of terminal voltage and field voltage	[1, 1.42734] pu

Table A.7 Parameters of the filter, transformer Tr1-1 and transmission line L1-1

Symbol	Quantity	Value
P_{Tr}	Transformer nominal power (T_{r1-1})	40 MVA
R_f	R_L filter resistance	0.027 (pu)
L_f	R_L filter inductance	0.186 (pu)
R_{1-eq}	Resistance of Primary of the transformer	0.0083333 Ω
R_{2-eq}	Resistance of secondary of the transformer	9.9188.10-6 Ω
L_{1-eq}	Inductance of primary of transformer	7.9577.10-4 H
L_{2-eq}	Inductance of secondary of transformer	9.4717. 10-7 H
R_{L-eq}	Resistance of PI section line	0.4291 Ω
L_{L-eq}	Inductance of PI section line	0.0036 H
C_{L-eq}	Capacitor value of PI section line	5.3889.10-8 F

A.3 Primary Frequency Control

The fuzzy logic controller parameters are: $k_e = 0.5$, $k_{pe} = 0.2$, $k_{de} = 0.01$, $k_{dp} = 1.4$, $k_i = 0.6$ and $k_p = 0.8$.

The PI controller parameters are $k_p = 1.1$ and $k_i = 0.6$ (Tables A.2).

Table A.6 summarizes the parameters of the excitation system and Table A.7 gives Parameters of the filter, transformer Tr1-1 and transmission line L1-1. Table A.8 summarizes Parameters of the grid synchronous generator.

Table A.8 Parameters of the grid synchronous generator

Symbol	Quantity	Value
D	Load damping coefficient	1.0 s
R	Droop referred to percent speed regulator	0.6
ω_0	Rated rotor speed	1 pu
SG	Rated power of the grid generator	200 MW
V_n	Rated voltage (RMS Ph-Ph)	13.8 KV
H_G	Inertia constant of the grid generator	3.7 pu
T_G	Governor time constant	0.2 s
T_{CH}	Turbine time constant	0.3 s

A.4 Experimental Test Bench

The board that will be used to control the system is a dSPACE board of reference DS1104 (Fig. E. 1a). It is a board that allows easy development of applications in direct connection with a Matlab/Simulink interface. DS1104 makes the PC a powerful development system for fast execution of control laws. The Real-Time Interface provides Simulink blocks for graphical configuration of ADC inputs, DAC outputs, incremental encoder and PWM interface, etc.

The board is based on a 64-bit MPC8240 processor of the Power PC 630e type operating at 250 MHz, and a set of integrated peripherals. It also has:

- 4 multiplexed inputs with a resolution of 16 bits: ADCH1 to ADCH4
- 4 parallel inputs with 12-bit resolution: ADCH5 to ADCH8.

These inputs are BNC connectors placed on console and their voltage range is between $-10V$ and $+10V$. The maximum sampling frequency of the DSPace board is 100kHz, it also has :

- TMS320F240 DSP at 20 MHz
- 32-bit timer/counters
- Single and three phase PWM outputs
- 2 Incremental encoder interfaces
- A serial interface (UART)
- An interrupt controller.

Table A.9 Single phase parameters of the LCL filter

LCL filter element	Symbol	Required values	Available values	Percentage (%) of base values
Inductance of converter side	Li	1.5 mH	1.4 mH	9.396
Grid side inductance	Lg	197 uH	84 uH	1.224
The filter capacitor	Cf	15.7 uF	15 uF	2.5
The damping resistor	Rf	10 Ω	15 Ω	197.482

A.4.1 Measurement Circuits

The measurement circuits are designed in Proteus software for three current and five voltage sensors measurement. The two measurement circuit boards are designed to :

- Measure instantaneous voltages up to 500 V and instantaneous currents up to 25 A. This measurement is carried out using a LV25-P type voltage and LA55-P type current HALL effect sensor.
- The ADCs are protected so that the input voltage does not exceed the range $[-10\text{ V} + 10\text{ V}]$. Two acquisition cards are made, one with 3 current sensors and 3 voltage sensors and the other acquisition card with 2 voltage sensors and 2 current sensors. The circuit is designed in the Proteus software as shown in Fig. A.1.

The LCL filter parameters of the Fig. A.2 are listed in Table A.9.

A.4.2 RL Filter

The RL filter is designed with an inductance L and a resistance R to obtain a THD of less than 5% during nominal power injection and a voltage drop of less than 10% of the nominal voltage. The filter parameters and values are listed in Table A.10.

Table A.10 The RL filter parameters of Single phase

Filter element	Symbol	Value	Percentages (%) of base values
Inductance	Lf	3 mH	61.964
Resistance	Rf	2 ω	19.72

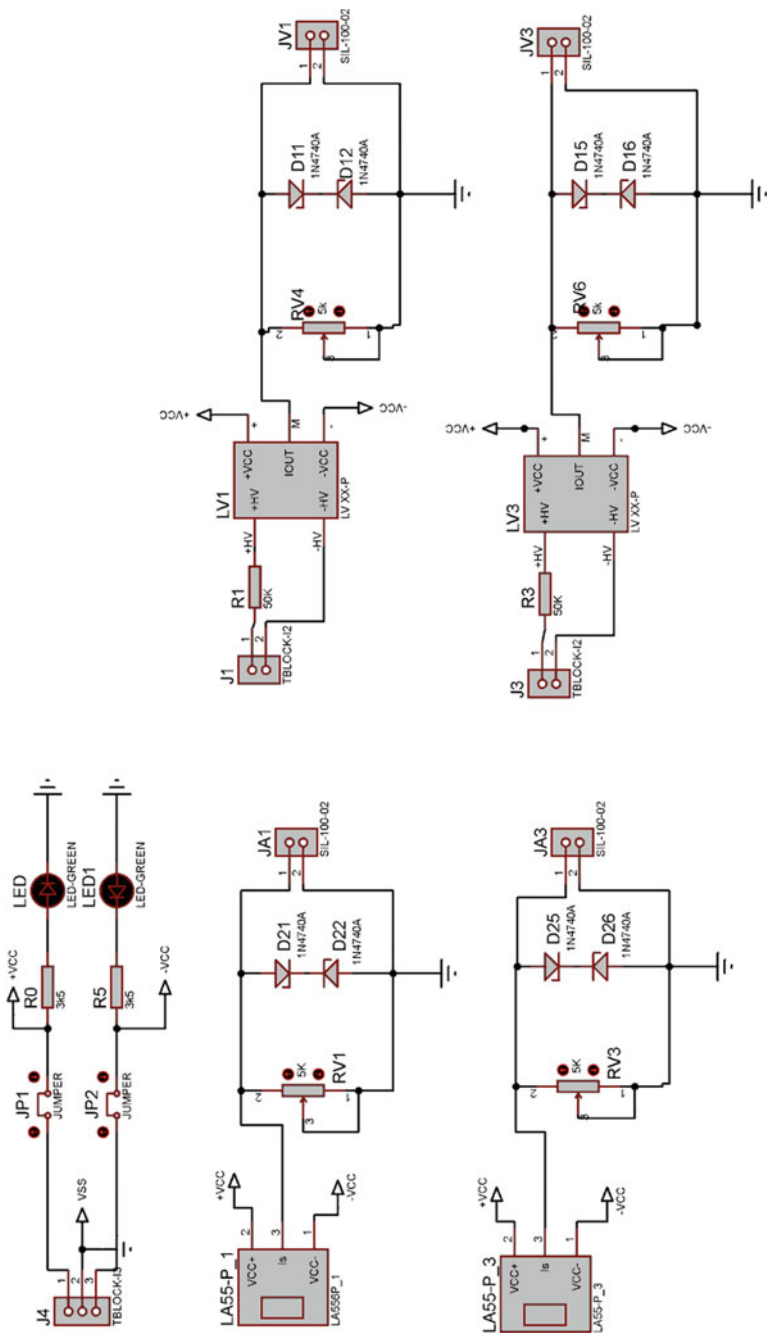


Fig. A.1 The realised measurement circuits

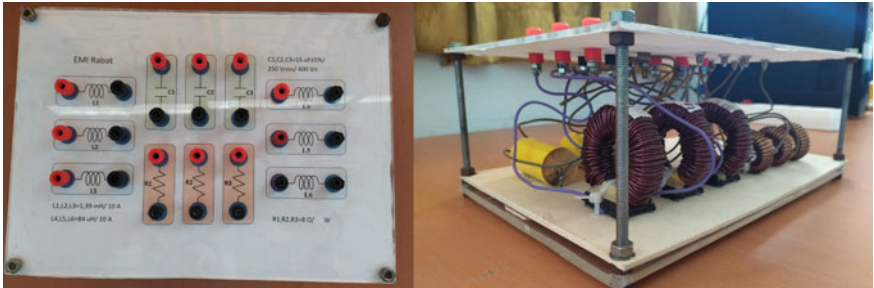


Fig. A.2 Photo of the designed LCL filter

The adaptation circuit is used to convert the PWM signals from DSPace (0–5 V) to the control signals for the inverter (0–15 V). This circuit is designed using Proteus (ISIS and ARES) design software and it is based on TLP250 optocouplers.

A.4.3 The SEMIKRON Three-Phase Inverter

The inverter used in this application is 3KW. It consists of an uncontrolled rectifier, a DC bus and the inverter. The picture of the inverter and its connectors is given in Fig. A.3.

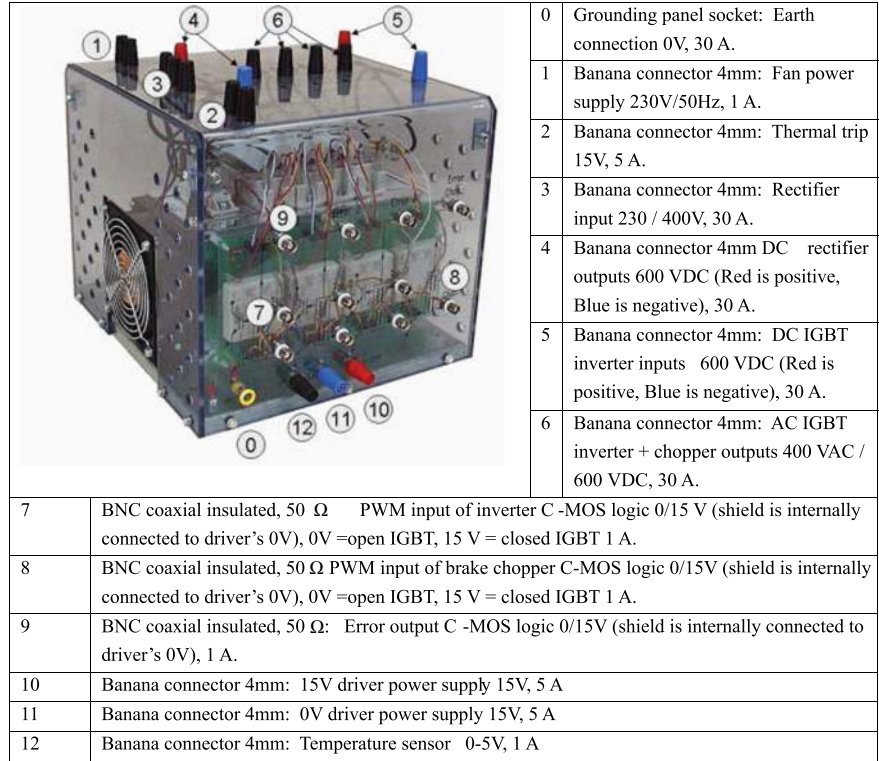


Fig. A.3 SEMIKRON three-phase inverter and its connectors

Appendix B

Part II: Technical and Economic Parameters of PV and CSP Plants

See Tables B.1, B.2, B.3 and B.4.

Table B.1 Technical parameters of the PV plant

Parameter	Symbol	Value
PV module		
Solar cell technology		Multi-cSi
Module power	P_{module}	250 W
Maximum voltage	$V_{mp,ref}$	30.4 V
Maximum current	$I_{mp,ref}$	8.2 A
Open circuit voltage	V_{oc}	38.4 V
Global reference radiation	G_{ref}	1000 W/m ²
Reference temperature	T_{ref}	25 °C
Efficiency of the module	η_{ref}	15.33%
Module area	A_{ref}	1.63 m ²
Temperature coefficient	γ_t	−0.456%/ C
Nominal temperature (NOCT)	T_{noct}	44.8 °C
Referencenominal temperature (NOCT)	$T_{noct,ref}$	20 °C
Nominal global radiation	$G_{noct,ref}$	800 W/m ²
Nominal heat transfer coefficient	U_{lnoct}	9.5
Inverter		
Inverter power	$P_{inverter}$	5000 W
Efficiency	$\eta_{inverter}$	96.3%

Table B.2 Economic parameters of the PV plant

Parameter	Symbol	Value
Cost of solar module	c_{mod}	0.45 \$/W
Cost of inverter	c_{inv}	0.13 \$/W
Installation labor	c_{eng}	0.15 \$/W
Balance of system	c_{elec}	0.10 \$/W
Installer margin and overhead	c_{str}	0.22 \$/W
Annual operating and maintenance costs	C_{pv}	10 \$/kW/year
Inflation factor	r	5%
Degradation factor	d	1%/year
Lifetime	T	25 year

Table B.3 Technical parameters of the CSP plant

Parameter	Symbol	Value
Solar field		
Type of technology CSP		Parabolic-trough
Nominal beam radiation	$B_{n,ref}$	950 W/m ²
Nominal temperature	$T_{amb,ref}$	25 °C
Nominal wind velocity	$v_{wind,ref}$	5 m/s
Spacing between the collector's rows,	$L_{spacing}$	15 m
Inlet temperature	$T_{ref}^{sf,in}$	293 °C
Outlet temperature	$T_{ref}^{sf,out}$	391 °C
Solar collector		
Type		Euro trough ET 150
Length of solar collector	L_{col}	150 m
Focal length	L_{focale}	
Aperture of the collector	A_{col}	817.5 m ²
Efficiency	η_{col}	86%
Receiver		
Type		Schott PTR70
Efficiency	η_{rec}	93%
Power block		
Type		Cycle de Rankine
Efficiency	η_{pb}	40%
Thermal storage		
Storage fluid		Hitec solar salt
Efficiency	η_{tes}	98.5%

Table B.4 Economic parameters of the PV plant

Parameter	Symbol	Value
Solar field	c_{col}	120\$/m ²
Heat transfer fluid	c_{htf}	50\$/m ²
Thermal storage system	c_{tes}	60\$/kWh _{th}
Power block	c_{pb}	1050\$/kWh _{el}
Balance of plant	c_{plant}	110\$/kWh _{el}
Fixed cost of operation and maintenance	C_{fixe}	20\$/MWh _{el}
Variable cost of operation and maintenance	C_{var}	0\$/MWh _{el}
Inflation factor	r	5%
Degradation factor	d	1%/year
Lifetime	T	25 years